UNIVERSIDADE FEDERAL DE MINAS GERAIS
Instituto de Geociências
Programa de Pós-Graduação em Geologia

Ricardo Pagung de Carvalho

GUANHÃES BASEMENT INLIER: a história tectônica de um fragmento do paleocontinente São Francisco e consequências regionais

Belo Horizonte
2024

Ricardo Pagung de Carvalho

GUANHÃES BASEMENT INLIER: a história tectônica de um fragmento do paleocontinente São Francisco e consequências regionais

Tese apresentada ao Programa de Pós-Graduação em Geologia da Universidade Federal de Minas Gerais como requisito parcial para obtenção do título de doutor em Geologia.

Orientador(a): Prof. Dr. Carlos Alberto Rosière

Coorientador(a): Prof. Dr. Tiago Amâncio Novo

Belo Horizonte
2024

C331g
2024

Carvalho, Ricardo Pagung de.

Guanhães Basement Inlier [manuscrito] : a história tectônica de um fragmento do paleocontinente São Francisco e consequências regionais / Ricardo Pagung de Carvalho. – 2024.

169 f., enc. il. (principalmente color.)

Orientador: Carlos Alberto Rosière.

Coorientador: Tiago Amâncio Novo.

Tese (doutorado) – Universidade Federal de Minas Gerais, Instituto de Geociências, 2024.

Área de concentração: Geologia Regional.

Bibliografia: f. 113-133.

Inclui apêndices.

1. Geologia estrutural – Teses. 2. Geoquímica – Teses. 3. Tempo geológico – Teses. I. Rosière, Carlos Alberto. II. Novo, Tiago Amâncio. III. Universidade Federal de Minas Gerais. Instituto de Geociências. IV. Título.

CDU: 551.243:550.93

Ficha catalográfica elaborada por Elisabete Quatrini Vieira – CRB-6/2210
Biblioteca “Vitória Pedersoli”, Instituto de Geociências da UFMG

UNIVERSIDADE FEDERAL DE MINAS GERAIS

PROGRAMA DE PÓS-GRADUAÇÃO EM GEOLOGIA DO IGC-UFMG

FOLHA DE APROVAÇÃO

"GUANHÃES BASEMENT INLIER: A HISTÓRIA TECTÔNICA DE UM FRAGMENTO DO PALEOCONTINENTE SÃO FRANCISCO E CONSEQUÊNCIAS REGIONAIS"

RICARDO PAGUNG DE CARVALHO

Tese submetida à Banca Examinadora designada pelo Colegiado do Programa de Pós-graduação em GEOLOGIA, como requisito para obtenção do grau de Doutor em GEOLOGIA, área de concentração GEOLOGIA REGIONAL, pelo Programa de Pós-graduação em Geologia do Instituto de Geociências da Universidade Federal de Minas Gerais.

Aprovada em 05 de março de 2024, pela banca constituída pelos membros:

Prof. Carlos AlbertoRosière - Orientador
UFMG

Profa Dra. Flávia Cristina Silveira Braga
UFMG

gov.br Documento assinado digitalmente
MATHEUS HENRIQUE KUCHENBECKER DO AMAR
Data: 05/03/2024 16:20:04-0300
Verifique em https://validar.iti.gov.br

Prof. Dr. Matheus Henrique Kuchenbecker do Amaral
UFVJM

Profa.Dra. Simone Cerqueira Pereira Cruz
UFBA

Prof. Dr. Ticiano José Saraiva dos Santos
UNICAMP

Belo Horizonte, 05 de março de 2024.

AGRADECIMENTOS

Primeiramente agradeço à minha família. À minha esposa Helga pelo apoio incondicional, paciência e compreensão dados os momentos de ausência decorrentes da elaboração da tese. Dedico também a minha filha Teresa que, vindo ao mundo durante a elaboração desta tese, arrancou de mim sorrisos alegres e sinceros em momentos de aflição. A meus pais e irmã que sempre acreditaram e me apoiaram nas minhas decisões.

Um agradecimento especial ao meu orientador Prof. Carlos Alberto Rosière por todo apoio e oportunidades criadas ao longo do trabalho. Levo comigo as críticas, lições e discussões como experiências que, sem dúvida, contribuíram para o meu amadurecimento tanto acadêmico quanto pessoal.

Ao meu coorientador Prof. Tiago Amâncio Novo pelas discussões esclarecedoras ao longo do trabalho.

Aos companheiros geológicos que me acompanharam nas várias campanhas de campo deste trabalho: Tamires Miranda, Humberto Júnior e Gustavo Miranda.

Gostaria de agradecer os então alunos de geologia do UniBH, hoje todos geólogos e geólogas, que me deram a oportunidade de orientar seus trabalhos de conclusão de curso em algumas regiões abrangidas por essa tese.

A empresa Anglo American pela parceria, particularmente ao geólogo Geraldo Sarquis e toda sua equipe. A geóloga Erika Conceição por facilitar o acesso a furos de sondagem para os estudos acadêmicos.

Ao CNPq pela bolsa de estudos (Pr. Nr. 163930/2021–0), fundamental para alunos de pós-graduação e para ciência brasileira. A oportunidade de participar do projeto de pesquisa: “A configuração tectônica do Complexo Guanhães e consequências metalogenéticas para a formação de seus depósitos de minério de ferro”. O presente trabalho foi realizado com apoio da Coordenação de Aperfeiçoamento de Pessoal de Nível Superior - Brasil (CAPES) - Código de Financiamento 001.

RESUMO

O Guanhães *Basement Inlier* (GBI) abrange uma extensa área do domínio externo do Orógeno Araçuaí no estado de Minas Gerais. Sua assembleia Arqueana e Paleoproterozoica é composta por ortognaisses e granitos Meso a Neoarqueanos, pela grande província ígnea silícica Borrachudos de idade Estateriana e por duas sequências metassedimentares distintas, as quais são separadas por uma discordância erosiva: o Grupo Serra da Serpentina, portador de formação ferrífera bandada, e o Grupo Serra de São José, relacionado ao Supergrupo Espinhaço Inferior. Com o objetivo de elucidar a evolução tectônica Paleoproterozoica do GBI, diversos métodos investigativos foram empregados. A análise geoquímica de rocha total da Formação Meloso, a unidade basal do Grupo Serra da Serpentina, revela que seus sedimentos clásticos compreendem componentes de fonte derivados do manto e da crosta superior, resultantes da erosão da Suíte máfico-ultramáfica Serro-Alvorada de Minas, das rochas magmáticas do Orógeno Minas-Bahia e de terrenos arqueanos. Os resultados, em conjunto com dados publicados, sugerem a abertura de uma bacia de retroarco ao longo do arco magmático Mantiqueira em resposta ao Orogêno Minas-Bahia, onde o Grupo Serra da Serpentina foi depositado associado ao afinamento crustal e ao desenvolvimento local de vulcanismo submarino. Esta assembleia apresenta similaridades com o Supergrupo Minas superior, que compreende os Grupos Piracicaba, Sabará e Itacolomi, sugerindo sedimentos correlatos, embora sejam necessárias investigações adicionais. A análise geológica e estrutural, combinada com estudos de isótopos U-Pb-Hf de zircões detríticos de unidades siliciclásticas distribuídas no GBI, juntamente com dados publicados dos arredores, delineia a direta ligação entre a deposição das unidades do Espinhaço Inferior e à colocação e exumação da Suíte Borrachudos durante o Estateriano. Esta ligação traz o conceito da porção sul do GBI representar um *Crustal Core Complex* funcionando como um alto estrutural que emergiu durante os estágios iniciais da abertura da bacia Espinhaço. Os resultados demonstram que a evolução tectônica Paleoproterozoica do GBI é caracterizada pela superposição de dois eventos tectônicos distintos, o mais antigo relacionado ao Orógeno Riaciano-Orosiriano Minas-Bahia, onde o Grupo Serra da Serpentina foi depositado em uma bacia de retroarco associada ao magmatismo máfico- ultramáfico da Suíte Serro-Alvorada de Minas. Posteriormente, durante o sistema de rifteamento Estateriano Espinhaço, o Grupo Serra de São José e o

magmatismo da Suíte Borrachudos representaram uma interação prolongada entre o crescimento do *crustal core complex* e o desenvolvimento do rift. Este trabalho contribui para uma compreensão mais abrangente da evolução crustal Paleoproterozoica do GBI e abre portas para pesquisas futuras em diversas direções, como por exemplo o refinamento geocronológico de unidades tanto metassedimentares e ígneas, investigações estruturais mais detalhadas do Guanhães *Crustal Core Complex*, além de análises geoquímicas e isotópicas para fornecer interpretações adicionais sobre a evolução tectônica do GBI.

Palavras-chave: Paleoproterozóico; Guanhães Basement Inlier; Grupo Serra da Serpentina; Sequência Espinhaço Inferior; geoquímica de rochas siliciclásticas; isótopos U-Pb-Hf em zircão detrítico; Evolução tectônica.

ABSTRACT

The Guanhães Basement Inlier (GBI) covers a large area of the western external domain of the Araçuaí Orogen in the Minas Gerais state. Its Archean and Paleoproterozoic assembly is composed of Meso- to Neoarchean orthogniesses and granites, Statherian Borrachudos silicic large igneous province and two distinguish metasedimentary sequences, which are separated by an erosional unconformity: the BIF-bearing Serra da Serpentina Group and the Lower Espinhaço Supergroup-related Serra de São José Group. With the purpose to elucidate the Paleoproterozoic tectonic evolution of the GBI, several investigative methods were employed. Whole-rock geochemical analysis of the Meloso Formation, the basal unit of the Serra da Serpentina Group, reveal that its clastic sediments comprise mantle and upper crustal-derived source components, resultant from erosion of the mafic-ultramafic Serro-Alvorada de Minas Suite, the Minas-Bahia Orogen magmatic rocks, and the Archean terranes. The results, in combination with published data, suggest the opening of a back-arc basin stretching along the Mantiqueira magmatic arc in response to the Minas-Bahia Orogen, where the Serra da Serpentina Group was deposited associated with crustal thinning and local development of submarine volcanism. This assembly shares similarities with the upper Minas Supergroup that comprises the Piracicaba, Sabará, and Itacolomi groups suggesting a cogenetic sedimentation, although further investigations are demanded. Geological and structural analysis, coupled with U-Pb-Hf isotope studies of detrital zircons from siliciclastic units across the GBI, in combination with published data from the surroundings, delineates the link between the provenance and timing of deposition of the Lower Espinhaço units and the contemporaneous Borrachudos Suite emplacement and exhumation during the Statherian. This link brings the concept of the Guanhães Crustal Core Complex as a structural high that emerged during the lately stages of the Lower Espinhaço basin opening. The results demonstrate that the Paleoproterozoic tectonic evolution of the GBI is characterized by superposition of two distinct tectonic events, the earlier related to the Rhyacian-Orosirian Minas-Bahia Orogen where the Serra da Sepentina were deposited in a possible back-arc basin associated with the mafic-ultramafic Serro-Alvorada de Minas Suite. Later, during the Statherian Espinhaço rift system, the Serra de São José Group and the coeval Borrachudos Suite magmatism represented a protracted interplay between crustal core complex growth and rift development. This

work contributes to a more comprehensive understanding of the Paleoproterozoic crustal evolution of the GBI, and it opens doors for further research in several directions such as refinement of the geochronological framework, Structural detailed investigations of the Guanhães Crustal Core Complex, and geochemical and isotopic analyses to provide additional constraints about the tectonic evolution of the GBI.

Keywords: Paleoproterozoic; Guanhães Basement Inlier; Serra da Serpentina Group; Lower Espinhaço Sequence; siliciclastic rock geochemistry; detrital zircon U-Pb-Hf isotopes; tectonic evolution.

LISTA DE ILUSTRAÇÕES

Figure 1: Geological map of the Guanhães Basement inlier and its surroundings. ...18

Figure 2: (a) Structural interpretation of the Conceição do Mato Dentro mining district; inversion of the stratigraphic sequence and duplication by folding. (b) Detail of Monomitic metaconglomerate interbed with quartzite that occurs between the Serra do Sapo Fomation and the Meloso Formation. (c) Harmonic folded banded iron formation clast within the basal SJG conglomerate. 20

Figure 3: Chart showing the main units that comprise the Quadrilátero Ferrífero, Southern Espinhaço Range, Eastern border of Southern Espinhaço Range, Guanhães Basement Inlier and Eastern border of the GBI terranes versus time. References: (1) Lana et al. (2013), (2) Teixeira et al. (1998), (3) Noce et al., 1998), (4) Moreno et al. (2017), (5) Romano et al. (2013), (6) Machado et al. (1989), (7) Silva et al., 2002), (8) Teixeira et al. (2015), (9) Hartmann et al. (2006), (10) Babinski et al. (1995), (11) Rossignol et al. (2020), (12) Brueckner et al. (2000), (13) Dopico et al. (2017), (14) Dutra et al. (2019), (15) Machado et al. (1996), (16) Jordt-Evangelista et al. (2015), (17) Duque et al. (2020), (18) Caxito et al. (2020), (19) Dutra et al. (2020), (20) Freimann et al. (2021), (21) Cabral and Zeh (2015), (22) Cabral et al., 2022), (23) Chemale et al. (2012), (24) Chaves and Coelho (2018), (25) Guadagnin et al. (2015), (26) Hagedorn (2004), (27) Rolim et al. (2016), (28) Barrote et al. (2017), (29) Carvalho et al. (2014), (30) Magalhães et al. (2018), (31) Gomes et al. (2020), (32) Silveira Braga et al. (2019), (33) Silveira Braga et al. (2015), (34) Noce et al. (2007), (35) Heilbron et al. (2010). 26

Figure 4: (a) Regional tectonic context of the study area emphasizing the Precambrian rocks distribution. (b) Geological map of the southeastern border of the southern Espinhaço Range and its relationship with the western border of the Guanhães Basement Inlier. It=Itapanhoacanga, CMD=Conceição do Mato Dentro, MP=Morro do Pilar, RMC=Rio Mata Cavalo, ME=Morro Escuro, MTT=Minas Tectonic Terranes, Mb=Mineiro belt, M=Mantiqueira Complex, JF=Juiz de Fora Complex. Adapted and modified after Carvalho et al. (2014), Pinto and Silva (2014) and Rolim et al. (2016). 37

Figure 5: Paleoproterozoic assembly of the Minas Tectonic Terranes (MTT), the eastern border of the southern Espinhaço Range, the Guanhães basement inlier, and the southernmost portion of the Minas-Bahia Orogen. (1) Hartmann et al. (2006), (2) Babinski et al. (1995), (3) Cabral and Zeh (2015), (4) Cabral et al. (2022), (5) Rossignol et al. (2020), (6) Brueckner et al. (2000), (7) Dopico et al. (2017), (8) Dutra et al. (2019), (9) Machado et al. (1996), (10) Jordt-Evangelista et al. (2015), (11) Duque et al. (2020), (12) Caxito et al. (2020), (13) Dutra et al. (2020), (14) Hagedorn (2004), (15) Rolim et al. (2016), (16) Machado et al. (1989), (17) Barrote et al. (2017), (18) Magalhães et al. (2018), (19) Silveira Braga et al. (2015), (20) Silveira Braga et al. (2019), (21) Barbosa

et al. (2019), (22) Teixeira et al. (2015), (23) Noce et al. (2007), (24) Heilbron et al. (2010). 39

Figure 6: (a) The lithological profile of the Serra da Serpentina and Serra de São José groups in the Conceição do Mato Dentro mining district, Morro do Pilar, Morro Escuro ridge and Guanhães depositional domain. The samples distribution was bound by the contact between the Meloso and Serra do Sapo formations as vertical reference datum to cluster samples collected from different drill cores. CMD = Conceição do Mato Dentro Suite. (b) Basal turbiditic-like quartzite in the Guanhães depositional domain. (c) Detailed of the turbiditic-like quartzite. 44

Figure 7: Photomicrographs showing the mineral association and microstructural features of the main lithotypes of the Meloso Formation. (a-b) Green schist exhibiting well-developed foliation defined by alternation of fine quartz grains and sericite/chlorite layers. Garnet can occur associated with the phyllonitic fabric commonly developed in the serite/chlorite rich layers. (c, d) Green schist showing unmetamorphosed cores where sedimentary fabric is preserved; sub-rounded to well-rounded quartz and rare plagioclase grains occur immersed in a very fine matrix. (e) Carbonaceous(?)-sericite crenulated gray phyllite. (f) Oxide-rich quartzite showing conspicuous foliation. (g, h) garnet-staurolite-mica schist from the Morro Escuro amphibolite facies domain. (i) Photograph of MOES-20 thin section showing folded compositional bedding layers; note the association of well-formed garnet with the carbonaceous(?) layer. (j, k, l) Detail of the MOES-20 sample: tremolite-biotite rich layer, garnet-bearing layer and microstructural relationship between the carbonaceous layer with the biotite-quartz rich layer. Qz = quartz, Ser = sericite, Chl = chlorite, Grt = garnet, Plag = plagioclase, Carb = amorphous carbonaceous material, Bt = biotite, St = staurolite, Trem = tremolite. 47

Figure 8: Log of the Fe_2O_3/K_2O vs. log of SiO_2/Al_2O_3 diagram (Herron, 1988) of the Meloso Formation to determine the protolith of metamorphic sedimentary rock. 49

Figure 9: PAAS-normalized trace elements plots for the Meloso Formation. PAAS after Taylor and McLennan (1985). Diagrams a, b and c exhibit the three different elemental patterns distribution for the analyzed samples. The colors are related to the analyzed lithotype, see Figure 8. 52

Figure 10: Rare-earth element concentrations normalized to the PAAS (Taylor and McLennan, 1985) for the metasedimentary rocks from the Meloso Formation. Diagrams a, b, c and d exhibit the various REE patterns distribution for the analyzed samples. The colors are related to the analyzed lithotype, see Figure 8. 54

Figure 11: (a) A-CN-K (Al_2O_3 – CaO* + Na_2O – K_2O) triangular diagram and CIA (Chemical Index of Alteration) scale (Nesbitt and Young, 1984). (b) A-CNKM-F (Al_2O_3, CaO*+Na_2O+K_2O+MgO, Fe_2O_3) triangular diagram and MIA(O) (Mafic Index of Alteration) (Babechuk et al., 2014). (c) AF-CNK-M (Al_2O_3+Fe_2O_3, CaO*+Na_2O+K_2O, MgO) diagram and MIA(O). Pink arrows indicate the weathering trend of analyzed

samples, dashed arrows indicate the predicted weathering trend. References are from (Condie, 1993).....57

Figure 12: Sedimentary provenance diagrams of the Meloso Formation. (a) La/Th vs. Hf (ppm) plot (Floyd and Leveridge, 1987). (b) Plot of Th/Sc versus Zr/Sc showing trend for modern turbidites (McLennan et al., 2003). (c) Th/Co vs. La/Sc plot (Cullers, 2002). (d) Plot of Th/U versus Th based in modern turbidite muds from various tectonic settings (McLennan et al., 1993). (e) Discriminant diagram for sedimentary rocks (Roser and Korsch, 1988). (f) Cr/V versus Y/Ni plot monitoring exotic (ultramafic) components (McLennan et al., 1993). 59

Figure 13: Ternary tectonic discrimination diagrams of trace elements for the Meloso Formation, (a) Sc-Th-Zr/10, (b) La-Th-Sc and (c) Co-Th-Zr/10 (Bhatia and Crook, 1986). New discriminant function multidimensional diagrams for (d) high-silica and (e) low-silica clastic sediments of the Meloso Formation (Verma and Armstrong-Altrin, 2013). 61

Figure 14: Schematic model of the evolution of the Serra da Serpentina back-arc basin in response to the Rhyacian Minas-Bahia Orogen. See text for explanation.....66

Figure 15: Distribution of the back-arc system during the Minas-Bahia orogeny.1 = Serra da Serpentina Basin, 2 = Piracicaba, Sabará, Itacolomi assembly, 3 = Riacho dos Machados meta-volcanosedimentary sequence, 4 = Caetité Sequence, 5 = Colomi Group. Gray color represents Archean Blocks. 69

Figure 16: (a) Simplified geotectonic map of the São Francisco craton with distribution of Archean to Paleoproterozoic rock units, and position of the Guanhães Basement Inlier. (b) Geological map of the Guanhães Basement Inlier and surrounding units (Pinto and Silva, 2014). 76

Figure 17: (a) Geological map of the study are with sample locations and published geochronological data, modified from Pinto and Silva (2014). (b) Detailed geological map of the Morro Escuro ridge region (modified from Carvalho et al. (2014). (1) Rolim et al. (2016), (2) Silveira Braga et al. (2015), (3) Carvalho et al. (2014), (4) Barrote et al. (2017), (5) Silveira Braga et al. (2019), (6) Gomes et al. (2020), (7) Magalhães et al. (2018), (8) Silveira (2016), (9)Dutra et al. (2020), (10) Oliveira et al. (2019). 79

Figure 18: (a) Lithological profiles of metasedimentary sequences of the southern border of the Espinhaço Range and the Interior supracrustal units (Morro Escuro BIF-bearing sequence, Guanhães BIF-bearing succession and undivided schist and quartzite packages). (b) Lithostratigraphic position of Paleoproterozoic rock units exposed within the Southern Espinhaço Range, eastern border of the southern Espinhaço Range, and in the Guanhães basement inlier. Age references: (1) Machado et al. (1989), (2) Chaves and Coelho (2018), (3) Chemale et al. (2012) (4) Hagedorn (2004), (5) Rolim et al. (2016), (6) Magalhães et al. (2018); (7) Barrote et al. (2017),

(8) Carvalho et al. (2014), (9) Silveira Braga et al. (2019) (10) Silveira Braga et al. (2015) and (11) Cabral and Zeh (2015).....81

Figure 19: (a) Mylonitic fabric with rootless, sub-horizontal NNE-SSW-trending asymmetrical east-verging intrafolial Z-folds. (b) Centimeter-scale folded mylonitic foliation suggesting progressive evolution of the deformation. Younger N-S reverse faults with a top-to-west motion intersecting the mylonitic gneissic banding. (c) Metric-scale asymmetrical east-verging fold pointing to normal sense movement. (d) centimeter-scale asymmetrical southeast-verging fold near Ipatinga. (e) Vertical oriented contact between the Borrachudos Suite (B) and the Archean gneiss of the Guanhães Complex (G) showing tight to isoclinal asymmetrical folds suggesting a pluton-side-up movement sense. 83

Figure 20: Structural map of the southern segment of the Guanhães basement inlier, with pole figures showing the orientation of foliation (contoured fields) and mineral/stretching lineations (dots). White star - foliation maximum; red star - lineation maximum; blue star - calculated b-axis. 85

Figure 21: (a) Sabinópolis shear zone: d-porphyroclasts (K-feldspar) in granite mylonite of the Borrachudos Suite indicating eastward tectonic movement. (b) shear bands of the Sabinópolis shear zone disrupting magmatic structure of the Borrachudos Suite. (c) Sigmoidal geometry indicates dextral motion of the southernmost portion of the Sabinópolis shear zone. (d) S-C structure defining sinistral sense of movement of the Morro Escuro shear zone (e) S-C -C' foliation of the Dom Silvério shear zone. (f) Mylonitic foliation indicating sinistral sense of movement of the Virgolândia shear zone. (g) Borrachudos Suite (Açucena pluton) overthrusting gneissic rocks of the Guanhães Complex. (h) Isoclinal SW verging-folds associated to shear bands of the Braúnas shear zone.....88

Figure 22: Back-scattered electron (BSE) images of zircon grains with spot positions for U-Pb and Lu-Hf isotope analyses by LA-ICP-MS. For each spot the following results are presented: Th/U ratio, εHf(t) value, $^{207}Pb/^{206}Pb$ age (with 2 sigma error), and degree of concordances (in percent). m – image of zircon morphology, i – image of internal structure. Analyses of zircon rims, with Th/U<0.1 are highlighted in blue.....90

Figure 23: Zircon core and rim analyses plotted in Th/U versus age diagram.....91

Figure 24: Age spectra of detrital zircon populations from the Serra de São José Group, presented in relative probability plots and histograms. (a) Sample 03-084. (b) Sample 07-001. (c) Sample 08-001. (d) Sample 08-002. (e) Sample 10-001. (only zircon grains with concordance level 90-110%).....92

Figure 25: Epsilon Hf vs. age diagrams showing the results of (a) detrital zircon analyses from the Serra de São José Group (this study), and (b) comparison with published data from the São Francisco Craton (data sources: M'2018 – Magalhães et

al., 2018; G'2020 – Gomes et al., 2020; D'2018 – Degler et al., 2018; C'2020 – Cutts et al., 2020; D'2017 – Dopico et al., 2017; K'2014 – Koglin et al., 2014). Fields with numbers 1 to 6 refer to tectono-magmatic events on the São Francisco Craton: 1-Espinhaço rift system and associated magmatism, 2-Minas-Bahia Orogeny, 3-Mamona event, 4-Rio das Velhas II event, 5-Rio das Velhas I event, 6-Santa Barbara event. CHUR-chondritic uniform reservoir, DM-depleted mantle evolution, Stath.-Statherian, Orosi.- Orosirian, Rhyac.- Rhyacian, Sider.- Siderian. Diagonal lines represent crustal evolutionary trends for 176Lu/177Hf = 0.0113 that intersect the DM evolutionary line at 2.5, 3.0, 3.5 and 4.0 Ga, respectively. 93

Figure 26: Detrital age distribution of the Lower Espinhaço Sequence (only data with concordance level 90-110%). 98

Figure 27: Conceptual evolutionary model of the long-term development of the crustal core complex-rift Borrachudos Suite (Guanhães gneiss)-Lower Espinhaço Sequence. 101

Figure 28: BSE images of zircon (z) and baddeleyite (b) crystals from samples colected in the Rio Mata Cavalo metavolcanosedimentary sequence and Serro ultramafic Suite. 106

Figure 29: Lithological profile of the Serra da Serpentina and Serra de São José groups in the Conceição do Mato Dentro mining district and Frequency histogram and probability curve of the sample 351, collected from the fine-grained quartzite interlayered with Serra do Sapo banded iron formation. 108

Figure 30: (a) Geological map emphasizing the east to southeast-verging N-S structural trend from Sabinópolis to João Monlevade (modified from Pinto and Silva (2014). (b) Geological map of the Monlevade and Rio Piracicaba quadrangles (Reevers, 1966) and sample locations. 110

LISTA DE TABELAS

Table 1: Pearson correlation coefficient (r) of major and trace elements for siliciclastic metasedimentary rocks from the Meloso Formation.....50

Table 2: Compilation of maximum depositional ages (MDA) derived from the Lower Espinhaço Sequence 96

SUMMARY

1 INTRODUCTION 17

1.1 Problem statement #1 19

1.1.1 Hypothesis statement 20

1.2 Problem statement #2 22

1.1.2 Hypothesis statement 23

1.2 Thesis objectives 23

1.3 Methodology 24

2 GEOLOGICAL SETTING 26

2.1 Archean assembly 28

2.2 Siderian to Orosirian assembly 29

2.3 Statherian assembly 32

3 RESEARCH PAPER - THE SERRA DA SERPENTINA GROUP: A BACK-ARC BASIN RELATED TO THE PALEOPROTEROZOIC MINAS-BAHIA OROGENY? .35

3.1 Introduction 36

3.2 Geological background 38

3.2.1 The Minas-Bahia Orogen 39

3.2.2 The eastern border of the southern Espinhaço Range 40

3.2.3 The Guanhães basement inlier 41

3.2.4 The Minas Tectonic Terranes (MTT) 42

3.3 Sampling and analytical methods 43

3.4 Results 43

3.4.1 Petrography of the Meloso Formation 45

3.4.2 Whole-rock geochemistry 46

3.4.2.1 Major and trace elements characteristics 48

3.4.2.2 Rare earth elements 52

3.4.2.3 Paleo-weathering 55

3.4.2.4 Provenance 57

3.4.2.5 Tectonic setting 60

3.5 Discussion 61

3.5.1 The Serra da Serpentina basin: geochemistry of the Meloso Formation 62

3.5.2 The Serra da Serpentina back-arc basin: a new proposition 64
3.5.3 Regional implications 67
3.6 Conclusions 69
4 RESEARCH MANUSCRIPT - UNCOVERING THE ESPINHAÇO SUPERGROUP IN THE GUANHÃES BASEMENT INLIER, MINAS GERAIS, BRAZIL: TECTONIC IMPLICATIONS BASED ON STRUCTURAL GEOLOGY AND DETRITAL ZIRCON U-PB-HF ISOTOPE RECORD 71
4.1 Introduction 72
4.2 Geological setting 74
4.2.1 Guanhães Basement Inlier (GBI) 74
4.2.2 The eastern border of the southern Espinhaço Range 75
4.2.3 The interior supracrustal units 77
4.2.4 The Espinhaço Supergroup and associated volcanism 77
4.3 Samples 78
4.4 Analytical methods 80
4.4.1 Zircon separation and imaging 80
4.4.2 U-Pb zircon geochronology 80
4.4.3 Lu-Hf isotope analyses 81
4.5 Structural analyses 82
4.5.1 Archean to Paleoproterozoic structures 82
4.5.2 Shear zones related to the Araçuaí Orogen 84
4.5.2.1 Sabinópolis and Conceição shear zones 84
4.5.2.2 Pedra Branca-Morro Escuro shear system 84
4.5.2.3 Dom Silvério and Coroací shear zones 86
4.5.2.4 Virgolândia shear zone 86
4.5.2.5 GBI internal shear zones 86
4.6 Results of zircon U-Pb dating 89
4.7 Results of Lu-Hf isotope analyses 92
4.8 Discussion 94
4.8.1 Maximum depositional age of the Lower Espinhaço Sequence 94
4.8.2 Source of detrital zircons 96
4.8.3 The Guanhães Crustal Core Complex 99
4.9 Conclusions 103

5 RESEARCH IN PROGRESS 105

5.1 The age of the Serra da Serpentina back-arc basin 105

5.1.1 Crystallization age of the Serro-Alvorada de Minas Suite 105

5.1.2 Maximum depositional age of the Serra da Serpentina Group 107

5.2 Serra da Serpentina basin and Upper Minas units: chrono-correlates? 109

6 CONCLUDING REMARKS 111

6.1 Rhyacian to Orosirian crustal evolution of the Guanhães Basement inlier 111

6.2 Statherian crustal evolution of the Guanhães Basement inlier 111

6.3 Future approaches 112

REFERENCES 113

APPENDIX A – CHEMICAL COMPOSITION OF THE MELOSO FORMATION 134

APPENDIX B – U-PB LA-ICPMS DATA 138

APPENDIX C – LU-HF ISOTOPE DATA 154

APPENDIX D – U-PB LA-ICPMS DATA – SAMPLE 351 164

1 INTRODUCTION

Located in the central portion of Minas Gerais State, at the external domain of the Araçuaí Orogen (Alkmim et al., 2017), the poorly understood Guanhães Basement Inlier (GBI) occupies a significant area of ca. 24,000 km^2. It is bordered on the west by the Statherian to Stenian Espinhaço Supergroup (Alkmim and Martins-Neto, 2012; Chemale et al., 2012), to the south by the Neoarchean to Rhyacian Quadrilátero Ferrífero mining district (Chemale et al., 1994; Rosière et al., 2008), and the east and north by the Cryogenian Macaúbas Group (Kuchenbecker et al., 2015) (Figure 1). The GBI is interpreted as a structural-erosive window that exposes igneous, metamorphic, and sedimentary rocks from a wide range of ages, from the Archean to the Mesozoic (Kuchenbecker and Barbuena, 2023). The present thesis explores the development of the GBI's Paleoproterozoic assembly, with a focus on the crustal evolution from the Rhyacian to the Statherian periods.

In the GBI, the occurrences of economically banded iron formations (BIF), and associated rocks (Serra da Serpentina Group – SSG; Rolim et al., 2016), have been studied in detail since the volatile market price of iron ore increased worldwide in 2005 (Almeida-Abreu and Renger, 2007; Barrote et al., 2017; Carvalho et al., 2014; Rolim et al., 2016; Silveira Braga et al., 2021, 2019, 2015). Although significant results have been achieved, the tectonic environment in which the BIF-bearing Serra da Serpentine Group sedimented, as well as its relationship with the Espinhaço Supergroup is still a matter of debate.

Almeida-Abreu and Renger (2007) incorporate the SSG, in combination with ultramafic rocks of the Serro-Alvorada de Minas Suite (Hagedorn, 2004; Zapparoli, 2001), into the basal sequence of the Statherian-Stenian Espinhaço rift system. In contrast, Rolim et al. (2016) not only attribute an Orosirian maximum depositional age to the SSG but also recognize an erosional unconformity separating it from the overlying Statherian Espinhaço system-related Serra de São José Group (SJG), suggesting that the SSG's deposition predates the sedimentation of the basal units of Espinhaço Supergroup.

Figure 1: Geological map of the Guanhães Basement inlier and its surroundings.

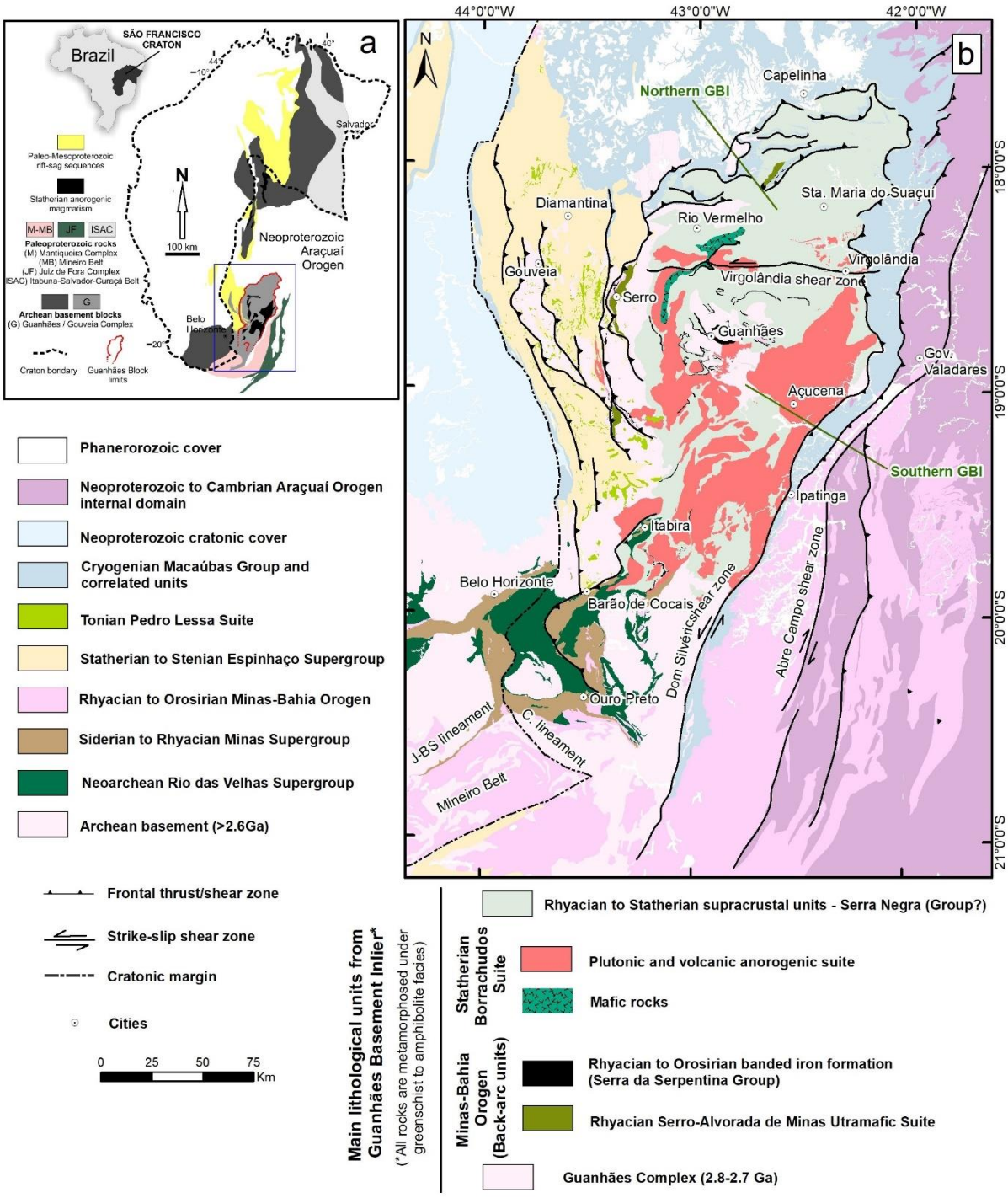

Source: Pinto and Silva (2014)

Sedimentary rocks hold invaluable records of Earth's dynamic past, preserving a wealth of information about the ancient environments in which they were deposited, the erosion and transport processes that shaped them, and the tectonic events that influenced their formation. In this thesis, a combination of techniques including geochemistry of siliciclastic rocks, U-Pb-Hf detrital geochronology, and structural

analyses were applied to address some questions and problems that remain open to effectively unravel the intricate history of the Paleoproterozoic tectonic evolution of the Guanhães Basement Inlier. The current geological issues and the hypothesis tested in this study are presented in the following sections.

1.1 Problem statement #1

Rolim et al. (2016) acknowledged an unconformity surface that delineates the upper boundary between the Serra da Serpentina Group (SSG) and the overlying Serra de São José Group (SJG) in the western boundary of the GBI. The unconformity is characterized by quartzites and rudaceous rocks containing reworked banded iron formation and dolomite fragments. Rolim et al. (2016), based on robust detrital zircon dataset, postulate, based on the youngest zircon grain, the maximum depositional age (MDA) of the SJG at 1666 ± 32 Ma (SHRIMP U-Pb) and correlated it as a facies variation of the Espinhaço basal São João da Chapada Formation (Lower Espinhaço Sequence – 1.80 to 1.68 Ga; Chemale et al., 2012).

Conversely, the MDA of the SSG (SHRIMP U-Pb 1999 ± 16 Ma; Rolim et al., 2016) is established based on a single Orosirian detrital zircon grain recovered from a quartzite, which is located right below the contact with the upper Serra do Sapo iron formation in the vicinity of the Conceição do Mato Dentro mining district. This quartzite package is interpreted as belonging to the metapelitic Meloso Formation, the basal unit of the SSG (Rolim et al., 2016).

As a result of the development of iron ore mining in the Conceição do Mato Dentro region, the identification of new geological relationships in outcrop scale has emerged, leading to new questions regarding the stratigraphic position of the horizon that counts the youngest zircon grain dated at 1990 ± 16 Ma by Rolim et al. (2016). At the open pit mine, sheared, clast-supported, monomictic (BIF clasts largely predominating over quartzite and vein quartz) metaconglomerate interlayered with oxide-rich quartzites and schists are exposed between the Serra do Sapo iron formation and the Meloso Formation (Figure 2). This sequence is typically attributed to the Statherian Lapão Formation, the basal unit of the Serra de São José Group (Rolim et al., 2016).

An extensive drill core description, however, reveals a lateral continuity of this rudaceous package (up to 35 m thick) for, at least, 10 kilometers along the regional

NNW-SSE structural trending of the Serra do Sapo ridge, including the location of the sample JC-176 that delivered the youngest zircon age of 1999 ± 16 Ma (Rolim et al., 2016). These new findings suggest that the key sample responsible for the interpretation of the MDA of the Serra da Serpentina Group may have been collected within the erosional unconformity surface, thus belonging stratigraphically to the younger Serra de São José Group.

1.1.1 Hypothesis statement

The frequent occurrence of tight to isoclinal asymmetric S-Z fold pair (metric in size) associated with west-verging shear zones recognized within the Serra do Sapo iron formation (compressional phases 1 and 2 of Rolim et al., 2016), in combination with the under-layered metaconglomerate, indicates inversion of the stratigraphic sequence and possibly duplication by folding of the iron ore layer (Figure 2a and b). Moreover, harmonic folded banded iron formation clasts are ubiquitous in the SJG conglomerate (Figure 2b and c), indicating folding (or shearing) of Serra da Serpentina Group previous to the deposition of the Serra de São José Group.

Figure 2: (a) Structural interpretation of the Conceição do Mato Dentro mining district; inversion of the stratigraphic sequence and duplication by folding. (b) Detail of Monomitic metaconglomerate interbed with quartzite that occurs between the Serra do Sapo Fomation and the Meloso Formation. (c) Harmonic folded banded iron formation clast within the basal SJG conglomerate.

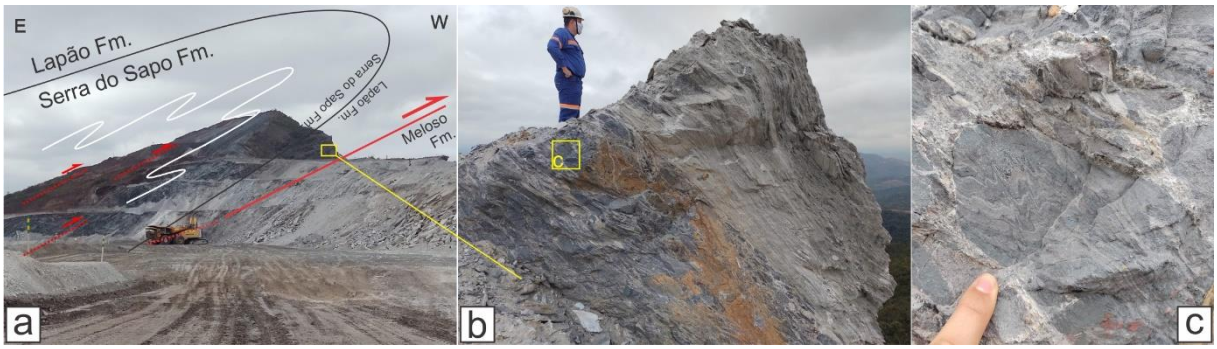

Source: Prepared by the author

This evidence contradicts the correlation between the SSG with the Statherian Espinhaço rocks as proposed by Almeida-Abreu and Renger (2007). Instead, it suggests that the Serra da Serpentina BIF-bearing sequence, indeed, predates the Espinhaço Sequence (Chemale et al., 2012), agreeing with the interpretation of Rolim et al. (2016). Nevertheless, its precise maximum depositional age remains uncertain

due to the lack of suitable coarse-grained siliciclastic rocks and/or interlayered igneous rocks within the Serra da Serpentina Group on the eastern border of the southern Espinhaço Range (type locality).

Barrote et al. (2017), based on geochemistry and detrital age spectrum distributions, correlated the banded iron formations that occur in the interior of the Guanhães Basement Inlier with the Serra da Serpentina Group. In contrast with the eastern border of the Southern Espinhaço Range, the BIF-bearing sequence from Guanhães is frequently associated with coarse-grained quartzites, which produced a slightly older maximum depositional age (SHRIMP U-Pb 2.18 Ga; Barrote et al. 2017) when compared to the Orosirian sample reported by Rolim et al. (2016).

Rhyacian to Orosirian crystallization ages are widely reported in the Minas-Bahia orogenic system (MBO), which occurs further east. The MBO was responsible for amalgamating Archean blocks to consolidate the São Francisco-Congo proto-craton from at ca. 2.2 to 1.9 Ga (eg. Aguilar et al., 2017; Alkmim and Teixeira, 2017; Ávila et al., 2014; Barbosa et al., 2015; Cutts and Lana, 2019; Heilbron et al., 2010; Noce et al., 2007; Seixas et al., 2013; Teixeira et al., 2017). The erosional products of rocks related with the MBO are interpreted as the Rhyacian-Orosirian sources for the basin infilling of the SSG, as well as the SJG in the Guanhães Basement Inlier (Barrote et al., 2017; Carvalho et al., 2014; Rolim et al., 2016; Silveira Braga et al., 2019, 2015).

If the 2.18 Ga MDA of the Serra da Serpentina Group is correct, which deformational event affected the banded iron formation prior to the deposition of the Serra de São José Group?

It is reported Late Rhyacian to Early Orosirian zircon and monazite metamorphic ages from samples associated with the MBO: 2043-2077 Ma, Marinho, (2014); 2060 Ma, Medeiros Júnior et al. (2016); 2085-2041 Ma, Noce et al. (2007); 2015 Ma, Cutts et al. (2018). Thus, the combination of these ages indicate a metamorphic/deformational event around 2.05 Ga in the region.

Considering the emerging evidence of a possible Rhyacian maximum depositional age for the SSG and the regional Orosirian metamorphic event associated with the Minas-Bahia Orogen, an important question arises: was the Serra da Serpentina Group deposited and deformed between 2.18 and 2.05 Ga?

1.2 Problem statement #2

The poorly understood Guanhães Basement Inlier (also referred to as Guanhães Block) has been interpreted as a single puzzle piece (microcontinent) in the reconstruction of the paleotectonic framework of the São Francisco protocraton during the Minas-Bahia Orogen (eg. Bruno et al., 2021; Teixeira et al., 2017), without the direct evidence of tectonic sutures with the neighboring terranes. Kuchenbecker and Barbuena (2023) bring a critical review concerning the Rhyacian-Orosirian paleotectonic configuration of the GBI and expose two different interpretative alternatives involving the Minas-Bahia orogenic system to form the São Francisco protocraton. Both interpretations show the Guanhães Block as part of a bigger paleocontinent encompassing the Archean terranes exposed in the Quadrilátero Ferrífero Tectonic Block. They further highlight the numerous extensional events that affected this paleocontinental block from the Statherian to the Tonian periods before the Neoproterozoic-Cambrian Araçuaí Orogen. In this context, unraveling the complex geological history of the GBI requires a comprehensive understanding of these extensional processes, particularly those associated with the Statherian period, as the Tonian rocks, which are relatively better constrained, represent the precursor basin infill of the Araçuaí Orogen (eg. Alkmim et al., 2017, 2006; Amaral et al., 2020; Kuchenbecker et al., 2015; Pedrosa-Soares et al., 2001).

The record of the Statherian extensional event in the GBI is envisaged by the emplacement of a voluminous amount of A-type granites in combination with subordinate amphibolite bodies, characterizing the bimodal silicic large igneous province named Borrachudos Suite (Dussin et al., 2000; Gomes et al., 2020; Magalhães et al., 2018). The Borrachudos Suite is directly linked to the nucleation of the Espinhaço rift system, which occurs in its typical location further west in the Southern Espinhaço Range (eg. Almeida-Abreu, 1995; Almeida-Abreu et al., 1989; Almeida-Abreu and Renger, 2007; Chemale et al., 2012; Dussin and Dussin, 1995; Herrgesell and Pflug, 1986; Knauer, 2013; Machado et al., 1989; Santos et al., 2013). In this region, Statherian volcanic rocks correlated to the Borrachudos Suite are interbedded with the basal syn-depositional units of the Espinhaço Supergroup. These volcanic rocks also are interpreted as responsible for fertilizing those basal units with the younger Statherian zircon population at around 1710 Ma (eg. Alkmim and Martins-

Neto, 2012; Chemale et al., 2012; Dussin and Dussin, 1995; Guadagnin et al., 2015; Santos et al., 2013).

In the interior of GBI, Barrote et al. (2017) and Silveira Braga et al. (2019, 2015) recognized Statherian detrital ages in siliciclastic rocks associated with the BIF-bearing Serra da Serpentina Group, indicating that the basal units of the Espinhaço Supergroup occur also beyond the Southern Espinhaço Range.

These findings raise new questions about the Statherian crustal evolution in the region: (i) what is the extent of the Espinhaço Supergroup within the GBI? (ii) What is the relationship between the Statherian sedimentary rocks and the plutonic rocks of the Borrachudo Suite in the GBI terrane? (iii) What role did the emplacement of the Borrachudos Suite play during the formation of the Espinhaço basin?

1.1.2 Hypothesis statement

To effectively address these questions, it is essential to establish two fundamental hypothetical scenarios: 1) the Statherian sedimentary units were originally deposited directly over the basement rocks of the present-day Guanhães Basement Inlier (autochthonous hypothesis), or 2) these units were tectonically transported to their current location (allochthonous hypothesis).

1.2 Thesis objectives

The main objectives of this work are:

- To investigate the interplay between the depositional histories of the Serra da Serpentina and Serra de São José groups, and the tectonic significance of the intervening erosional unconformity.
- To clarify the tectonic setting on which the aforementioned groups were deposited**.**
- To establish the Paleoproterozoic crustal evolution of the Guanhães Basement Inlier and its implications for the broader tectonic context.

The specific objectives of this work are:

- To delineate the tectono-structural framework of the Guanhães Basement Inlier

- To investigate the geochemical signature of metapelitic rocks of the Meloso Formation, thereby elucidating the prevailing conditions at the source area related to paleo-weathering and constraining their tectonic setting and provenance.
- To examine the extent of the occurrence of the Lower Espinhaço Sequence within the Guanhães Basement Inlier through detrital zircon U-Pb age and its relationship with the contemporaneous Statherian Borrachudos Suite.
- To characterize the isotopic signature of Lu-Hf in detrital zircon grains to determine the provenance of the material that contributed to the deposition in the Lower Espinhaço basin.

1.3 Methodology

The following are the methods applied to achieve the proposed objectives.

- Geological mapping and structural analyses:

A comprehensive geological survey was conducted through the implementation of conventional field mapping methods. A total of 1,018 sites were described, generating 1,562 measurements of planar structures and 484 measurements of linear structures. The field work was complemented by the in-depth analysis and interpretation of airborne geophysical data (magnetometry and gamma-spectrometry), provided by the Companhia de Desenvolvimento de Minas Gerais (CODEMGE). Detailed analysis of borehole cores provided by mining companies in the area contributed to the interpretation of the subsurface geology.

- Geochemistry characterization:

Chemical analyses were carried out at the Bureau Veritas Labs, Vancouver. Whole-rock major and minor elements compositions were obtained by Inductively Coupled Plasma Emission Spectrometry (ICP-ES) and Inductively Coupled Plasma Mass Spectroscopy (ICP-MS) were used for determining trace and rare earth elements.

- U-Pb zircon geochronology:

The methodology applied for the U-Pb zircon dating are detailed described in the section 4.4 of this thesis.

- Lu-Hf isotope analyses:

The methodology applied for the Lu-Hf isotopic analyses are detailed describe in the section 4.4 of this thesis.

2 GEOLOGICAL SETTING

To understand the regional geological setting through a time-based approach involves reconstructing the sequence of geological events highlighting the evolution of the crust through time. By referencing geologic time, the regional setting is placed within a chronological framework, focusing on the major stratigraphic units, their ages, and the geological processes that formed them. In this section, it is presented the geologic terranes that surround the Guanhães Basement Inlier and share temporal similarities with it. The terranes are the Quadrilátero Ferrífero, the Southern Espinhaço Range, the Easter Border of Southern Espinhaço Range, and the Eastern Border of Guanhães Basement Inlier, as prime examples of this time-based approach. Figure 3 illustrates the geochronological distribution (from Mesoarchean to Mesoproterozoic) of the main geologic terranes mentioned above, as well as the tectonic and magmatic events responsible to shape them. The geologic map illustrating the spatial distribution of these terranes is shown in the Figure 1.

Figure 3: Chart showing the main units that comprise the Quadrilátero Ferrífero, Southern Espinhaço Range, Eastern border of Southern Espinhaço Range, Guanhães Basement Inlier and Eastern border of the GBI terranes versus time. References: (1) Lana et al. (2013), (2) Teixeira et al. (1998), (3) Noce et al., 1998), (4) Moreno et al. (2017), (5) Romano et al. (2013), (6) Machado et al. (1989), (7) Silva et al., 2002), (8) Teixeira et al. (2015), (9) Hartmann et al. (2006), (10) Babinski et al. (1995), (11) Rossignol et al. (2020), (12) Brueckner et al. (2000), (13) Dopico et al. (2017), (14) Dutra et al. (2019), (15) Machado et al. (1996), (16) Jordt-Evangelista et al. (2015), (17) Duque et al. (2020), (18) Caxito et al. (2020), (19) Dutra et al. (2020), (20) Freimann et al. (2021), (21) Cabral and Zeh (2015), (22) Cabral et al., 2022), (23) Chemale et al. (2012), (24) Chaves and Coelho (2018), (25) Guadagnin et al. (2015), (26) Hagedorn (2004), (27) Rolim et al. (2016), (28) Barrote et al. (2017), (29) Carvalho et al. (2014), (30) Magalhães et al. (2018), (31) Gomes et al. (2020), (32) Silveira Braga et al. (2019), (33) Silveira Braga et al. (2015), (34) Noce et al. (2007), (35) Heilbron et al. (2010).

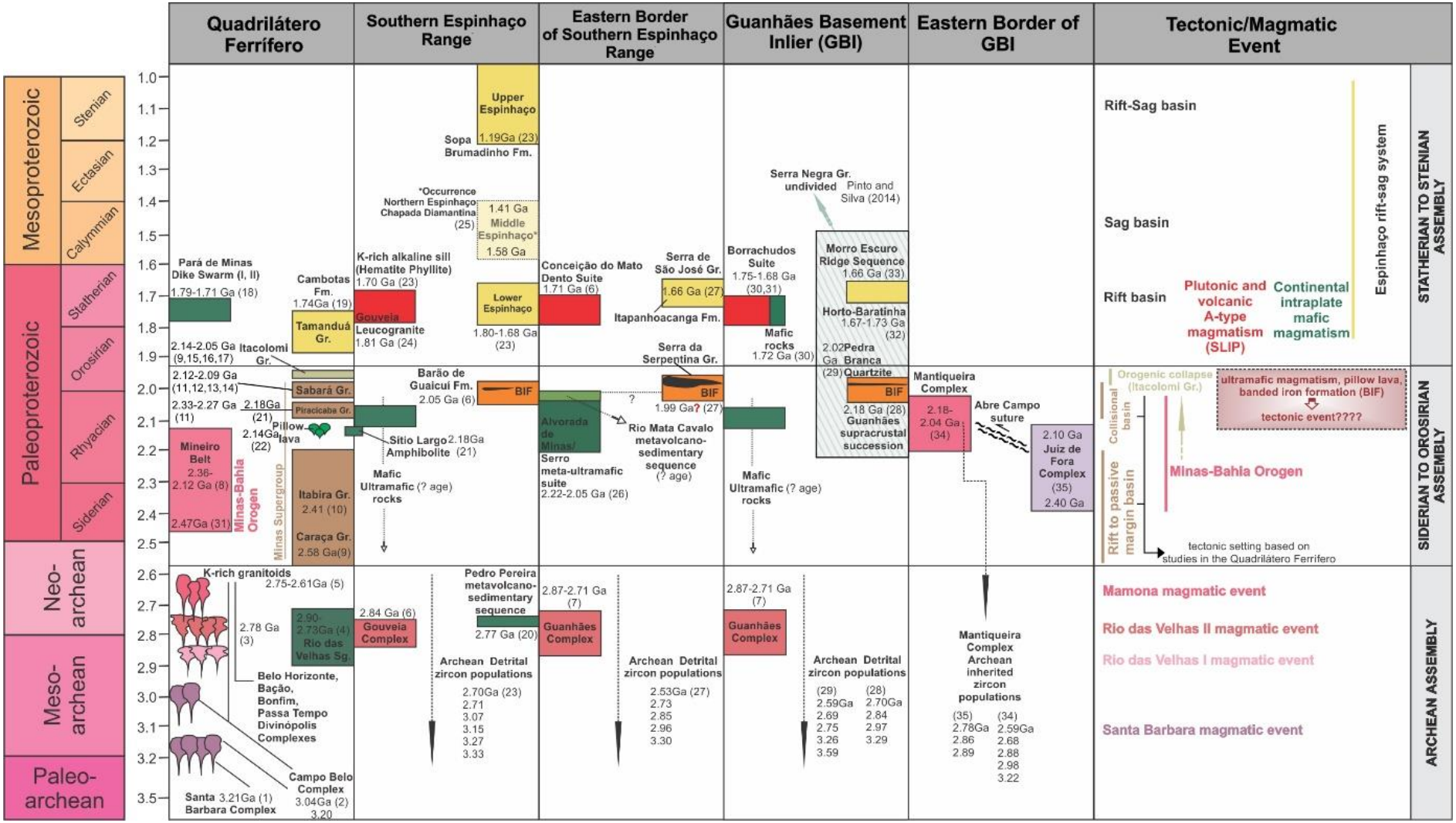

Source: Prepared by the author

2.1 Archean assembly

The Archean core is well constrained in the southern portion of the São Francisco Craton by extensive geological studies conducted in the polymetallic world-class Quadrilátero Ferrífero mining district. This area is characterized by a dome-shaped terrane composed primarily of Archean gneiss and granitoid rocks, where it is recognized the presence of older tonalite-trondhjemite-granodiorite (TTG) rocks at its core, while younger granitoids preferentially occur towards the margins. Traditionally, seven main complexes have been identified: Santa Bárbara, Bonfim, Belo Horizonte, Bação, Divinópolis, Campo Belo, and Passa Tempo (Albert et al., 2016; Brando Soares et al., 2020; Farina et al., 2015; Lana et al., 2013; Machado and Carneiro, 1992; Moreno et al., 2017; Romano et al., 2013).

Four main magmatic and tectonic events are recognized in the Quadrilátero Ferrífero area (Albert et al., 2016; Farina et al., 2015; Lana et al., 2013; Romano et al., 2013): Santa Barbara, Rio das Velhas I and II, and Mamonas. The Santa Bárbara event marks the emplacement of the 3.2 Ga TTG rocks in the Santa Bárbara complex. The Rio das Velhas I and II events are considered to be a response to the initiation of subduction and arc formation at ca. 2.9 and 2.8 Ga, respectively, and coeval deposition of the Rio das Velhas Supergroup. The Mamona event which is related to a late (ca. 2.7 Ga) collisional stage and stabilization of the continental mass that yielded the widespread late Neoarchean potassium-rich magmatism.

The Rio das Velhas Supergroup, an Archean greenstone belt, is subdivided in the Nova Lima and Maquiné groups (Baltazar and Zucchetti, 2007; Dorr II, 1969). The basal Nova Lima Group exhibits a distinctive association of mafic and ultramafic rocks, with immature clastic sediments indicative of a submarine volcanic environment. Three felsic volcanic events at ca. 2792 to 2751 Ma (Machado and Carneiro, 1992; Noce et al., 2005)and sandstones with a maximum depositional age of 2749 ± 7 Ma (Hartmann et al., 2006) records the final stages of deposition of the Nova Lima Group. The Maquiné Group is comprised by a 2 km-thick flysch to molasse-type sequence of conglomerates and sandstones, with a maximum depositional age of approximately 2730 Ma (Moreira et al., 2016) that resulted from the erosion of a continental block with ages spanning from 3260 to 2877 Ma (Machado et al., 1996).

A less detailed Archean assembly is exposed in the Southern Espinhaço Range and its eastern border as well as in the Guanhães Basement Inli~~n~~er, comprised by the Gouveia and Guanhães complexes. In the Espinhaço Range, a granite body belonging to the Gouveia Complex yields a crystallization age of 2840 Ma (U-Pb-zircon) (Machado et al., 1989). In the same area, basic to ultrabasic schists, banded iron formation, ferruginous chert, and metarhyolite (2771 Ma; Freimann et al., 2021) encompass the Pedro Pereira metavolcanosedimentary sequence tectonically juxtaposed to the gneissic rocks. This sequence is time-correlatable to other Neoarchean greenstone belts such as the Rio das Velhas Supergroup in the Quadrilátero Ferrífero. In the eastern border of Espinhaço Range, Rolim (2016) determinates a crystallization age for the Jacém granite (Guanhães Complex) at 2711 Ma. In the GBI, Silva et al. (2002) obtained crystallization ages ranging from 2870 to 2710 Ma for granite-gneiss rocks from the Guanhães Complex.

Detrital zircon analyses from metasedimentary rocks from the Southern Espinhaço Range, its eastern border, and the GBI reveal a broad spectrum of Archean ages spanning from the Paleo- to Neoarchean periods (Barrote et al., 2017; Carvalho et al., 2014; Chemale et al., 2012; Rolim et al., 2016; Silveira Braga et al., 2015, 2019). In the eastern border of the Guanhães Basement Inlier, situated within the Rhyacian-Orosirian Minas-Bahia Orogen terranes, Archean inherited zircon cores are widely distributed (Bruno et al., 2021; Cutts et al., 2020; Cutts and Lana, 2019; Degler et al., 2018; Heilbron et al., 2010; Noce et al., 2007).

2.2 Siderian to Orosirian assembly

In the Quadrilátero Ferrífero, the Minas Supergroup has been extensively studied through zircon U–Pb provenance analyses, offering crucial insights into its evolution and tectonic significance during the transition Archean to Paleoproterozoic. The Minas Supergroup is viewed as a <2.58–2.0 Ga passive margin transitioning to a syn-orogenic succession (Minas-Bahia Orogen) (e.g., Alkmim and Marshak, 1998; Bekker et al., 2003; Cabral et al., 2012; Duque et al., 2020; Dutra et al., 2019; Gonçalves and Uhlein, 2022; Hartmann et al., 2006; Rossignol et al., 2020). The basal Caraça Group was deposited during the early mechanical-subsidence phase of a precursor Archean passive margin basin at <2580 Ma (Hartmann et al., 2006; Koglin et al., 2014). The intermediate units of the Minas Supergroup are represented by the Itabira Group

followed by the Piracicaba Group. The former consists mainly by banded iron formations and carbonates dated at 2420 Ma (Babinski et al., 1995). The Itabira Group is unconformity overlayed by thick deltaic and shallow-marine strata as young as 2333 Ma (Rossignol et al., 2020), representing the Piracicaba Group. Cabral and Zeh (2015) limited the depositional age of the Piracicaba Group based on crystallization age of the N-MORB affinity Sítio Largo amphibolite at 2188 Ma, which unconformably overlies the banded iron formation of the Itabira Group. Similar Rhyacian crystallization age is reported from a pillow lava at Rola Moça Ridge, in the Quadrilátero Ferrífero, at 2141 Ma (Cabral et al., 2022).

The Sabará Group, the uppermost unit of the Minas Supergroup, is composed of clastic immature and flysch-like metasedimentary rocks that contains detrital zircon grains bracketed between ca. 2125 Ma and 2098 (Brueckner et al., 2000; Dutra et al., 2019; Dopico et al., 2017; Rossignol et al., 2020). The alluvial and fluvial sediments of the Itacolomi Group are regarded as a molasse sequence (Alkmim and Marshak, 1998) yielding Rhyacian maximum depositional age at 2059 Ma (Machado et al., 1996).

The Mineiro Belt (Quadrilátero Ferrífero area), Mantiqueira Complex, and Juiz de Fora Complex (eastern border of the GBI) are recognized as fragments of the Rhyacian-Orosirian Minas-Bahia Orogen (Transamazonian orogeny), amalgamated to the paleocontinent São Francisco during the inversion and closure of the Minas basin.

The Mineiro Belt comprises plutonic suites spanning in age from 2.47 to 2.0 Ga, accompanied by associated supracrustal sequences that include carbonaceous phyllites, gondites, quartzites, metagreywackes, and mafic to ultramafic metavolcanics (eg. Ávila et al., 2014; Barbosa et al., 2015; Teixeira et al., 2015). Positioned adjacent to the Archaean São Francisco Craton, the Mineiro Belt is delineated by the NE-SW trending Jeceaba-Bom Sucesso Lineament and the NW-SE trending Congonhas Lineament (Moreira et al., 2018). The supracrustal rocks in the Mineiro Belt, deposited between 2.3 and 2.1 Ga, and reveal a significant contribution of Archaean detritus (Ávila et al., 2014; Seixas et al., 2013; Teixeira et al., 2015).

The Mantiqueira Complex, situated in the easternmost section of the Archaean crust of the southern São Francisco Craton, underwent significant modification during the Palaeoproterozoic (Bruno et al., 2021, 2020; Duarte et al., 2004; Heilbron et al., 2010;

Noce et al., 2007). This complex comprises an heterogeneous assemblage of calc-alkaline gneiss–migmatitic suites with amphibolite layers, primarily composed of banded biotite-amphibole orthogneisses. U–Pb isotopic data depict a complex and prolonged evolution for the magmatic arc plutons, recording magmatic crystallization ages ranging from around 2203 to 2041 Ma in their rims, along with a substantial number of inherited Archaean zircon cores dating between approximately 3200 Ma and 2600 Ma. The rocks of Mantiqueira Complex are interpreted as originated from crustal-contaminated magmas in an active-margin setting (Heilbron et al., 2010; Noce et al., 2007).

The eastern boundary of the Mantiqueira Complex is interpreted as a Palaeoproterozoic suture (Degler et al., 2018; Alkmim and Teixeira, 2017) defined by the Abre Campo shear zone, which separates the predominantly amphibolite facies Mantiqueira Complex from the granulite facies Juiz de Fora Complex. The Juiz de Fora Complex is primarily composed of metamorphosed juvenile granitic orthogneisses, including enderbites and mafic rocks, exhibiting magmatic ages ranging from 2400 to 2100 Ma probably from an intra-oceanic magmatic arc (Machado et al., 1996; Fischel et al., 1998; Silva et al., 2002; Noce et al., 2007; Heilbron et al., 2010; Degler et al., 2018).

Rhyacian to Orosirian detrital and crystallization ages are reported from the Costa Sena Group in the southern Espinhaço range, and from the Serra da Serpentina Group and Serro-Alvorada de Minas metautramafic to mafic suite in the eastern border of the Espinhaço range.

Santos (2015) ascribes a single detrital age (95% concordant) of the Barão do Guaicuí Formation (Costa Sena Group) at 2114 ± 13 Ma. A metarhyolite from the same group was dated at 2049 Ma by Machado et al. (1989). The Serra da Serpentina Group, in the eastern border of Espinhaço range, makes up the mountain crests protected by the Serra do Sapo iron formation and canga duricrust. In the low-lands and valleys, psammopelitic units are poorly exposed between quartzite crests comprising the Meloso Formation. The Serra da Serpentina Group is interpreted as deposited in a tectonically stable sag basin, and a few Orosirian detrital zircon grains indicate 1.99 Ga maximum depositional age (Rolim et al., 2016). In the Guanhães Basement Inlier, several BIF-bearing metasedimentary strata tectonically inserted in gneissic rocks of

the Guanhães Complex yields a maximum depositional age of 2.18 Ga age (Barrote et al., 2017). Discontinuous bodies of ultramafic rocks exposed along the eastern border of the southern Espinhaço range (Serro-Alvorada de Minas meta-ultramafic Suite) yield crystallization age at 2.05 to 2.22 Ga (Hagedorn, 2004).

2.3 Statherian assembly

In the southern Espinhaço Range outcrop the Espinhaço Supergroup, which comprises an approximately 6000-meter-thick sequence of sandstones, pelites, conglomerates, volcanic rocks, and minor carbonates, all rocks metamorphosed under greenschist facies (eg. Alkmim et al. 2017; Pflug 1965, 1968; Scholl and Fogaça 1979; Dussin et al. 1984; Almeida-Abreu 1993; Uhlein et al. 1998; Martins-Neto 1998, 2000, 2009). Along the southern Espinhaço range, the units encompass a basal rift sequence followed by a rift-sag accumulation developed within an intracontinental basin between 1.8 to 1.0 Ga (Chemale et al. 2012; Alkmim and Martins-Neto 2012; Santos et al. 2013; Guadagnin and Chemale 2015).

The Lower Espinhaço Sequence, in the type locality of Diamantina, is composed of the basal Bandeirinha Formation (MDA = 1785 Ma, Santos et al., 2013), which is separated from the overlying São João da Chapada Formation by an apparent unconformity, although a gradational contact is locally exposed. The Bandeirinha Formation comprises an approximately 200 m-thick package of quartz-rich sandstones and coarse-grained conglomerates, deposited in fault-bonded depocenters (Martins-Neto, 1998; Santos et al., 2013).

The São João da Chapada Formation comprises a 300-meter-thick sequence of coarse-grained sandstones with pelitic intercalations deposited in a braided fluvial system (Martins-Neto, 1998; Schöll and Fogaça, 1979). Detrital zircon grains indicate a Paleoproterozoic MDA of ca. 1710 Ma for the São João da Chapada Formation (Chemale et al., 2012; Santos et al., 2013).

In the eastern border of the Espinhaço range, the Serra de São José Group, is comprised, from the botton to top, by the Lapão, Itapanhoacanga, Jacém, and Canjica formations (Rolim et al., 2016) that embodies a comprehensive cycle of transgressive sedimentary deposits, sedimented during the extension of the Espinhaço intracontinental rift-basin around 1.66 Ga (Rolim, 2016; Rolim et al., 2016). These

authors propose a lateral facies variation with the São João da Chapada Formation. Silveira (2016) assigns a somewhat younger maximum depositional age of 1.63 Ga for the Itapanhoacanga Formation.

Statherian maximum depositional ages are also described in two distinct localities within the Guanhães Basement Inlier: Morro Escuro ridge and the Horto-Baratinha iron ore deposit. Silveira Braga et al. (2015) attribute a maximum depositional age of approximately 1.68 Ga to a metaconglomerate and quartzites from Morro Escuro ridge. A similar maximum depositional age of 1.67 Ga was obtained from the upper quartzite unit of the Horto-Baratinha iron ore deposit (Silveira Braga et al., 2019). These authors correlate those units with the Lower Espinhaço Sequence.

In the Cambotas ridge at the NE limit of the Quadrilátero Ferrífero terrane, ruditic and psammitic rocks constitute the Tamanduá Group, which is correlated with the Lower Espinhaço Sequence. This group yield a Statherian maximum depositional age of approximately 1740 Ma (Dutra et al., 2020). Similar siliciclastic rocks are exposed in the surroundings of Altamira and Ipoema region with depositional age of 1750 Ma (Oliveira et al., 2019).

A coeval Statherian magmatism, considered as the source rocks responsible for providing the youngest zircon populations during the deposition of the Lower Espinhaço Sequence, is recognized in the Quadrilátero Ferrífero, southern Espinhaço Range, and the eastern border of the Espinhaço Range, as well as in the Guanhães Basement Inlier, however are absent in the eastern border of the Guanhães Basement Inlier.

In the Quadrilátero Ferrífero region is recognized the Pará de Minas tholeiitic dyke swarm. Zircon and baddeleyite U-Pb dating demonstrate two magmatic pulses at approximately 1795 and 1710 Ma, concordant with mafic and felsic volcanic intercalations at the base of the rift-related Espinhaço Supergroup in the Espinhaço range region (Caxito et al., 2020). In the Espinhaço range region, the sedimentary succession represented by the São João da Chapada Formation is transected and stratiform interlayered by alkaline volcanic rocks, which intruded at of ca. 1710 Ma (Chemale et al., 2012; Machado et al., 1989). Chaves and Coelho (2013) report U-Th-Pb chemical ages of monazite grains within K-feldspar of leucogranite, which intruded

the Gouveia Complex, revealing crystallization age around 1810 Ma. The Conceição do Mato Dentro Suite, mostly composed of metarhyolites and metarhyodacites, represents the Statherian magmatism in the eastern border of the Espinhaço range and has been dated at 1715 Ma (Machado et al., 1989). In the Guanhães Basement Inlier, extensive granitic batholiths belonging to the Borrachudos Suite occupied a vast area. This suite, alongside smaller amphibolite bodies, are considered as evidence of a Statherian SLIP (silicic large igneous province) that crystallized between from 1790 to 1690 Ma, coinciding with the Espinhaço rifting event (eg. Gomes et al., 2020; Kuchenbecker & Barbuena, 2023; Magalhães et al., 2018).

3 RESEARCH PAPER - THE SERRA DA SERPENTINA GROUP: A BACK-ARC BASIN RELATED TO THE PALEOPROTEROZOIC MINAS-BAHIA OROGENY?

Authors: *Ricardo Pagung[a], Carlos Alberto Rosière[b], Rosaline C. Figueiredo e Silva[b]

[a] Programa de Pós-Graduação em Geologia, Instituto de Geociências, Universidade Federal de Minas Gerais, Belo Horizonte, MG, Brazil.

[b] Instituto de Geociências, Universidade Federal de Minas Gerais, Belo Horizonte, MG, Brazil.

* Corresponding author. Universidade Federal de Minas Gerais, CPMTC, Instituto de Geociências, Av. Presidente Antônio Carlos, 6627 Pampulha, Belo Horizonte, MG, Brazil.

E-mail addresses: ripagung@gmail.com (R. Pagung), crosiere@gmail.com (C.A. Rosière), rosalinecris@yahoo.com.br (R.C. Figueiredo e Silva)

Keywords: Serra da Serpentina Group, Geochemistry, Back-arc basin, Minas-Bahia Orogen

DOI: 10.1016/j.jsames.2023.104427

Abstract

In the Rhyacian and Orosirian periods, Archean crustal fragments and Paleoproterozoic magmatic arcs were amalgamated into the São Francisco-Congo Paleocontinent during the Minas-Bahia orogeny. In the foreland terranes of the orogen, a BIF-bearing metasedimentary sequence including the Serra da Serpentina Group and its correlates is extensively exposed but still poorly characterized. A geochemical study undertaken in the basal succession of Serra da Serpentina Group comprising schists, phyllites, and quartzites of the Meloso Formation, delineates the characteristics of the sediment source and constrain the tectonic environment and crustal evolution of the Serra da Serpentina basin. Trace and REE geochemistry studies reveal that clastic sediments of the Meloso Formation comprise mantle and upper crustal-derived source components. The meta-ultramafic Serro-Alvorada de Minas Suite, the Minas-Bahia magmatic rocks, and the Archean TTG terranes are the main potential source rocks for the Meloso basin infilling, as also suggested by the detrital zircon age spectra. Our results suggest the opening of a back-arc basin stretching along the Mantiqueira magmatic arc in response to the Minas-Bahia Orogen during the Rhyacian-Orosirian. The Serra da Serpentina Group was deposited in this environment associated with crustal thinning and local development of submarine volcanism. This assembly shares similarities with the upper Minas Supergroup that comprises the Piracicaba and Sabará groups, suggesting a cogenetic sedimentation.

3.1 Introduction

The São Francisco-Congo paleocontinent is the result of the amalgamation of Archean fragments sutured in the Rhyacian-Orosirian. Orogenic terranes that comprise the Paleoproterozoic Minas-Bahia Belt are exposed in two different segments: (i) the northern portion of the São Francisco craton, represented by the Gavião, Jequié, Serrinha and Itabuna-Salvador-Curaçá blocks (Barbosa et al., 2008; Barbosa and Sabaté, 2004; Martins de Sousa et al., 2020; Teixeira de Souza et al., 2019), and (ii) the reworked basement inliers within the surrounding Neoproterozoic Araçuaí orogen system further south, which comprises Archean granite-greenstone terranes, the Minas Supergroup, the Mineiro Belt, and the Mantiqueira and Juiz de Fora complexes (Figure 4a) (Alkmim and Marshak, 1998; Barbosa et al., 2015; Bruno et al., 2021; Cutts et al., 2018; Degler et al., 2018; Heilbron et al., 2010; Noce et al., 2007).

Three distinct units, which are still tectonically poorly understood, occur in the foreland terrane of the Minas counterpart of the Paleoproterozoic Minas-Bahia orogeny, stretching north-south along the eastern border of the Serra do Espinhaco Range: (i) the Serro-Alvorada de Minas meta-ultramafic suite (Almeida-Abreu and Renger, 2007), (ii) the Rio Mata Cavalo meta-volcanosedimentary sequence (RMC) (Angeli et al., 2011), and (iii) the banded iron formation-bearing Serra da Serpentina Group (SSG) (Rolim et al., 2016) (Figure 4b). These three units occur associated with the anorogenic Conceição do Mato Dentro suite as well as the clastic Serra de São José Group (SJG), both of Statherian age and related to the Espinhaço rift system (Chemale et al., 2012; Santos et al., 2013).

Figure 4: (a) Regional tectonic context of the study area emphasizing the Precambrian rocks distribution. (b) Geological map of the southeastern border of the southern Espinhaço Range and its relationship with the western border of the Guanhães Basement Inlier. It=Itapanhoacanga, CMD=Conceição do Mato Dentro, MP=Morro do Pilar, RMC=Rio Mata Cavalo, ME=Morro Escuro, MTT=Minas Tectonic Terranes, Mb=Mineiro belt, M=Mantiqueira Complex, JF=Juiz de Fora Complex. Adapted and modified after Carvalho et al. (2014), Pinto and Silva (2014) and Rolim et al. (2016).

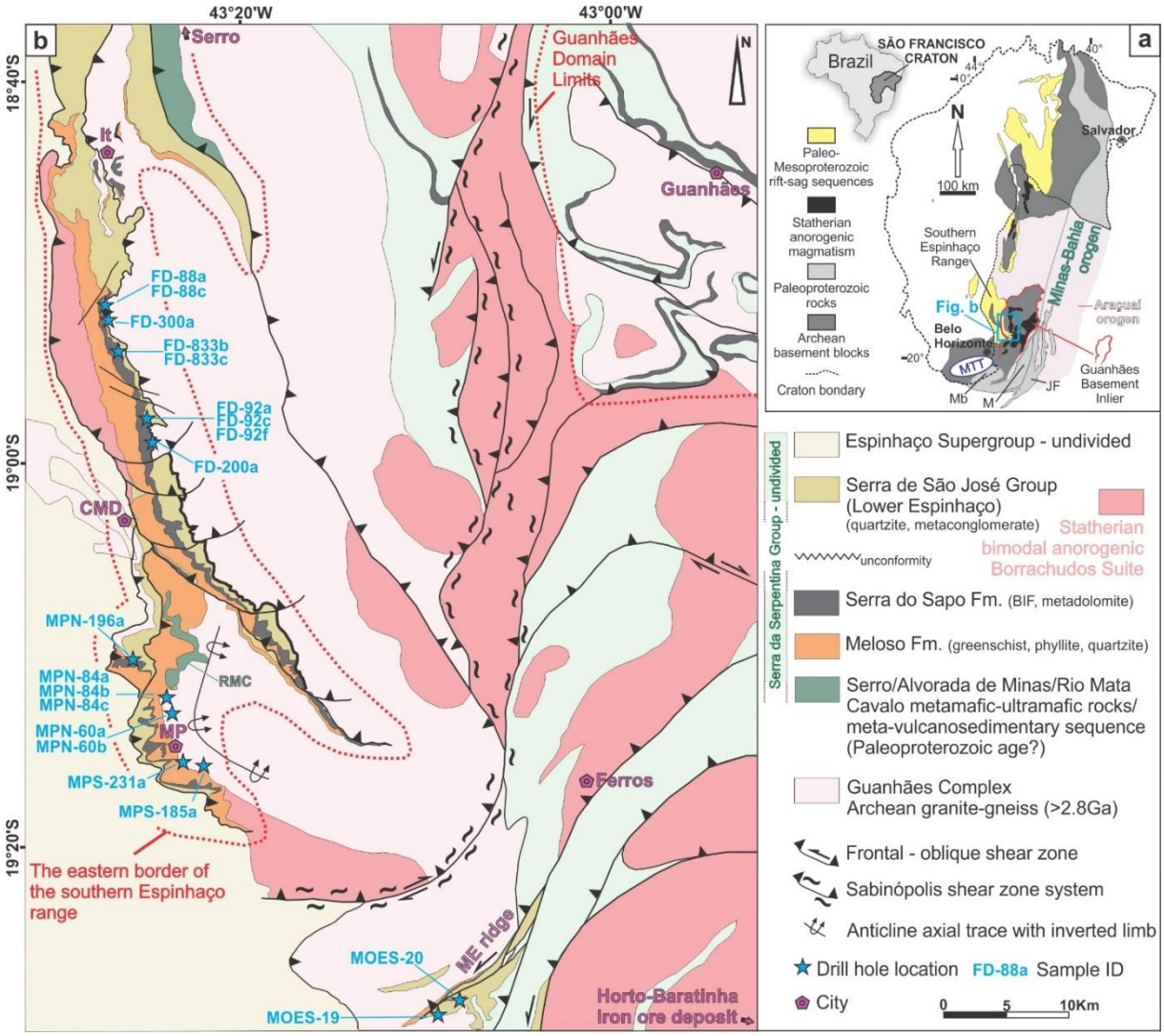

Source: Prepared by the author

The SSG is composed of the basal meta-siliciclastic Meloso Formation (focus of this work) and the upper banded iron formation-bearing Serra do Sapo Formation (Rolim et al., 2016). The stratigraphic position of SSG has been controversially correlated with the Siderian Cauê iron formation exposed further south in the world class Quadrilátero Ferrífero mining district, but also belonging to the Statherian Lower Espinhaço Sequence (Almeida-Abreu et al., 1989; Almeida-Abreu and Renger, 2007; Herrgesell and Pflug, 1986; Pflug, 1968, 1965). Based on structural analyses and detrital-zircon

geochronology, Rolim et al. (2016) interpreted the deposition of the SSG as older than the Espinhaço age Serra de São José Group (SJG). These authors recognized that both sequences are separated by an erosional unconformity, with the SSG understood as deposited in an epicontinental sag basin with little tectonic activity, while the SJG represents a tectonically active continental rift-basin deposit probably correlatable with the São João da Chapada Formation of the Espinhaço Supergroup (Chemale et al., 2012).

The Serra do Sapo Formation (SSG), which mostly comprises chemical sediments with banded iron formation and minor dolomite lenses, was subject of geochemical studies by Rolim et al. (2016), Silveira Braga et al. (2015) and Barrote et al. (2017). These studies provided evidence regarding the evolution of the atmosphere and ocean chemistry during the Serra do Sapo Formation deposition. In the present work, we complementarily focus on the geochemical characteristics of the siliciclastic rocks associated with the iron formations with the purpose to determine the provenance, and tectonic setting as well the degree of weathering of the source area, providing a more robust interpretation of the depositional environment of the Serra da Serpentina Group.

Our current findings, when paired with a compilation of geochronologic data, also encourage a more in-depth examination of the potential correlation between the Serra da Serpentina assembly and the upper Minas Supergroup, comprised by the Piracicaba and Sabará groups (Bekker et al., 2003; Dorr II, 1969; Machado et al., 1996; Rossignol et al., 2020).

3.2 Geological background

The study area is located in the external terranes of the Neoproterozoic Brasiliano – Pan-African Araçuaí orogen, which bounds the eastern border of the São Francisco craton (Alkmim et al., 2017, 2006; Pedrosa-Soares et al., 2001). During the Brasiliano Orogeny, the pre-Rhyacian basement rocks, Paleoproterozoic supracrustal units, Statherian anorogenic magmatism as well as the Minas-Bahia orogeny related rocks were reworked with the development of several tectonic terranes separated by major shear zones. The Paleoproterozoic assembly of these terranes and its geochronological inventory (the Minas-Bahia Orogen, the eastern border of the

southern Espinhaço Range, the Guanhães basement inlier, and the Minas Tectonic Terranes) are summarized in Figure 5.

3.2.1 The Minas-Bahia Orogen

In eastern Brazil and southwestern Africa, the basement of the Congo-São Francisco paleocontinent comprises mostly Archaean blocks amalgamated by the Rhyacian-Orosirian Minas-Bahia orogenic system, also known as the Transamazonian Orogenic Event (Barbosa et al., 2019; Heilbron et al., 2010; Noce et al., 2007; Teixeira et al., 2015). In its southern segment, the Minas-Bahia orogeny incorporates the Mineiro belt, the Mantiqueira and the Juiz de Fora arcs (Figure 4a) accreted to the consolidated crust of the São Francisco protocraton.

Figure 5: Paleoproterozoic assembly of the Minas Tectonic Terranes (MTT), the eastern border of the southern Espinhaço Range, the Guanhães basement inlier, and the southernmost portion of the Minas-Bahia Orogen. (1) Hartmann et al. (2006), (2) Babinski et al. (1995), (3) Cabral and Zeh (2015), (4) Cabral et al. (2022), (5) Rossignol et al. (2020), (6) Brueckner et al. (2000), (7) Dopico et al. (2017), (8) Dutra et al. (2019), (9) Machado et al. (1996), (10) Jordt-Evangelista et al. (2015), (11) Duque et al. (2020), (12) Caxito et al. (2020), (13) Dutra et al. (2020), (14) Hagedorn (2004), (15) Rolim et al. (2016), (16) Machado et al. (1989), (17) Barrote et al. (2017), (18) Magalhães et al. (2018), (19) Silveira Braga et al. (2015), (20) Silveira Braga et al. (2019), (21) Barbosa et al. (2019), (22) Teixeira et al. (2015), (23) Noce et al. (2007), (24) Heilbron et al. (2010).

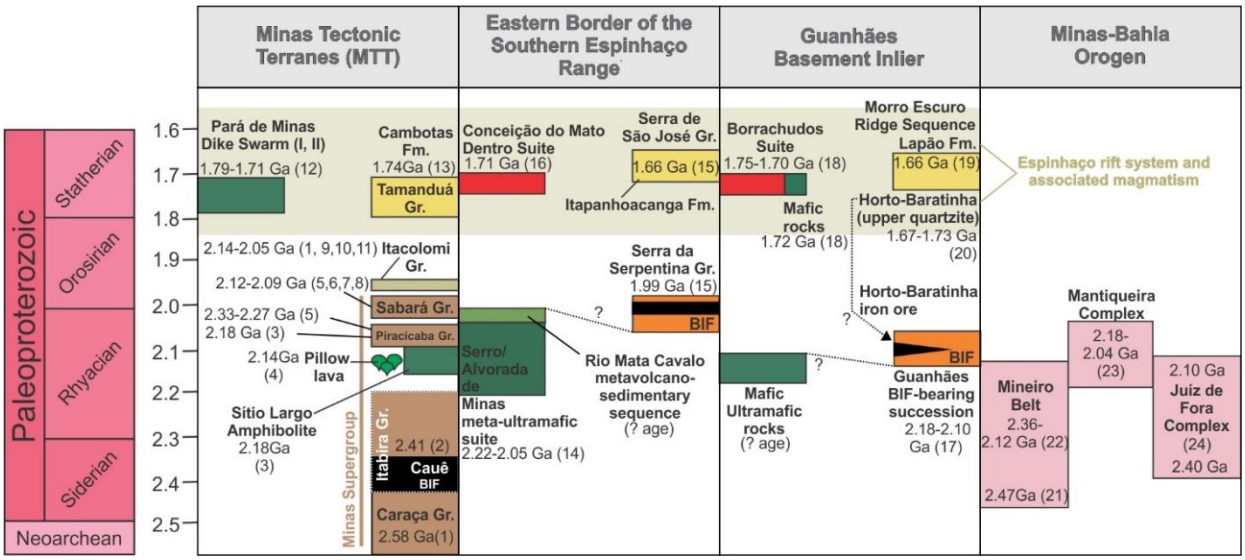

Source: Prepared by the author

The southern extremity of the protocraton is defined by Meso- to Neoarchean TTG domes (e.g. Santa Bárbara, Campo Belo, Passa Tempo, Belo Horizonte, Bonfim, Bação, Florestal, and Pequi), surrounded by Neoarchean metavolcanosedimentary

sequences (2.9 to 2.7 Ga Rio das Velhas and Pitangui greenstone belts; Baltazar and Zucchetti, 2007; Noce et al., 2005). The crystalline basement is covered by the Paleoproterozoic clastic and chemical metasedimentary rocks of the ca. 2.58 to 2.09 Ga Minas Supergroup and the ca. 2.05 Ga Itacolomi Group exposed in the Minas Tectonic Terranes (Figure 5) (e.g. Babinski et al., 1995; Duque et al., 2020; Hartmann et al., 2006; Dopico et al., 2017; Rossignol et al., 2020).

The Mineiro belt involved accretions of igneous bodies with both, juvenile and continental signatures, from the Siderian to Late Rhyacian (Aguilar et al., 2017; Alkmim and Teixeira, 2017; Ávila et al., 2014; Barbosa et al., 2015; Cutts and Lana, 2019; Seixas et al., 2013; Teixeira et al., 2017). The Mantiqueira complex represents a magmatic arc built on a Late Rhyacian continental margin with significant inheritance of Archaean continental crust (Aguilar et al., 2017; Heilbron et al., 2010; Noce et al., 2007). Farther east, the juvenile Juiz de Fora Complex is interpreted as a Paleoproterozoic island arc. The NE-SW-trending Abre Campo shear zone sutured the Mantiqueira and Juiz de Fora magmatic arcs in the Early Orosirian (Alkmim et al., 2006b; Degler et al., 2018; Noce et al., 2007).

3.2.2 The eastern border of the southern Espinhaço Range

A series of slightly bow-shaped elongated ridges between deeply weathered valleys and lowlands comprise the eastern border of the southern Espinhaço Range (Figure 4b). They are formed by roughly N-S trending tectonic slivers with repetition of the stratigraphic sequence between Archean TTG gneissic rocks (Figure 4b), comprising imbricate fans west of the Guanhães basement inlier. This tectonic scenario stretched southward to the Paleoproterozoic Minas Tectonic Terrane. In this area four main metasedimentary sequences (i to iv) are exposed: (i) the Serra da Serpentina Group (SSG) makes up the mountain crests protected by the Serra do Sapo iron formation and canga duricrust. In the low-lands and valleys, psamo-pelitic units are poorly exposed between quartzite crests comprising the Meloso Formation. The SSG is interpreted as deposited in a tectonically stable sag basin, and a few Orosirian detrital zircon grains indicate 1.99 Ga maximum depositional age (Rolim et al., 2016). (ii) The 2.05 to 2.22 Ga Serro-Alvorada de Minas meta-ultramafic Suite (Almeida-Abreu et al., 1989; Almeida-Abreu and Renger, 2007; Hagedorn, 2004; Zapparoli, 2001). The magmatic contact relationship with the gneissic rocks suggests serpentinitic diapirs

emplaced along fractures related to the crustal extension of the Espinhaço basin, interpreted as an oceanic proto-crust (Almeida-Abreu and Renger, 2007). The term Serro-Alvorada de Minas Suite is used here to discriminate discontinuous bodies of ultramafic metamorphic rocks that occur in the eastern border of the southern Espinhaço Range. (iii) The Rio Mata Cavalo metavolcanosedimentary sequence is composed of quartzites, carbonaceous phyllites, and banded iron formations, which occur in contact with the Meloso Formation (Figure 4b). Quartz veins enriched in gold and platinum group minerals (PGE) crosscut the RMC sequence (Angeli et al., 2011). (iv) The Serra de São José Group unconformably overlies the SSG, in physical continuity with the São João da Chapada Formation (Lower Espinhaço). It represents a complete cycle of transgressive sedimentary deposits deposited in the tectonically active continental Espinhaço rift-basin around 1.66 Ga (Rolim et al., 2016).

South of the Espinhaço Range, in the Minas Tectonic Terrane, the imbricate thrust slivers bend SW, overprinted by the transpressive domain of the Fundão-Cambotas Thrust System (Chemale et al., 1994), interposing with tectonic slices containing Paleoproterozoic Minas Supergroup and Archean greenstone belts.

3.2.3 The Guanhães basement inlier

The studied area is located in the western border of the Guanhães basement inlier (Figure 4), which is mostly composed of Archean orthogneisses, Statherian A-type granitic magmatism, and metasedimentary rocks. The Archean crystalline rocks correspond to the basement of the São Francisco Craton and they are represented by the Guanhães Complex (Grossi-Sad et al., 1997). This complex is composed of an undivided assemblage of magmatic rocks characterized by Meso-Neoarchean trondhjemite, tonalite and granodiorite (TTG) gneisses (Figure 4b) (Dussin et al., 2000; Noce et al., 2007). The Statherian assembly mostly includes anorogenic meta-granites, and minor meta-mafic rocks, all grouped in the Borrachudos Suite (Gomes et al., 2020; Machado et al., 1989; Magalhães et al., 2018). Interlayered with the metasedimentary rocks from the eastern border of the southern Espinhaço Range (or the western border of the Guanhães basement inlier) are the meta-rhyolites of the Conceição do Mato Dentro suite (ca. 1.7 Ga) (Machado et al., 1989), chrono-correlated with the Borrachudos granitic bodies.

An association of BIF-bearing supracrustal rocks, tectonically juxtaposed to the Borrachudos Suite and Archean TTG rocks, occurs in distinct geographic positions within the Guanhães basement inlier (Figure 4b). Several BIF-bearing metasedimentary strata encased in Guanhães Complex gneissic rocks yielded a maximum depositional age of 2.18 Ga age (Barrote et al., 2017; Grossi-Sad et al., 1997). MDAs of 2.02 and 1.68 Ga were found from detrital zircons from quartzites exposed in the Morro Escuro ridge (Carvalho et al., 2014; Silveira Braga et al., 2015), respectively, while an MDA of 1.67 Ga was obtained from the Horto-Baratinha iron ore deposit (Silveira Braga et al., 2019). These three sequences are linked to the Serra da Serpentina and Serra de São José groups, which may be found on the eastern edge of the southern Espinhaço Range.

3.2.4 The Minas Tectonic Terranes (MTT)

A Rhyacian age spectrum, similar to those found in the Serra da Serpentina Group and its correlates, is also recognized in the Minas Tectonic Terrane. The MTT (Figure 4a) embraces a roughly square-shaped region that covers ca. 7,000 sq. km south of the Serra do Espinhaço Mountain Range. It comprises the Neoarchean to Early Paleoproterozoic Minas Supergroup that overlies Archean granite-greenstone terranes, and its distribution defines the characteristic NE-SW / NW-SE configuration (Iron Quadrangle). This shape results from the superposition of structures separated from the N-S linear trend of the Espinhaco Range by NE-SW shear zones (Chemale et al., 1994; Rosière et al., 2008).

The basal succession of the Minas basin represents a passive margin deposit that took place between 2.58 and 2.41 Ga (Babinski et al., 1995; Hartmann et al., 2006). It consists of the Caraça and the BIF-bearing Itabira groups, with the Minas basal succession being unconformably overlain by the younger 2.22-2.10 Ga old Piracicaba Group. The layers of the Piracicaba Group were deposited in a regressive marine and deltaic environment (Babinski et al., 1995; Bekker et al., 2003), separated from the Itabira Group by a hiatus probably related to a long erosional period. Relicts of the basinal floor are recognized in two scarcely exposed mafic bodies: the N-MORB Sítio Largo amphibolite (2.18 Ga) (Cabral and Zeh, 2015) and the 2.14 Ga subaqueous pillow-lava from the Rola Moça Ridge (Cabral et al., 2022).

The uppermost sequences of the Minas basin comprise the Sabará and Itacolomi groups, interpreted as syn-tectonic foreland basins. The Sabará Group corresponds to mass flow and turbidity currents of high and low density representing proximal and distal turbidites, while the Itacolomi Group is related to alluvial and fluvial molasse, with subordinate tidal flat depositional systems (Gonçalves and Uhlein, 2022). It shows an Archaean detrital zircon age peak and the Minas-Bahia accretionary orogeny detrital zircon age peak (Duque et al., 2020; Dutra et al., 2019; Gonçalves and Uhlein, 2022). The ages of metamorphic monazite and titanite constrain the peak of metamorphism at the late stage of the Minas-Bahia orogeny to ca. 2.06–2.03 Ga (Aguilar et al., 2017).

3.3 Sampling and analytical methods

Nineteen samples of the Meloso Formation (greenschist, phyllite and quartzite) were collected from twelve different drill cores placed in the Conceição do Mato Dentro mining district, Morro do Pilar, and Morro Escuro ridge (Figure 4b). Idealized geological profiles are presented based on extensive drill core descriptions from all three regions (Figure 6a). The sample interval is constrained by the lower contact with the Serra do Sapo Formation as reference surface aiming to correlate samples from different drill cores (Figure 6a). Chemical analyses were carried out at the Bureau Veritas Labs, Vancouver. Whole-rock major and minor elements compositions were obtained by Inductively Coupled Plasma Emission Spectrometry (ICP-ES) and Inductively Coupled Plasma Mass Spectroscopy (ICP-MS) were used for determining trace and rare earth elements. The chemical analyses results are presented in the Appendix A.

3.4 Results

The clastic metasedimentary rocks of the Serra da Serpentina Group display distinct facies that can be separated in two domains delineating a lateral variability of the depositional environment: the Conceição do Mato Dentro depositional domain, exposed along the N-S tectonic slivers between Itapanhoacanga and Morro do Pilar and in the Morro Escuro ridge and the Guanhães domain, farther east, comprising discontinuously exposed supracrustal rocks covering the homonymous basement inlier (Figure 4).

In the Conceição do Mato Dentro domain, the basal Meloso Formation is up to 500 meters thick underlying the up to 350 meters thick Serra do Sapo Formation (Rolim et

al., 2016), suggesting a shallow platformal environment. The Meloso Formation is dominantly represented by a homogeneous pelitic (greenschist) succession interlayered with phyllite and quartzite layers with variable thickness. The Serra do Sapo iron formation records detrital input with thin layers of very fine-grained sandy to silty sediments and display metadolomite lenses at the top (Rolim et al., 2016). Interlayered with the iron formation, there is a quartzite in gradational contact, which can reach a thickness of up to 45 m (Figure 6a).

Figure 6: (a) The lithological profile of the Serra da Serpentina and Serra de São José groups in the Conceição do Mato Dentro mining district, Morro do Pilar, Morro Escuro ridge and Guanhães depositional domain. The samples distribution was bound by the contact between the Meloso and Serra do Sapo formations as vertical reference datum to cluster samples collected from different drill cores. CMD = Conceição do Mato Dentro Suite. (b) Basal turbiditic-like quartzite in the Guanhães depositional domain. (c) Detailed of the turbiditic-like quartzite.

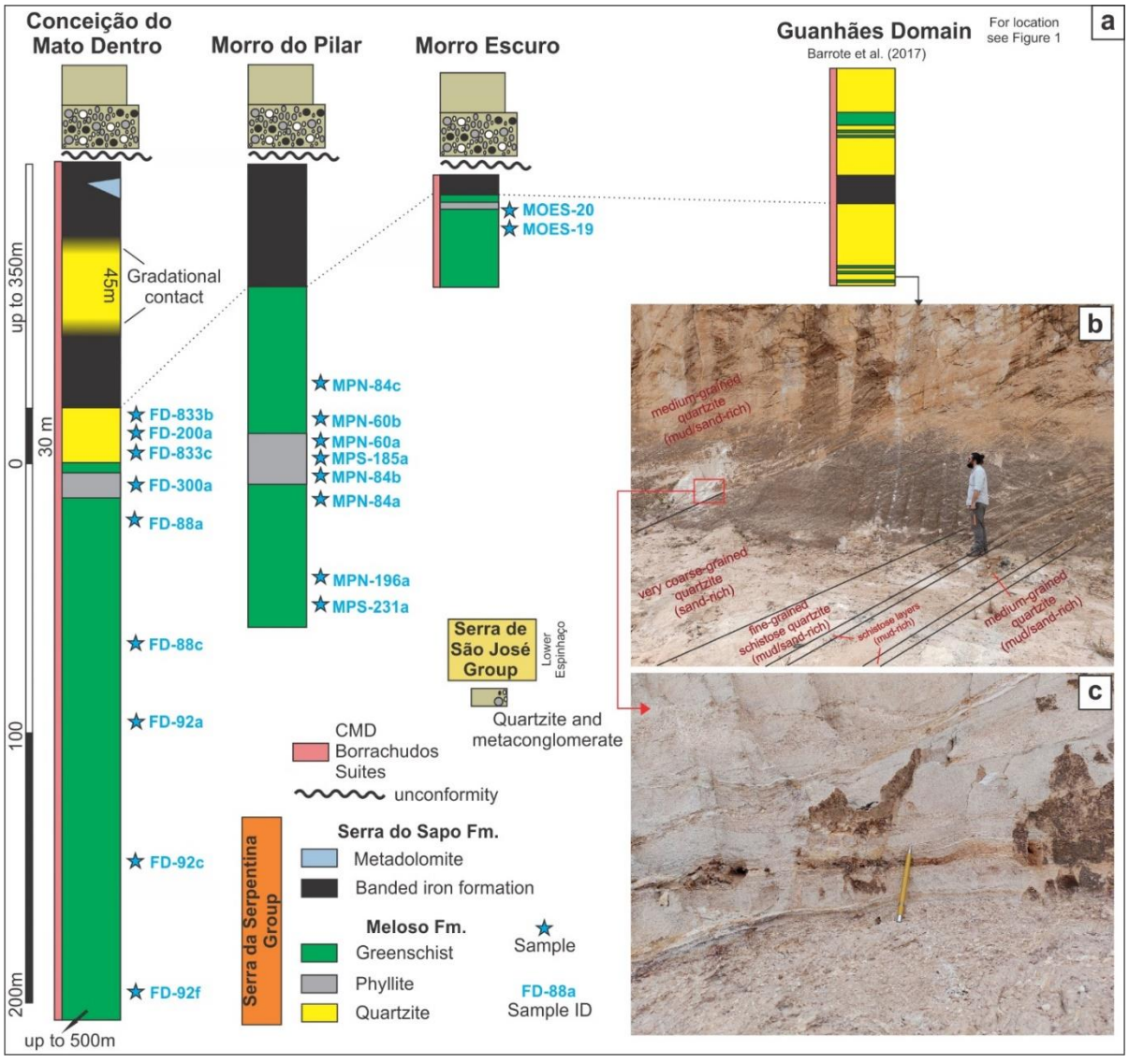

Source: Prepared by the author

In the Guanhães depositional domain, two quartzitic packages (lower and upper) correlated with the Meloso Formation are ubiquitously exposed, separated by an intermediate banded iron formation with subordinate detrital input. The contacts between these units are sharp and frequently sheared (Barrote et al., 2017). The lower and upper units comprise intercalated fine- to coarse-grained quartzite layers with a variable compositional range (pure, sericitic and arkosic), associated with sillimanite-rich schists (Figure 6). Fine-grained laminated rhythmites display alternating metapelitic and fine-grained sandy layers. Quartz laminae may be massive or graded, plane parallel or convoluted (Figure 6b and c). The iron formation with subordinate clastic input (Barrote et al., 2017), its close association with interbedded quartzite, and the sedimentary structures exhibited in the terrigenous rocks suggest that the Meloso succession in the Guanhães domain was deposited by turbiditic currents in a shallow marine environment.

3.4.1 Petrography of the Meloso Formation

The Meloso Formation comprises a meta-psammopelitic series that includes greenschists, gray phyllites and quartzites. Most samples for petrographic analysis were collected along the Serra da Serpentina ridge, between the locations of Itapanhoacanga and Morro do Pilar (Figure 4b), where the regional metamorphic inventory exhibits paragenesis of lower greenschist facies (Uhlein et al., 1998).

Greenschist is the most abundant lithotype with a homogenous and monotonous macroscopic fabric. These rocks are light to dark green with a continuous to phyllonitic foliation. Under the microscope, the greenschist is characterized by sericite and chlorite-rich layers (~0.1 mm) with very fine granoblastic quartz grains (Figure 7a). Plagioclase-sericite-chlorite schists with minor garnet are rare (Figure 7b). One greenschist sample (FD-92a) exhibits preserved sedimentary fabrics characterized by granulometric variations. Sub-rounded to well-rounded quartz (and rare plagioclase) grains up to 1.5 mm in size occurs immersed in a very fine-grained matrix (Figure 7c). Plagioclase grains are more common in the coarse-grained members (Figure 7d).

The gray phyllite is composed of sericite (50%), dark gray amorphous carbonaceous(?) material (40%), quartz (8%) and oxides (2%) (Figure 7e). Associated with gray phyllite,

Rolim et al. (2016) describe carbonaceous black phyllite lenses that fingerprints the top of the Meloso Formation.

The quartzite samples present grano-lepidoblastic fabrics and are relatively rich in hematite and magnetite (15%). In general, the quartzite is medium-grained (up to 0.5 mm) and exhibits conspicuous foliation marked by anastomosed aggregates of recrystallized quartz and sericite-rich domains (Figure 7f).

Two samples (MOES-19 and MOES-20) were collected at Morro Escuro ridge (Figure 4b), which exhibits a paragenetic assembly of amphibolite facies (Silveira Braga et al., 2015). Sample MOES-19 comprises a garnet-staurolite-mica schist. This rock is mainly composed of quartz (30%), biotite (25%) and chlorite (20%) and minor staurolite (15%), garnet (5%) and oxides (5%) (Figure 7g and h). Sample MOES-20 is characterized by a centimeter-sized alternation of folded layers of tremolite-biotite schist, chlorite-quartz schist, garnet-carbonaceous(?) phyllite with tremolite and chlorite-quartz-biotite schist with garnet porphyroblasts (Figure 7i, j, k and l). Garnet is idiomorphic to sub-idiomorphic in shape and relatively large (up to 5 mm), often exhibiting a discrete retrograde alteration halo to biotite (Figure 7k).

3.4.2 Whole-rock geochemistry

The geochemical signature of siliciclastic rocks provides support for a comprehensive analysis of the nature of the source areas and subsequent alteration processes, such as weathering, diagenesis or metamorphism. The abundance of some elements, such as rare earth elements (REE), Hf, Ti, Cr, Co, Zr, Nb, Ta, Y, Th and Sc, is preserved in marine sedimentary rocks due to their immobile behavior. Hence, they can be used as discriminating factors for determining the provenance and help interpreting the tectonic setting of sedimentary rocks (Bhatia, 1983; Bhatia and Crook, 1986; Hegde and Chavadi, 2009; Roser and Korsch, 1988, 1986; Taylor and McLennan, 1985).

Th/Sc, La/Sc, Zr/Sc, La/Th ratios have been commonly used to investigate provenance according to the compatibility of these elements during magmatic crystallization. In some specific cases, Cr/V and Y/Ni ratios can provide important clues about tectonic settings during the deposition period (McLennan et al., 1993). Additionally, discrimination diagrams based on immobile trace elements can be used to investigate

tectonic settings of sedimentary basins (Bhatia and Crook, 1986; Verma and Armstrong-Altrin, 2013).

Figure 7: Photomicrographs showing the mineral association and microstructural features of the main lithotypes of the Meloso Formation. (a-b) Green schist exhibiting well-developed foliation defined by alternation of fine quartz grains and sericite/chlorite layers. Garnet can occur associated with the phyllonitic fabric commonly developed in the serite/chlorite rich layers. (c, d) Green schist showing unmetamorphosed cores where sedimentary fabric is preserved; sub-rounded to well-rounded quartz and rare plagioclase grains occur immersed in a very fine matrix. (e) Carbonaceous(?)-sericite crenulated gray phyllite. (f) Oxide-rich quartzite showing conspicuous foliation. (g, h) garnet-staurolite-mica schist from the Morro Escuro amphibolite facies domain. (i) Photograph of MOES-20 thin section showing folded compositional bedding layers; note the association of well-formed garnet with the carbonaceous(?) layer. (j, k, l) Detail of the MOES-20 sample: tremolite-biotite rich layer, garnet-bearing layer and microstructural relationship between the carbonaceous layer with the biotite-quartz rich layer. Qz = quartz, Ser = sericite, Chl = chlorite, Grt = garnet, Plag = plagioclase, Carb = amorphous carbonaceous material, Bt = biotite, St = staurolite, Trem = tremolite.

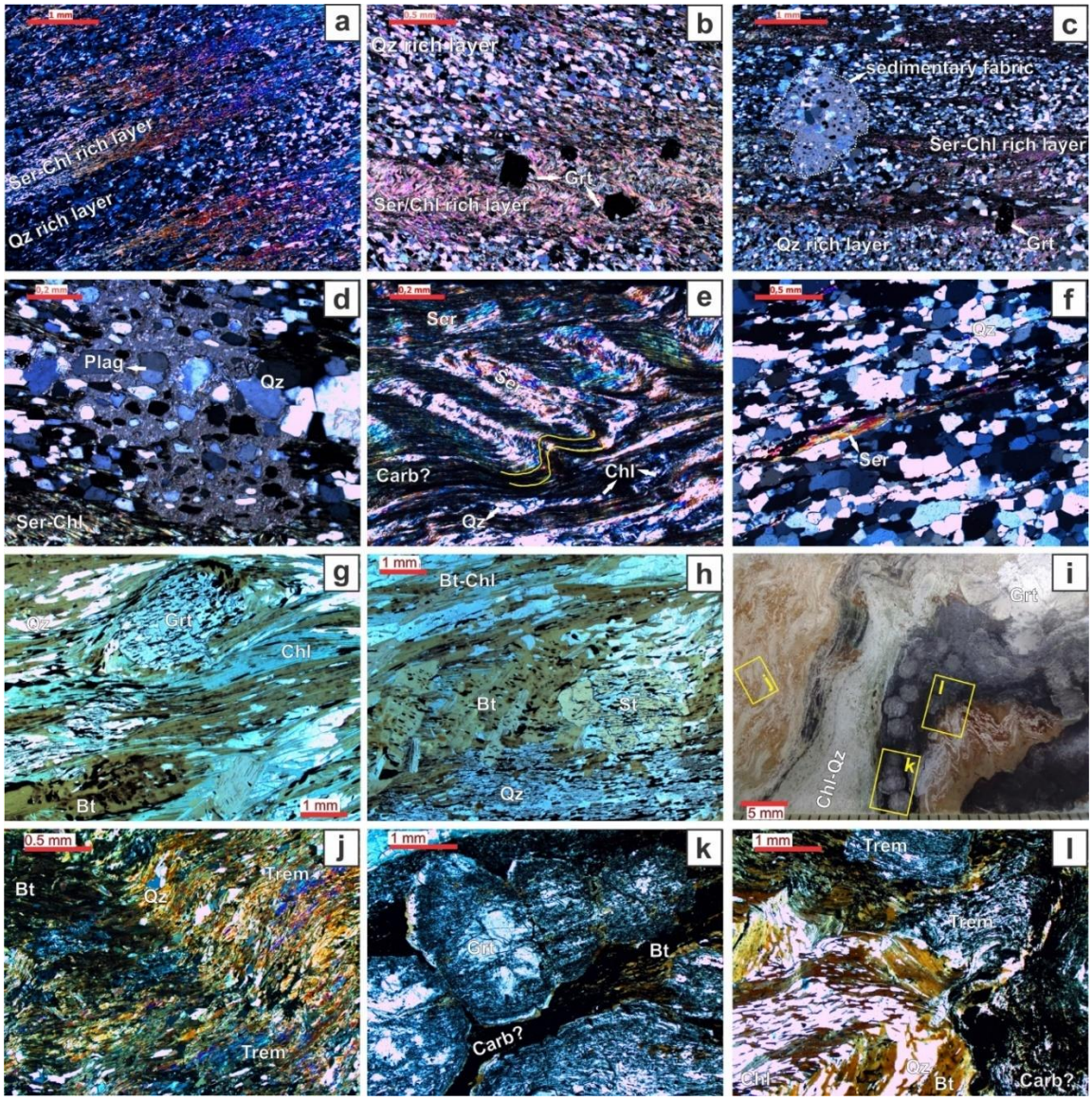

Source: Prepared by the author

3.4.2.1 Major and trace elements characteristics

The worldwide applied chemical classification based on major elements proposed by Herron (1988) helps to determine the protolith of a metasedimentary rock (e.g. Bakkiaraj et al., 2010; De et al., 2015; Fuenlabrada et al., 2012; Henrique-Pinto et al., 2015). The log(Fe_2O_3/K_2O) vs. log(SiO_2/Al_2O_3) chart (Figure 8) shows that the metasedimentary rocks from the Meloso Formation originally comprised wackes, shales, Fe-shales, and less frequently impure arenites. Two samples (MPN-196a and MPN-84c) have high Fe_2O_3/K_2O ratios and fall outside the plotted region of the diagram. Although the protolith classification plot (Herron, 1988) is widely applied for metasedimentary rocks, caution should be exercised due to the high mobility of potassium (further discussion in section 3.4.2.3).

The analyzed samples display a significant variation in the major element composition. Quartzites yield high contents of SiO_2, ranging from 79.52 to 92.36 wt% and low Al_2O_3 (1.35 to 2.71 wt%). Fe_2O_3 contents, on the other hand, yielded a broad variation from 2.87 to 14.71 with average of 10.18 wt%, falling in the classification of Fe-sandstone (Figure 8). The greenschists, including sample MOES-19, exhibit a wide variation in the composition with averages of 57.30 wt% SiO_2, 8.73 wt% Fe_2O_3 and 5.28 wt% MgO, as well as uniform Al_2O_3 content (averaged 13.78 wt%). The greenschist samples plot in both the wacke and Fe-shale fields. The phyllites plot dominantly in the shale field, with a single outlier in the Fe-shale domain (Figure 8). The phyllites are the most Al and K rich lithotypes. These samples exhibit high average concentration of Fe_2O_3 and MgO, 9.23 and 5.06 wt%, respectively. In general, the results confirm petrographic observations and display a wide range of detrital rocks that vary from phyllosilicate dominated shale to impure arenites.

Figure 8: Log of the Fe_2O_3/K_2O vs. log of SiO_2/Al_2O_3 diagram (Herron, 1988) of the Meloso Formation to determine the protolith of metamorphic sedimentary rock.

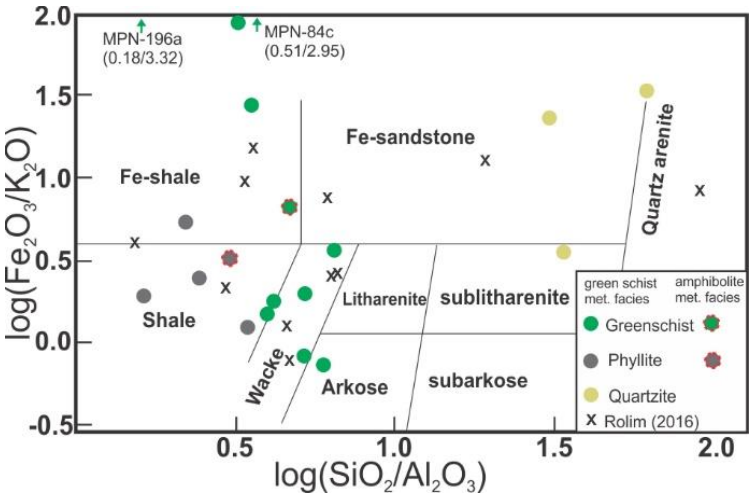

Source: Prepared by the author

SiO_2 shows a marked negative correlation with TiO_2, MgO, Sc, V and Co, as well as moderate negative correlation with Al_2O_3, Fe_2O_3, MnO and CaO (Table 1). The average SiO_2/Al_2O_3 ratio for most samples is low (3.71), while the quartzite samples have high SiO_2/Al_2O_3 ratios (ranging from 30.58 to 62.26). This suggests that the fine-grained rocks are largely immature. TiO_2 exhibits positive correlation with Fe_2O_3, MnO, MgO, P_2O_5, Zr and Pb (Table 1), suggesting that ilmenite and rutile were originally associated with iron-magnesium minerals, monazite and zircon, as confirmed by the positive correlation between P_2O_5 and Fe_2O_3, MnO, MnO, Pb and Zr. The K_2O/Na_2O ratio in the quartzite samples is high, ranging from 22.00 to 76.33. In contrast, the fine-grained rocks (greenschist and phyllite) have much lower K_2O/Na_2O ratios, ranging from 0.20 to 3.32.

According to Feng and Kerrich (1990), the ferromagnesian trace elements (Sc, V, Cr, Co, and Ni) behave similarly during magmatic processes. However, if exposed to weathering, these elements can fractionate independently. The ferromagnesian elements were here evaluated individually, and it was possible to observe high positive correlations between Sc with V (r=0.87) and Co (r=0.86), V with Co (r=0.73), and Cr with Ni (r=0.95). Scandium shows moderate positive correlation with Al_2O_3 (Table 1), however, if quartzites are excluded and just fine-grained rocks are used, the correlation significantly decrease (r=0.32). This suggests that the most Sc was not adsorbed by clay minerals, being instead possibly incorporated by mafic or oxide mineral particles

during the basin infilling. Sc, V and Co exhibit moderate positive correlation with Fe_2O_3, MnO and high correlation with MgO. Cr and Ni show no correlation with Fe-Mn-Mg oxides (Table 1).

Large-ion lithophile elements (Cs, Rb, Ba) display strong positive correlation with K_2O but not with Al_2O_3, indicating that K-feldspars may control the concentration of these elements. Strontium exhibits moderate positive correlation with Na, suggesting its association with plagioclase (Table 1).

Table 1: Pearson correlation coefficient (r) of major and trace elements for siliciclastic metasedimentary rocks from the Meloso Formation.

	SiO_2	TiO_2	Al_2O_3	Fe_2O_3	MnO	MgO	CaO	Na_2O	K_2O	P_2O_5
SiO_2	1.00									
TiO_2	-0.71	1.00								
Al_2O_3	-0.62	0.21	1.00							
Fe_2O_3	-0.55	0.69	-0.08	1.00						
MnO	-0.65	0.83	0.12	0.60	1.00					
MgO	-0.86	0.79	0.34	0.70	0.81	1.00				
CaO	-0.58	0.30	-0.02	0.25	0.36	0.44	1.00			
Na_2O	-0.08	-0.26	0.29	-0.39	-0.04	-0.02	0.21	1.00		
K_2O	0.10	-0.27	0.49	-0.41	-0.33	-0.29	-0.51	-0.26	1.00	
P_2O_5	-0.49	0.91	0.01	0.69	0.84	0.73	0.10	-0.30	-0.37	1.00
Sc	-0.93	0.61	0.59	0.52	0.53	0.83	0.49	0.12	-0.14	0.44
V	-0.91	0.73	0.45	0.66	0.57	0.76	0.54	-0.18	-0.13	0.51
Cr	-0.32	-0.14	0.51	0.05	-0.20	0.22	-0.04	0.24	0.13	-0.24
Co	-0.82	0.61	0.55	0.59	0.47	0.81	0.34	0.09	-0.18	0.46
Ni	-0.37	-0.08	0.54	0.13	-0.14	0.25	-0.01	0.22	0.13	-0.20
Zn	-0.58	0.70	0.33	0.40	0.63	0.62	0.12	-0.12	-0.09	0.73
Sr	-0.58	0.17	0.58	-0.01	0.31	0.43	0.47	0.65	-0.24	0.05
Zr	-0.36	0.64	0.18	0.32	0.62	0.52	-0.06	-0.29	0.17	0.66
Nb	-0.09	0.29	0.05	0.03	0.24	0.21	-0.07	-0.27	0.25	0.32
Cs	0.26	-0.26	0.26	-0.45	-0.20	-0.34	-0.47	-0.13	0.82	-0.30
Rb	0.19	-0.32	0.46	-0.53	-0.35	-0.37	-0.52	-0.16	0.95	-0.38
Ba	0.17	-0.24	0.26	-0.38	-0.36	-0.39	-0.44	-0.23	0.67	-0.27
Hf	-0.22	0.43	0.15	0.15	0.43	0.35	-0.11	-0.28	0.30	0.45
Ta	-0.06	0.22	0.07	-0.03	0.18	0.16	-0.10	-0.26	0.31	0.23
Pb	-0.53	0.71	0.14	0.38	0.88	0.64	0.27	-0.04	-0.14	0.75
Th	0.15	-0.16	0.15	-0.31	-0.10	-0.14	-0.27	-0.14	0.59	-0.15
U	-0.05	0.01	0.20	-0.12	0.14	0.03	-0.15	-0.26	0.61	-0.03

Source: Prepared by the author

Zirconium is positively correlated with TiO_2, MnO, MgO and P_2O_5 (Table 1) illustrating a possible sedimentary relationship between zircon, oxides, and monazite. Zirconium

and Hf are positively correlated (r=0.96) and the average Zr/Hf value (36.89) of the studied rocks may indicate zircon controls the HFSE (Anani et al., 2019; Toulkeridis et al., 1999).

According to the multi-element diagrams normalized to the Post-Archean Australia Shale-PAAS (McLennan, 1989), the rocks of the Meloso Formation exhibit three different distribution patterns based on compatible (ferromagnesian) and incompatible (LILE and HFSE) elements content (Figure 9). Upper Continental Crust (UCC) reference (Rudnick and Gao, 2003) is plotted for comparison. In addition, samples collected in the Meloso Formation, analyzed by Rolim (2016) are also used.

Most of the tested samples fall in the first group (Figure 9a), which presents enrichment in Sc, V, Cr, Co, and Ni (average 26.50 ppm, 170.70 ppm, 270.94 ppm, 30.23 ppm and 134.20 ppm, respectively) and, in general, is depleted in LILE and HFSE. The quartzite samples (FD-833b and FD-833c) are depleted in both, compatible and incompatible elements. However, the distribution patterns exhibit a high content of ferromagnesian elements when compared with the incompatible elements. The second group exhibits an inverse trend regarding the former, with all samples depleted in ferromagnesian elements with averages of 7.33 ppm Sc, 22.50 ppm V, 44.47 ppm Cr, 8.22 ppm Co and 16.22 ppm Ni, whereas, in general, LILE and HFSE yield contents close to the reference values (PAAS and UCC), except for sample MPN-60b that exhibits anomalous values for Zr, Nb, Hf and Ta (Figure 9b). The third group consists of five samples with a very ambiguous distribution pattern (MOES-19, MOES-20, FD-200a, MPN-196A, and MPN-84a), (Figure 9c). Nonetheless, the schists and phyllite samples in the third group are enriched in Sc, V, and Co and have low incompatible element levels, which is remarkably similar to the first group, despite being depleted in Cr and Ni.

Figure 9: PAAS-normalized trace elements plots for the Meloso Formation. PAAS after Taylor and McLennan (1985). Diagrams a, b and c exhibit the three different elemental patterns distribution for the analyzed samples. The colors are related to the analyzed lithotype, see Figure 8.

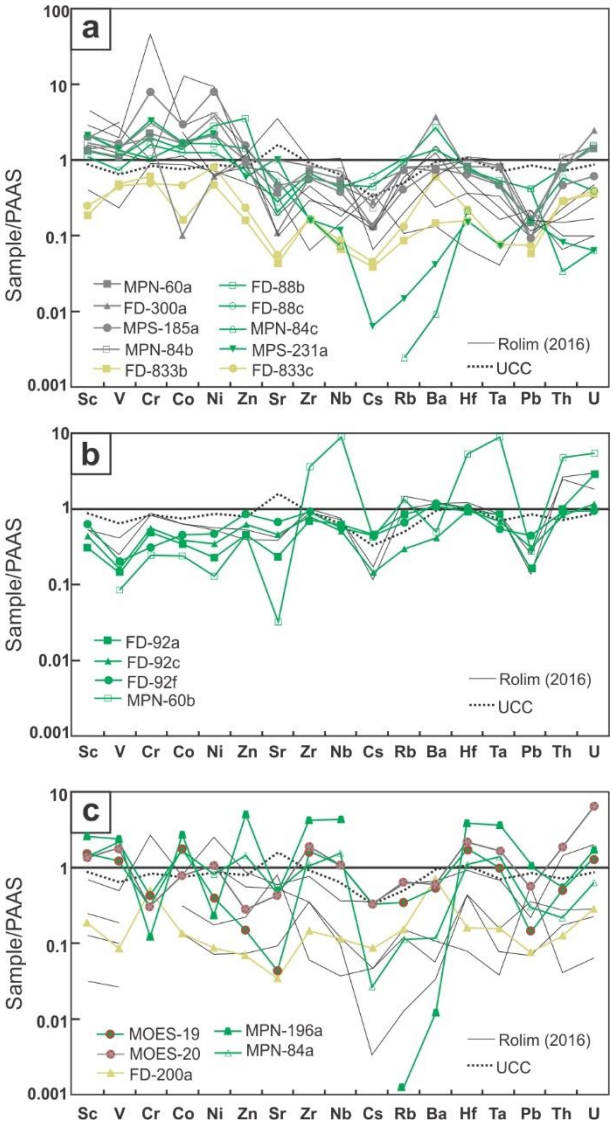

Source: Prepared by the author

Th/Sc ratios for the fine-grained rocks of the first and third groups display the tendence of presenting low values, ranging from 0.01 to 0.59 and 0.14 to 1.17, respectively, while the second group has 2.08 Th/Sc average ratios. These distinct distribution patterns suggest at least, two different source areas.

3.4.2.2 Rare earth elements

The rare earth element (REE) content of all samples is very low, with ΣREE values ranging from 3.62 ppm in quartzite sample FD-200a to 45.04 ppm in sample MPN-60b.

The Y/Ho ratio averages 27.60. Based on the REE diagram normalized to PAAS (McLennan, 1989), the Meloso Formation exhibits four REE fractionation patterns (Figure 10). Regardless of lithology, most samples present low $(La/Yb)_N$ ratios exhibiting slight to moderate enrichment of heavy rare earth elements (HREE) relative to light rare earth elements (LREE), defining group 1 (Figure 10a). All quartzites and samples MPN-84c and MPS-231a are significantly depleted in REE when compared to PAAS, whereas phyllites and samples MPN-84a and MOES-19 exhibit modest fractionation between LREE and HREE when PAAS-normalized. All group 1 samples exhibit slight but significant positive Eu anomaly; six samples from Rolim (2016) show the same pattern.

When compared to group 1, group 2 (Figure 10b) displays a similar REE fractionation pattern. However, it exhibits a marked negative Eu anomaly (FD-92a=0.38 and MPN-60b=0.10). Sample MPN-60b likewise shows a positive Ce anomaly ($Ce/Ce^* = 2.55$), which is most likely due to the occurrence of metasomatic Ce-allanite in the Morro Escuro ridge, as described by Silveira Braga et al. (2015)

The samples FD-88b and FD-88c display $(La/Yb)_N$ ratios of 1.23 and 1.18, respectively, indicating a moderate enrichment of light rare earth elements (LREE) against heavy rare earth elements (HREE). This pattern is also observed in three samples from Rolim (2016). These five samples comprise group 3 (Figure 10c), which exhibits a flat LREE pattern (PAAS-like) with a small positive Eu anomaly (averaging 1.33) and slight HREE depletion. This group includes the sample MPN-196a, which is enriched in REE and exhibits no difference between LREE and HREE content.

The group 4 consists of the samples FD-92c, FD-92f, and Fs-300a and exhibits a PAAS-like behavior (Figure 10d). Two samples from Rolim (2016) have anomalous positive Y values (Figure 10a and c), and display a high Y/Ho ratio (sample 073-710=61.22 and sample 073-708=34.78).

Figure 10: Rare-earth element concentrations normalized to the PAAS (Taylor and McLennan, 1985) for the metasedimentary rocks from the Meloso Formation. Diagrams a, b, c and d exhibit the various REE patterns distribution for the analyzed samples. The colors are related to the analyzed lithotype, see Figure 8.

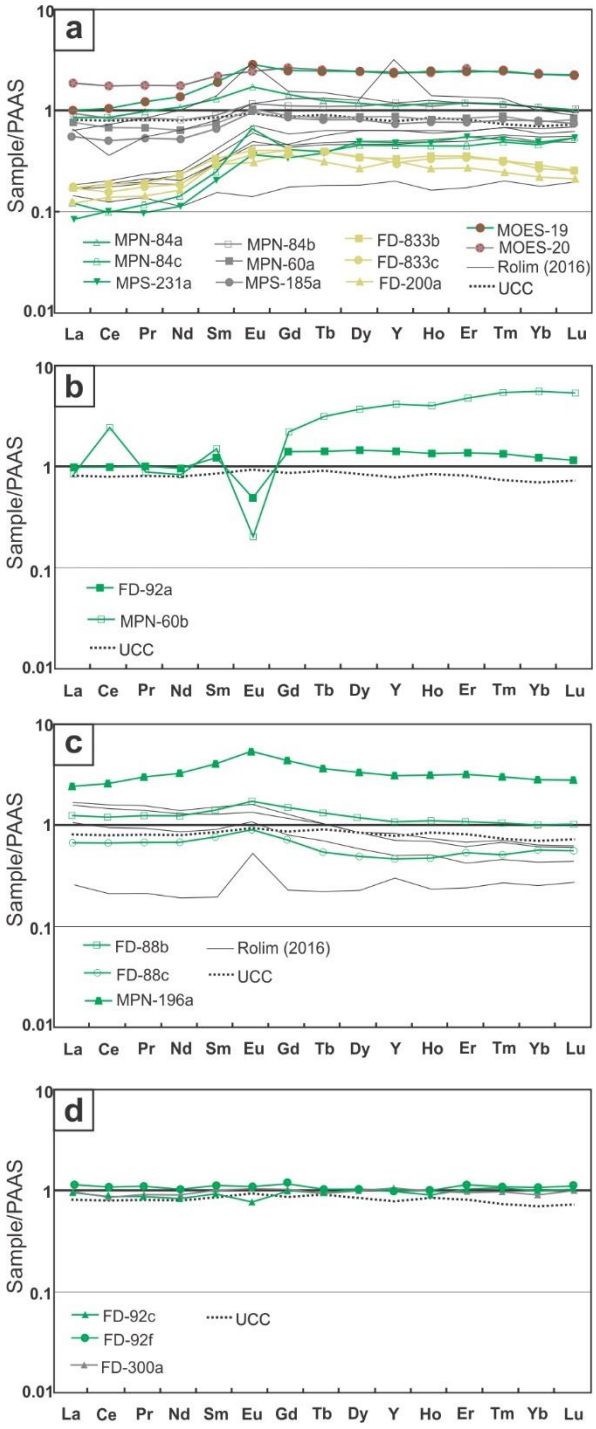

Source: Prepared by the author

3.4.2.3 Paleo-weathering

The geochemical characteristics of sediments are determined by the source rock as well as the process during or post-deposition (McLennan et al., 1993). Chemical weathering may strongly affect geochemical characteristics of the sediments and should be evaluated (Fedo et al., 1995; Nesbitt and Young, 1989, 1982). The most significant influence on the composition of the source rocks is K- metasomatism (Fedo et al., 1995; Nesbitt and Young, 1989), which can be reflected by the transformation of either aluminous clay minerals to illite or plagioclase to K-feldspar (Fedo et al., 1995; Liu et al., 2021). The introduction of the A-CN-K (Al_2O_3, CaO^*+Na_2O, K_2O) system and the Chemical Index of Alteration (CIA) provided an ideal perspective to evaluate the trend of weathering, monitoring potassium addition and constraining initial compositions of source rocks (Fedo et al., 1995).

Plotted in the A–CN–K space, the samples from the Meloso Formation are distributed as a distinct linear array that is a less steep slope than the predicted weathering trend, suggesting K addition during weathering (Figure 11a). As a source rock monitor, the extended weathering line to the interception with the horizontal K-feldspar – plagioclase line indicates a high proportion of the latter, suggesting possible mafic rocks as source for the sediments. Samples MPN-84a and MPS-231a and two others from Rolim (2016), align with the Early Proterozoic basalts reference values proposed by Condie (1993). Sample MOES-20 plots near the K-feldspar-plagioclase line between the analytical references for Archean TTG and Proterozoic granites (Condie, 1993), indicating a possible felsic source. As shown in Figure 11a, the studied metasedimentary rocks exhibited a high range of CIA values, from 32 to 80. An important character is the considerable number of samples that have CIA values below 60, indicating poorly weathered to fresh source rocks.

The mafic index of alteration (MIA) considers the mafic elements Mg and Fe, which are not included in the equation of the CIA. The MIA, when used alongside ternary diagrams, allows for both, the measurement of the level of weathering of mafic minerals and the examination of the trend of weathering (Babechuk et al., 2014). The susceptibility of many mafic minerals such as pyroxene and olivine to chemical weathering leads to the loss of Mg from weathering profiles. Unlike Mg, the fate of Fe during mafic mineral weathering is dependent on redox conditions. When the alteration

environment is oxidizing and Fe is retained, total Fe is considered an immobile element along with Al_2O_3. Conversely, when the alteration environment is reducing and Fe is leached along with Mg, total Fe is considered a mobile element along with Mg, Ca, Na, and K.

Based on the association of the investigated meta-siliciclastic rocks with the oxide facies Serra do Sapo iron formation (Rolim et al., 2016), the Meloso Formation was deposited in an oxidic environment possible driven by turbidity currents from the shallow parts of the basin. The MIA($_{OXIDIZING}$) was calculated and presented in conjunction with the A-CNKM-F (Al_2O_3, CaO*+Na_2O+K_2O+MgO, Fe_2O_3) and AF-CNK-M (Al_2O_3+Fe_2O_3, CaO*+Na_2O+K_2O, MgO) diagrams (Figure 11b and c).

The studied samples exhibit a high range of MIA values, from 29 to 87. The A-CNKM-F plot (Figure 11b) shows a rock weathering trend parallel to the A-CNKM join, suggesting a slight variability in the Fe content during weathering. The observed trend reveals a minor departure from the predicted weathering vector, this behavior also is described by Babechuk et al. (2014) based on an empirical weathering pattern. An important feature apparent in the A-CNKM-F chart (Figure 11b) is the presence of several samples (MPN-84a, MPN-84c, MPN-196-a, MPS-231a) with values resembling the Early Proterozoic basalt reference (Condie, 1993), indicating that at least part of the source rocks is either poorly weathered or even fresh. The quartzite samples have the highest values of MIA and show a distinct trend, indicating Fe enrichment throughout the chemical weathering history.

The AF-CNK-M plot (Figure 11c) discriminates the immobile behavior of Fe in oxidized weathering environments from the typically mobile behavior of Mg. The advantage of this arrangement is the ability to assess the extent to which CNK (feldspar) dissolution contributes to the overall weathering vector in comparison to the loss of Mg. Despite the dispersed distribution of points obtained from the analyzed metasedimentary rocks of the Meloso Formation, a path similar to the predicted weathering profile is still discernible in the AF-CNK-M plot (Figure 11c). These results combined with the MIA values indicate that part of the sediments originated from a poorly weathered source of basic composition. MgO appears to have been more influential and played a more important role in branding a geochemical “footprint” during weathering than feldspar

alteration with the development of a weathering trend line that emerges from the M vertex of the AF-CNK-M plot (Figure 11c).

Figure 11: (a) A-CN-K (Al_2O_3 – CaO* + Na_2O – K_2O) triangular diagram and CIA (Chemical Index of Alteration) scale (Nesbitt and Young, 1984). (b) A-CNKM-F (Al_2O_3, CaO*+Na_2O+K_2O+MgO, Fe_2O_3) triangular diagram and MIA(O) (Mafic Index of Alteration) (Babechuk et al., 2014). (c) AF-CNK-M (Al_2O_3+Fe_2O_3, CaO*+Na_2O+K_2O, MgO) diagram and MIA(O). Pink arrows indicate the weathering trend of analyzed samples, dashed arrows indicate the predicted weathering trend. References are from (Condie, 1993).

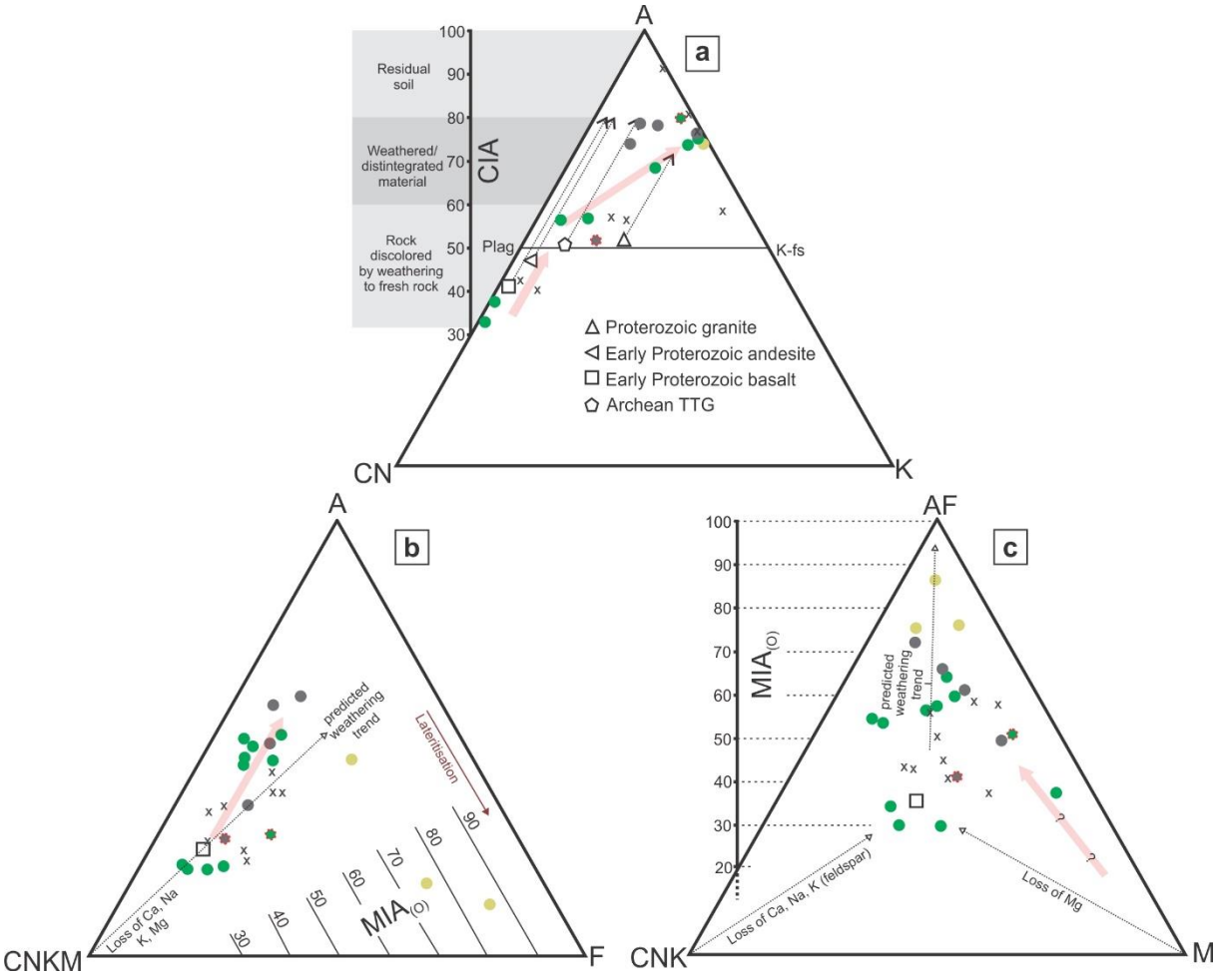

Source: Prepared by the author

3.4.2.4 Provenance

Geochemical provenance studies are based on the analysis of trace and rare earth elements. Rare earth elements, due to their unique coherent behavior, have contributed for the understanding of the geochemical processes in various fields (Bhatia and Crook, 1986; Taylor and McLennan, 1985). The relative contribution of felsic to mafic input into the sedimentary basins can be established in several plots of different compatible to incompatible element pairs (Figure 12).

The correlation between La/Th vs. Hf shows that eight of the analyzed samples plot within the field of acid rocks, with a slight distribution tendency to the andesitic and tholeiitic source fields and sedimentary recycling pathway (Figure 12a). Th/Sc and Zr/Sc ratios are directly proportional to the igneous differentiation of the source rocks. Therefore, the Th/Sc vs Zr/Sc plot is used to distinguish between the contrasting effects of the source and sedimentary processes on the composition of clastic sedimentary rocks (McLennan et al., 1993). The values obtained from our samples plot along the MORB-Andesite-Granodiorite trend, which suggests deposition in an active tectonic setting where sediment recycling is poorly represented (Figure 12b). The greenschist samples are the most diverse, straddling the mafic to felsic trend, while quartzites and phyllites reflect the andesite compositional variations in respect to the upper crust (Figure 12b). The Th/Co vs La/Sc diagram (Figure 12c) exhibits a linear tendency concurrent with the basic to felsic rocks trend similar to the Th/Sc vs Zr/Sc plot (Figure 12b). In both diagrams, the values calculated for samples MPN-84c and MPS-231a display a significant contribution of a mafic source.

During weathering, there is a tendency for an elevation of Th/U above upper crustal igneous values of 3.5 to 4.0 that is reflected in the composition of shales. Contrastingly, active margin tectonic settings deliver sediments with major components of young undifferentiated crust with low Th and U contents and Th/U ratios significantly lower than 3.5, proportional to the values from the source rocks (McLennan, 1989; McLennan et al., 1993; McLennan and Hemming, 1992). The Th/U vs Th diagram depicted in Figure 12d illustrates that most of the samples plot below the upper crust field while some fall within the depleted mantle source field.

Figure 12: Sedimentary provenance diagrams of the Meloso Formation. (a) La/Th vs. Hf (ppm) plot (Floyd and Leveridge, 1987). (b) Plot of Th/Sc versus Zr/Sc showing trend for modern turbidites (McLennan et al., 2003). (c) Th/Co vs. La/Sc plot (Cullers, 2002). (d) Plot of Th/U versus Th based in modern turbidite muds from various tectonic settings (McLennan et al., 1993). (e) Discriminant diagram for sedimentary rocks (Roser and Korsch, 1988). (f) Cr/V versus Y/Ni plot monitoring exotic (ultramafic) components (McLennan et al., 1993).

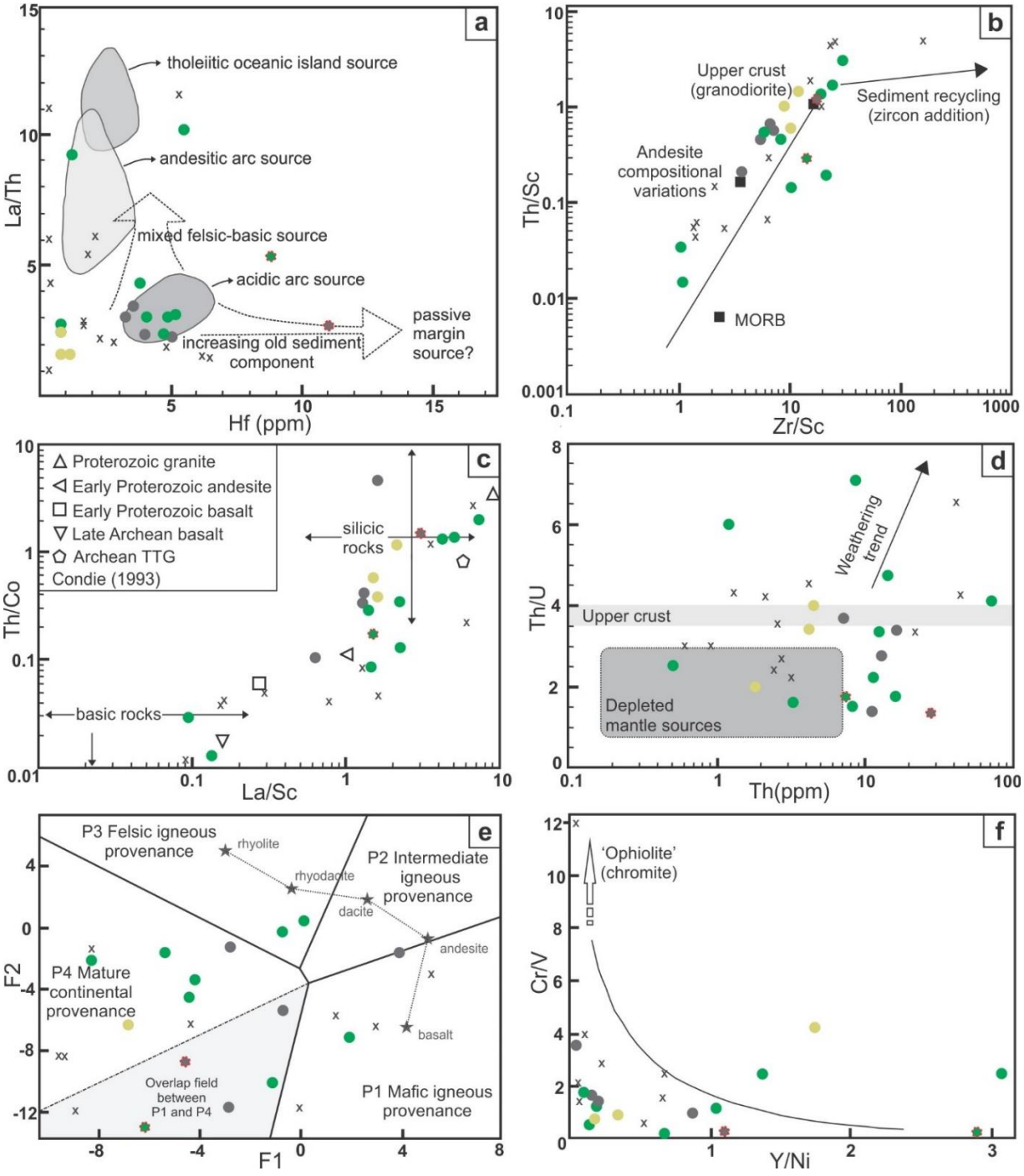

Source: Prepared by the author

The Roser and Korsch (1988) discrimination diagram (Figure 12e) exhibits a dispersed distribution of the samples in all four domains (P1-mafic igneous provenance, P2-intermediate igneous provenance, P3-felsic igneous provenance, and P4-mature continental provenance). Most samples plot in the mature continental provenance (P4) and in the overlap field between P1 and P4. Some samples (MPN-84a, MPN-84b and FD-92c) orbit the basalt-rhyolite pathway, which is compatible with the results presented in Th/Sc vs. Zr/Sc and Th/Co vs. La/Sc diagrams. McLennan et al. (1993) recognize that the identification of certain exotic components can have very important tectonic implications: thus, the Cr/V ratio is an index of the enrichment of Cr over the other ferromagnesian trace elements, whereas Y/Ni monitors the general level of ferromagnesian trace elements (Ni) compared to a proxy for HREE (Y). Figure 12f shows that most samples present low Y/Ni ratio and some of them exhibit high (~4) to very high (~12) Cr/V ratio, indicating mafic-ultramafic sources.

3.4.2.5 Tectonic setting

The tectonic nature and depositional environment of a basin can be estimated according to the geochemical characteristics of its sediments (McLennan et al., 1993). Bhatia and Crook (1986), based on the immobile trace elements, developed discrimination diagrams describing four tectonic environments: oceanic island arc, continental island arc, active continental margin, and passive margin.

The current data exhibit a scattered pattern in all tectonic discriminatory plots, Th–Sc–Zr/10, La–Th–Sc and Th–Co–Zr/10 (Figure 13a, b and c). Nevertheless, most samples are grouped within or around both, active continental margin and continental island arc fields, suggesting a tectonically active depositional environment.

Verma and Armstrong-Altrin (2013) proposed two multi-dimensional diagrams to discriminate three basic tectonic settings: arc (active volcanism), continental rift (extension), and continental collision (compression). Both diagrams, adjusted for high and low silica content, are depicted in Figure 13d and e. They display the same diffuse pattern, whereas all samples fill the three tectonic settings. The ternary discrimination diagrams (Figure 13 a, b and c) describe the remarkable contribution of scandium and cobalt in the sediments, suggesting that the rock source exhibits higher concentration of these elements when compared with those produced by oceanic island arc.

Figure 13: Ternary tectonic discrimination diagrams of trace elements for the Meloso Formation, (a) Sc-Th-Zr/10, (b) La-Th-Sc and (c) Co-Th-Zr/10 (Bhatia and Crook, 1986). New discriminant function multidimensional diagrams for (d) high-silica and (e) low-silica clastic sediments of the Meloso Formation (Verma and Armstrong-Altrin, 2013).

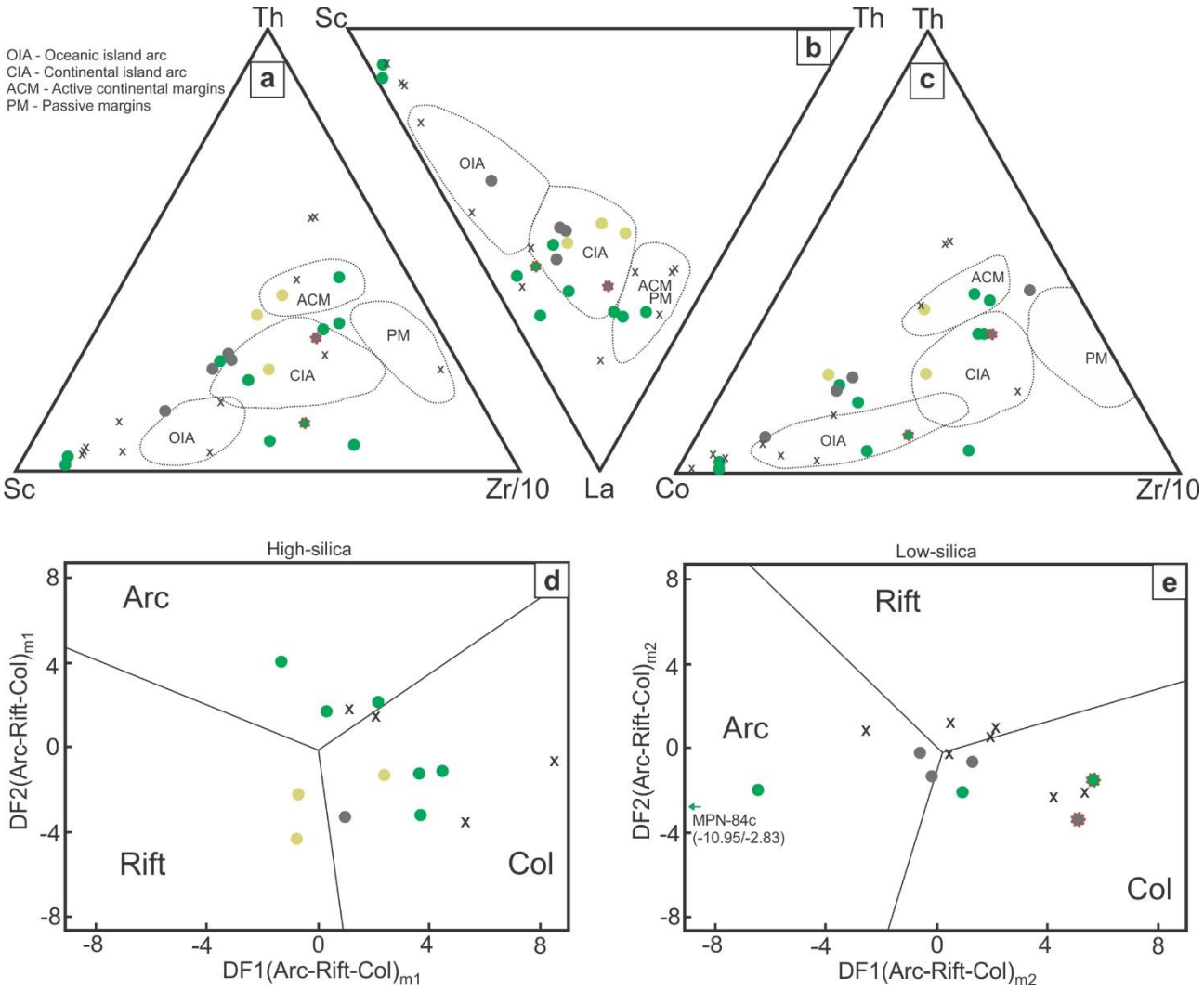

Source: Prepared by the author

3.5 Discussion

Almeida-Abreu and Renger (2007) propose a cogenetic relationship between the sedimentary units of the Serra da Serpentina Group and the Serro-Alvorada de Minas meta-ultramafic suite, based on detailed analyses of the lithological association supported by extensive field work, geochemical, and structural data. According to these authors, the Serra da Serpentina Group comprise a depositional system deposited in an extensional environment related to the opening of the Espinhaço basin and intruded by serpentinite diapirs, rejecting the interpretation of an Archean greenstone belt suggested by Uhlein (1991).

Recent works of our group (Barrote et al., 2017; Carvalho et al., 2014; Rolim et al., 2016; Silveira Braga et al., 2019, 2015) indicated that the Serra da Serpentina Group is truncated in its upper limit by an erosional unconformity that separates it from the Statherian Serra de São José Group with the development of a BIF-pebble conglomerate-rich sandstone layer. While the Serra de São José Group (maximum depositional age = 1666 ± 16 Ma) represents a facies variation of the Espinhaço basal São João da Chapada Formation. Rolim et al. (2016) propose an epicontinental sag basin during the Orosirian (youngest detrital zircon U-Pb SHRIMP age = 1990 ± 16 Ma) for the Serra da Serpentina Group.

The BIF-bearing successions that occur interleaved with gneissic rocks of the Guanhães Complex are correlated with the Serra da Serpentina Group and the detrital age spectra of the associated siliciclastic units yielded a conservative maximum depositional age of approximately 2.18 Ga (Barrote et al., 2017), although these authors recognize a very small, but still younger population aged 2.10 Ga. Based on ID-TIMS U-Pb analyses on zircon grain, a similar age spectrum (2.05-2.22 Ga) is attributed for the crystallization of the Alvorada de Minas meta-ultramafic suite (Hagedorn, 2004). The Rhyacian-Orosirian ages obtained from the geochronological studies of the Alvorada de Minas suite, and the Serra da Serpentina Group indicate a contemporaneity of these units with the development of the Mantiqueira cordilleran arc during the Minas-Bahia Orogen, east of the study area (e.g. Bruno et al., 2021; Degler et al., 2018; Kuribara et al., 2019; Noce et al., 2007).

3.5.1 The Serra da Serpentina basin: geochemistry of the Meloso Formation

The plots of the data from the Meloso Formation in the multidimensional diagrams of Verma and Armstrong-Altrin (2013) display a disperse distribution, with most analyzed samples deposited in a continental collision tectonic scenario with active volcanism. Part of the data, on the other hand, suggests an extensional setting, indicating a possible rift environment (Figure 13d and e). The same scattered pattern can be seen in the discrimination ternary graphs Sc-Th-Zr/10, La-Th-Sc and Co-Th-Zr/10 (Bhatia and Crook, 1986), where most samples occupy the active margin setting fields (Figure 13a, b and c). Furthermore, the Th/Sc vs. Zr/Sc (Figure 12b), and the Th/Co vs. La/Sc (Figure 12c) diagrams as well as the discriminative chart proposed by Roser and

Korsch (1988) (Figure 12e) exhibit a wide compositional range for the source rocks, consistent with an accretionary to collisional tectonic paleoenvironment (Figure 12b, c and e).

The intensity and rate of weathering are functions primarily of climate and rates of tectonic uplift (Wronkiewicz and Condie, 1987). According to Jacobson and Blum (2003), the lower extent of chemical weathering might be ascribed to either, an increase in tectonic activity or a shift in climatic conditions, which rendered chemical weathering less favorable in the source area. A significant proportion of samples from the Meloso Formation plotted in the (Al_2O_3 – CaO* + Na_2O – K_2O) triangle diagram and CIA scale (Nesbitt and Young, 1984) indicate that the source rocks of this unit were slightly weathered (Figure 11a). According to the A-CNKM-F and AF-CNK-M diagrams of the analyzed samples, in combination with the mafic index of alteration (MIA) (Babechuk et al., 2014) also suggest that the source rocks experienced slight weathering (Figure 11b and c). In addition, the Th/U vs. Th diagram (Figure 12d) indicates that the source rocks were weakly weathered suggesting, once again, an active tectonic setting during the deposition.

The geochemical data of most samples varied significantly from PAAS and UCC (Figure 9 and Figure 10). The Meloso Formation distinct geochemistry signature is understood as originated from exotic components that played an essential role during the basin filling (McLennan et al., 1993). Most analyzed samples collected at the upper levels of the Meloso succession, up to 100 meters below the contact with the Serra do Sapo iron formation, are enriched in ferromagnesian trace elements (Sc, V, Cr, Co, and Ni) and depleted in LILE and HFSE (Figure 6 and Figure 9a). They also present low $(La/Yb)_N$ ratios indicating a minor to moderate enrichment of HREE in comparison to the LREE (Figure 10a). The samples collected in greater depths (FD-92-a, FD-92c and FD-92f), on the other hand, show a different pattern of trace elements, being slightly depleted in ferromagnesian elements, combined with LILE and HFSE concentrations similar to the PAAS (Figure 9b). These three samples present REE concentrations similar to the PAAS, except for sample FD-92-a, which is slightly enriched in HREE. The vertical geochemical variance of the Meloso Formation reflects a drastic change of rock source during the basin infilling. The results show that the basal portion of the Meloso succession was formed by the erosion and accumulation

of upper crustal material, while the topmost layers are the result of erosion and sedimentation of mafic to ultramafic sources.

The weak correlation (r=0.32) between Al_2O_3 and Sc in the greenschist samples supports the incorporation of scandium by mafic affinity particles during the sedimentation. This is consistent with the strong positive correlation between most incompatible elements and MgO, as well as the weak to moderate positive correlation with Fe_2O_3 (Table 1). The low SiO_2/Al_2O_3 ratios presented by the fine-grained rocks (greenschists and phyllites) attest the predominantly immature character for these sedimentary rocks. The La/Th vs. Hf and Th/Sc vs. Zr/Sc diagrams (Figure 12a and b) show poor sediment recycling. These features point to an intrabasinal mafic input in the upper Meloso Formation.

Given the spatial distribution of the rocks, the tectonic scenario, and the spectra of detrital age (Barrote et al., 2017; Rolim et al., 2016) the potential sources for the sediment load that comprise the Meloso Formation are the Archean TTG terranes older than 2.7 Ga (most likely the Guanhães Complex), the mafic-ultramafic Serro-Alvorada de Minas Suite as well as the Rhyacian Minas-Bahia orogeny related rocks, accumulated in foreland terranes contemporaneously with magmatic activity during the Transamazonian event.

3.5.2 The Serra da Serpentina back-arc basin: a new proposition

The back-arc basin concept has been expanded on since Karig (1971) advanced the idea that some convergent margins were spatially and temporally associated with zones of active seafloor spreading formed over an active subduction zone (Artemieva, 2023; Stern and Dickinson, 2010). The mafic-ultramafic Serro-Alvorada de Minas Suite, the Rio Mata Cavalo meta-volcanosedimentary sequence, the geochemistry of the clastic sediments Serra da Serpentina Group and the presence of clastic-contaminated iron formations point to a back-arc type basin in response to the Minas-Bahia Orogen.

The occurrences of chromite deposits, Au+PGE-bearing quartz veins hosted by the Serro-Alvorada de Minas Suite (Angeli et al., 2011; Cabral et al., 2017; Zapparoli, 2001) supports the Almeida-Abreu and Renger (2007) interpretation of the mafic-ultramafic bodies as representing fragments of oceanic crust. The chrono-correlation

between the Serro-Alvorada de Minas Suite (2.05 to 2.22 Ga) (Hagedorn, 2004) with the Rhyacian-Orosirian detrital age of the Serra da Serpentina supracrustals (Barrote et al., 2017 and Rolim et al., 2016) advocated by Almeida-Abreu and Renger (2007) strengthen the back-arc basin hypothesis. However, caution should be exercised when considering the validity of a Rhyacian crystallization age for the mafic-ultramafic rocks, as suggested by Hagedorn, 2004, since it is unclear whether the published dates represent the age of igneous crystallization or a metamorphic overprint. In this perspective, the proposed interpretation of the Serra da Serpentina back-arc (Figure 14) must still be viewed as a compelling hypothesis.

The Serra da Serpentina back-arc extension took place in the overriding plate (Guanhães TTG terranes) along the hinge line of the subducting lithosphere with the concurrent deposition of the volcanosedimentary succession of the Rio Mata-Cavalo sequence and emplacement of the mafic-ultramafic Serro-Alvorada de Minas. This assembly represents an initial stage of oceanic crust formation and the lowest stratigraphic unit of the Serra da Serpentina back-arc basin (Figure 14a).

The following stage is characterized by subsidence and evolution of the basin infilling, commencing when the Rio Mata Cavalo volcanosedimentary sequence transitions into the basal Meloso succession deposition (Figure 14b), serving as a transitional phase between the mafic-ultramafic magmatism and the sedimentary deposition of the clastic Meloso Formation. The REE chemistry of the basal Meloso package (possibly up to 400 meters thick) exhibits a flat PAAS-like pattern (samples FD-92c, FD-92f, and FD-92a), which indicates upper crustal affinity rocks as source. The presence of exclusive Archean detrital zircon grains in some samples from this layer (Barrote et al., 2017), together with its chemistry, suggests that during the beginning of this stage the back-arc basin was surrounded by an assembly of rocks older than 2.7 Ga (Guanhães Complex). Paleoproterozoic detrital zircon grains were eventually eroded and transported to the basin, indicating that the Minas-Bahia magmatic rocks (possibly from the Mantiqueira arc) also contributed as source material for the basin filling (Barrote et al., 2017; Rolim et al., 2016).

The final stage is distinguished by the drastic change in the source rock of the uppermost layer of the Meloso Formation (100 meters thick) (Figure 14c). Most analyzed samples from this package yield low Th/U ratios (Figure 12d) and generate

high contents of Cr and Ni when compared to V and Y, respectively (Figure 12f) , both of which are rather common in mantle-derived volcanic rocks. This suggests that part of the Serro-Alvorada de Minas Suite was exposed and eroded while active hydrothermal vents fertilized with iron-rich fluids the Serra da Serpentina Sea, causing the deposition of the Serra do Sapo iron formation, comprising the Upper Sequence of the Serra da Serpentina basin.

Figure 14: Schematic model of the evolution of the Serra da Serpentina back-arc basin in response to the Rhyacian Minas-Bahia Orogen. See text for explanation.

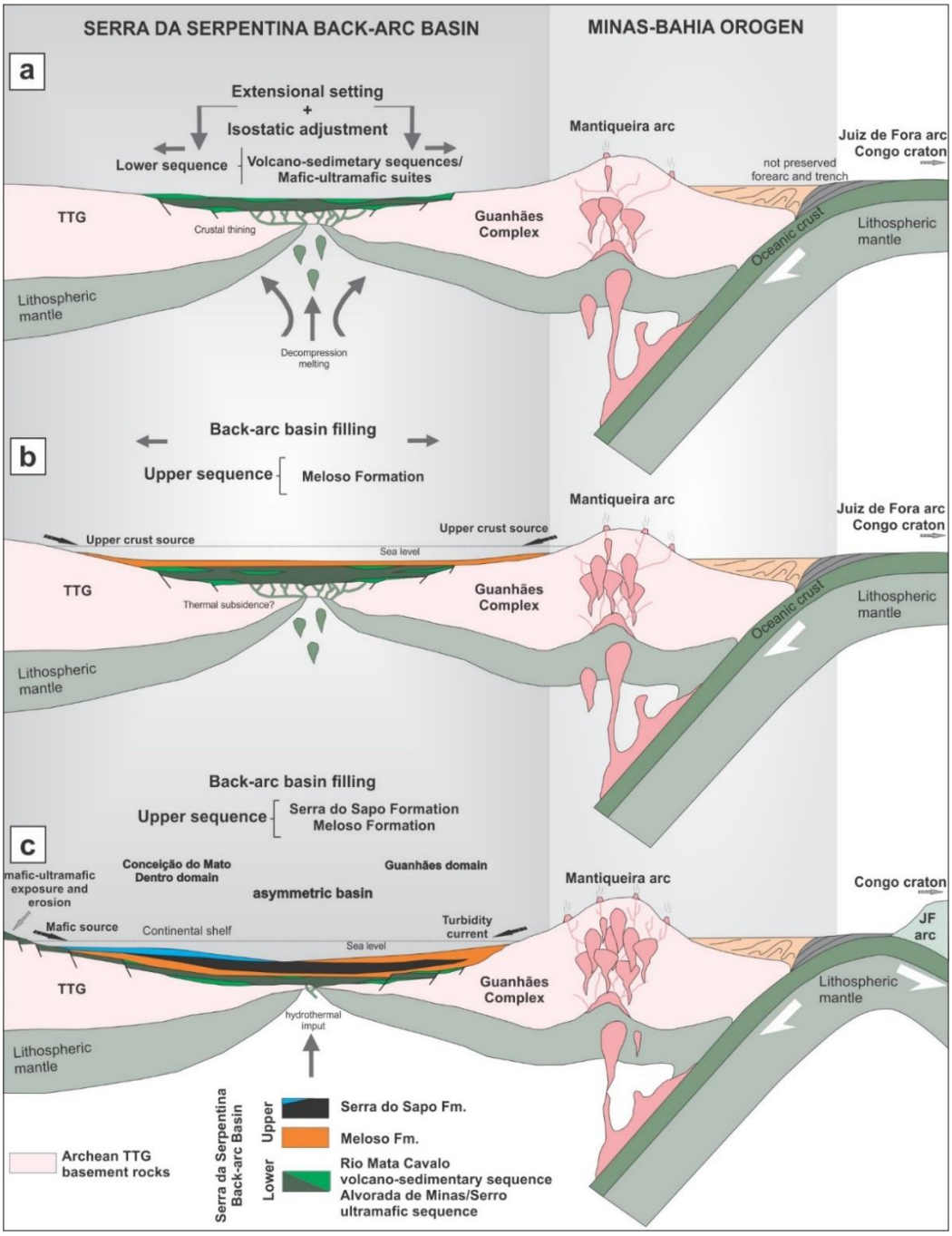

Source: Prepared by the author

Back-arc sedimentological, stratigraphic, geophysical, and analogue model studies reveal a typical asymmetric geometry (Artemieva, 2023; Balázs et al., 2016; Schellart et al., 2002) as indicated by the significant difference between the Conceição do Mato Dentro and Guanhães depositional domains (Figure 14c). According to the analogue modelling for back-arc extension proposed by Schellart et al. (2002), the Conceição do Mato Dentro domain represents the relatively stable west margin of a main zone of extension, interpreted by Rolim et al. (2016) as deposited on a continental shelf margin environment. The sediment record of the Guanhães domain reflects a more energetic environment with the association of coarse to fine sediments in a turbiditic-like sequence (Figure 6b, c and Figure 14c).

3.5.3 Regional implications

The proposed model of the Serra da Serpentina back-arc basin in response to the Minas-Bahia orogeny raises relevant regional problems. In the Minas Tectonic Terranes (MTT), foreland deposits related to the southern portion of the Minas-Bahia orogeny are represented by the Sabará and Itacolomi groups. The Sabará Group comprises a flysch sequence developed by gravitational subaqueous debris flow and frequent turbidite sedimentation (Dorr II, 1969; Gonçalves and Uhlein, 2022; Reis et al., 2002), with age bracketed between ca. 2125 Ma and 2098 ± 33 Ma (H. K Brueckner et al., 2000; Dopico et al., 2017; Dutra et al., 2019; Rossignol et al., 2020). The alluvial and fluvial sediments of the Itacolomi Group are regarded as a molasse sequence (Alkmim and Marshak, 1998) yielding Rhyacian maximum depositional ages: 2059 ± 58 Ma (Machado et al., 1996), 2143 ± 16 Ma (Hartmann et al., 2006), 2087 ± 19 Ma (Jordt-Evangelista et al., 2015), and 2129 ± 11 Ma (Duque et al., 2020).

The active tectonic depositional environment attributed to the marine sediments of the Serra da Serpentina Group combined with its Rhyacian-Orosirian depositional age is congruent with the foreland deposits exemplified by the Sabará and Itacolomi groups further south in the MTT. This suggests that these three successions could be deposited in the same sedimentary system, although they denote distinct sedimentary facies. If this correlation is correct, the following questions emerge. Are there marine sediments equivalent to the Serra da Serpentina Group further south within the MTT? If yes, are they related to Rhyacian mafic to ultramafic rocks potentially compatible with the Serro-Alvorada de Minas Suite?

In the MTT, Cabral et al. (2022) recognized at the Rola Moça Ridge the occurrence of pillow lava yielding crystallization age at 2141 ± 6 Ma. In the westernmost region of the MTT crop out E-MORB affinity metaultramafic and amphibolites rocks (aged 2.1 Ga) associated with metasedimentary rocks, which are interpreted by Miranda and Chaves (2021) as an ophiolitic sequence. Near Monlevade, Cabral and Zeh (2015) describe the N-MORB affinity Sítio Largo amphibolite, which yields a crystallization age at 2188 ± 24 Ma. In its type locality, the Sítio Largo amphibolite intercalates with quartzite and quartz-mica schist (Reeves, 1966), and unconformably overlies the Cauê iron formation.

The Sítio Largo amphibolite underlies the marine sequence represented by the Piracicaba Group. This group has been interpreted tentatively as deposited in a passive margin and foreland basin (Alkmim and Martins-Neto, 2012; Bekker et al., 2003; Gonçalves and Uhlein, 2022; Sayão Valladares et al., 2004). Using statistical analyses of age distributions, Rossignol et al. (2020) estimate 2333 ± 11 Ma as the maximum depositional age for the Piracicaba Group, despite the presence of younger zircon grains yielding a concordant age at 2271 ± 15 Ma. The youngest zircon population in the Piracicaba Group is inferred to originate from reworked volcanic ashes expelled from volcanos derived from the Mineiro Belt (southmost portion of the Minas-Bahia Orogen) (Rossignol et al., 2020). Cabral and Zeh (2015) alternatively adopt the crystallization age of the Sítio Largo amphibolite (2188 ± 24 Ma – LA-SF-ICPMF) to constrain the onset of sedimentation of the Piracicaba Group, suggesting a foreland depositional environment as already proposed by Bekker et al. (2003).

If the assembly of mafic igneous bodies such as the Sitio Largo amphibolite and the Rola Moça lavas is contemporaneous with the Serro-Alvorada de Minas Suite, both the Serra da Serpentina and Piracicaba Groups were deposited in an oceanized back-arc basin constituting lateral facies variations, while the Sabará and Itacolomi groups represent proximal to continental foreland sequences of the Minas-Bahia orogen.

Additionally, based on geochemistry and U–Pb zircon ages of metamafic-ultramafic rocks, Leal et al. (2021) interpret the Riacho dos Machados meta-volcanosedimentary sequence, exposed further north, as formed in a back-arc basin during the assembly of São Francisco-Congo paleocontinent in the Late Rhyacian. Moreover, in the northern portion of the Minas-Bahia Orogen, Rosière et al. (2019) describe and

correlate Fe-rich sequences that extend from the northwestern border of the São Francisco protocraton (Colomi Group and Caetité sequence located in the state of Bahia) with the Serra da Serpentina Group. The Riacho dos Machados meta-volcanosedimentary sequence, the Colomi Group, and the Caetité sequence are located in conformity to where the Minas-Bahia foreland back-arc basin relicts should be found (Figure 15).

Figure 15: Distribution of the back-arc system during the Minas-Bahia orogeny.1 = Serra da Serpentina Basin, 2 = Piracicaba, Sabará, Itacolomi assembly, 3 = Riacho dos Machados meta-volcanosedimentary sequence, 4 = Caetité Sequence, 5 = Colomi Group. Gray color represents Archean Blocks.

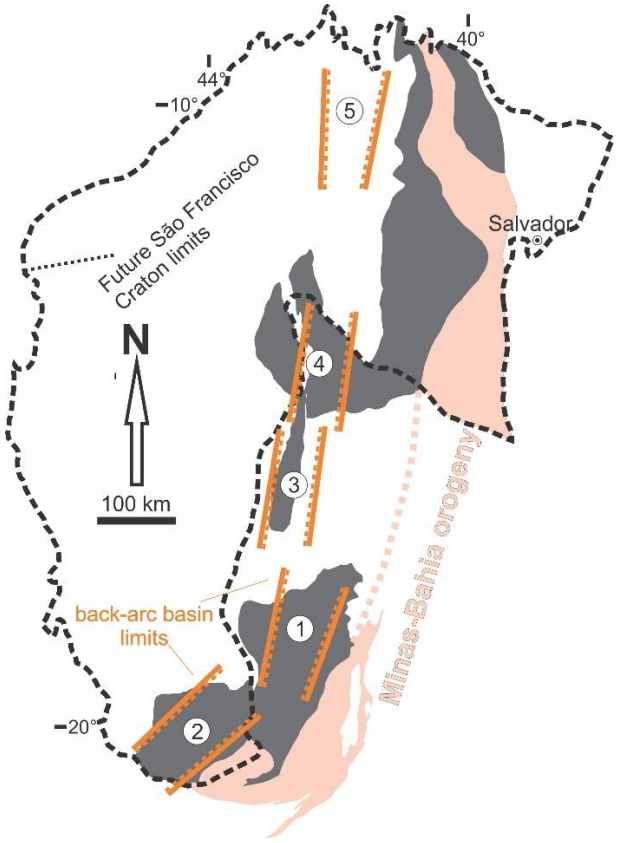

Source: Prepared by the author

3.6 Conclusions

The combination of field data, petrography and geochemical analyses supported by geochronological data available in the literature leads to the following conclusions:

(i) The Serra da Serpentina Group was deposited in an active continental margin in the foreland terrane during the compressive tectonism related to the Minas-Bahia Orogen.

(ii) The metasedimentary rocks from the Meloso Formation originated from sediments whose protoliths were crustal- (lower portion) and mantle-derived (upper portion).

(iii) The assembly composed of the Serro-Alvorada de Minas Suite, the Rio Mata Cavalo meta-volcanosedimentary sequence, and the Serra da Serpentina Group suggest evolution of a back-arc basin in response to the Minas-Bahia Orogen during Rhyacian time.

(iv) Future research will concentrate on the tectonic correlation between the Piracicaba, Sabará, Itacolomi, and Serra da Serpentina Groups in the Minas-Bahia orogen context. Similar investigations are also required in the Riacho dos Machados meta-volcanosedimentary sequence, the IF-bearing Caetité sequence and Colomi Group as potential candidates to integrate the same Rhyacian back-arc system underlying the Espinhaço rift sequence.

Acknowledgements

This study was financially supported by the technical-scientific UFMG-Anglo American Company collaboration project. A special thanks to G. Sarquis and his team for supplying drill hole data and assistance in the field work. The authors also wish to acknowledge funding from CNPq (Pr. Nr. 163930/2021-0 - RP) and (Pr. Nr. 472602/2009-8 - CAR). We also thank the anonymous reviewer and Dr. S. Oriolo for their critical comments and constructive suggestions and G. Uhlein for the fruitful discussions. The Centro de Pesquisas Professor Manoel Teixeira da Costa (Universidade Federal de Minas Gerais) provided valuable infrastructure.

4 RESEARCH MANUSCRIPT - UNCOVERING THE ESPINHAÇO SUPERGROUP IN THE GUANHÃES BASEMENT INLIER, MINAS GERAIS, BRAZIL: TECTONIC IMPLICATIONS BASED ON STRUCTURAL GEOLOGY AND DETRITAL ZIRCON U-PB-HF ISOTOPE RECORD

Authors: *Ricardo Pagung[a], Carlos Alberto Rosière[b], Armin Zeh[c], Tiago Amâncio Novo[b]

[a] Programa de Pós-Graduação em Geologia, Instituto de Geociências, Universidade Federal de Minas Gerais, Belo Horizonte, MG, Brazil.

[b] Universidade Federal de Minas Gerais, Programa de Pós-Graduação em Geologia, CPMTC-IGC-UFMG, Campus Pampulha, 31270-901 Belo Horizonte, MG, Brazil

[c] Karlsruher Institut für Technologie, Institut für Angewandte Geowissenschaften, Karlsruher, Germany

* Corresponding author. Universidade Federal de Minas Gerais, CPMTC, Instituto de Geociências, Av. Presidente Antônio Carlos, 6627 Pampulha, Belo Horizonte, MG, Brazil.

E-mail addresses: ripagung@gmail.com (R. Pagung), crosiere@gmail.com (C.A. Rosière), armin.zeh@kit.edu (A. Zeh), tiagoanovo@gmail.com (T.A. Novo)

Keywords: Guanhães Basement Inlier, Lower Espinhaço Sequence, Structural analyses, Detrital U-Pb dating, Lu-Hf isotope, Crustal core complex

Abstract

The Guanhães Basement Inlier (GBI) covers a large area of the western external domain of the Araçuaí Orogen. In its southern segment, plutonic bodies of the Statherian anorogenic Borrachudos Suite are extensively exposed, comprising a domal structure in tectonic contact with Archean gneissic rocks and Rhyacian to Statherian metasediments including Statherian quartzite layers crono-correlated with units of the Lower Espinhaço Sequence. In this study we combine geological mapping and structural analysis with U-Pb-Hf isotope studies of detrital zircons from siliciclastic units exposed in the GBI and Eastern Espinhaco Range. We compare our results with available geochronological and stratigraphic data of the Espinhaço Supergroup, to better understand the relationship between the source and time of deposition of the Lower Espinhaço units and the coeval Borrachudos Suite magmatism during the opening of the Espinhaço rift system. The analyzed detrital zircon grains yielded U-Pb ages distributed in a wide range of periods clustered at Archean (3500-2500 Ma), Neoarchean-Siderian (2500-2400 Ma), Rhyacian-Orosirian (2300-1915 Ma), and Statherian (1800-1675 Ma) consistent with earlier results. The distributions of ages and εHf(t) values of zircon grains show: (1) the Lower Espinhaço Sequence in the GBI have

a diverse source comprising recycled Archean old crust as well as juvenile crust produced between 2.5 to 2.1 Ga, (2) the youngest age peak of 1725 Ma delivered by the zircons from units in the GBI's interior records a concordant maximum depositional age when compared with its equivalent units such as the Bandeirinha and São João da Chapada formations exposed in the southern Espinhaco Range. These ages are currently documented in zircon grains from the anorogenic Borrachudos Suite plutonic rocks as well as its volcanic equivalents such as the Conceição do Mato Dentro metarhyolite and K-rich dikes and sills from Diamantina area. This suggests that the deep-seated magmatic body crystallized and reached shallower crustal levels concurrently with the opening of the western sector of the rift, following the initial sub-volcanic rift-related magmatism of the Conceição do Mato Dentro metarhyolite and K-rich dikes. The uplift, exhumation and exposure of the voluminous bodies comprising the Borrachudos Suite developed during the Statherian period, during to the Lower Espinhaço sedimentation in the GBI, suggesting a magmatic-driven core complex that compartmentalized the basin into deeper Western and shallow Eastern domains. The age spectrum for the Espinhaço Supergroup basal units in the studied area is most likely the result of a protracted crustal thinning and eastward asymmetrical lateral expansion of the Espinhaço rift basin which was controlled by buoyant plutonic bodies.

4.1 Introduction

The Guanhães Basement Inlier (GBI) is a structural-erosive window in the western Araçuaí orogen (Kuchenbecker and Barbuena, 2023). It can be subdivided into a northern and southern segment, separated by the E-W trending Virgolândia sinistral transcurrent shear zone (Figure 16). The northern segment is made up by Archean orthogneisses with local metasedimentary covers, and magmatic rocks related to the Rhyacian-Orosirian Minas-Bahia orogeny (Grochowski et al., 2021; Kuchenbecker and Barbuena, 2023; Morais et al., 2023). The southern segment, which is the focus of this study, exposes the Borrachudos anorogenic suite of Statherian age, along with poorly constrained Archean rocks and BIF-bearing metasedimentary sequence (Barrote et al., 2017; Carvalho et al., 2014; Grossi-Sad et al., 1997; Silveira Braga et al., 2019, 2015).

At the western margin of the GBI, Rolim et al. (2016) describe an erosional discontinuity between the basal Rhyacian-Orosirian BIF-bearing Serra da Serpentina Group and the Statherian Serra de São José Group. The same authors further distinguish two cycles of basinal infill: an older cycle, related to deposition of the Serra da Serpentina Group in a back-arc basin during the Minas-Bahia orogeny (Pagung et al., 2023), and a younger cycle related to deposition of the Statherian Serra de São José Group, which is correlated to the Lower Espinhaço Sequence (Rolim et al., 2016). Statherian maximum depositional ages are also reported from metasedimentary rocks of two localities from the center part of the GBI by Silveira Braga et al. (2015, 2019), indicating the occurrence of the Lower Espinhaço Sequence also in this region.

The igneous rocks of the Borrachudos anorogenic suite are identified as the source for the youngest zircon grains in the basal strata of the Espinhaço rift system (Chemale et al., 2012; Dussin and Dussin, 1995; Dussin et al., 2000; Santos et al., 2013). Extensive research encompassing geochemical, U-Pb geochronology, and more recently Lu-Hf isotopic analyses has been undertaken to investigate the Borrachudos Suite (e.g. Dussin and Dussin, 1995; Dussin et al., 2000; Fernandes et al., 2000; Gomes et al., 2020; Grossi-Sad et al., 1997; Machado et al., 1989; Magalhães et al., 2018; Silva et al., 2002). Nevertheless, despite these efforts, the geodynamic evolution of this suite remains poorly understood, particularly its role during magmatic rock emplacement and exhumation, directly linked to the formation of the Espinhaço rift system (Alkmim and Martins-Neto, 2012; Chemale et al., 2012; Dussin and Dussin, 1995; Guadagnin et al., 2015; Santos et al., 2013).

To address this problem, we present in this study new sets of U-Pb ages and Hf isotopic data of detrital zircon populations from siliciclastic rock units exposed in the interior of the GBI, along with results of geological mapping and structural analysis. These new data provide new constraints on the extent of the Lower Espinhaço Sequence within the GBI area and its relationship with associated plutonites of Statherian age. Furthermore, these will help to establish a geodynamic model for the evolution of the GBI during the Statherian.

4.2 Geological setting

4.2.1 Guanhães Basement Inlier (GBI)

The GBI, also referred as the Guanhães Block, (Alkmim et al., 2006; Brito Neves et al., 2021; Kuchenbecker and Barbuena, 2023) spans an area of about 24,000 km^2 at the southeastern margin of the São Francisco Craton (e.g. Alkmim et al., 2006, 2017; Amaral et al., 2020; Pedrosa-Soares et al., 2001; Peixoto et al., 2015, 2018) (Figure 16a). At its eastern and northern margins, the GBI is limited by metasedimentary rocks of the Neoproterozoic Macaúbas Group and correlates units (Kuchenbecker et al., 2015), and tectonically juxtaposed against rocks related to the Rhyacian-Orosirian Minas-Bahia Orogen (Barbosa et al., 2019; Bruno et al., 2021; Cutts et al., 2020; Degler et al., 2018; Heilbron et al., 2010; Teixeira et al., 2015). At its western margin, the GBI is juxtaposed to Paleo-Mesoproterozoic rocks of the Espinhaço Supergroup (Chemale et al., 2012; Rolim et al., 2016; Santos et al., 2013), and at its southern margin by Archean to Paleoproterozoic rock units of the Quadrilatero Ferrífero District, in particular by wedge-shaped slices of the Rio das Velhas and Minas Supergroups (e.g. Alkmim and Marshak, 1998; Bekker et al., 2003; Chemale et al., 1994; Hartmann et al., 2006; Rosière et al., 2008).

The GBI consists of poorly constrained Archean TTG orthogneisses and migmatites, formed between 3.1 and 2.7 Ga (Barrote et al., 2017; Peixoto et al., 2015; Rolim, 2016; Silva et al., 2002), tectonically intercalated with Paleoproterozoic volcano-sedimentary sequences (Barrote et al., 2017; Carvalho et al., 2014; Silveira Braga et al., 2019, 2015) and the Borrachudos anorogenic suite. The Borrachudos Suite represents relics of a silicic large igneous province (SLIP) of Statherian age, which is dominated by A-type granites and felsic volcanic, and minor amphibolites (Magalhães et al., 2018) (Figure 16b).

Results of U-Pb dating of felsic and mafic rocks of the Borrachudos Suite delivered a wide range of crystallization ages from 1.80 to 1.67 Ga (Dutra et al., 2020; Gomes et al., 2020; Machado et al., 1989; Magalhães et al., 2018). The igneous rocks of this suite are tectonically intercalated by slices of supracrustal units belong either to the Serra da Serpentina Group, deposited at >1.99 Ga (Rolim et al., 2016), or the basal strata of Espinhaço Supergroup, deposited at 1.80-1.68 Ga (Chemale et al., 2012).

The GBI is considered to represent a dome structure bounded by high-angle reverse shear zones (Alkmim et al., 2006, 2017; Amaral et al., 2020; Pedrosa-Soares et al., 2001; Peixoto et al., 2015, 2018). Locally the top of this dome structures is made up by hosting a thick-skinned imbricate system, which is well exposed in the foreland terrane of the Araçuaí Orogen.

4.2.2 The eastern border of the southern Espinhaço Range

The GBI-Espinhaço Range boundary is characterized by a series of north-south trending ridges, slightly bow-shaped, made up by rock units of the Serra da Serpentina Group (Rhyacian-Orosirian), comprising from bottom to top of the Meloso and Serra do Sapo formations (Figure 16b). Detrital zircon grains from fine-grained quartzite constrain a maximum depositional age (MDA) of the Serra da Serpentina Group at 1.99 Ga (Rolim et al., 2016). Canga duricrusts of the Serra do Sapo iron formation commonly form the mountain crests, and psamo-pelitic units of the Meloso Formation the deeper slopes of the valleys. Tectonic slivers of Archean TTG's (2711 ± 5 Ma, Rolim, 2016) and rhyolites of the Statherian Conceição do Mato Dentro Suite (ca. 1715 Ma, Machado et al., 1989) are exposed in deeply weathered lowlands (Figure 17a).

Discontinuous bodies of meta-ultramafic to -mafic rocks of the Serro-Alvorada de Minas Suite yield a wide range in crystallization ages between 2.22 and 2.05 Ga (Almeida-Abreu et al., 1989; Almeida-Abreu and Renger, 2007; Hagedorn, 2004; Zapparoli, 2001). The contact relationships of the mantle-derived (meta)ultramafic rocks with Archean basement rocks, mostly TTGs, suggest emplacement of serpentinitic diapirs along fractures, perhaps related to crustal extension during formation of the Espinhaço basin (Almeida-Abreu and Renger, 2007). Pagung et al., (2023) proposed that the Serra da Serpentina Group and mafic-ultramafic rocks result from the successive opening of a continental back-arc basin towards an oceanic basin behind the Mantiqueira magmatic arc during the Rhyacian-Orosirian Minas-Bahia orogeny.

The Serra de São José Group, which is made up from bottom to top by the Lapão, Itapanhoacanga, Jacém and Canjica formations, covers unconformably the Serra da Serpentina Group, and it is interpreted as lateral facies of the São João da Chapada Formation (Lower Espinhaço Sequence) by Rolim et al. (2016). It comprises a

complete cycle of transgressive sedimentary deposits that were accumulated during extension of the Espinhaço intracontinental rift-basin at ca. 1.66 Ga (Rolim et al., 2016). Silveira (2016) attributed a somewhat younger maximum depositional age of 1.63 Ga for the Itapanhoacanga Formation in the surroundings of Serro.

Figure 16: (a) Simplified geotectonic map of the São Francisco craton with distribution of Archean to Paleoproterozoic rock units, and position of the Guanhães Basement Inlier. (b) Geological map of the Guanhães Basement Inlier and surrounding units (Pinto and Silva, 2014).

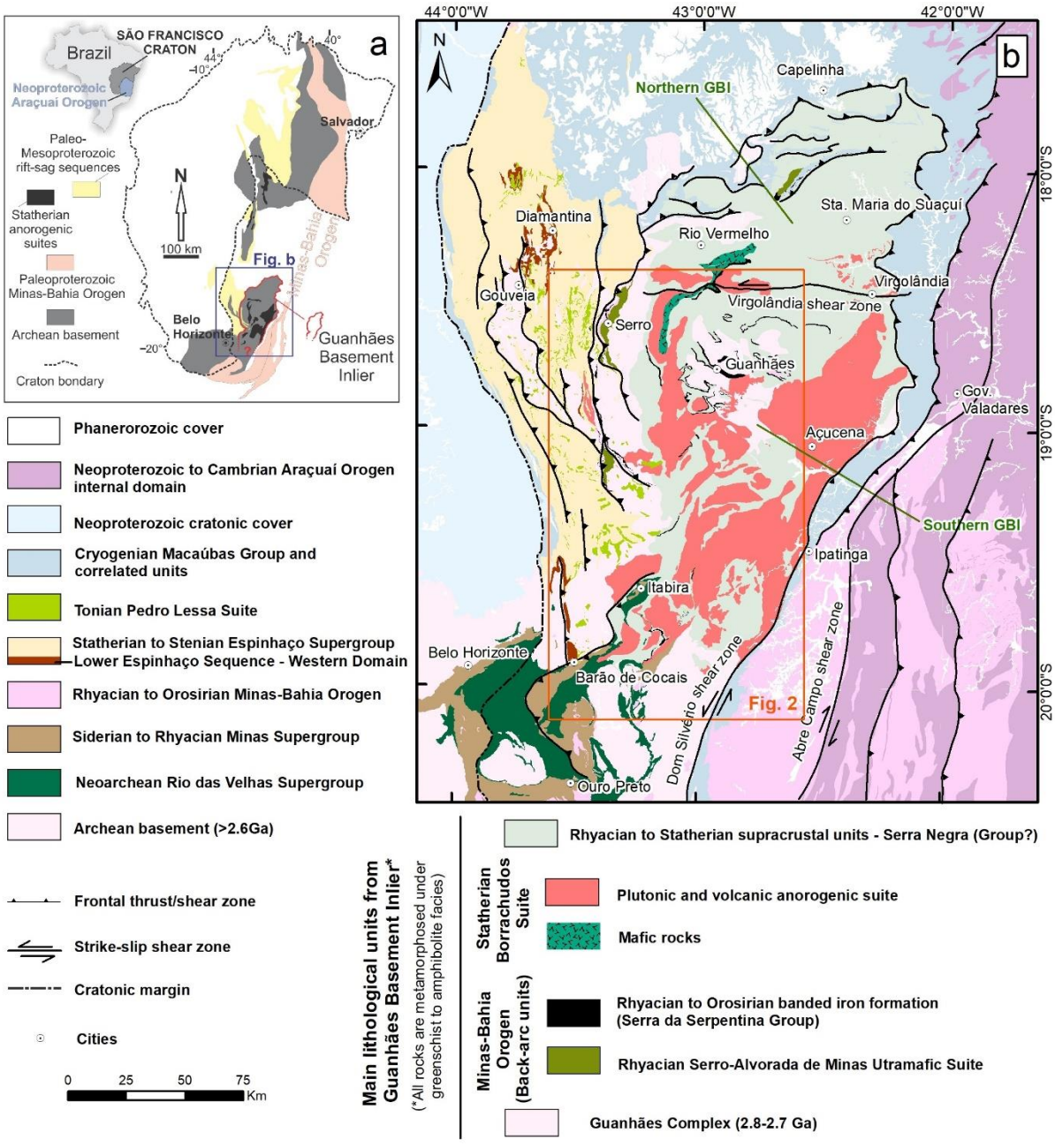

Source: Prepared by the author

4.2.3 The interior supracrustal units

In the GBI, BIF-bearing supracrustal rock units are tectonically juxtaposed to the Borrachudos anorogenic suite and Archean TTG rocks (Figure 17a). Results of detrital zircon dating define a Rhyacian MDA of 2.18 Ga for quartzites interbedded with iron formations in the surroundings of the city of Guanhães (Barrote et al., 2017; Grossi-Sad et al., 1997). Further to the south, detrital zircon grains in quartzites of the Pedra Branca ridge yield a MDA of 2.02 Ga (Carvalho et al., 2014), and meta-conglomerates from the Morro Escuro ridge a younger MDA of 1.68 Ga (Silveira Braga et al., 2015) (Figure 17b). A similarly young MDA of 1.67 Ga was also obtained from the upper quartzite unit of the Horto-Baratinha iron ore deposit (Silveira Braga et al., 2019). All supracrustal units mentioned above were included in an earlier regional mapping program within the undivided Serra Negra Group (Pinto and Silva, 2014) (Figure 16).

4.2.4 The Espinhaço Supergroup and associated volcanism

The Espinhaço Supergroup comprises an approximately 6000-meter-thick sequence of sandstones, pelites, conglomerates, volcanic rocks, and minor carbonates (Figure 16) (Alkmim et al., 2017; Alkmim and Martins-Neto, 2012; Almeida-Abreu, 1995; Almeida-Abreu et al., 1989; Almeida-Abreu and Renger, 2007; Martins-Neto, 1998; Martins-Neto et al., 2001; Pflug, 1965; Schöll and Fogaça, 1979). Along the southern Espinhaço range, the units encompass a basal rift sequence followed by a rift-sag accumulation developed within an intracontinental basin between 1.8 to 1.0 Ga (Alkmim and Martins-Neto, 2012; Chemale et al., 2012; Guadagnin et al., 2015; Santos et al., 2013).

The Lower Espinhaço Sequence (Figure 16b), in its type locality, is composed of the basal Bandeirinha Formation (MDA = 1785 Ma, Santos et al., 2013), which is separated from the overlying São João da Chapada Formation by an unconformity, although a gradational contact is locally exposed. The Bandeirinha Formation comprises an approximately 200 m-thick packages of quartz-rich sandstones and coarse-grained conglomerates, deposited in fault-bonded depocenters (Martins-Neto, 1998; Santos et al., 2013).

The São João da Chapada Formation comprises a 300m thick sequence of coarse-grained sandstones with pelitic intercalations deposited in a braided fluvial system

(Martins-Neto, 1998; Schöll and Fogaça, 1979). Detrital zircon grains indicate a Paleoproterozoic MDA of ca. 1710 Ma (Chemale et al., 2012; Santos et al., 2013). This sedimentary succession is transected and stratiform interlayered by alkaline volcanic rocks, which intruded at ca. 1710 Ma (Chemale et al., 2012; Machado et al., 1989).

In the Cambotas ridge, near Barão de Cocais, ruditic and psammitic rocks encompasses the Tamanduá Group (correlated with the Lower Espinhaço Sequence) (Figure 17a). The youngest zircon population reflects a Statherian MDA of ca. 1740 Ma (Dutra et al., 2020). Siliciclastic rocks of the Lower Espinhaço Sequence in the Altamira and Ipoema region yield a slightly older Statherian depositional age of 1750 Ma (Oliveira et al., 2019) (Figure 17a).

4.3 Samples

During this study, zircon grains were extracted from five samples of metasedimentary rocks located in the interior of the GBI, these rocks are mapped as belonging to the Serra Negra Group. The samples were affected by a different degree of metamorphic overprint and weathering alteration. Sample location, stratigraphic position and regional Paleoproterozoic assembly are shown in the Figure 17 and Figure 18.

Sample 03-084 is a coarse-grained biotite-sillimanite quartzite exposed at the Santo Antônio River valley (UTM 23K-723789/7876154). Sample 07-001 is a mylonitic kyanite-bearing quartzite, which was collected on the southeastern slope of the Morro Escuro ridge (UTM 23K-695378/7853664).

The two samples 08-001 and 08-002 represent fine-grained, deeply weathered sericite quartzite exposed at a tectonic surface, identified as the basal décollement that separates the Archean basement rocks and supracrustal units. Sample 08-001 was taken at the base of the Morro Escuro ridge (UTM 23K-696058/7852065), and sample 08-002 near to the town of Ferros (UTM 23K-708157/7868836). Sample 10-001 represents a poorly sorted, polymitic meta-conglomerate with large boulders from the top of the Pedra Branca ridge (UTM 23K-694142/7830393).

Figure 17: (a) Geological map of the study are with sample locations and published geochronological data, modified from Pinto and Silva (2014). (b) Detailed geological map of the Morro Escuro ridge region (modified from Carvalho et al. (2014). (1) Rolim et al. (2016), (2) Silveira Braga et al. (2015), (3) Carvalho et al. (2014), (4) Barrote et al. (2017), (5) Silveira Braga et al. (2019), (6) Gomes et al. (2020), (7) Magalhães et al. (2018), (8) Silveira (2016), (9)Dutra et al. (2020), (10) Oliveira et al. (2019).

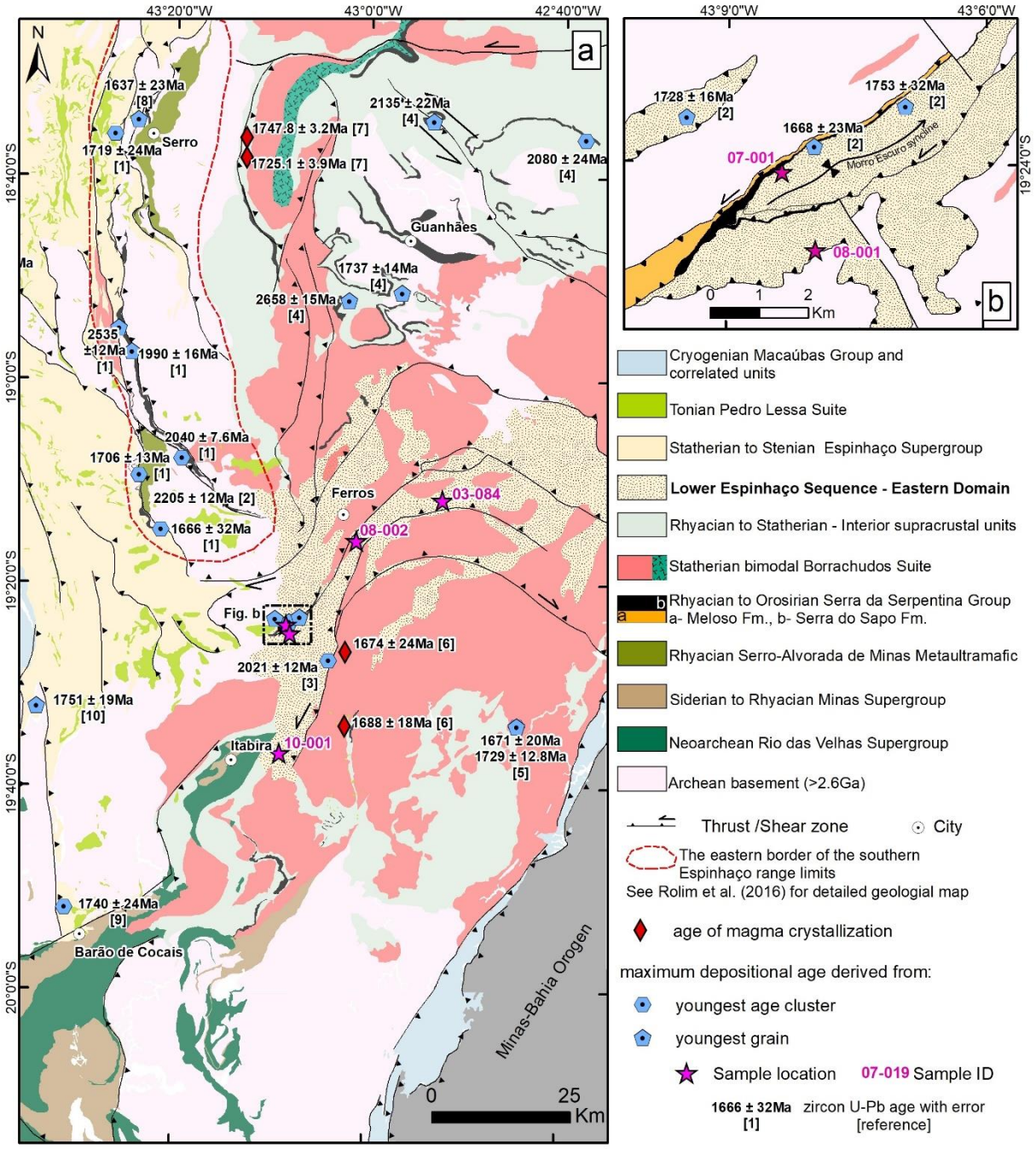

Source: Prepared by the author

4.4 Analytical methods

4.4.1 Zircon separation and imaging

Zircon grains were extracted by standard techniques at SEPURA laboratory of UFMG (Universidade Federal de Minas Gerais, Brazil), comprising crushing, grinding, panning, magnetic separation (Frantz isodynamic separator) and heavy liquids. Finally, zircon grains were manually picked under ethanol, mounted on double-sided tape, sputtered with Au for 10 s, and imaged for their morphologies (prior to epoxy mounting), and internal structures (after epoxy mounting and polishing) using a TESCAN VEGA2 scanning electron microscope at the Department of Mineralogy and Petrology at Karlsruhe Institute of Technology (KIT). Based on these images the best zircon grains/domains were selected for in-situ U-Pb dating and Lu-Hf isotope analyses.

4.4.2 U-Pb zircon geochronology

Uranium-Th-Pb analysis were performed by LA-SF-ICP-MS (laser ablation - sector-field - inductively coupled plasma - mass spectrometry) using a 193nm ArF Excimer laser (Analyte Excite+, Teledyne Photon Machines) coupled to a Thermo-Scientific Element XR instrument at KIT, Karlsruhe, Germany. Zircon grains of unknown age were analyses together with the reference zircon material BB-1 (primary standard), Plešovice and KA1 (KaapValley), using a laser spot diameter of 25 µm, a laser fluence of 3.0 J/cm2, at 8 Hz repletion rate, RF=1106 W, and a mixed Ar-He-N2 carrier gas consisting of Ar=0.78 L/min, He=0.3cell+0.2cup (both L/min), and N2=0.013 L/min. Three pulses of pre-ablation were obtained prior to each analysis of 15 s duration following 15 s background measurement. All raw data were corrected offline using an in-house MS Excel© spreadsheet program (Gerdes and Zeh, 2006, 2009). A common Pb correction based on the interference and background corrected 204Pb signal and a model Pb composition were applied (Stacey and Kramers, 1975).

Multiple measurement of the reference zircon BB (used as primary standard), Plešovice and KA1 yielded Concordia ages of 562.2 ± 1.8 Ma (MSWD=0.57, Probability=0.45, n= 22), 337.9 ± 1.1 Ma (MSWD=2.7, Probability=0.10, n=22), and 3227.7 ± 6.7 Ma (MSWD=0.005, Probability=0.94, n=14), respectively, in agreement with published TIMS ages (Santos et al., 2017; Schoene et al., 2006; Sláma et al., 2008). Concordia ages and age spectra diagrams were plotted by means of the

software ISOPLOT 3.75 (Ludwig, 2012), and AgeDisplay (Sircombe, 2008), respectively. Age spectra comprises 207Pb/206Pb ages of analyses with a concordance level of 90-110%.

Figure 18: (a) Lithological profiles of metasedimentary sequences of the southern border of the Espinhaço Range and the Interior supracrustal units (Morro Escuro BIF-bearing sequence, Guanhães BIF-bearing succession and undivided schist and quartzite packages). (b) Lithostratigraphic position of Paleoproterozoic rock units exposed within the Southern Espinhaço Range, eastern border of the southern Espinhaço Range, and in the Guanhães basement inlier. Age references: (1) Machado et al. (1989), (2) Chaves and Coelho (2018), (3) Chemale et al. (2012) (4) Hagedorn (2004), (5) Rolim et al. (2016), (6) Magalhães et al. (2018); (7) Barrote et al. (2017), (8) Carvalho et al. (2014), (9) Silveira Braga et al. (2019) (10) Silveira Braga et al. (2015) and (11) Cabral and Zeh (2015).

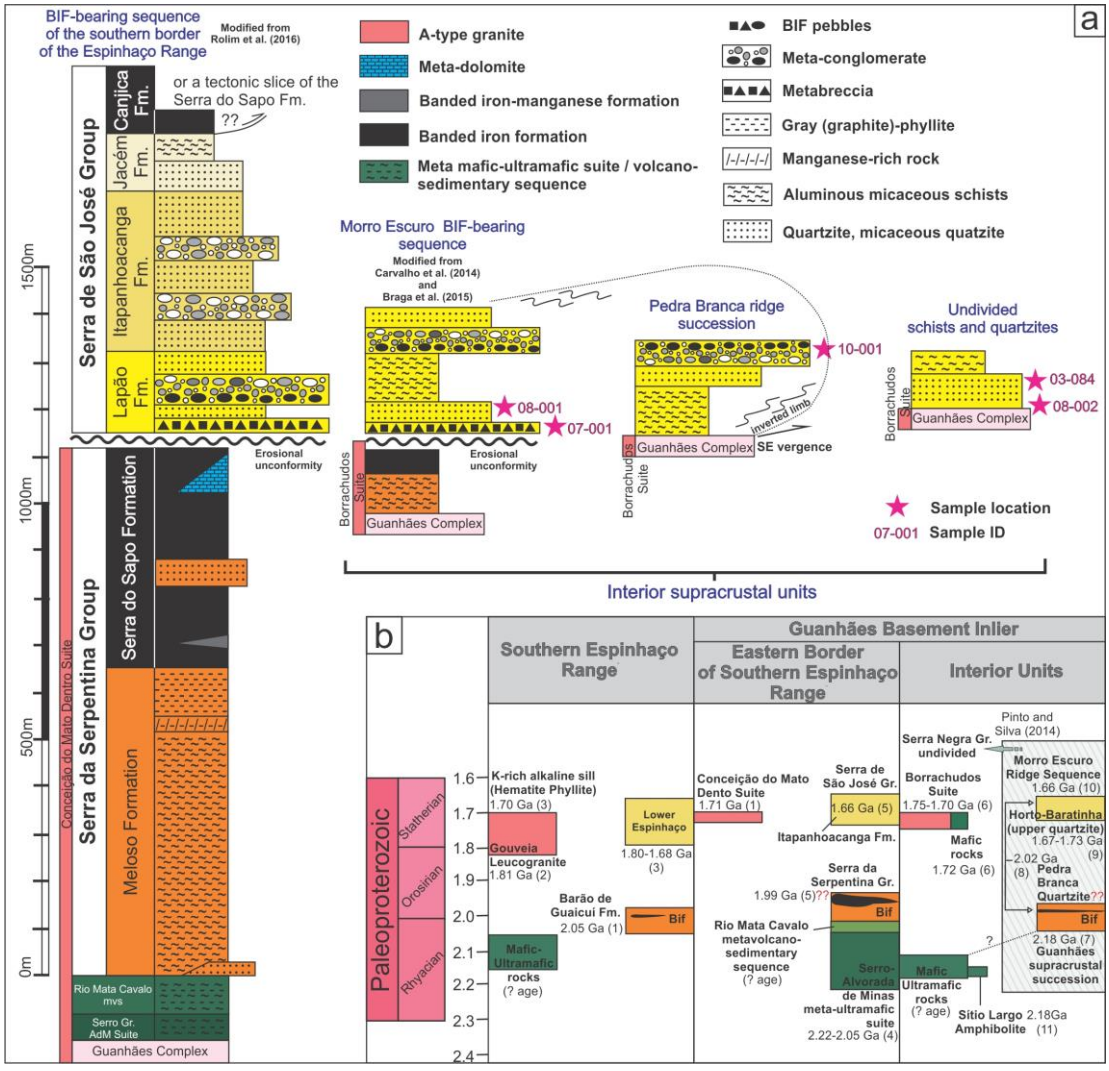

Source: Prepared by the author

4.4.3 Lu-Hf isotope analyses

Lutetium-Hf isotope analysis were carried out with a Resolution M-50 193nm ArF Excimer laser system coupled to a Thermo-Scientific multicollector (MC)-SF-ICP-MS

(Neptune) at Goethe University of Frankfurt, Germany. The analytical protocol used is the same as described in detail by Gerdes and Zeh (2006) and Zeh and Gerdes (2012). For calculation of the epsilon Hf [εHft], the chondritic uniform reservoir (CHUR) was used as recommend by Bouvier et al. (2008); 176Lu/177Hf and 176Hf/177Hf of 0.0336 and 0.282785, respectively, and a decay constant of 1.867 x 10-11 (Scherer et al., 2001; Söderlund et al., 2004). All two stage hafnium model ages (TDM) were calculated by applying 176Lu/177Hf = 0.03945 and 176Hf/177Hf = 0.28324, resulting in a depleted mantle (DM) evolutionary line ranging from zero (at 4.0 Ga) to +16 (today), in agreement with compilation of Archean mafic rocks (Zeh et al., 2011). Crustal evolutionary trends were modelled by applying 176Lu/177Hf = 0.0113 for average continental crust (average of Wedepohl, 1995; Taylor and McLennan, 1985). For all detrital zircons initial 176Hf/177Hf, εHft and TDM were calculated using the 207Pb/206Pb ages obtained for the respective zircon domains.

4.5 Structural analyses

During this study, detailed field work and structural analyses were carried out to gain new information about the structural evolution in the southern GBI, in particular about field relationships between Archean and Paleoproterozoic rocks, magmatic and supracrustal rocks, and about shear zone kinematics.

4.5.1 Archean to Paleoproterozoic structures

The northeastern boundary of the southern GBI (Figure 20) comprises narrow slivers of sheared ortho-gneisses. These gneisses exhibit a low-angle east-dipping pervasive mylonitic fabric with rootless, sub-horizontal NNE-SSW-trending, asymmetrical east-verging intrafolial Z-folds (Figure 19a, b and c), which are the oldest tectonic structures observed in the crystalline rocks. The mesoscopic asymmetric structures indicate an eastward hanging wall-down displacement associated with folded mylonicit foliation at the centimeter to meter scale suggests a progressive evolution of the deformation (Fossen et al., 2019) (Figure 19b and c). The extensional mylonitic fabric occurs discontinuously to the south until the vicinity of Ipatinga (Figure 19d). At the northeastern edge of the GBI, younger N-S reverse brittle faults with a top-to-west motion intersect the mylonitic gneissic banding, suggesting deformation at a shallow crustal level (Figure 19b).

Figure 19: (a) Mylonitic fabric with rootless, sub-horizontal NNE-SSW-trending asymmetrical east-verging intrafolial Z-folds. (b) Centimeter-scale folded mylonitic foliation suggesting progressive evolution of the deformation. Younger N-S reverse faults with a top-to-west motion intersecting the mylonitic gneissic banding. (c) Metric-scale asymmetrical east-verging fold pointing to normal sense movement. (d) centimeter-scale asymmetrical southeast-verging fold near Ipatinga. (e) Vertical oriented contact between the Borrachudos Suite (B) and the Archean gneiss of the Guanhães Complex (G) showing tight to isoclinal asymmetrical folds suggesting a pluton-side-up movement sense.

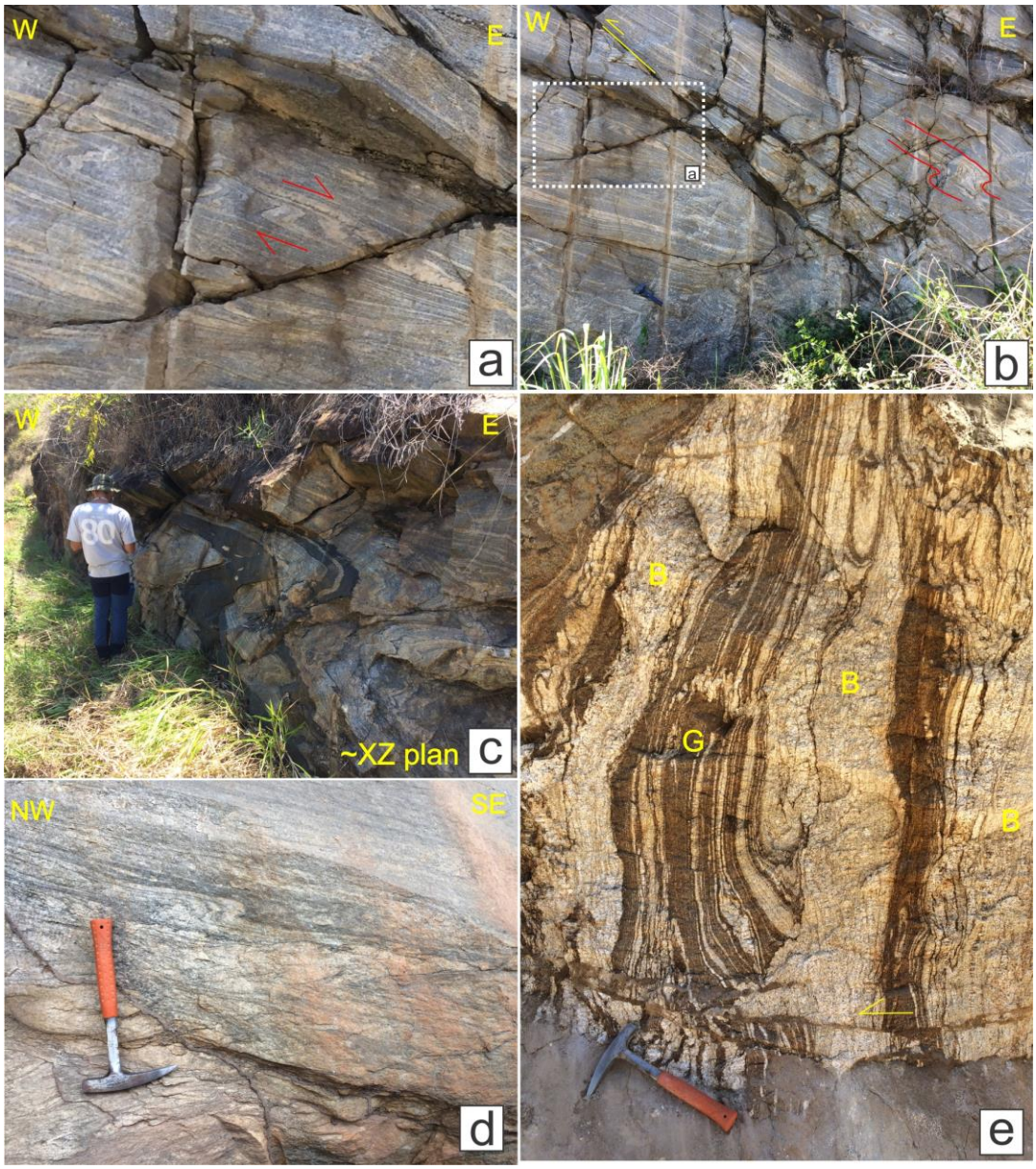

Source: Prepared by the author

Several outcrops exhibit a vertically oriented contact between the plutonic rocks of the Borrachudos anorogenic suite and Archean gneiss of the Guanhães Complex. The plutonic rocks commonly show a magmatic foliation at interfaces, reflected by the alignment of hornblende, biotite, and tabular feldspars crystals. These syn-intrusive

structures, in combination with tight to isoclinal asymmetrical upright folds observed in the contact zones on the overburden (Figure 19e), suggest a forced granitic intrusion.

4.5.2 Shear zones related to the Araçuaí Orogen

4.5.2.1 Sabinópolis and Conceição shear zones

The Sabinópolis shear zone juxtaposes a wedge of gneissic rocks with a granite of the Borrachudos Suite, which is exposed for ca. 80 kilometers in north-south direction, dipping westward (max.: 278/42) with a NW-plunging stretching lineation (max.: 329/41) (Figure 20). The deformation along the shear zone is characterized by imbricated slices of alternating gneissic basement rocks and granites, and pervasive mylonitic zones with asymmetric features, indicating an eastward reverse tectonic (Figure 21a and b). The southernmost part of the Sabinópolis shear zone bends to the west and dips to the north (max.: 008/26). Mineral lineation plunges to the east with a low angle (085/12) (Figure 20), and sigmoidal features suggest a right-lateral dislocation (Figure 21c).

The western border of the GBI is delimited by the conjugate west-vergent Conceição shear zone that emplaces gneissic rocks upon the imbricated supracrustal units of the Serra da Serpentina and Espinhaço sequences. The regional foliation dips eastward (max.: 076/29), and a mineral lineation cluster mostly exhibits a low-angle eastward plunge (max.: 094/24) (Figure 20).

4.5.2.2 Pedra Branca-Morro Escuro shear system

To the south of the Sabinópolis shear zone the deformation is accommodated by two majors regional transpressive oblique shear zones (Pedra Branca and Morro Escuro) in association with southeast-verging folds (Carvalho et al., 2014), that control the shape of NE-SW to NNE-SSW homonymous ridges (Figure 20). The mylonitic foliation controlled by the Pedra Branca and Morro Escuro shear system dips northwest (max.: 303/38) with asymmetric shear sense indicators suggesting a dominantly sinistral movement (Figure 21d).

Two distinctive mineral and stretching lineations on the mylonitic planes plunge to NW (max.: 319/32) and NNE (max.:025/27). The direction of the Pedra Branca and Morro Escuro shear zones towards WNW-ESE in the interior of the GBI (max.: 021/24) with

constant mineral lineation (max.: 319/19 and 33/25). In this region, southwest-verging folds in combination with the analyses of shear sense indicators of the shear zones point to a dextral oblique-slip movement (Figure 20). At the SW edges of the GBI, near Itabira, outcrop scale shear zones indicate that the deformation of the Pedra Branca-Morro Escuro shear system is also accommodated by reversal top-to-SW directed displacement (max.: 042/35) (Figure 20).

Figure 20: Structural map of the southern segment of the Guanhães basement inlier, with pole figures showing the orientation of foliation (contoured fields) and mineral/stretching lineations (dots). White star - foliation maximum; red star - lineation maximum; blue star - calculated b-axis.

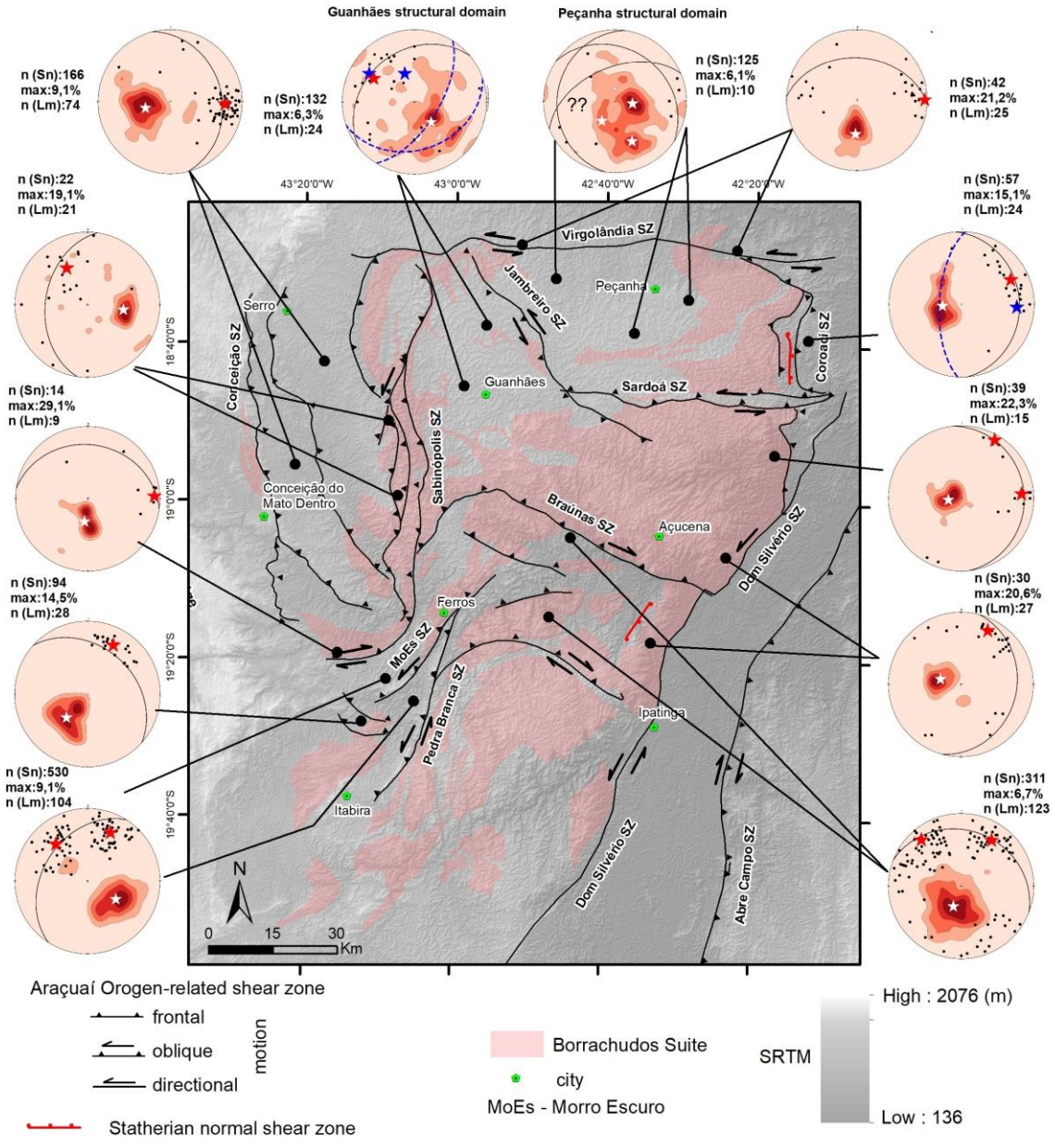

Source: Prepared by the author

4.5.2.3 Dom Silvério and Coroací shear zones

The NNE-SSW trending, sinistral Dom Silvério shear zone juxtaposes Neoproterozoic rocks against the GBI (Figure 16 and Figure 20). The shear zone extents for more than 60 km north to the limits previously suggested by Alkmim et al. (2006) and Peres et al. (2004). The shear zone is characterized by a low angle mylonitic foliation (max.:105/24), and a shallow plunging mineral lineation (max.: 029/17). Outcrop-scale northwest-verging folds indicate oblique sinistral movement (Figure 21e).

To the north of the 19° S latitude, the Dom Silvério shear zone bifurcates into the north-south trending Coroací shear zone, which extends for approximately 60 km further to the North and is intersected by the E-W trending sinistral oblique-slip Sardoá shear zone and by the E-W trending sinistral strike-slip Virgolândia shear zone (Figure 20). Between the Virgolândia and Sardoá shear zones, the mylonitic foliation poles of the Coroací shear zone reveal a girdle pattern with a calculated b-axis at 093/25. The rake of the mineral lineation is variable from NE to E, with a maximum at 063/24 (Figure 20).

4.5.2.4 Virgolândia shear zone

The Virgolândia shear zone forms the northern limit of the southern segment of the GBI, and it can be traced for up to 110 kilometers (Figure 20). It exhibits an E-W trending, dips to the north (max.: 003/40) and shows low-angle mineral lineation (max.: 87/8). Asymmetric shear sense indicators, in combination with the foliation-lineation relationship, point to sinistral strike-slip displacement (Figure 21f). To the north of the Virgolândia shear zone, within the northern GBI segment, metric to decametric south-verging folds have been described by Baars and Fonseca (1997) associated with E-W structural trends, suggesting a far-reaching influence of the Virgolândia shear zone.

4.5.2.5 GBI internal shear zones

Around the cities of Peçanha and Guanhães, the recognition of regional structural trends is difficult, mainly due to the development of complex interference pattern (Barrote et al., 2017). However, near Guanhães two girdle geometries can be distinguish in the pole figures, outlined by the regional foliation. These point to an overall NW-plunge of calculated b-axis (Figure 20), in agreement with the geometry of local parasitic folds. The geometric relationship between the structures in this area is

mostly controlled by the NW-SE trending Jambreiro shear zone (Barrote et al., 2017), which kinematic indicators point to a northeast-verging sinistral oblique-slip displacemnt (Figure 20). The Jambreiro shear zone separates the Guanhães and Peçanha structural domains (Figure 20). The Peçanha structural domain exhibits a complex distribution of the regional foliation, although the main attitude of low-angle planes, dipping westward, is recognized (Figure 20).

Near the town of Açucena, in the center part of the Borrachudos Suite, the granitic rocks exhibit a phaneritic magmatic texture that is overprinted by a mylonitic fabric, in particular in vicinity to the Sardoá shear zone to the North, the Braúnas shear zone to the South, and Dom Silvério and Coroací shear zones to the East.

Along the Sardoá shear zone, rocks of the Peçanha structural domain are southwards juxtaposed over granites of the Borrachudos Suite, whereas along the Braúnas shear zone the granites were thrust upon metasedimentary rocks of the Serra da Serpentina and Serra de São José groups and gneissic rocks (Figure 21g and h). The displacement relationship along both Sardoá and Braúnas shear zones indicates eastward tectonic transport of granite belonging to the Açucena pluton (Figure 20).

Figure 21: (a) Sabinópolis shear zone: d-porphyroclasts (K-feldspar) in granite mylonite of the Borrachudos Suite indicating eastward tectonic movement. (b) shear bands of the Sabinópolis shear zone disrupting magmatic structure of the Borrachudos Suite. (c) Sigmoidal geometry indicates dextral motion of the southernmost portion of the Sabinópolis shear zone. (d) S-C structure defining sinistral sense of movement of the Morro Escuro shear zone (e) S-C -C' foliation of the Dom Silvério shear zone. (f) Mylonitic foliation indicating sinistral sense of movement of the Virgolândia shear zone. (g) Borrachudos Suite (Açucena pluton) overthrusting gneissic rocks of the Guanhães Complex. (h) Isoclinal SW verging-folds associated to shear bands of the Braúnas shear zone.

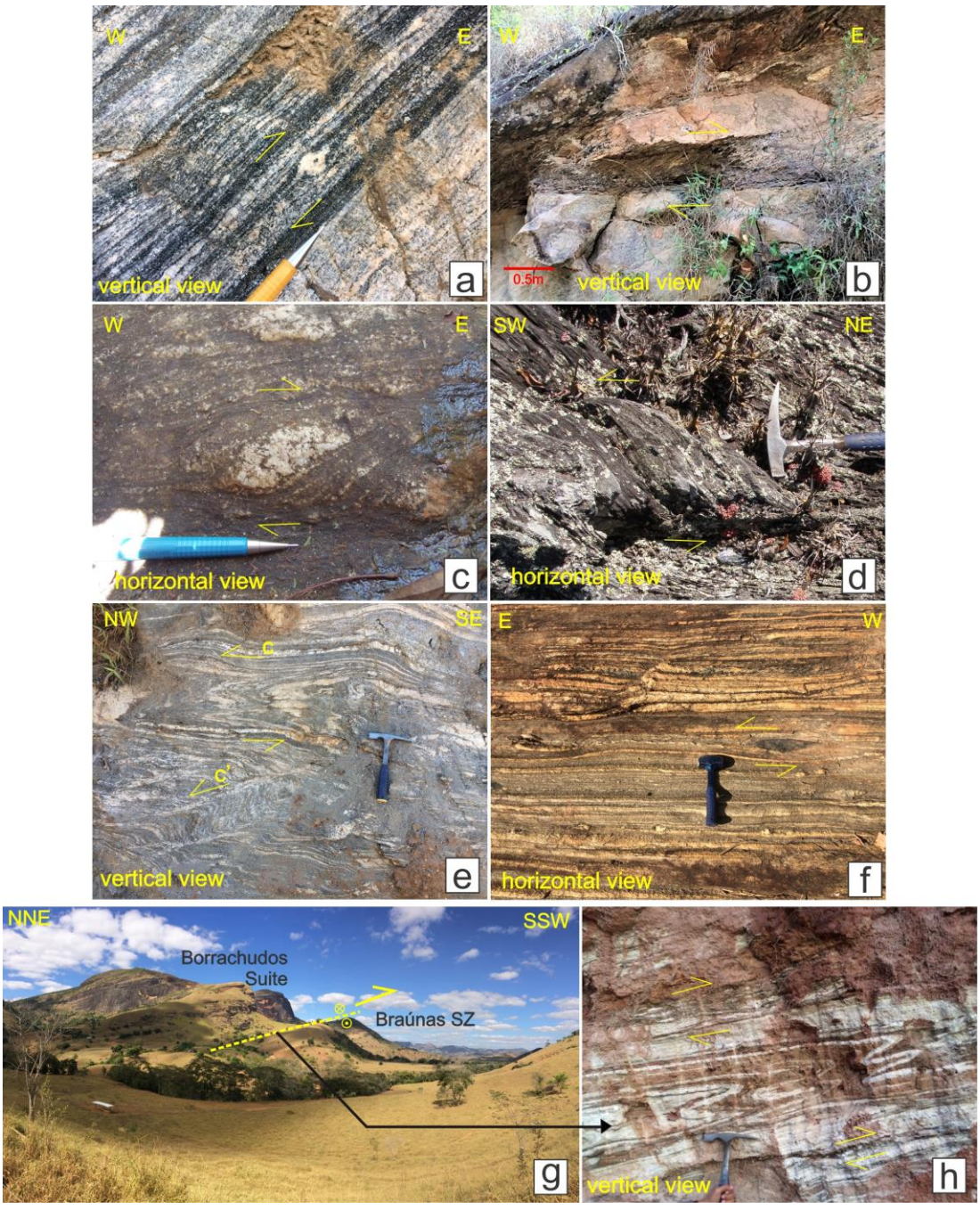

Source: Prepared by the author

4.6 Results of zircon U-Pb dating

A total of 389 U-Pb spot analyses were conducted on detrital zircon grains of five samples. The results are presented in the Appendix B. The zircon crystals of all samples exhibit a wide range in color from light yellow to light red to colorless. The grains are long-prismatic to short-stubby, with lengths varying from 50 to 325 μm. Most grains are subhedral and round, and many of these show evidence for alteration in contact with sheet silicates (chlorite, muscovite), caused by post-depositional tectono-metamorphic overprint (Figure 22). Internal structures mostly reveal banded and oscillatory zoning patterns, and laser spot analyses Th/U >0.1 (0.17-2.99; Figure 23), pointing to zircon crystallization in magmatic rocks (Belousova et al., 2002; Yakymchuk et al., 2018). Exceptions are presented by a few zircon crystals in the samples 03-084 and 08-002, displaying core-rim relationships (Figure 22). Some of these rims show a faint-diffuse zoning and very low Th/U ratios, commonly << 0.1 (Figure 23), pointing to a metamorphic origin.

Figure 22: Back-scattered electron (BSE) images of zircon grains with spot positions for U-Pb and Lu-Hf isotope analyses by LA-ICP-MS. For each spot the following results are presented: Th/U ratio, εHf(t) value, $^{207}Pb/^{206}Pb$ age (with 2 sigma error), and degree of concordances (in percent). m – image of zircon morphology, i – image of internal structure. Analyses of zircon rims, with Th/U<0.1 are highlighted in blue.

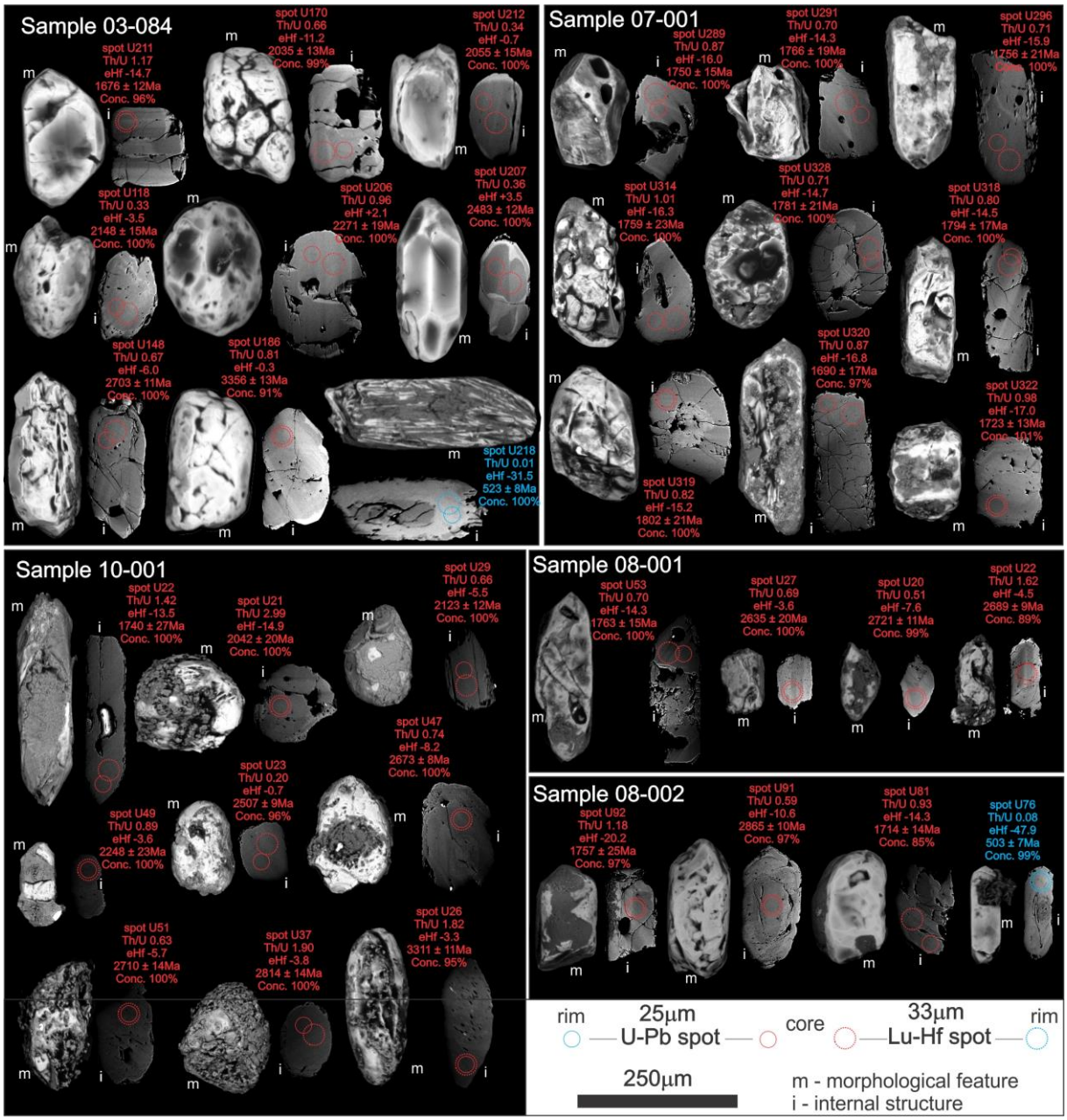

Source: Prepared by the author

Figure 23: Zircon core and rim analyses plotted in Th/U versus age diagram.

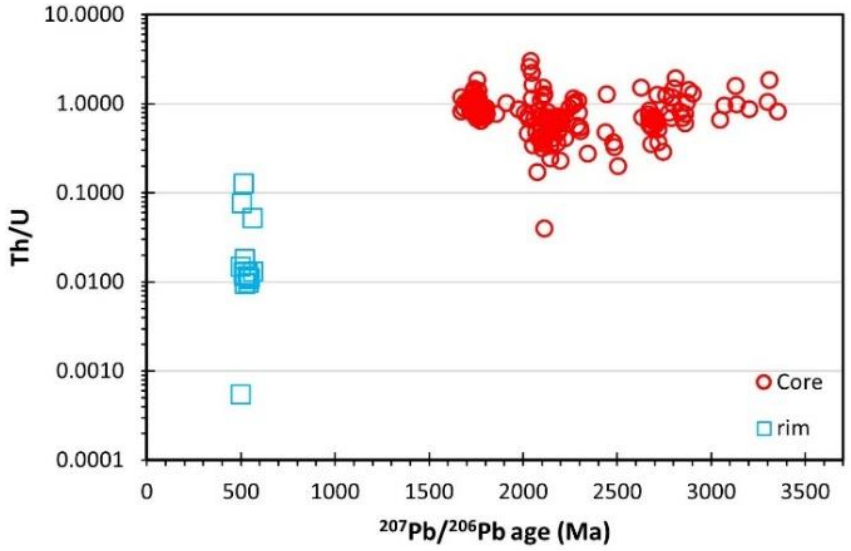

Source: Prepared by the author

From the three samples 03-084, 07-001 and 10-001, between 52 and 70 concordant zircon analyses could be obtained (out of 90-115 analyses), and only 5 from the two samples 08-001 and 08-002. The zircon age spectra of the 3 samples with >50 concordant analyses are different (Figure 24). The age spectrum of sample 07-001 is dominated by a single peak at ca. 1760 Ma (95%), whereas zircon populations of the samples 03-084 and 10-001 show a wide range in ages (03-084: 3356 to 1676 Ma; 10-001: 3311 to 1758 Ma). The age spectrum of sample 03-084 is dominated by Neoarchean ages at ca. 2685 Ma (20%) and Rhyacian ages at 2100-2200 Ma (60%), and a few minor peaks reflecting Meso- to Paleoarchean (7%); Siderian (6%) and Orosirian (6%) ages. Sample 10-001 predominately shows ages peaks during the Neo- to Mesoarchean (2630-2880 Ma; ca. 40%), and Rhyacian (2170-2280 Ma: ca. 20%), but also during the Orosirian (mainly at 1980-2050 Ma), and Statherian (at ca.1760 Ma). Concordant zircon ages derived from sample 08-001 and 08-008 ranges from 2865 to 1757 Ma, and overlap ages derived for sample 10-001.

Metamorphic zircon rims with low Th/U of the samples 03-084 and 08-002 yield Cambrian ages between 523 ± 8 and 503 ± 7 Ma (Figure 22 and Figure 23).

Figure 24: Age spectra of detrital zircon populations from the Serra de São José Group, presented in relative probability plots and histograms. (a) Sample 03-084. (b) Sample 07-001. (c) Sample 08-001. (d) Sample 08-002. (e) Sample 10-001. (only zircon grains with concordance level 90-110%).

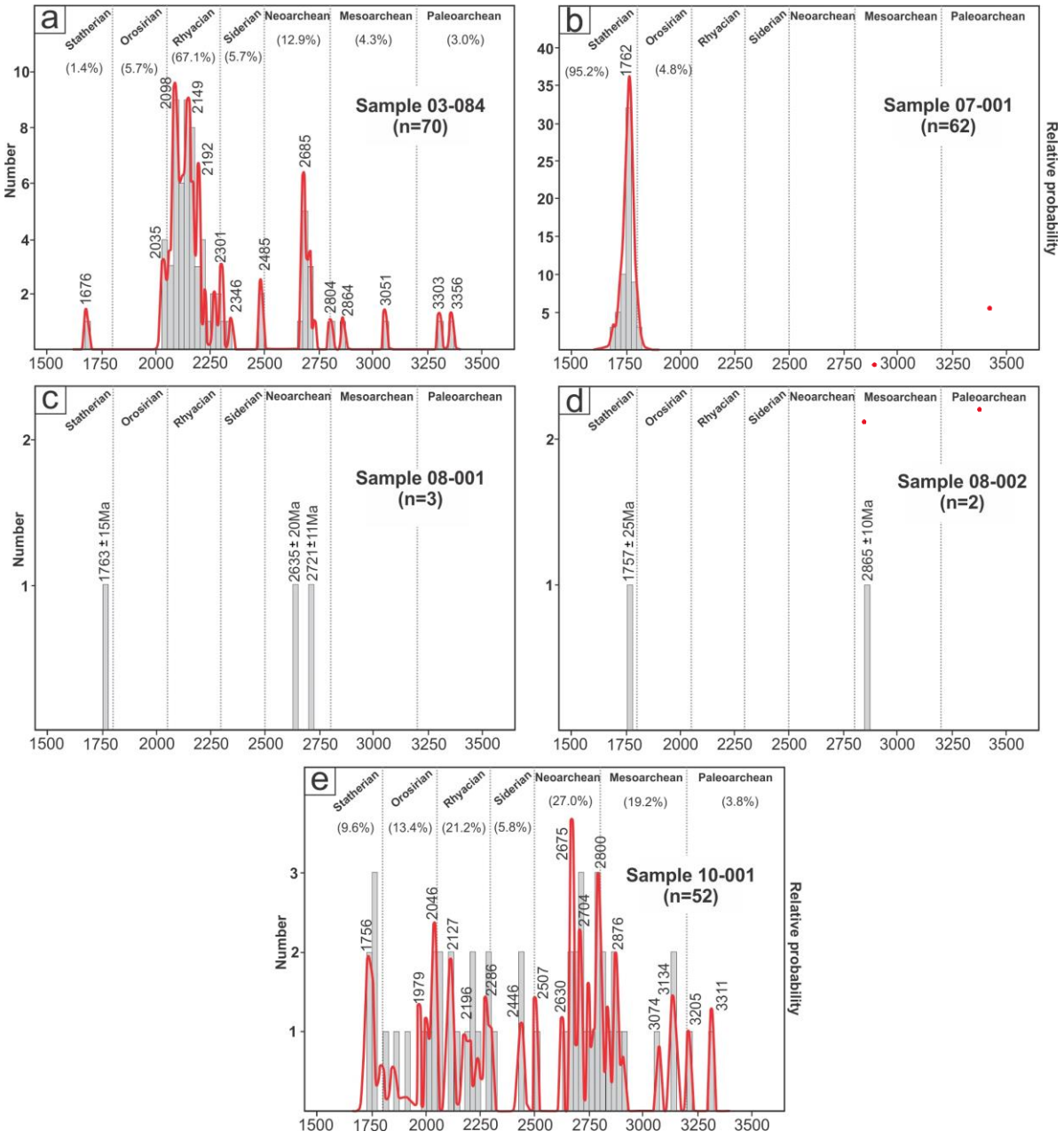

Source: Prepared by the author

4.7 Results of Lu-Hf isotope analyses

From all five samples, a total of 147 zircon grains with concordant U-Pb ages (90-110%) were analyzed for their Lu-Hf isotope compositions. The results, which are presented in the Appendix C, reveal a wide range in initial $^{176}Hf/^{177}Hf$ from 0.280409 to

0.281516, and in εHf(t) from -20.2 to 3.5, but also a great overlap in the age-Hf isotope signatures for all five samples (Figure 25).

Figure 25: Epsilon Hf vs. age diagrams showing the results of (a) detrital zircon analyses from the Serra de São José Group (this study), and (b) comparison with published data from the São Francisco Craton (data sources: M'2018 – Magalhães et al., 2018; G'2020 – Gomes et al., 2020; D'2018 – Degler et al., 2018; C'2020 – Cutts et al., 2020; D'2017 – Dopico et al., 2017; K'2014 – Koglin et al., 2014). Fields with numbers 1 to 6 refer to tectono-magmatic events on the São Francisco Craton: 1-Espinhaço rift system and associated magmatism, 2-Minas-Bahia Orogeny, 3-Mamona event, 4-Rio das Velhas II event, 5-Rio das Velhas I event, 6-Santa Barbara event. CHUR-chondritic uniform reservoir, DM-depleted mantle evolution, Stath.- Statherian, Orosi.- Orosirian, Rhyac.- Rhyacian, Sider.- Siderian. Diagonal lines represent crustal evolutionary trends for 176Lu/177Hf = 0.0113 that intersect the DM evolutionary line at 2.5, 3.0, 3.5 and 4.0 Ga, respectively.

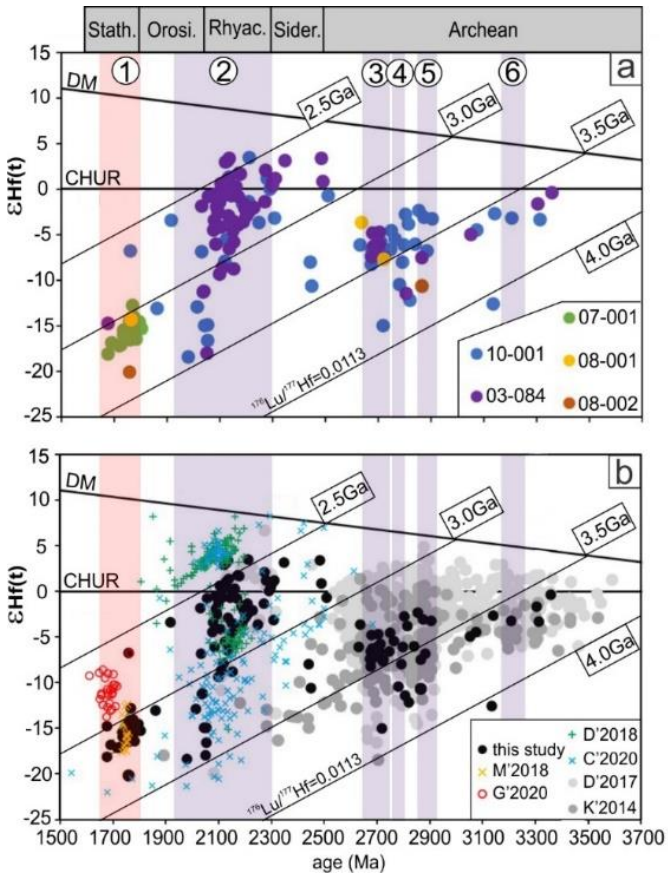

Source: Prepared by the author

The Archean zircon grains show initial $^{176}Hf/^{177}Hf$ from 0.280409 to 0.281156, corresponding to subchondritic εHf(t) from -14.9 to -0.3, and two-stage hafnium model ages (TDM) from 4.09 to 3.15 Ga. Seven zircon grains of Siderian age reveal chondritic to subchondritic εHf(t) values ranging from -10.6 to 3.2, and TDM from 2.55 to 3.38 Ga. Zircon grains of Rhyacian to Orosirian age yield the very wide range in initial $^{176}Hf/^{177}Hf$ from 0.280971 to 0.281516, corresponding to εHf(t) values from -18.2 to

3.5, and TDM from 2.37 to 3.47 Ga. Zircon grains of Statherian age show initial $^{176}Hf/^{177}Hf$ ranging from 0.280097 to 0.281500. Most of those analyses (except two) form a cluster in εHf(t) vs. age diagram (Figure 25), with a very limited range in subchondritic εHf(t) ranging from -18.0 to -13.0 (all data: -20.2 to -6.8), corresponding to Hf model ages between 3.20 and 2.96 Ga (all data: 2.64 to 3.37 Ga).

4.8 Discussion

4.8.1 Maximum depositional age of the Lower Espinhaço Sequence

The youngest U-Pb age of a detrital zircon grain found in a (meta)sedimentary rock provides a maximum age for sediment deposition (Cawood et al., 2012; Dickinson and Gehrels, 2009; Zeh et al., 2021), providing that the U-Pb system of the analyzed zircon was not disturbed by post-depositional alteration (see discussions in Cabral et al., 2012 and Zeh et al., 2013).

The youngest detrital zircon grains found in the five investigated samples from the GBI yield variable Statherian ages at 1676 ± 12 Ma (sample 03-084), 1721 ± 22 Ma (sample 07-001), 1740 ± 27 Ma (sample 10-001), 1757 ± 25 Ma (sample 08-002), and 1763 ± 15 Ma (sample 08-001). It is noted that for the samples 08-001 and 08-002 the maximum depositional ages (MDA) are only constrained by single zircon analyses, while for the other three samples robust MDA's can be calculated, comprising several analyses defining the youngest age cluster. For sample 07-001, the robust MDA is at 1726.6 ± 7.4 Ma (n=6; MSWD=0.50, Probability = 0.90), and for sample 10-001 at 1754.0 ± 8.1 Ma (n=5; MSWD=0.91, Probability = 0.52), overlapping within error the ages of the youngest zircon grains. In contrast, for sample 03-084 the robust MDA is significantly older at 2041.7 ± 9.3 Ma (n=3; MSWD=1.5, Probability = 0.19). Taking the data robustness (and stratigraphic variations) into account, deposition of the Lower Espinhaço Sequence in the GBI most likely occurred at <1727 Ma (Table 2). The significantly younger MDA at <1676 Ma derived for sample 03-084, is not robust, and might results from post-depositional zircon alteration, perhaps minor Pb-loss during the Brasiliano orogeny. Evidence for such an overprint is reflected by (i) the relatively low concordance level of the youngest zircon analysis (only 96%), and (ii) the finding metamorphic zircon rims with ages at ca. 525 Ma in sample 03-084.

The robust MDA's estimated during this study for the Lower Espinhaço Sequence in the GBI overlap those derived during previous provenance studies in the same region, ranging between 1677 ± 16 and 1746 ± 3 Ma (for details and references see Table 2). They overlap data derived for metasedimentary rocks exposed along the western margin of the GBI in the Diamantina, Barão de Cocais, and Altamira areas, i.e. from the São João da Chapada, Bandeirinha, and Cambotas formations. Detrital zircon grains from these formations yield robust MDA's between 1706 ± 16 and 1772 ± 14 Ma (Table 2), consistent with crystallization ages of K-rich alkaline subvolcanic dikes transecting the sedimentary sequences at 1703 ± 12 Ma (Chemale et al., 2012), 1715 ± 2 Ma (Machado et al., 1989) and 1710 ± 12 Ma (Dussin and Dussin, 1995).

It is pertinent to note that robust MDA's derived for GBI rocks are mostly much older than the MDA's reflected by the youngest detrital zircon grains, with difference of 50 Ma (see Table 2). Considering the fact that the sedimentary rocks of the GBI, but also associated magmatic rocks of the anorogenic Borrachudos Suite were affected by a structural-metamorphic overprint during the Brasiliano orogeny at 575-530 Ma (Alkmim et al., 2017), it cannot be excluded that at least some of the detrital zircon grains in all samples experienced significant post-depositional Pb-loss (this and previous studies).

The Brasiliano overprint in the GBI is well reflected by metamorphic zircon grains/rims in samples 03-084 and 08-002 (this study), and in A-type granitoid rocks of the Borrachudos Suite (Gomes et al., 2020). Furthermore, it is important to note that plutonic rocks of the anorogenic Borrachudos Suite in the GBI emplaced at ca. 1695 Ma (upper intercept ages are at 1701 ± 4 Ma, 1702 ± 22 Ma, 1699 ± 12 Ma, and concordant age at 1688 ± 18 Ma; Gomes et al., 2020), nearly synchronous with the K-rich volcanic rocks in Diamantina region. This overlap suggests that magmatic activity in the center of the GBI, and along its western margin occurred coeval between 1715 ± 2 Ma (Machado et al., 1989) and 1688 ± 18 Ma (Gomes et al., 2020), and that the magmatic activity syn- and post-dates the deposition of the Lower Espinhaço Sequence.

Table 2: Compilation of maximum depositional ages (MDA) derived from the Lower Espinhaço Sequence

Location	Unit	Rock type	MDA[a] (in Ma)	robust MDA[b] (in Ma)	Reference
eastern domain					
Guanhães Basement Inlier	Serra de São José Gr.	qz-conglo	1676 ± 12	1727 ± 7 [6]	this study
Sapo and São José ridges	Itapanhoacanga Fm.	qz-conglo	1666 ± 32	1677 ± 16 [4]	Rolim et al. (2016)
Morro Escuro ridge	Lapão Fm.	conglo	1668 ± 23	1746 ± 3 [13]	Silveira Braga et al. (2015)
Horto-Baratinha iron ore deposits	Lapão/Itapanhoacanga Fm.	mica schist	1671 ± 20	1714 ± 55 [3]	Silveira Braga et al. (2019)
Serro	Itapanhoacanga Fm.	quartzite	1629 ± 13	1717 ± 17 [17]	Silveira (2016)
western domain					
Diamantina	São João da Chapada Fm.	not described	1660 ± 21	1706 ± 16 [20]	Santos et al. (2013)
Diamantina	Bandeirinha Fm.	not described	1709 ± 10	1772 ± 14 [21]	Santos et al. (2013)
Diamantina	São João da Chapada Fm.	not described	1704 ± 19	1728 ± 15 [5]	Chemale et al. (2012)
Diamantina	Bandeirinha Fm.	not described	1781 ± 23	2067 ± 28 [5]	Chemale et al. (2012)
Altamira and Ipoema	Lapão Fm.	quartzite	1751 ± 19	1761 ± 13 [2]	Oliveira et al. (2019)
Cambotas ridge	Cambotas Fm.	quartzite	1512 ± 25	1740 ± 24 [14]	Dutra et al. (2020)

a - MDA - maximum depositional age reflected by the youngest detrital zircon grain
b - robust MDA - maximum depositional age based on several analyses of the youngest age cluster, [number of grains]
qz-conglo: quartzite to metaconglometarte

4.8.2 Source of detrital zircons

The age spectra derived from detrital zircon populations during this and previous studies (for compilation see Figure 26) indicate that the protoliths of the metasedimentary rocks of the Lower Espinhaço Sequence in the GBI and surrounding units were deposited during the Statherian, mainly prior to 1700 Ma, and derived from similar sources in the hinterland. Oscillatory internal zoning patterns, euhedral to subhedral morphologies (Figure 22), and Th/U>0.1 (Figure 23) provide evidence that the majority of the analyzed zircon grains are of magmatic origin, and supplied from proximal sources made up by felsic igneous rocks (or by reworking of older sedimentary rocks), and in minor extent Siderian to Rhyacian juvenile rocks.

The age spectra of the detrital zircon populations indicates that the hinterland of the Lower Espinhaço Sequence was affected by magmatic activity during four periods: 1-

Archean, 2-Siderian, 3- Rhyacian to Late Orosirian, 4-Statherian (Figure 26). The ages of the detrital zircon grains in the Lower Espinhaço Sequence correlate well with magmatic and metamorphic events known from the GBI and adjacent areas.

Archean TTG gneisses are reported from the Guanhães Complex, but also from the Quadrilátero Ferrífero mining district, located immediately South to the GBI. The protoliths of the TTG gneisses were formed during different Paleo to Neoarchean magmatic pulses (Santa Barbara, Rio das Velhas I and II, and Mamona events), as is indicated by published data (eg. Farina et al., 2015; Lana et al., 2013; Piuzana et al., 2013; Romano et al., 2013; Silva et al., 2002). In addition, there is a significant overlap in the age-Hf isotope characteristics of the detrital zircon grains from the Lower Espinhaço Sequence (this study), and Archean quartzites and metaconglomerates of the Minas Supergroup in the Quadrilátero Ferrífero (for data compilation and references see Figure 25b). We note that all analyses (except one) reported here and by Koglin et al. (2014) show chondritic to subchondritic εHf(t) values (0 to -16), pointing to the reworking of Eo- to Paleoarchean crust, which has been derived from the depleted mantle between 3.75 and 3.30 Ga (Figure 25b). One detrital zircon of sample 10-001 yield an older Hadean Hf model age of 4.05 Ga.

Siderian zircon grains are relatively rare in samples of the GBI and adjacent units and show a wide range in εHf(t) values from 3.5 to -10.6 (at ca. 2.45 Ga). These data suggest reworking of Paleoarchean crust (TDM = 3.23 - 3.38 Ga) in addition to new crust formation (TDM = 2.64 - 2.89 Ga; Figure 25a). Our results are coherent with early dates obtained by Chemale et al. (2012) and Santos et al. (2013).

Figure 26: Detrital age distribution of the Lower Espinhaço Sequence (only data with concordance level 90-110%).

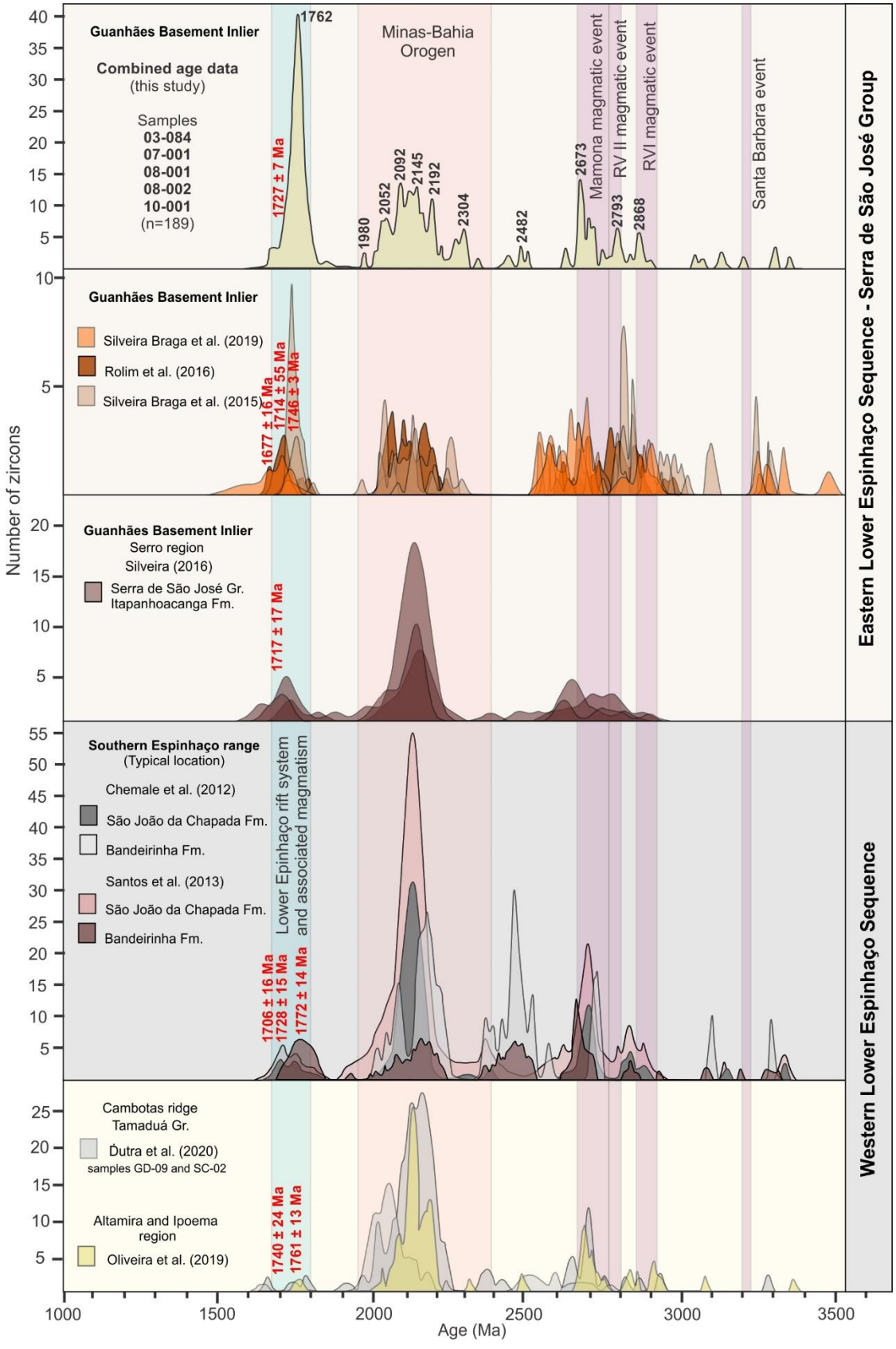

Source: Prepared by the author

The Late Orosirian-Rhyacian zircon population (2300-1915 Ma) is ubiquitous in all samples of the Lower Espinhaço Sequence (Figure 26). Such ages are well known from magmatic and metamorphic rocks of the Minas-Bahia orogenic belt (Mineiro Belt, Mantiqueira, Juiz de Fora and Pocrane complexes) (Alkmim and Marshak, 1998; Barbosa et al., 2015; Bruno et al., 2021, 2020; Cutts et al., 2020, 2018; Degler et al., 2018; Heilbron et al., 2010; Noce et al., 2007). The Hf isotope data of the analyzed zircon grains show wide range in εHf(t) values from 3.5 to -18.3 (Figure 25a). The majority of the data point to the reworking of Neo- to Mesoarchean crust (TDM = 2.5 - 2.9 Ga), and only a small number to reworking of Meso- to Paleoarchean crust (TDM = 3.0 - 3.5 Ga). Similar variations in εHf(t)-age patterns are also reported from detrital zircon grains of the Sabara Group in the Minas Basin of the Quadrilatero Ferrifero (Dopico et al., 2017), and from magmatic rocks from the southern portion of the Minas-Bahia Orogen (Cutts et al., 2020; Degler et al., 2018; see Figure 25b).

Zircon grains of Statherian age (1800-1675 Ma) show highly subchondritic εHf(t) values ranging from -12.7 to -20.2, except one grain with εHf(t) = -6.7. Hafnium model ages mostly suggest reworking of Meso- to Paleorarchean crust (TDM = 2.96 to 3.37 Ga), and minor Neoarchean crust (TDM = 2.64 Ga). The age-εHf(t) characteristics of the analyzed detrital zircon grains show significant overlap with data on anorogenic granites from the Borrachudos Suite presented by Magalhães et al. (2018) (Figure 25b). Conversely, εHf(t) values of the analyzed samples show poor correspondence with data presented by Gomes et al. (2020), which might reflect sampling bias (Figure 25b).

4.8.3 The Guanhães Crustal Core Complex

Core complexes are considered products of substantial continental extension, spanning from the Phanerozoic to the Precambrian. Numerous global examples highlight the coincidence of volcanism, plutonism, thermal events, and extensional deformation within many core complexes (e.g. Armstrong, 1982; Conor et al., 2005; Dewey, 1988; Neuwayr et al., 1998; Schenker et al., 2012). In general, core complexes are distinguished from other dome-shaped structures by the presence of a shallow-dipping, crustal-scale detachment zone surrounding a core of high-grade metamorphic-magmatic rocks, as it is typified by the basin-and-range province in the USA (eg. Coney, 1980; Coney and Harms, 1984; Gashawbeza et al., 2008;

Konstantinou et al., 2013). During crust extension, deformation is commonly concentrated along the detachment zone, which grades from brittle in the upper crust to mylonitic in the middle and lower crust and is the starting point for a series of steep dipping normal faults transecting the upper crust into blocks. During crustal extension, the mylonitic detachment zone is buckled up, resulting in (1) crustal thinning and upper mantle uplift commonly accompanied felsic and mafic melt production, and (2) juxtaposition of very high-grade metamorphic rocks (core of the complex) with low-grade rocks in the upper crust (Brun et al., 2018). In addition, successive extension causes (3) the rotation of upper crust blocks, creating the space for fault bounded basins filled with sedimentary rocks, while normal faults become pathways for magmatic dikes.

The combination of field observations, structural and geochronological-isotope data of sedimentary units tectonically juxtaposed with gneissic rocks of the GBI indicate they comprise a core complex, which has been formed by crust-scale extension during Statherian between 1715 and 1690 Ma. The center part of this area is composed of the anorogenic Borrachudos Suite, which is surrounded by a number of shallow dipping mylonitic shear zones, showing all the same sense of displacement (converging against the core; Figure 20), comprising the Dom Silvério, Coroací, Virgolândia, Sabinópolis shear zones and the Pedra Branca-Morro Escuro shear system. The growth and uplift of the anorogenic plutonic bodies of the Borrachudos Suite became the driving force for emplacement of the high-grade core complex between 1715 to >1690 Ma, while in the Diamantina region was intruded by felsic dikes, perhaps following block bounding extensional faults at ca. 1710 Ma. These magmatic rocks resulted from the reworking of underlying Neo- to Paleoarchean crust, as indicated by Hf-model ages between 2.6 and 3.4 Ga (this study; Gomes et al., 2020; Magalhães et al., 2018). In the southern GBI the magmatic activity was pre-, syn- and perhaps also post-dated by deposition of coarse-grained sedimentary rocks (conglomerates and sandstones) of the Lower Espinasho Sequence, as is indicated by robust MDA mostly ranging between 1746 ± 6 Ma and 1677 ± 16 Ma (Table 2).

Finally, we note that the core complex model for the GBI hinges on the assumption of a Statherian age for the recognized normal-sense shear zones. The geometric attributes and kinematic characteristics of the Araçuaí orogeny-related shear zones would be therefore reactivations of pre-existing Statherian structures.

A conceptual evolutive model for the geological evolution of the GBI during the Statherian is presented in Figure 27. This model is inspired from analogue modeling of core complex development in a two-layer brittle upper crust - ductile lower crust system with a viscosity anomaly placed in the brittle-ductile interface (Brun et al., 2018, 1994). It summarizes the progressive development of faulting in the upper brittle layer and how flow of the lower viscous layer progressively compensates the upper brittle layer thinning up to its exhumation, to form the core complex.

Figure 27: Conceptual evolutionary model of the long-term development of the crustal core complex-rift Borrachudos Suite (Guanhães gneiss)-Lower Espinhaço Sequence.

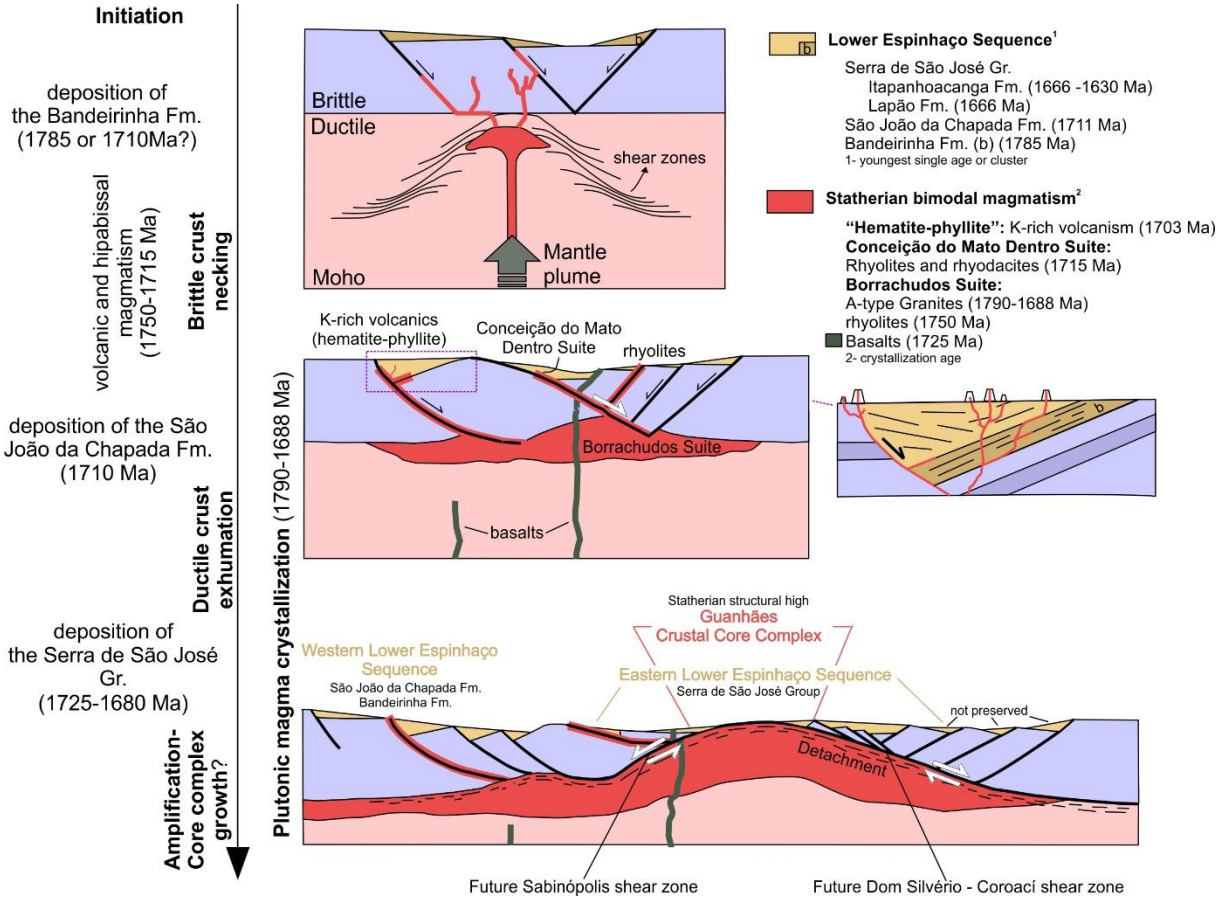

Source: Prepared by the author

The Lower Espinhaço extension starts with the development of a graben system (possible trigged by a mantle plume; Magalhães et al. 2018) and progressive stretching causes block rotation that is internally accommodated by new normal faults. The rotation controls strain localization along the graben border fault leading to the development of a detachment which delineates the upper brittle crust (Brun et al., 2018). By the early Statherian, the upper brittle crust, representing the basement of

the Lower Espinhaço Sequence, is composed of Archean basement overlain by sedimentary rocks of the Serra da Serpentina Group (Pagung et al., 2023; Rolim et al., 2016), and limited to the east by the Minas-Bahia Orogen.

The initial brittle extensional environment and its associated sedimentation are well exposed in the southern Espinhaço ridge (Western Domain; see Figure 16b). Within this area, sedimentation occurred during two distinct stages of rifting. The first stage resulted in deposition of the Bandeirinha Formation in restricted fault-bounded depocenters (Santos et al., 2013), while the São João da Chapada Formation was formed during the second stage (Almeida-Abreu, 1995).Deposition of the Bandeirinha Formation perhaps was accompanied by volcanic activities at 1785 Ma, as is reflected by a robust MDA (Santos et al., 2013), although a single detrital grain from the Bandeirinha Formation delivered an age of 1710 Ma (see Table 2). The contact relationship between the Bandeirinha and the overlying São João da Chapada Formation is marked by an unconformity, which has been a matter of extensive debate in the literature (e.g. Almeida-Abreu, 1995; Chemale Jr. et al., 2013; Knauer, 2013; Lopes-Silva & Knauer, 2013).

This unconformity might be explained by the rotation of an upper crust block, initiated by progressive crustal stretching and the *rolling hinge effect* in the detachment footwall, which according to Brun et al. (2018) may result in a whole block rotation up to 50°. Deposition of the younger São João da Chapada Formation was accompanied by magmatic activity at ~1710 Ma, as indicated by the presence of dykes and sills in the Western Domain, that are assumed to be formed during a period of brittle crust necking (Figure 27).

Successive crust extension caused exhumation of the mylonitic detachment zone and A-type “granites” in the center part of the southern GBI, and activation and rotation of brittle to mylonitic faults and rocks above the detachment zone. Localized ductile deformation is well reflected by the regional Dom Silvério, Coroací, Virgolândia and Sabinópolis shear zones, as well as in the Pedra Branca-Morro Escuro system, surrounding more or less deformed plutonic rocks of the Statherian Borrachudos Suite and minor Archean TTG gneisses. The activation of these shear zones and differential uplift of the core of the GBI should have controlled the opening of internal basins and the sedimentation of the Serra de São José Group (Eastern Domain, see Figure 17)

between ca. 1745 Ma and 1680 Ma (Figure 27). The deformed lit-par-lit structures contact relationship (Figure 19e) between the Borrachudos granite and surrounding Archean rocks, supports the interpretation of a forced emplacement of magma in a distensive setting during uplift, in agreement with processes of magmatic diapirism described by He et al. (2009).

Summarizing, the evolution of the Lower Espinhaço Sequence is characterized by the diachronic deposition of three main units: the basal Bandeirinha Formation followed by the São João da Chapada Formation in a typical continental rift environment and contemporaneous with magmatic eruption (Western Domain), while the Serra de São José sediments were deposited in the Eastern Domain of the basin, probably in several troughs separated by listric faults and delimited by the uplifted Guanhães Core Complex that exhumed the Borrachudos plutonic bodies.

4.9 Conclusions

1. Detrital zircon grains in metasedimentary rocks from the interior of the Guanhães Basement Inlier yield maximum depositional ages between 1676 ± 12 Ma and 1763 ± 15 Ma, with the youngest most robust MDA at 1727 ± 7 Ma.
2. Zircon age spectra and Hf isotope compositions suggest sediment supply from three major sources: (1) Archean, (2) Late Orosirian-Rhyacian and (3) Statherian rocks, similar to those exposed in the adjacent Quadrilátero Ferrífero terrane, Minas-Bahia Orogenic Belt, and in the Borrachudos silicic large igneous province exposed in the center part of the GBI. Zircon grains of Siderian age are rare.
3. Field relationships, age-Hf isotope characteristics, and MDA's suggest that the metasedimentary rocks in the interior of the GBI are equivalent to those of the Bandeirinha and São João da Chapada formations, encompassing the basal sequence of the Espinhaço Supergroup.
4. Hafnium isotope characteristics indicate substantial crust reworking during Archean (εHf_t = 0 to -16), Late Orosirian-Rhyacian (εHf_t = +3 to -18), Siderian (εHf_t = +3 to -11), and Stratherian (εHf_t = -7 to -21), and only minor new crust addition during the Siderian and Rhyacian.

5. The combination of new structural data, field relationships, and geochronological data suggest that the southern GBI represents a magmatic-metamorphic (crustal) core complex formed as a result of ongoing crust extension during the Statherian, mainly between 1725 and 1680 Ma.
6. Reverse shear zones found in the GBI probably result from the reactivation of pre-existing extensional Statherian structures related to basin inversion during the Araçuaí Orogen.

Acknowledgements

The authors wish to acknowledge funding from CNPq (Pr. Nr. 163930/2021–0 - RP) and (Pr. Nr. 311917/2020-8 - CAR). We also thanks G. Sarquis and his team (Anglo American Mining Company) for supplying drill hole data and assistance in the field work.

5 RESEARCH IN PROGRESS

5.1 The age of the Serra da Serpentina back-arc basin

As exposed in the section 1.1 (Problem statement #1) and discussed in the chapter 3 of this thesis, the age of the Serra da Serpentina back-arc basin is based on a questionable Rhyacian crystallization age of the mafic-ultramafic Serro-Alvorada de Minas Suit presented by Hagedorn (2004), and a still poorly constrained Rhyacian detrital zircon age found within the BIF-bearing sequence in the Guanhães region, provided by Barrote et al. (2017). In an attempt to accurately define the age of the Serra da Serpentina back-arc basin, two approaches are being developed: the definition of a reliable crystallization age for the Serro-Alvorada de Minas Suite and a robust maximum depositional age for the Serra da Serpentina clastic sediments.

5.1.1 Crystallization age of the Serro-Alvorada de Minas Suite

Direct dating of mafic-ultramafic rocks is crucial for understanding mantle geodynamic evolution and crust-mantle interaction, but it is also challenging. A reliable approach for dating the crystallization of mantle-derived rocks is through an integrated investigation of U–Pb isotopes in coexisting baddeleyite and zircon. (Li et al., 2021).

However, locating baddeleyite grains of sufficient size for conventional separation and concentration techniques (>50μm in length) can pose a challenge. Acknowledging that medium to large baddeleyite crystals are scarce, it has been observed that micro-baddeleyite needles (≤10–40 μm long by a few μm wide) are plentiful in a diverse range of mafic rocks. In this context, an alternative dating method was devised by Chamberlain et al. (2010) and Schmitt et al. (2010) to take advantage of the more recognized prevalence of micro-baddeleyite crystals, specifically through in situ secondary ionization mass spectrometry (IN-SIMS).

The method complements the isotope dilution thermal ionization mass spectrometry (ID-TIMS) geochronology by broadening the spectrum of crystals that can be dated, encompassing sizes smaller than those achievable through physical separation. X-ray mapping and BSE imaging are employed for pinpointing specific grains in thin sections, followed by SIMS analysis on a CAMECA *ims* 1270. Anticipated internal age precisions for the method range from 0.1% for Precambrian rocks to 3–7% for Phanerozoic rocks. A detailed description of the method can be seen in Chamberlain et al. (2010).

Figure 28: BSE images of zircon (z) and baddeleyite (b) crystals from samples colected in the Rio Mata Cavalo metavolcanosedimentary sequence and Serro ultramafic Suite.

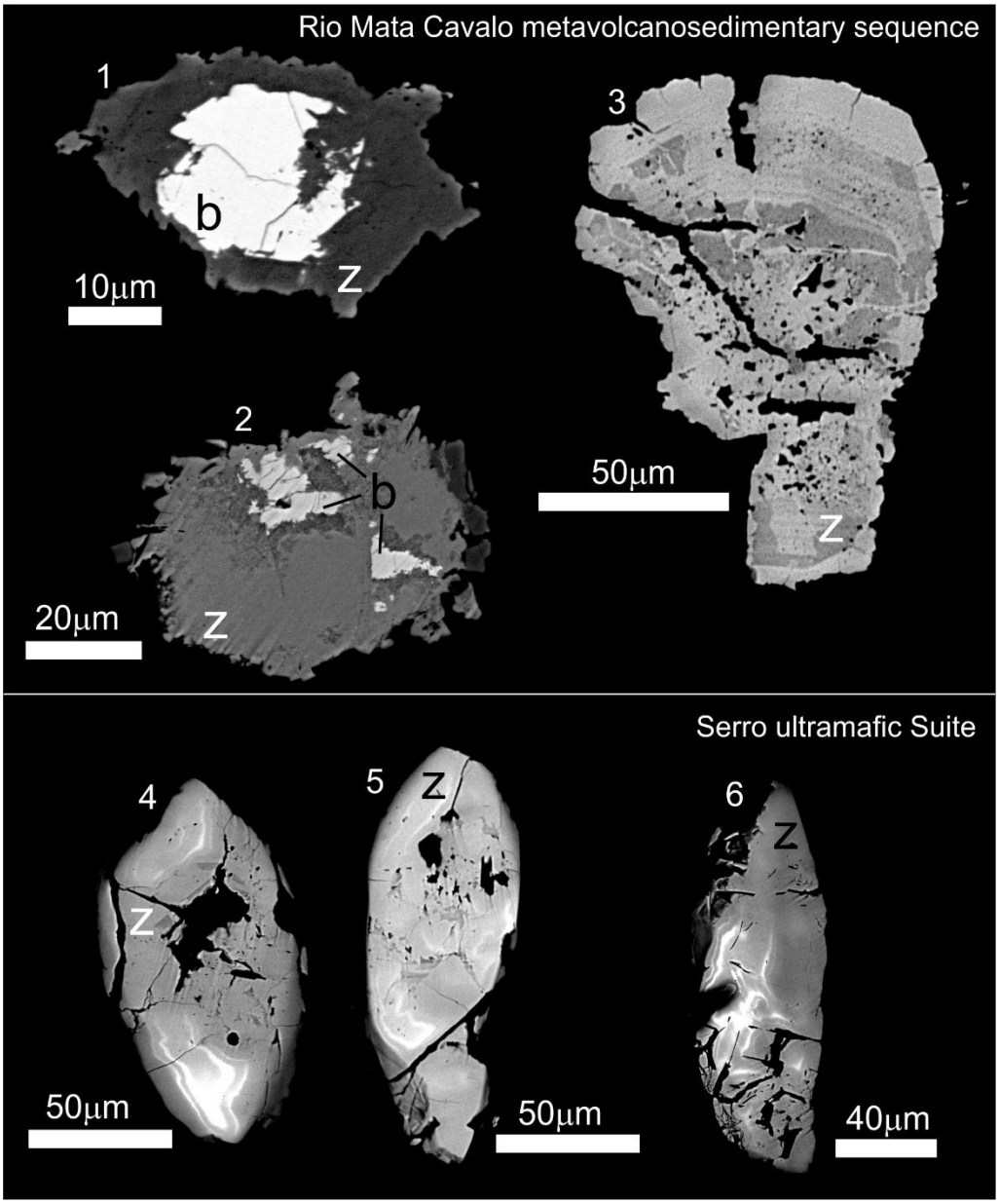

Source: Prepared by the author

To determine the crystallization age of the Serro-Alvorada de Minas Suite, two samples were collected from distinct locations (Serro and Morro do Pilar), and they are current under investigarion (Figure 30a). In the Morro do Pilar area, the sample RMC-1 was collected from the Mata Cavalo river valley, where rocks of to the Rio Mata Cavalo metavolcanosedimentary sequence are exposed. In this sample is observed coexistent baddeleyite cores and zircon rim relationship where all domains are large enough to be dated. A single zircon crystal exhibits three distinct domains: a pitted interior which may have represent an older inherited zircon core, an intermediary portion present

concentric zoning which could represent magmatism in a felsic magma, and a smooth outer rim may be metamorphic growth (Figure 28). The sample SERRO-3 was collected in the vicinity of Serro. This sample has no baddeleyite, but many smooth zircons grains, whose origin could be either magmatic or metamorphic (Figure 28). This work has been developed in collaboration with Prof. Kevin Chamberlain from the University of Wyoming (USA).

Concurrent with the geochronology study, a whole-rock geochemical investigation of this unit (in both localities) is also underway to achieve a comprehensive understanding of its tectonic significance.

5.1.2 Maximum depositional age of the Serra da Serpentina Group

In the Conceição do Mato Dentro mining district, a fine-grained quartzite occurs, in gradational contact, interlayered with the banded iron formation of the Serra do Sapo Formation. This siliciclastic package reaches a thickness of up to 45 m, as determined from drill cores data (Figure 29). Two alternative interpretations for the presence of the quartzite horizon are presented below: (i) it may indicate a period of detrital input in a shallow continental shelf environment, thus representing a sedimentary vertical variation within the basin, or (ii) based on the structural interpretation presented in the section 1.1.1 (Hypothesis statement; see Figure 2a), it may represent an older quartzite package (Meloso Formation?) which was potentially enfolded by the banded iron formation in a first order isoclinal folding. Regardless of the interpretation, this package is recognized as a compelling target for constraining the maximum depositional age of the Serra da Serpentina Group.

Sample 351, collected from the interlayered quartzite, has been already subjected to U-Pb dating using the same methods outlined in sections 4.4.1 and 4.4.2 (the original data are presented in the Appendix D). One hundred and thirty-two out of 150 zircon analyses yielded exclusively Archean concordant ages (90-110%) between 2537 ± 19 Ma and 3429 ± 18 Ma, with main peaks at 2710 Ma, 2854 Ma and 2963 Ma (Figure 29).

Figure 29: Lithological profile of the Serra da Serpentina and Serra de São José groups in the Conceição do Mato Dentro mining district and Frequency histogram and probability curve of the sample 351, collected from the fine-grained quartzite interlayered with Serra do Sapo banded iron formation.

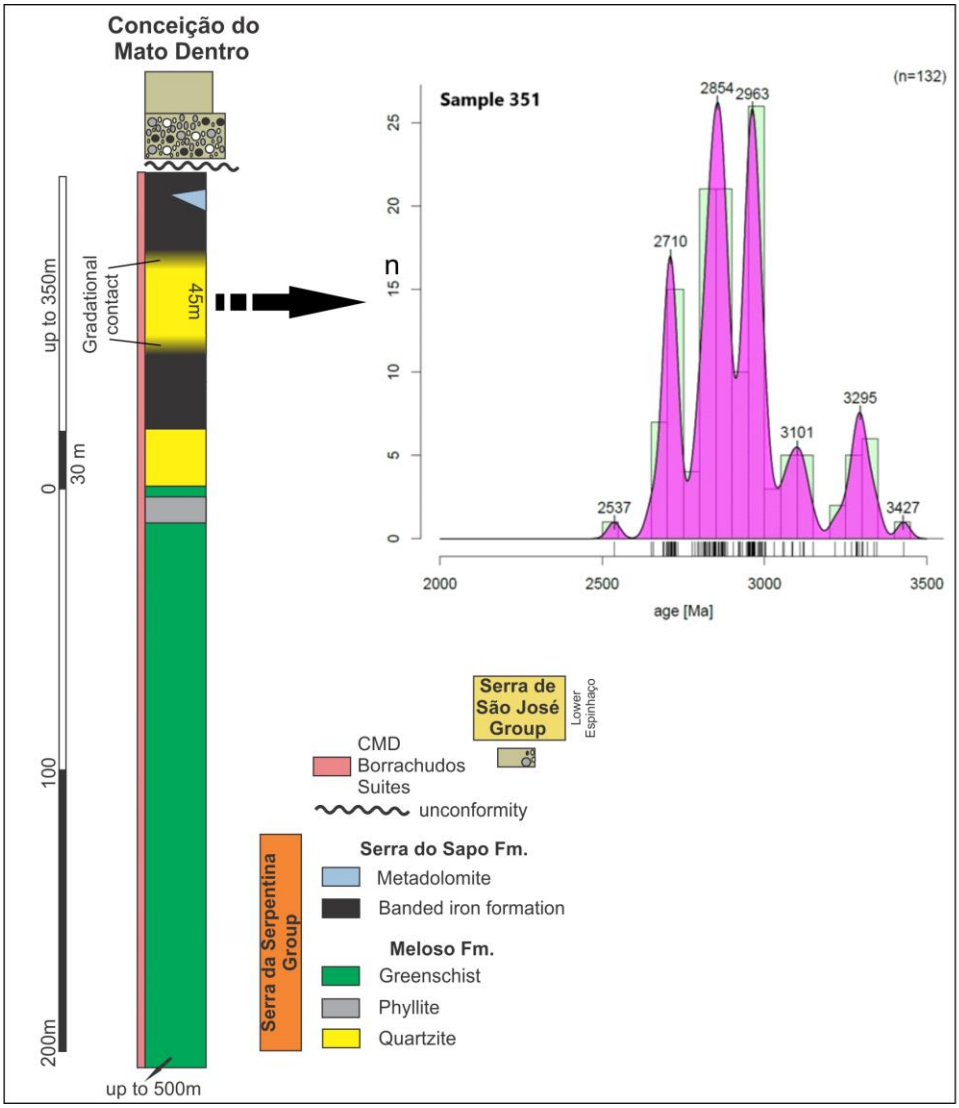

Source: Prepared by the author

These Archean detrital ages seem to reflect an unconclusive result since it is inconsistent with the Rhyacian detrital ages presented by Barrote et al. (2017) in the Guanhães region, suggesting the need for further investigation. Nevertheless, due to the stratigraphic/structural relationship with the Serra do Sapo banded iron formation, the study of this siliciclastic horizon remains a viable option for establishing a robust maximum depositional age for the Serra da Serpentina Group. Therefore, five additional samples were collected from the quarzitic horizon across different drill cores to further refine this age through geochronological analyses (Figure 30a).

5.2 Serra da Serpentina basin and Upper Minas units: chrono-correlates?

The proposed model of the Serra da Serpentina back-arc basin, in the Minas-Bahia orogeny geotectonic context, carries significant regional implications. As outlined in Chapter 3, the Serra da Serpentina Group, including the Serro-Alvorada de Minas Suite, shares stratigraphical and chronological similarities with the Upper Minas units, comprising the Piracicaba, Sabará, and Itacolomi groups.

The Sabará and Itacolomi groups are reasonably estimated to have their maximum depositional ages during the Rhyacian to Orosirian period, with a depositional history interpreted as being connected to the Minas-Bahia Orogen. Conversely, the precise MDA of the Piracicaba Group is still a matter of debate. Rossignol et al. (2020), however, studing rocks of the Piracicaba Group, presented a Rhyacian detrital zircon age population and pointed the Mineiro Belt (Minas-Bahia Orogen) as source area that delivered the younger zircon cluster.

The Rhyacian detrital age aligns with the crystallization age assigned to the underlying Sítio Largo amphibolite (2188 ± 24 Ma), exposed in the vicinity of João Monlevade, where the Piracicaba Group was originally defined by Reeves (1966) (Figure 30b).

In this context, this region was selected as a compelling target area to investigate the nature of detrital zircons of the Piracicaba Group. A total of nine samples composed of quartzite, quarzt-mica schist, and biotite-quartz paragneiss were collected from five different locations (Figure 30b). The purpose of this analyzes is better constrained the maximum depositional age and investigate the source areas of this unit, besides the regional correlation.

After interpreting the results of this study, the confirmation (or not) of the hypothesis emphasizes the significance of thoroughly examining the concept of a continental-scale back-arc/foreland basin system. This idea focuses on studying possible correlatable units exposed further north, encompassing rocks of the Riacho dos Machados meta-volcanosedimentary sequence, the Colomi Group, and the Caetité Sequence.

In doing so, we take another significant stride in the pursuit of comprehending the Minas-Bahia back-arc/foreland terranes.

Figure 30: (a) Geological map emphasizing the east to southeast-verging N-S structural trend from Sabinópolis to João Monlevade (modified from Pinto and Silva (2014). (b) Geological map of the Monlevade and Rio Piracicaba quadrangles (Reevers, 1966) and sample locations.

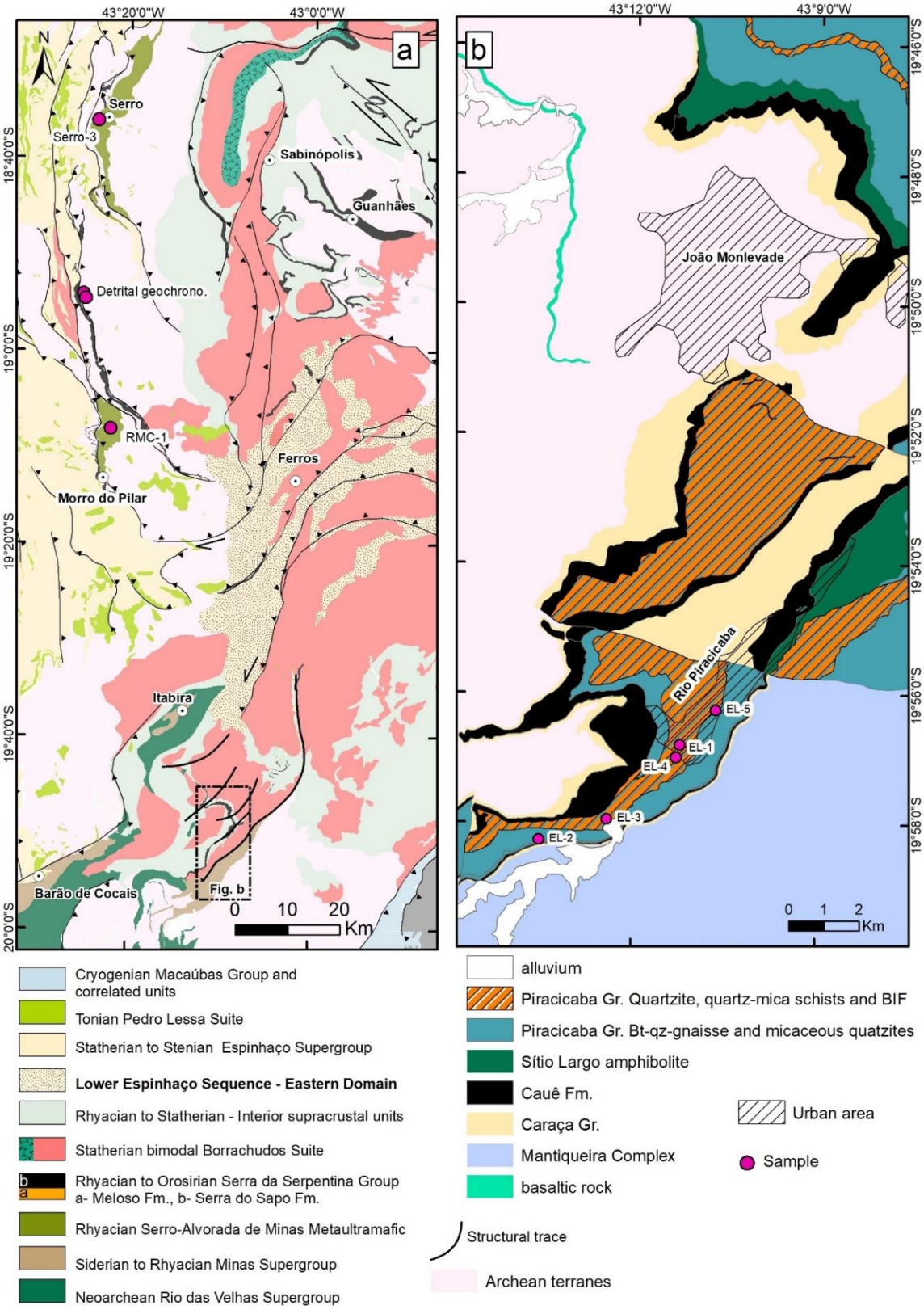

Source: Prepared by the author

6 CONCLUDING REMARKS

This study has addressed the previously poorly constrained crustal evolution of the Guanhães Basement Inlier. It demonstrated that the Paleoproterozoic tectonic evolution of the GBI is characterized by superposition of two distinct tectonic events, the older one related to the Rhyacian-Orosirian Minas-Bahia Orogen followed by the Statherian Espinhaço rift system.

6.1 Rhyacian to Orosirian crustal evolution of the Guanhães Basement inlier

Through detailed whole-rock geochemistry investigation across the vertical variation of the Meloso Formation, it has shed light on critical aspects of this rock assembly, providing a more comprehensive understanding of the tectonic significance of the BIF-bearing Serra da Sepentina Group.

The findings presented here, in combination with published data, allow the interpretation that the deposition of the Serra da Serpentina Group occurred in an active continental margin environment during the Minas-Bahia Orogeny. The Meloso Formation composition uncover crustal and mantle-derived sources reveals complex interactions between continental and juvenile crustal components during its sedimentation. The association of the Serro-Alvorada de Minas Suite, Rio Mata Cavalo sequence, and Serra da Serpentina Group strongly suggests the evolution of a back-arc basin in response to the Minas-Bahia Orogen during Rhyacian period, providing a new perspective on the region's geodynamic evolution with a significative regional implication (Figure 14).

6.2 Statherian crustal evolution of the Guanhães Basement inlier

Through detailed geological and isotopic investigations, it has revealed insights into the GBI's tectonic history during the Statherian. The geometric and kinematic framework, coupled with the coeval Borrachudos magmatism and basin opening, suggests a prolonged interplay between crustal core complex growth and rift development. In addition, it brings the concept of the Guanhães Crustal Core Complex as a structural high that emerged during the early stages of the Espinhaço basin

opening. The Guanhães Crustal Core Complex played a crucial role in shaping the architecture of the basin in the interior and surroundings of the GBI (Figure 27).

6.3 Future approaches

This thesis contributes to a more comprehensive understanding of the Paleoproterozoic crustal evolution of the GBI and it opens doors for further research in several directions:

- Refinement of the geochronological framework: further studies can refine the age constraints of specific rock units and tectonic events within the GBI, providing a more precise timeline for its evolution.
- Structural detailed investigations: targeted studies of the Guanhães Crustal Core Complex, shear zones, and other critical structures can offer deeper insights into their formation, role in the basin development, and potential mineral resource implications.
- Geochemical and isotopic analyses: geochemical and isotopic investigations of various rock types can provide additional clues about the tectonic evolution of the GBI.

REFERENCES

Aguilar, C., Alkmim, F.F., Lana, C., Farina, F., 2017. Palaeoproterozoic assembly of the São Francisco craton, SE Brazil: New insights from U–Pb titanite and monazite dating. Precambrian Res 289, 95–115. https://doi.org/10.1016/j.precamres.2016.12.001

Albert, C., Farina, F., Lana, C., Stevens, G., Storey, C., Gerdes, A., Dopico, C.M., 2016. Archean crustal evolution in the Southern São Francisco craton, Brazil: Constraints from U-Pb, Lu-Hf and O isotope analyses. Lithos 266–267, 64–86. https://doi.org/10.1016/j.lithos.2016.09.029

Alkmim, F.F., Kuchenbecker, M., Reis, H.L.S., Pedrosa-Soares, A.C., 2017. The Araçuaí Belt, in: Heilbron, M., Cordani, U.G., Alkmim, F.F. (Eds.), São Francisco Craton, Eastern Brazil. pp. 255–276. https://doi.org/10.1007/978-3-319-01715-0_14

Alkmim, F.F., Marshak, S., 1998. Transamazonian Orogeny in the Southern São Francisco Craton Region, Minas Gerais, Brazil: evidence for Paleoproterozoic collision and collapse in the Quadrilátero Ferrífero. Precambrian Res 90, 29–58. https://doi.org/10.1016/S0301-9268(98)00032-1

Alkmim, F.F., Marshak, S., Pedrosa-Soares, A.C., Peres, G.G., Cruz, S.C.P., Whittington, A., 2006. Kinematic evolution of the Araçuaí-West Congo orogen in Brazil and Africa: Nutcracker tectonics during the Neoproterozoic assembly of Gondwana. Precambrian Res 149, 43–64. https://doi.org/10.1016/j.precamres.2006.06.007

Alkmim, F.F., Martins-Neto, M.A., 2012. Proterozoic first-order sedimentary sequences of the São Francisco craton, eastern Brazil. Mar Pet Geol 33, 127–139. https://doi.org/10.1016/j.marpetgeo.2011.08.011

Alkmim, F.F., Teixeira, W., 2017. The Paleoproterozoic Mineiro Belt and the Quadrilátero Ferrífero, in: Heilbron, M., Cordani, U.G., Alkmim, F.F. (Eds.), São Francisco Craton, Eastern Brazil. Springer, pp. 71–94. https://doi.org/10.1007/978-3-319-01715-0_5

Almeida-Abreu, P.A., 1995. O Supergrupo Espinhaço da serra do Espinhaço Meridional (Minas Gerais): o rift, a bacia e o orógeno. Geonomos. https://doi.org/10.18285/geonomos.v3i1.211

Almeida-Abreu, P.A., Knauer, L.G., Hartmann, M.B., Santos, G.G.V., Guimarães, M.L.V., Abreu, F.R., Schrank, A., Pflug, R., 1989. Estratigrafia, faciologia e tectônica do Supergrupo Espinhaço na região de Serro - Conceição do Mato Dentro, Minas Gerais, Brasil. Zbl. Geol. Palaont. 857–873.

Almeida-Abreu, P.A., Renger, F.E., 2007. Stratigraphy and facies of the southern Serra do Espinhaco, Minas Gerais, Brazil. Zeitschrift der Deutschen Gesellschaft für Geowissenschaften 158, 9–29. https://doi.org/10.1127/1860-1804/2007/0158-0009

Amaral, L., Caxito, F. de A., Pedrosa-Soares, A.C., Queiroga, G., Babinski, M., Trindade, R., Lana, C., Chemale, F., 2020. The Ribeirão da Folha ophiolite-bearing accretionary wedge (Araçuaí orogen, SE Brazil): New data for Cryogenian plagiogranite and metasedimentary rocks. Precambrian Res 336. https://doi.org/10.1016/j.precamres.2019.105522

Anani, C.Y., Bonsu, S., Kwayisi, D., Asiedu, D.K., 2019. Geochemistry and provenance of Neoproterozoic metasedimentary rocks from the Togo structural unit, Southeastern Ghana. Journal of African Earth Sciences 153, 208–218. https://doi.org/10.1016/j.jafrearsci.2019.03.002

Angeli, N., Penha, U.C., Knauer, L.G., Ito, G.M., 2011. The Rio Mata Cavalo group: The gold mineralization and its origin. Revista Geociencias, UNESP 30, 301–310.

Armstrong, R.L., 1982. Cordilleran Metamorphic Core Complexes -- From Arizona to Southern Canada. Annu Rev Earth Planet Sci 10, 129–154. https://doi.org/10.1146/annurev.ea.10.050182.001021

Artemieva, I.M., 2023. Back-arc basins: A global view from geophysical synthesis and analysis. Earth Sci Rev 236, 104242. https://doi.org/10.1016/j.earscirev.2022.104242

Ávila, C.A., Teixeira, W., Bongiolo, E.M., Dussin, I.A., Vieira, T.A.T., 2014. Rhyacian evolution of subvolcanic and metasedimentary rocks of the southern segment of the Mineiro belt, São Francisco Craton, Brazil. Precambrian Res 243, 221–251. https://doi.org/10.1016/j.precamres.2013.12.028

Baars, F.J., Fonseca, E., 1997. Geologia da Folha São Sebastião do Maranhão. In: GROSSI-SAD, J. H.; Lobato, L. M.; Pedrosa-Soares, A. C. & Soares-Filho, B. S. (coordenadores e editores). PROJETO ESPINHAÇO EM CD-ROM (textos, mapas e anexos). COMIG - Companhia Mineradora de Minas Gerais., Belo Horizonte.

Babechuk, M.G., Widdowson, M., Kamber, B.S., 2014. Quantifying chemical weathering intensity and trace element release from two contrasting basalt profiles, Deccan Traps, India. Chem Geol 363, 56–75. https://doi.org/10.1016/j.chemgeo.2013.10.027

Babinski, M., Chemale, F., van Schmus, W.R., 1995. The Pb/Pb age of the Minas Supergroup carbonate rocks, Quadrilátero Ferrífero, Brazil. Precambrian Res 72, 235–245. https://doi.org/10.1016/0301-9268(94)00091-5

Bakkiaraj, D., Nagendra, R., Nagarajan, R., Armstrong-Altrin, J.S., 2010. Geochemistry of sandstones from the Upper Cretaceous Sillakkudi Formation, Cauvery Basin, southern India: Implication for provenance. Journal of the Geological Society of India 76, 453–467. https://doi.org/10.1007/s12594-010-0128-3

Balázs, A., Matenco, L., Magyar, I., Horváth, F., Cloetingh, S., 2016. The link between tectonics and sedimentation in back-arc basins: New genetic constraints from the analysis of the Pannonian Basin. Tectonics 35, 1526–1559. https://doi.org/10.1002/2015TC004109

Baltazar, O.F., Zucchetti, M., 2007. Lithofacies associations and structural evolution of the Archean Rio das Velhas greenstone belt, Quadrilátero Ferrífero, Brazil: A review of the setting of gold deposits. Ore Geol Rev 32, 471–499. https://doi.org/10.1016/j.oregeorev.2005.03.021

Barbosa, J., Peucat, J., Martin, H., Silva, F., Moraes, A., Correa Gomes, L., Sabate, P., Marinho, M., Fanning, C., 2008. Petrogenesis of the late-orogenic Bravo granite and surrounding high-grade country rocks in the Palaeoproterozoic orogen of Itabuna-Salvador-Curaçá block, Bahia, Brazil. Precambrian Res 167, 35–52. https://doi.org/10.1016/j.precamres.2008.06.002

Barbosa, J.S.F., Sabaté, P., 2004. Archean and Paleoproterozoic crust of the São Francisco Craton, Bahia, Brazil: geodynamic features. Precambrian Res 133, 1–27. https://doi.org/10.1016/j.precamres.2004.03.001

Barbosa, N., Teixeira, W., Ávila, C.A., Montecinos, P.M., Bongiolo, E.M., Vasconcelos, F.F., 2019. U-Pb geochronology and coupled Hf-Nd-Sr isotopic-chemical constraints of the Cassiterita Orthogneiss (2.47–2.41-Ga) in the Mineiro belt, São Francisco craton: Geodynamic fingerprints beyond the Archean-Paleoproterozoic Transition. Precambrian Res 326, 399–416. https://doi.org/10.1016/j.precamres.2018.01.017

Barbosa, N.S., Teixeira, W., Ávila, C.A., Montecinos, P.M., Bongiolo, E.M., 2015. 2.17-2.10Ga plutonic episodes in the Mineiro belt, São Francisco Craton, Brazil: U-Pb ages, geochemical constraints and tectonics. Precambrian Res 270, 204–225. https://doi.org/10.1016/j.precamres.2015.09.010

Barrote, V.R., Rosiere, C.A., Rolim, V.K., Santos, J.O.S., McNaughton, N.J., 2017. The proterozoic guanhães banded iron formations, southeastern border of the São Francisco Craton, Brazil: Evidence of detrital contamination. Geologia USP - Serie Cientifica 17, 303–324. https://doi.org/10.11606/issn.2316-9095.v17-352

Bekker, A., Sial, A.N., Karhu, J.A., Ferreira, V.P., Noce, C.M., Kaufman, J., Romano, A.W., Pimentel, M.M., 2003. Chemostratigraphy of Carbonates from the Minas Supergroup, Quadrilatero Ferryifero (Iron Quadrangle), Brazil: A Stratigraphic

Record of Early Proterozoic Atmospheric, Biogeochemical and Climactic Change. Am J Sci 303, 865–904. https://doi.org/10.2475/ajs.303.10.865

Belousova, E., Griffin, W., O'Reilly, S.Y., Fisher, N., 2002. Igneous zircon: trace element composition as an indicator of source rock type. Contributions to Mineralogy and Petrology 143, 602–622. https://doi.org/10.1007/s00410-002-0364-7

Bhatia, M.R., 1983. Plate Tectonics and Geochemical Composition of Sandstones. J Geol 91, 611–627. https://doi.org/10.1086/628815

Bhatia, M.R., Crook, K.A.W., 1986. Trace element characteristics of graywackes and tectonic setting discrimination of sedimentary basins. Contributions to Mineralogy and Petrology 92, 181–193. https://doi.org/10.1007/BF00375292

Bouvier, A., Vervoort, J.D., Patchett, P.J., 2008. The Lu–Hf and Sm–Nd isotopic composition of CHUR: Constraints from unequilibrated chondrites and implications for the bulk composition of terrestrial planets. Earth Planet Sci Lett 273, 48–57. https://doi.org/10.1016/j.epsl.2008.06.010

Brando Soares, M., Corrêa Neto, A.V., Fabricio-Silva, W., 2020. The development of a Meso- to Neoarchean rifting-convergence-collision-collapse cycle over an ancient thickened protocontinent in the south São Francisco craton, Brazil. Gondwana Research 77, 40–66. https://doi.org/10.1016/j.gr.2019.06.017

Brito Neves, B.B. de, Fuck, R.A., Campanha, G.A. da C., 2021. Basement inliers of the Brasiliano structural provinces of South America. J South Am Earth Sci 110, 103392. https://doi.org/10.1016/j.jsames.2021.103392

Brueckner, H. K., Cunningham, D., Alkmin, F.F., Marshak, S., 2000. Tectonic implications of Precambrian Sm–Nd dates from the southern São Francisco craton and adjacent Araçuaí and Ribeira belts, Brazil. Precambrian Res 99, 255–269. https://doi.org/10.1016/S0301-9268(99)00065-0

Brueckner, H. K, Cunningham, D., Alkmin, F.F., Marshak, S., 2000. Tectonic implications of Precambrian Sm-Nd dates from the southern São Francisco craton and adjacent Araçuaí and Ribeira belts, Brazil. Precambrian Res 99, 255–269. https://doi.org/10.1016/S0301-9268(99)00065-0

Brun, J.-P., Sokoutis, D., Tirel, C., Gueydan, F., Van Den Driessche, J., Beslier, M.-O., 2018. Crustal versus mantle core complexes. Tectonophysics 746, 22–45. https://doi.org/10.1016/j.tecto.2017.09.017

Brun, J.-P., Sokoutis, D., Van Den Driessche, J., 1994. Analogue modeling of detachment fault systems and core complexes. Geology 22, 319–322. https://doi.org/10.1130/0091-7613(1994)022<0319:AMODFS>2.3.CO;2

Bruno, H., Elizeu, V., Heilbron, M., de Morisson Valeriano, C., Strachan, R., Fowler, M., Bersan, S., Moreira, H., Dussin, I., Guilherme do Eirado Silva, L., Tupinambá, M., Almeida, J., Neto, C., Storey, C., 2020. Neoarchean and Rhyacian TTG-Sanukitoid suites in the southern São Francisco Paleocontinent, Brazil: Evidence for diachronous change towards modern tectonics. Geoscience Frontiers 11, 1763–1787. https://doi.org/10.1016/j.gsf.2020.01.015

Bruno, H., Heilbron, M., de Morisson Valeriano, C., Strachan, R., Fowler, M., Bersan, S., Moreira, H., Motta, R., Almeida, J., Almeida, R., Carvalho, M., Storey, C., 2021. Evidence for a complex accretionary history preceding the amalgamation of Columbia: The Rhyacian Minas-Bahia Orogen, southern São Francisco Paleocontinent, Brazil. Gondwana Research 92, 149–171. https://doi.org/10.1016/j.gr.2020.12.019

Cabral, A.R., Tupinambá, M., Zeh, A., Lehmann, B., Wiedenbeck, M., Brauns, M., Kwitko-Ribeiro, R., 2017. Platiniferous gold–tourmaline aggregates in the gold–palladium belt of Minas Gerais, Brazil: implications for regional boron metasomatism. Mineral Petrol 111, 807–819. https://doi.org/10.1007/s00710-017-0496-0

Cabral, A.R., Zeh, A., 2015. Celebrating the Centenary of “The Geology of Central Minas Gerais, Brazil”: An Insight from the Sítio Largo Amphibolite. J Geol 123, 337–354. https://doi.org/10.1086/682047

Cabral, A.R., Zeh, A., Koglin, N., Seabra Gomes, A.A., Viana, D.J., Lehmann, B., 2012. Dating the Itabira iron formation, Quadrilátero Ferrífero of Minas Gerais, Brazil, at 2.65Ga: Depositional U–Pb age of zircon from a metavolcanic layer. Precambrian Res 204–205, 40–45. https://doi.org/10.1016/j.precamres.2012.02.006

Cabral, A.R., Zeh, A., Pires, F.R.M., da Silva, J.F., do Carmo, V.E.F., Tupinambá, M., 2022. Unconformity-covering pillow lava dated at 2.14 Ga: Challenging the “stable-shelf” Minas Supergroup of the Quadrilátero Ferrífero, Minas Gerais, Brazil. Geological Journal 57, 2046–2057. https://doi.org/10.1002/gj.4397

Carvalho, R.P. de, Rosière, C.A., Rolim, V.K., Lana, C. de C., Santos, J.O.S., 2014. A sequência orosiriana-estateriana e geometria transpressiva na região de Santa Maria de Itabira, Minas Gerais. Geologia USP. Série Científica 14, 111–120. https://doi.org/10.5327/Z1519-874X201400020006

Cawood, P.A., Hawkesworth, C.J., Dhuime, B., 2012. Detrital zircon record and tectonic setting. Geology 40, 875–878. https://doi.org/10.1130/G32945.1

Caxito, F. de A., Hagemann, S., Dias, T.G., Barrote, V., Dantas, E.L., Chaves, A. de O., Campello, M.S., Campos, F.C., 2020. A magmatic barcode for the São Francisco Craton: Contextual in-situ SHRIMP U–Pb baddeleyite and zircon dating of the Lavras, Pará de Minas and Formiga dyke swarms and implications for

Columbia and Rodinia reconstructions. Lithos 374–375. https://doi.org/10.1016/j.lithos.2020.105708

Chaves, A. de O., Coelho, R.M., 2018. Reinterpretação da ambiência tectônica de formação do leucogranito de Gouveia (Minas Gerais). Geonomos. https://doi.org/10.18285/geonomos.v26i1.1239

Chaves, A. de O., Coelho, R.M., 2013. Petrografia, geoquimica e geocronologia do leucogranito peraluminoso do Complexo Gouveia-MG 21, 1–12.

Chemale, F., Dussin, I.A., Alkmim, F.F., Martins, M.S., Queiroga, G., Armstrong, R., Santos, M.N., 2012. Unravelling a Proterozoic basin history through detrital zircon geochronology: The case of the Espinhaço Supergroup, Minas Gerais, Brazil. Gondwana Research 22, 200–206. https://doi.org/10.1016/j.gr.2011.08.016

Chemale, F., Dussin, I.A., Martins, M., Santos, M.N. dos, 2013. Nova abordagem tectono-estratigráfica do Supergrupo Espinhaço em sua porção meridional (MG). Geonomos. https://doi.org/10.18285/geonomos.v19i2.52

Chemale, F., Rosière, C.A., Endo, I., 1994. The tectonic evolution of the Quadrilátero Ferrífero, Minas Gerais, Brazil. Precambrian Res 65, 25–54. https://doi.org/10.1016/0301-9268(94)90098-1

Condie, K.C., 1993. Chemical composition and evolution of the upper continental crust: Contrasting results from surface samples and shales. Chem Geol 104, 1–37. https://doi.org/10.1016/0009-2541(93)90140-E

Coney, P.J., 1980. Cordilleran metamorphic core complexes: An overview. Mem. Geol. Soc. Am. Bull. 153, 7–31.

Coney, P.J., Harms, T.A., 1984. Cordilleran metamorphic core complexes: Cenozoic extensional relics of Mesozoic compression. Geology 12, 550. https://doi.org/10.1130/0091-7613(1984)12<550:CMCCCE>2.0.CO;2

Conor, C.H.H., Preiss, W.V., Page, R.W., Stevens, B.P.J., Plimer, I.R., Ashley, P.M., Gibson, G.M., Nutman, A.P., 2005. Discussion on detachment faulting and bimodal magmatism in the Palaeoproterozoic Willyama Supergroup, south-central Australia: keys to recognition of a multiply deformed Precambrian metamorphic core complex. J Geol Soc London 162, 409–416. https://doi.org/10.1144/0016-764904-111

Cullers, R.L., 2002. Implications of elemental concentrations for provenance, redox conditions, and metamorphic studies of shales and limestones near Pueblo, CO, USA. Chem Geol 191, 305–327. https://doi.org/10.1016/S0009-2541(02)00133-X

Cutts, K., Lana, C., 2019. The complex tale of Mantiqueira and Juiz de Fora: A comment on “Eoarchean to Neoproterozoic crustal evolution of the Mantiqueira and the Juiz de Fora Complexes, SE Brazil: Petrology, geochemistry, zircon U-Pb

geochronology and Lu-Hf isotopes." Precambrian Res 332. https://doi.org/10.1016/j.precamres.2019.03.006

Cutts, K., Lana, C., Alkmim, F., Peres, G.G., 2018. Metamorphic imprints on units of the southern Araçuaí belt, SE Brazil: The history of superimposed Transamazonian and Brasiliano orogenesis. Gondwana Research 58, 211–234. https://doi.org/10.1016/j.gr.2018.02.016

Cutts, K., Lana, C., Moreira, H., Alkmim, F., Peres, G.G., 2020. Zircon U-Pb and Lu-Hf record from high-grade complexes within the Mantiqueira Complex: First evidence of juvenile crustal input at 2.4–2.2 Ga and implications for the Palaeoproterozoic evolution of the São Francisco Craton. Precambrian Res 338, 105567. https://doi.org/10.1016/j.precamres.2019.105567

De, S., Mazumder, R., Ohta, T., Hegner, E., Yamada, K., Bhattacharyya, T., Chiarenzelli, J., Altermann, W., Arima, M., 2015. Geochemical and Sm–Nd isotopic characteristics of the Late Archaean-Palaeoproterozoic Dhanjori and Chaibasa metasedimentary rocks, Singhbhum craton, E. India: Implications for provenance, and contemporary basin tectonics. Precambrian Res 256, 62–78. https://doi.org/10.1016/j.precamres.2014.10.020

Degler, R., Pedrosa-Soares, A., Novo, T., Tedeschi, M., Silva, L.C., Dussin, I., Lana, C., 2018. Rhyacian-Orosirian isotopic records from the basement of the Araçuaí-Ribeira orogenic system (SE Brazil): Links in the Congo-São Francisco palaeocontinent. Precambrian Res 317, 179–195. https://doi.org/10.1016/j.precamres.2018.08.018

Dewey, J.F., 1988. Extensional collapse of orogens. Tectonics 7, 1123–1139. https://doi.org/10.1029/TC007i006p01123

Dickinson, W.R., Gehrels, G.E., 2009. Use of U–Pb ages of detrital zircons to infer maximum depositional ages of strata: A test against a Colorado Plateau Mesozoic database. Earth Planet Sci Lett 288, 115–125. https://doi.org/10.1016/j.epsl.2009.09.013

Dopico, C.I.M., Lana, C., Moreira, H.S., Cassino, L.F., Alkmim, F.F., 2017. U–Pb ages and Hf-isotope data of detrital zircons from the late Neoarchean-Paleoproterozoic Minas Basin, SE Brazil. Precambrian Res 291, 143–161. https://doi.org/10.1016/j.precamres.2017.01.026

Dorr II, J.V.N., 1969. Physiographic, stratigraphic and structural development of the Quadrilátero Ferrífero, Minas Gerais, Brazil. U.S. Geol. Surv. Prof. Pap. 641-A.

Duarte, B.P., Valente, S.C., Heilbron1t3, ? M, Campos, M.C., 2004. Petrogenesis of the Orthogneisses of the Mantiqueira Complex, Central Ribeira Belt, SE Brazil: An Archaean to Palaeoproterozoic Basement Unit Reworked During the Pan-African Orogeny, International Association for Gondwana Research.

Duque, T.R.F., Alkmim, F.F., Lana, C.D.C., 2020. Grãos detríticos de zircão do Grupo Itacolomi em sua área tipo, Quadrilátero Ferrífero, Minas Gerais: idades, proveniência e significado tectônico. Geologia USP. Série Científica 20, 101–123. https://doi.org/10.11606/issn.2316-9095.v20-151397

Dussin, I.A., Dussin, T.M., 1995. Supergrupo Espinhaço: modelo de evolução geodinâmica. Geonomos. https://doi.org/10.18285/geonomos.v3i1.212

Dussin, T.M., 2000. A tectônica extensional paleoproterozóica na borda sudeste do craton São Francisco (SE, Brasil): geoquímica e petrologia das metaígneas. Geonomos. https://doi.org/10.18285/geonomos.v8i1.149

Dussin, T.M., Duarte, P., Dussin, I.A., 2000. Registros da tectônica brasiliana na região de Guanhães (SE, Brasil): deformação e metamorfismo das rochas de idade pós-transamazônica. Geonomos. https://doi.org/10.18285/geonomos.v8i2.157

Dutra, L.F., Dias, S.P., Martins, M., Lana, C., Batista, A.C., Tavares, T.D., 2020. Detrital zircon records of the Paleo-Mesoproterozoic rift-sag Tamanduá Group in its type-section, Northern Quadrilátero Ferrífero, Minas Gerais, Brazil. Brazilian Journal of Geology 50. https://doi.org/10.1590/2317-4889202020190069

Dutra, L.F., Martins, M., Lana, C., 2019. Sedimentary and U-Pb detrital zircons provenance of the Paleoproterozoic Piracicaba and Sabará groups, Quadrilátero Ferrífero, Southern São Francisco craton, Brazil. Brazilian Journal of Geology 49. https://doi.org/10.1590/2317-4889201920180095

Farina, F., Albert, C., Lana, C., 2015. The Neoarchean transition between medium- and high-K granitoids: Clues from the Southern São Francisco Craton (Brazil). Precambrian Res 266, 375–394. https://doi.org/10.1016/j.precamres.2015.05.038

Fedo, C.M., Wayne Nesbitt, H., Young, G.M., 1995. Unraveling the effects of potassium metasomatism in sedimentary rocks and paleosols, with implications for paleoweathering conditions and provenance. Geology 23, 921. https://doi.org/10.1130/0091-7613(1995)023<0921:uteopm>2.3.co;2

Feng, R., Kerrich, R., 1990. Geochemistry of fine-grained clastic sediments in the Archean Abitibi greenstone belt, Canada: Implications for provenance and tectonic setting. Geochim Cosmochim Acta 54, 1061–1081. https://doi.org/10.1016/0016-7037(90)90439-R

Fernandes, M.L.S., Pedrosa Soares, A.C., Noce, C.M., Widemann, C., Correia Neves, J.M., 2000. U-Pb geochronology of the Borrachudos Suite: Evidence of Brasiliano tectonism recorded by late Paleoproterozoic anorogenic granites (Araçuaí Belt, Minas Gerais, Brazil), in: Inter. Geological Congress, Rio de Janeiro, Abstracts Volume, CD.

Floyd, P.A., Leveridge', B.E., 1987. Tectonic environment of the Devonian Gramscatho basin, south Cornwall: framework mode and geochemical evidence from turbiditic sandstones. Journal of rhe Geological Society, London 144, 531–542. https://doi.org/10.1144/gsjgs.144.4.0531

Fossen, H., Cavalcante, G.C.G., Pinheiro, R.V.L., Archanjo, C.J., 2019. Deformation – Progressive or multiphase? J Struct Geol 125, 82–99. https://doi.org/10.1016/j.jsg.2018.05.006

Freimann, M.A., Knauer, L.G., Kuchenbecker, M., 2021. New geochronologic and geochemical constraints for the Pedro Pereira metavolcanosedimentary sequence: Evidence for a 2.77 Ga oxygen oasis record in the São Francisco-Congo paleocontinent. J South Am Earth Sci 112. https://doi.org/10.1016/j.jsames.2021.103613

Fuenlabrada, J.M., Arenas, R., Díez Fernández, R., Sánchez Martínez, S., Abati, J., López Carmona, A., 2012. Sm–Nd isotope geochemistry and tectonic setting of the metasedimentary rocks from the basal allochthonous units of NW Iberia (Variscan suture, Galicia). Lithos 148, 196–208. https://doi.org/10.1016/j.lithos.2012.06.002

Gashawbeza, E.M., Klemperer, S.L., Wilson, C.K., Miller, E.L., 2008. Nature of the crust beneath northwest Basin and Range province from teleseismic receiver function data. J Geophys Res Solid Earth 113. https://doi.org/10.1029/2007JB005306

Gerdes, A., Zeh, A., 2009. Zircon formation versus zircon alteration — New insights from combined U–Pb and Lu–Hf in-situ LA-ICP-MS analyses, and consequences for the interpretation of Archean zircon from the Central Zone of the Limpopo Belt. Chem Geol 261, 230–243. https://doi.org/10.1016/j.chemgeo.2008.03.005

Gerdes, A., Zeh, A., 2006. Combined U–Pb and Hf isotope LA-(MC-)ICP-MS analyses of detrital zircons: Comparison with SHRIMP and new constraints for the provenance and age of an Armorican metasediment in Central Germany. Earth Planet Sci Lett 249, 47–61. https://doi.org/10.1016/j.epsl.2006.06.039

Gomes, S.D., Figueiredo e Silva, R.C., Kemp, A.I.S., Santos, J.O.S., Hagemann, S.G., Lobato, L.M., Rosière, C.A., Novo, T.A., 2020. Zircon U–Pb ages and Hf isotope compositions of Açucena Granite (Borrachudos Suite): Implications for Statherian-Cambrian tectono-magmatic evolution of the southern border of the São Francisco Craton, Brazil. J South Am Earth Sci 100, 102543. https://doi.org/10.1016/j.jsames.2020.102543

Gonçalves, G.F., Uhlein, A., 2022. Depositional systems, sequence stratigraphy, and sedimentary provenance of the Palaeoproterozoic Minas Supergroup and Itacolomi Group, Quadrilátero Ferrífero, Brazil. Brazilian Journal of Geology 52. https://doi.org/10.1590/2317-4889202220210081

Grochowski, J., Kuchenbecker, M., Barbuena, D., Novo, T., 2021. Disclosing Rhyacian/Orosirian orogenic magmatism within the Guanhães basement inlier, Araçuaí Orogen, Brazil: A new piece on the assembly of the São Francisco-Congo paleocontinent. Precambrian Res 363. https://doi.org/10.1016/j.precamres.2021.106329

Grossi-Sad, J.H., Lobato, L.M., Pedrosa-Soares, A.C., Soares Filho, B.S., 1997. Projeto Espinhaço em CD-ROM (textos, mapas e anexos). COMIG, Belo Horizonte, 2693 pp.

Guadagnin, F., Chemale, F., Magalhães, A.J.C., Santana, A., Dussin, I., Takehara, L., 2015. Age constraints on crystal-tuff from the Espinhaço Supergroup - Insight into the Paleoproterozoic to Mesoproterozoic intracratonic basin cycles of the Congo-São Francisco Craton. Gondwana Research 27, 363–376. https://doi.org/10.1016/j.gr.2013.10.009

Hagedorn, M.G., 2004. Contexto geotectônico da Serra do Espinhaço e domínios adjacentes a leste (Minas Gerais) com ênfase em aspectos geoquímicos e geocronológicos (PhD thesis). Universidade Estadual Paulista, 222p.

Hans Wedepohl, K., 1995. The composition of the continental crust. Geochim Cosmochim Acta 59, 1217–1232. https://doi.org/10.1016/0016-7037(95)00038-2

Hartmann, L.A., Endo, I., Suita, M.T.F., Santos, J.O.S., Frantz, J.C., Carneiro, M.A., McNaughton, N.J., Barley, M.E., 2006. Provenance and age delimitation of Quadrilátero Ferrífero sandstones based on zircon U–Pb isotopes. J South Am Earth Sci 20, 273–285. https://doi.org/10.1016/j.jsames.2005.07.015

He, B., Xu, Y.-G., Paterson, S., 2009. Magmatic diapirism of the Fangshan pluton, southwest of Beijing, China. J Struct Geol 31, 615–626. https://doi.org/10.1016/j.jsg.2009.04.007

Hegde, V.S., Chavadi, V.C., 2009. Geochemistry of late Archaean metagreywackes from the Western Dharwar Craton, South India: Implications for provenance and nature of the Late Archaean crust. Gondwana Research 15, 178–187. https://doi.org/10.1016/j.gr.2008.09.006

Heilbron, M., Duarte, B.P., Valeriano, C. de M., Simonetti, A., Machado, N., Nogueira, J.R., 2010. Evolution of reworked Paleoproterozoic basement rocks within the Ribeira belt (Neoproterozoic), SE-Brazil, based on U-Pb geochronology: Implications for paleogeographic reconstructions of the São Francisco-Congo paleocontinent. Precambrian Res 178, 136–148. https://doi.org/10.1016/j.precamres.2010.02.002

Henrique-Pinto, R., Janasi, V.A., Tassinari, C.C.G., Carvalho, B.B., Cioffi, C.R., Stríkis, N.M., 2015. Provenance and sedimentary environments of the Proterozoic São Roque Group, SE-Brazil: Contributions from petrography, geochemistry and Sm–

Nd isotopic systematics of metasedimentary rocks. J South Am Earth Sci 63, 191–207. https://doi.org/10.1016/j.jsames.2015.07.015

Herrgesell, G., Pflug, R., 1986. The Thrust Belt of the Southern Serra do Espinhaço, Minas Gerais, Brazil. Zentralblatt für Geologie und Paläontologie, Teil I 1985, 1405–1414. https://doi.org/10.1127/zbl_geol_pal_1/1985/1986/1405

Herron, M.M., 1988. Geochemical classification of terrigenous sands and shales from core or log data. J Sediment Petrol 58, 820–829. https://doi.org/10.1306/212f8e77-2b24-11d7-8648000102c1865d

Jacobson, A.D., Blum, J.D., 2003. Relationship between mechanical erosion and atmospheric CO2 consumption in the New Zealand Southern Alps. Geology 31, 865. https://doi.org/10.1130/G19662.1

Jordt-Evangelista, H., Alvarenga, J.P.M., Lana, C., 2015. Petrography and geochronology of the Furquim Quartzite, an eastern extension of the Itacolomi Group (Quadrilátero Ferrífero, Minas Gerais). Rem: Revista Escola de Minas 68, 393–399. https://doi.org/10.1590/0370-44672015680054

Karig, D.E., 1971. Origin and development of marginal basins in the western Pacific. J Geophys Res 76, 2542–2561. https://doi.org/10.1029/JB076i011p02542

Knauer, L.G., 2013. O Supergrupo Espinhaço em Minas Gerais: considerações sobre sua estratigrafia e seu arranjo estrutural. Geonomos. https://doi.org/10.18285/geonomos.v15i1.109

Koglin, N., Zeh, A., Cabral, A.R., Gomes, A.A.S., Neto, A.V.C., Brunetto, W.J., Galbiatti, H., 2014. Depositional age and sediment source of the auriferous Moeda Formation, Quadrilátero Ferrífero of Minas Gerais, Brazil: New constraints from U-Pb-Hf isotopes in zircon and xenotime. Precambrian Res 255, 96–108. https://doi.org/10.1016/j.precamres.2014.09.010

Konstantinou, A., Strickland, A., Miller, E., Vervoort, J., Fisher, C.M., Wooden, J., Valley, J., 2013. Synextensional magmatism leading to crustal flow in the Albion–Raft River–Grouse Creek metamorphic core complex, northeastern Basin and Range. Tectonics 32, 1384–1403. https://doi.org/10.1002/tect.20085

Kuchenbecker, M., Barbuena, D., 2023. Basement inliers of the Araçuaí-West Congo orogen: key pieces for understanding the evolution of the São Francisco-Congo paleocontinent. J South Am Earth Sci 125, 104299. https://doi.org/10.1016/j.jsames.2023.104299

Kuchenbecker, M., Pedrosa-Soares, A.C., Babinski, M., Fanning, M., 2015. Detrital zircon age patterns and provenance assessment for pre-glacial to post-glacial successions of the Neoproterozoic Macaúbas Group, Araçuaí Orogen, Brazil. Precambrian Res 266, 12–26. https://doi.org/10.1016/j.precamres.2015.04.016

Kuribara, Y., Tsunogae, T., Santosh, M., Takamura, Y., Costa, A.G., Rosière, C.A., 2019. Eoarchean to Neoproterozoic crustal evolution of the Mantiqueira and the Juiz de Fora Complexes, SE Brazil: Petrology, geochemistry, zircon U-Pb geochronology and Lu-Hf isotopes. Precambrian Res 323, 82–101. https://doi.org/10.1016/j.precamres.2019.01.008

Lana, C., Alkmim, F.F., Armstrong, R., Scholz, R., Romano, R., Nalini, H.A., 2013. The ancestry and magmatic evolution of Archaean TTG rocks of the Quadrilátero Ferrífero province, southeast Brazil. Precambrian Res 231, 157–173. https://doi.org/10.1016/j.precamres.2013.03.008

Leal, V.L.S., Kuchenbecker, M., Barbuena, D., Queiroga, G., Pinheiro, M.A.P., Freimann, M. de A., 2021. Geochemistry and U–Pb zircon ages of the metamafic-ultramafic rocks of the Riacho dos Machados metavolcanosedimentary sequence: Evidence of a late Rhyacian back-arc basin during the assembly of São Francisco-Congo paleocontinent. J South Am Earth Sci 105, 102972. https://doi.org/10.1016/j.jsames.2020.102972

Li, L., Shi, Y., Anderson, J.L., Ubide, T., Nemchin, A.A., Caulfield, J., Wang, X.-C., Zhao, J.-X., 2021. Dating mafic magmatism by integrating baddeleyite, zircon and apatite U–Pb geochronology: A case study of Proterozoic mafic dykes/sills in the North China Craton. Lithos 380–381, 105820. https://doi.org/10.1016/j.lithos.2020.105820

Liu, X., Zhang, J., Yin, C., Li, S., Liu, J., Qian, J., Zhao, C., 2021. A synthetic geochemical and geochronological dataset of the Mesoproterozoic sediments along the southern margin of North China Craton: Unraveling a prolonged peripheral subduction involved in breakup of Supercontinent Columbia. Precambrian Res 357. https://doi.org/10.1016/j.precamres.2021.106154

Lopes-Silva, L., Knauer, L.G., 2013. Posicionamento estratigráfico da Formação Bandeirinha na região de Diamantina, Minas Gerais: Grupo Costa Sena ou Supergrupo Espinhaço? Geonomos. https://doi.org/10.18285/geonomos.v19i2.49

Ludwig, K.R., 2012. Using Isoplot/Ex, version 3.75: a geochronological toolkit for Microsoft Excel. Berkeley Geochronology Center Special Pubublication.

Machado, N., Carneiro~, M., 1992. U-Pb evidence of late Archean tectono-thermal activity in the southern S5o Francisco shield, Brazil, Can. J. Earth Sci.

Machado, N., Schrank, A., Abreu, F.R., Knauer, L.G., Almeida-Abreu, P.A., 1989. Resultados preliminares da geocronologia U/Pb na Serra do Espinhaço Meridional. V Simp. Geol. Minas Gerais, Belo Horizonte, pp. 171–174.

Machado, N., Schrank, A., Noce, C.M., Gauthier, G., 1996. Ages of detrital zircon from Archean-Paleoproterozoic sequences: Implications for Greenstone Belt setting and evolution of a Transamazonian foreland basin in Quadrilátero Ferrífero,

southeast Brazil. Earth Planet Sci Lett 141, 259–276. https://doi.org/10.1016/0012-821X(96)00054-4

Magalhães, J.R., Pedrosa-Soares, A., Dussin, I., Müntener, O., Pinheiro, M.A.P., da Silva, L.C., Knauer, L.G., Bouvier, A.S., Baumgartner, L., 2018. First Lu-Hf, δ18O and trace elements in zircon signatures from the Statherian Espinhaço anorogenic province (Eastern Brazil): Geotectonic implications of a silicic large igneous province. Brazilian Journal of Geology 48, 735–759. https://doi.org/10.1590/2317-4889201820180046

Marinho, K.S.M., 2014. Petrogênese do Granulito Pedra Dourada,MG. (M.Sc.). Universidade Federal de Ouro Preto, Ouro Preto.

Martins de Sousa, D.F., Oliveira, E.P., Amaral, W.S., Baldim, M.R., 2020. The Itabuna-Salvador-Curaçá Orogen revisited, São Francisco Craton, Brazil: New zircon U–Pb ages and Hf data support evolution from archean continental arc to paleoproterozoic crustal reworking during block collision. J South Am Earth Sci 104, 102826. https://doi.org/10.1016/j.jsames.2020.102826

Martins-Neto, M.A., 1998. O Supergrupo Espinhaço em Minas Gerais: registro de uma bacia rifte-sag do Paleo/Mesoproterozóico. Brazilian Journal of Geology 28, 151–168.

Martins-Neto, M.A., Pedrosa-Soares, A.C., Lima, S.A.A., 2001. Tectono-sedimentary evolution of sedimentary basins from Late Paleoproterozoic to Late Neoproterozoic in the São Francisco craton and Araçuaí fold belt, eastern Brazil. Sediment Geol 141–142, 343–370. https://doi.org/10.1016/S0037-0738(01)00082-3

Mclennan, S.M., 1989. Rare earth elements in sedimentary rocks: influence of provenance and sedimentary process.

Mclennan, S.M., Bock, B., Hemming, S.R., Hurowitz, J.A., Steven, M.L., Mcdaniel, D.K., 2003. The roles of provenance and sedimentary processes in the geochemistry of sedimentary rocks, in: Lentz, D.R. (Ed.), Geochemistry of Sediments and Sedimentary Rocks/Evolutionary Considerations to Mineral Deposit-Forming Environments. Geological Association of Canada .

McLennan, S.M., Hemming, S., 1992. Samarium/neodymium elemental and isotopic systematics in sedimentary rocks. Geochim Cosmochim Acta 56, 887–898. https://doi.org/10.1016/0016-7037(92)90034-G

McLennan, S.M., Hemming, S., McDaniel, D.K., Hanson, G.N., 1993a. Geochemical approaches to sedimentation, provenance, and tectonics. Geol. Soc. Am. Spec. Pap.

McLennan, S.M., Hemming, S., McDaniel, D.K., Hanson, G.N., 1993b. Geochemical approaches to sedimentation, provenance, and tectonics. Special Paper Geol. Soc. Am. 248, 21–40.

Medeiros Júnior, E.B., Jordt-Evangelista, H., Queiroga, G.N., Schulz, B., Marques, R.A., 2016. Electron microprobe Th-U-Pb monazite dating and metamorphic evolution of the Acaiaca Granulite Complex, Minas Gerais, Brazil. Revista Escola de Minas 69, 21–32. https://doi.org/10.1590/0370-44672015690139

Miranda, D.A., Chaves, A. de O., 2021. Itapecerica metamafic-ultramafic rocks with e-morb signature: ophiolitic remnants of the Rhyacian-Orosirian orogeny in southern São Francisco craton? Revista Geociências, UNESP 40, 1–12.

Morais, G., Barbuena, D., Kuchenbecker, M., 2023. The Amaros and Dois Córregos plutons: Mesoarchean and Orosirian magmatism in the northern Guanhães basement inlier, Araçuaí orogen, Brazil. J South Am Earth Sci 127, 104405. https://doi.org/10.1016/j.jsames.2023.104405

Moreira, H., Lana, C., Nalini, H.A., 2016. The detrital zircon record of an Archaean convergent basin in the Southern São Francisco Craton, Brazil. Precambrian Res 275, 84–99. https://doi.org/10.1016/j.precamres.2015.12.015

Moreira, H., Seixas, L., Storey, C., Fowler, M., Lasalle, S., Stevenson, R., Lana, C., 2018. Evolution of Siderian juvenile crust to Rhyacian high Ba-Sr magmatism in the Mineiro Belt, southern São Francisco Craton. Geoscience Frontiers 9, 977–995. https://doi.org/10.1016/j.gsf.2018.01.009

Moreno, J.A., Baldim, M.R., Semprich, J., Oliveira, E.P., Verma, S.K., Teixeira, W., 2017. Geochronological and geochemical evidences for extension-related Neoarchean granitoids in the southern São Francisco Craton, Brazil. Precambrian Res 294, 322–343. https://doi.org/10.1016/j.precamres.2017.04.011

Nesbitt, H.W., Young, G.M., 1989. Formation and Diagenesis of Weathering Profiles. J Geol 97, 129–147. https://doi.org/10.1086/629290

Nesbitt, H.W., Young, G.M., 1984. Prediction of some weathering trends of plutonic and volcanic rocks based on thermodynamic and kinetic considerations. Geochim Cosmochim Acta 48, 1523–1534. https://doi.org/10.1016/0016-7037(84)90408-3

Nesbitt, H.W., Young, G.M., 1982. Early Proterozoic climates and plate motions inferred from major element chemistry of lutites. Nature 299, 715–717. https://doi.org/10.1038/299715a0

Neumayr, P., Hoinkes, G., Puhl, J., Mogessie, A., Khudeir, A.A., 1998. The Meatiq dome (Eastern Desert, Egypt) a Precambrian metamorphic core complex: petrological and geological evidence. Journal of Metamorphic Geology 16, 259–279. https://doi.org/10.1111/j.1525-1314.1998.00132.x

Noce, C., Zuccheti, M., Baltazar, O., Armstrong, R., Dantas, E., Renger, F., Lobato, L., 2005. Age of felsic volcanism and the role of ancient continental crust in the evolution of the Neoarchean Rio das Velhas Greenstone belt (Quadrilátero Ferrífero, Brazil): U–Pb zircon dating of volcaniclastic graywackes. Precambrian Res 141, 67–82. https://doi.org/10.1016/j.precamres.2005.08.002

Noce, C.M., Machado, N., Teixeira, W., 1998. U-Pb Geochronology of gneisses and granitoids in the Quadrilátero Ferrífero (Southern São Francisco Craton): age constraints for Archean and Paleoproterozoic magmatism and metamorphism. Revista Brasileira de Geociências 28, 95–102.

Noce, C.M., Pedrosa-Soares, A.C., da Silva, L.C., Armstrong, R., Piuzana, D., 2007. Evolution of polycyclic basement complexes in the Araçuaí Orogen, based on U-Pb SHRIMP data: Implications for Brazil-Africa links in Paleoproterozoic time. Precambrian Res 159, 60–78. https://doi.org/10.1016/j.precamres.2007.06.001

Oliveira, L.B.E. da R., Rosière, C.A., Rolim, V.K., Santos, J.O.S., 2019. Novos dados geocronológicos U-Pb de zircões detríticos na serra do Espinhaço Meridional, regiões de Altamira e Ipoema. Revista Geociências UNESP 38, 611–637.

Pagung, R., Rosière, C.A., Figueiredo e Silva, R.C., 2023. The Serra da Serpentina Group: a back-arc basin related to the Paleoproterozoic Minas-Bahia orogeny? J South Am Earth Sci 128, 104427. https://doi.org/10.1016/j.jsames.2023.104427

Pedrosa-Soares, A.C., Noce, C.M., Wiedemann, C.M., Pinto, C.P., 2001. The Araçuaí-West-Congo Orogen in Brazil: an overview of a confined orogen formed during Gondwanaland assembly. Precambrian Res 110, 307–323. https://doi.org/10.1016/S0301-9268(01)00174-7

Peixoto, E., Alkmim, F.F., Pedrosa-Soares, A., Lana, C., Chaves, A.O., 2018. Metamorphic record of collision and collapse in the Ediacaran-Cambrian Araçuaí orogen, SE-Brazil: Insights from *P-T* pseudosections and monazite dating. Journal of Metamorphic Geology 36, 147–172. https://doi.org/10.1111/jmg.12287

Peixoto, E., Pedrosa-Soares, A.C., Alkmim, F.F., Dussin, I.A., 2015. A suture–related accretionary wedge formed in the Neoproterozoic Araçuaí orogen (SE Brazil) during Western Gondwanaland assembly. Gondwana Research 27, 878–896. https://doi.org/10.1016/j.gr.2013.11.010

Peres, G.G., Alkmim, F.F., Jordt-Evangelista, H., 2004. The southern Araçuaí belt and the Dom Silvério Group: geologic architecture and tectonic significance 76, 771–790.

Pflug, R., 1968. Observações sobre a estratigrafia da Série Minas na região de Diamantina, Minas Gerais. DNPM, DGM, Notas Prelim. Estudos, 142: 20p.

Pflug, R., 1965. Zur Geologie der südlichen Espinhaço-Zone und ihrer präkambrischen Diamantvorkommen, Minas Gerais, Brasilien. Zeitschrift der Deutschen Gesellschaft für Geowissenschaften 115, 177–215. https://doi.org/10.1127/zdgg/115/1965/177

Pinto, C.P., Silva, M.A., 2014. Mapa Geológico do Estado de Minas Gerais, Brasil. Escala 1:1.000.000. Belo Horizonte, CODEMIG – Companhia de Desenvolvimento Econômico de Minas Gerais; CPRM – Companhia de Pesquisa de Recursos Minerais.

Piuzana, D., Castañeda, C., Noce, C.M., Pedrosa-Soares, A.C., Silva, L.C., 2013. Titanite crystal chemistry and U-Pb isotopic data: a petrogenetic indicator for Precambrian granitoid plutons of the eastern brazilian shield. Geonomos. https://doi.org/10.18285/geonomos.v16i1.91

Reeves, R.G., 1966. Geology and mineral resources of the Monlevade and Rio Piracicaba quadrangles,Minas Gerais, Brazil. U.S. Geol. Surv. Prof. Pap. 341-E.

Reis, L.A., Martins Neto, M.A., Gomes, N.S., Endo, I., Jordt-Evangelista, H., 2002. A bacia de antepaís paleoproterozóica Sabará, Quadrilátero Ferrífero, Minas Gerais. Revista Brasileira de Geociências 32, 27–42.

Rolim, V.K., 2016. As formações ferríferas da região de Conceição do Mato Dentro - MG: posicionamento estratigráfico, evolução tectônica, geocronologia, características geoquímicas e gênese dos minérios (PhD thesis). Universidade Federal de Minas Gerais, Belo Horizonte.

Rolim, V.K., Rosière, C.A., Santos, J.O.S., McNaughton, N.J., 2016. The Orosirian-Statherian banded iron formation-bearing sequences of the southern border of the Espinhaço Range, Southeast Brazil. J South Am Earth Sci 65, 43–66. https://doi.org/10.1016/j.jsames.2015.11.003

Romano, R., Lana, C., Alkmim, F.F., Stevens, G., Armstrong, R., 2013. Stabilization of the southern portion of the São Francisco craton, SE Brazil, through a long-lived period of potassic magmatism. Precambrian Res 224, 143–159. https://doi.org/10.1016/j.precamres.2012.09.002

Roser, B.P., Korsch, R.J., 1988. Provenance signatures of sandstone-mudstone suites determined using discriminant function analysis of major-element data. Chem Geol 67, 119–139. https://doi.org/10.1016/0009-2541(88)90010-1

Roser, B.P., Korsch, R.J., 1986. Determination of Tectonic Setting of Sandstone-Mudstone Suites Using SiO_2 Content and K_2O/Na_2O Ratio. J Geol 94, 635–650. https://doi.org/10.1086/629071

Rosière, C.A., Bekker, A., Rolim, V.K., Santos, J.O.S., 2019. Post-Great Oxidation Event Orosirian–Statherian iron formations on the São Francisco craton: Geotectonic implications. Island Arc 28. https://doi.org/10.1111/iar.12300

Rosière, C.A., Spier, C.A., Rios, F.J., Suckau, V.E., 2008. The Itabirites of the Quádrilátero Ferrífero and Related High-Grade Iron Ore Deposits: An Overview, in: Banded Iron Formation-Related High-Grade Iron Ore. Society of Economic Geologists. https://doi.org/10.5382/Rev.15.09

Rossignol, C., Lana, C., Alkmim, F., 2020. Geodynamic evolution of the Minas Basin, southern São Francisco Craton (Brazil), during the early Paleoproterozoic: Climate or tectonic? J South Am Earth Sci 101, 102628. https://doi.org/10.1016/j.jsames.2020.102628

Rudnick, R.L., Gao, S., 2003. Composition of the Continental Crust, in: Treatise on Geochemistry. Elsevier, pp. 1–64. https://doi.org/10.1016/B0-08-043751-6/03016-4

Santos, M.N. dos, 2015. Geocronologia U/PB em zircões detríticos e a evolução tectônica e estratigráfica da bacia espinhaço no setor meridional. Universidade de Brasília, Brasília. https://doi.org/10.26512/2015.07.T.19636

Santos, M.M., Lana, C., Scholz, R., Buick, I., Schmitz, M.D., Kamo, S.L., Gerdes, A., Corfu, F., Tapster, S., Lancaster, P., Storey, C.D., Basei, M.A.S., Tohver, E., Alkmim, A., Nalini, H., Krambrock, K., Fantini, C., Wiedenbeck, M., 2017. A New Appraisal of Sri Lankan BB Zircon as a Reference Material for LA-ICP-MS U-Pb Geochronology and Lu-Hf Isotope Tracing. Geostand Geoanal Res 41, 335–358. https://doi.org/10.1111/ggr.12167

Santos, M.N., Chemale, F., Dussin, I.A., Martins, M., Assis, T.A.R., Jelinek, A.R., Guadagnin, F., Armstrong, R., 2013. Sedimentological and paleoenvironmental constraints of the Statherian and Stenian Espinhaço rift system, Brazil. Sediment Geol 290, 47–59. https://doi.org/10.1016/j.sedgeo.2013.03.002

Sayão Valladares, C., Machado, N., Heilbron, M., Gauthier, G., 2004. Ages of Detrital Zircon from Siliciclastic Successions South of the São Francisco Craton, Brazil: Implications for the Evolution of Proterozoic Basins. Gondwana Research 7, 913–921. https://doi.org/10.1016/S1342-937X(05)71074-1

Schellart, W.P., Lister, G.S., Jessell, M.W., 2002. Analogue modelling of asymmetrical back-arc extension. Journal of the Virtual Explorer 7. https://doi.org/10.3809/jvirtex.2002.00046

Schenker, F.L., Gerya, T., Burg, J.-P., 2012. Bimodal behavior of extended continental lithosphere: Modeling insight and application to thermal history of migmatitic core complexes. Tectonophysics 579, 88–103. https://doi.org/10.1016/j.tecto.2012.07.002

Scherer, E., Münker, C., Mezger, K., 2001. Calibration of the Lutetium-Hafnium Clock. Science (1979) 293, 683–687. https://doi.org/10.1126/science.1061372

Schoene, B., Crowley, J.L., Condon, D.J., Schmitz, M.D., Bowring, S.A., 2006. Reassessing the uranium decay constants for geochronology using ID-TIMS U–Pb data. Geochim Cosmochim Acta 70, 426–445. https://doi.org/10.1016/j.gca.2005.09.007

Schöll, W.U., Fogaça, A.C.C., 1979. Estratigrafia da Serra do Espinhaço na região de Diamantina, in: SBG, Simp. Geol. Minas Gerais. pp. 276–290.

Seixas, L.A.R., Bardintzeff, J.-M., Stevenson, R., Bonin, B., 2013. Petrology of the high-Mg tonalites and dioritic enclaves of the ca. 2130Ma Alto Maranhão suite: Evidence for a major juvenile crustal addition event during the Rhyacian orogenesis, Mineiro Belt, southeast Brazil. Precambrian Res 238, 18–41. https://doi.org/10.1016/j.precamres.2013.09.015

Silva, L.C., Armstrong, R., Noce, C.M., Carneiro, M.A., Pimentel, M., Pedrosa-Soares, A.C., Leite, C.A., Vieira, V.S., Silva, M.A., Paes, V.J.C., Filho, J.M.C., 2002. Reavaliação da evolução geológica em terrenos pré-cambrianos brasileiros com base em novos dados U-Pb SHRIMP, parte II: Orógeno Araçuaí, Cinturão Mineiro e cráton São Francisco Meridional, Revista Brasileira de Geociências.

Silveira Braga, F.C., Rosière, C.A., Queiroga, G.N., Rolim, V.K., Santos, J.O.S., McNaughton, N.J., 2015. The Statherian itabirite-bearing sequence from the Morro Escuro Ridge, Santa Maria de Itabira, Minas Gerais, Brazil. J South Am Earth Sci 58, 33–53. https://doi.org/10.1016/j.jsames.2014.12.004

Silveira Braga, F.C., Rosière, C.A., Schneider Santos, J.O., Hagemann, S.G., Danyushevsky, L., Valle Salles, P., 2021. Geochemical and tectonic constraints on the genesis of iron formation-hosted magnetite-hematite deposits at the Guanhães Block (Brazil) by contact metasomatism with pegmatite intrusions. Ore Geol Rev 129, 103931. https://doi.org/10.1016/j.oregeorev.2020.103931

Silveira Braga, F.C., Rosière, C.A., Schneider Santos, J.O., Hagemann, S.G., McNaughton, N.J., Valle Salles, P., 2019. The Horto-Baratinha itabirite-hosted iron ore: A basal fragment of the Espinhaço basin in the eastern São Francisco Craton. J South Am Earth Sci 90, 12–33. https://doi.org/10.1016/j.jsames.2018.11.013

Silveira, V.D., 2016. Geologia e geocronologia de zircões detríticos da região de Serro, serra do Espinhaço Meridional, Minas Gerais, Brasil (M.Sc thesis). Universidade Federal de Minas Gerais, Belo Horizonte.

Sláma, J., Košler, J., Condon, D.J., Crowley, J.L., Gerdes, A., Hanchar, J.M., Horstwood, M.S.A., Morris, G.A., Nasdala, L., Norberg, N., Schaltegger, U., Schoene, B., Tubrett, M.N., Whitehouse, M.J., 2008. Plešovice zircon — A new

natural reference material for U–Pb and Hf isotopic microanalysis. Chem Geol 249, 1–35. https://doi.org/10.1016/j.chemgeo.2007.11.005

Söderlund, U., Patchett, P.J., Vervoort, J.D., Isachsen, C.E., 2004. The 176Lu decay constant determined by Lu–Hf and U–Pb isotope systematics of Precambrian mafic intrusions. Earth Planet Sci Lett 219, 311–324. https://doi.org/10.1016/S0012-821X(04)00012-3

Stacey, J.S., Kramers, J.D., 1975. Approximation of terrestrial lead isotope evolution by a two-stage model. Earth Planet Sci Lett 26, 207–221. https://doi.org/10.1016/0012-821X(75)90088-6

Stern, R.J., Dickinson, W.R., 2010. The Gulf of Mexico is a Jurassic backarc basin. Geosphere 6, 739–754. https://doi.org/10.1130/GES00585.1

Taylor, S.R., McLennan, S.M., 1985. The Continental Crust: its Composition and Evolution. Blackwell Scientific Publication, Oxford.

Teixeira de Souza, L., Correa-Gomes, L.C., Souza-Oliveira, J.S. de, 2019. Reinterpretation of the suture zone between the Itabuna-Salvador-Curaçá and Jequié blocks, of the São Francisco Craton, Bahia, Brazil, using structural and geophysical data. J South Am Earth Sci 96, 102353. https://doi.org/10.1016/j.jsames.2019.102353

Teixeira, W., Ávila, C.A., Dussin, I.A., Corrêa Neto, A.V., Bongiolo, E.M., Santos, J.O., Barbosa, N.S., 2015a. A juvenile accretion episode (2.35–2.32Ga) in the Mineiro belt and its role to the Minas accretionary orogeny: Zircon U–Pb–Hf and geochemical evidences. Precambrian Res 256, 148–169. https://doi.org/10.1016/j.precamres.2014.11.009

Teixeira, W., Ávila, C.A., Dussin, I.A., Corrêa Neto, A. V., Bongiolo, E.M., Santos, J.O., Barbosa, N.S., 2015b. A juvenile accretion episode (2.35-2.32Ga) in the Mineiro belt and its role to the Minas accretionary orogeny: Zircon U-Pb-Hf and geochemical evidences. Precambrian Res 256, 148–169. https://doi.org/10.1016/j.precamres.2014.11.009

Teixeira, W., Cordani, U.G., Nutman, A.P., Sato, K., 1998. Polyphase Archean evolution in the Campo Belo metamorphic complex, Southern São Francisco Craton, Brazil: SHRIMP U-Pb zircon evidence. J South Am Earth Sci 11, 279–289. https://doi.org/10.1016/S0895-9811(98)00011-X

Teixeira, W., Oliveira, E.P., Marques, L.S., 2017. Nature and Evolution of the Archean Crust of the São Francisco Craton, in: Heilbron, M., Cordani, U.G., Alkmim, F.F. (Eds.), São Francisco Craton, Eastern Brazil. Springer, pp. 29–56. https://doi.org/10.1007/978-3-319-01715-0_3

Toulkeridis, T., Clauer, N., Kröner, A., Reimer, T., Todt, W., 1999. Characterization, provenance, and tectonic setting of Fig Tree greywackes from the Archaean Barberton Greenstone Belt, South Africa. Sediment Geol 124, 113–129. https://doi.org/10.1016/S0037-0738(98)00123-7

Uhlein, A., 1991. Transição cráton-faixa dobrada: exemplo do Cráton do São Francisco e da Faixa Aracuai (ciclo brasiliano) no estado de Minas Gerais: aspectos estratigráficos e estruturais (PhD thesis). Universidade de São Paulo, São Paulo. https://doi.org/10.11606/T.44.1991.tde-27102015-092630

Uhlein, A., Trompette, R.R., Egydio-Silva, M., 1998. Proterozoic rifting and closure, SE border of the São Francisco Craton, Brazil. J South Am Earth Sci 11, 191–203. https://doi.org/10.1016/S0895-9811(98)00010-8

Verma, S.P., Armstrong-Altrin, J.S., 2013. New multi-dimensional diagrams for tectonic discrimination of siliciclastic sediments and their application to Precambrian basins. Chem Geol 355, 117–133. https://doi.org/10.1016/j.chemgeo.2013.07.014

Wronkiewicz, D.J., Condie, K.C., 1987. Geochemistry of Archean shales from the Witwatersrand Supergroup, South Africa: Source-area weathering and provenance. Geochim Cosmochim Acta 51, 2401–2416. https://doi.org/10.1016/0016-7037(87)90293-6

Yakymchuk, C., Kirkland, C.L., Clark, C., 2018. Th/U ratios in metamorphic zircon. Journal of Metamorphic Geology 36, 715–737. https://doi.org/10.1111/jmg.12307

Zapparoli, A.C., 2001. Os depósitos de cromita da borda leste da Serra do Espinhaço Meridional, Minas Gerais: Petrologia, quimismo e implicações genéticas (M.Sc thesis). Universidade Estadual de São Paulo, São Paulo.

Zeh, A., Franz, M., Obst, K., 2021. Zircon of Triassic Age in the Stuttgart Formation (Schilfsandstein)—Witness of Tephra Fallout in the Central European Basin and New Constraints on the Mid-Carnian Episode. Front Earth Sci (Lausanne) 9. https://doi.org/10.3389/feart.2021.778820

Zeh, A., Gerdes, A., 2012. U–Pb and Hf isotope record of detrital zircons from gold-bearing sediments of the Pietersburg Greenstone Belt (South Africa)—Is there a common provenance with the Witwatersrand Basin? Precambrian Res 204–205, 46–56. https://doi.org/10.1016/j.precamres.2012.02.013

Zeh, A., Gerdes, A., Heubeck, C., 2013. U–Pb and Hf isotope data of detrital zircons from the Barberton Greenstone Belt: constraints on provenance and Archaean crustal evolution. J Geol Soc London 170, 215–223. https://doi.org/10.1144/jgs2011-162

Zeh, A., Gerdes, A., Millonig, L., 2011. Hafnium isotope record of the Ancient Gneiss Complex, Swaziland, southern Africa: evidence for Archaean crust–mantle

formation and crust reworking between 3.66 and 2.73 Ga. J Geol Soc London 168, 953–964. https://doi.org/10.1144/0016-76492010-117

APPENDIX A – CHEMICAL COMPOSITION OF THE MELOSO FORMATION

Sample	Detection limit	FD-88b	FD-88c	FD-300a	FD-833b	FD-833c	FD-92a	FD-92c	FD-92f	FD-200a	MPN-196a
wt%											
SiO_2	0.01	64.27	63.14	59.14	84.05	79.52	72.65	76.11	69.91	92.36	24.79
Al_2O_3	0.01	16.73	15.74	17.19	1.35	2.60	14.17	11.82	13.46	2.71	16.33
Fe_2O_3	0.04	6.82	8.03	5.58	12.96	14.71	2.80	3.44	4.36	2.87	21.00
MgO	0.01	2.57	3.25	1.09	0.28	1.01	2.22	0.99	1.47	0.19	17.11
CaO	0.01	0.15	0.48	0.06	0.22	0.28	0.14	0.34	1.81	0.05	3.37
Na_2O	0.01	0.06	0.24	0.11	<0.01	<0.01	1.68	4.63	2.87	0.02	<0.01
K_2O	0.01	4.58	4.27	4.61	0.38	0.65	3.40	0.96	2.23	0.83	<0.01
TiO_2	0.01	0.60	0.74	0.68	0.05	0.05	0.26	0.27	0.44	0.18	5.09
P_2O_5	0.01	0.11	0.11	0.06	0.16	0.20	0.06	0.05	0.07	0.17	2.02
MnO	0.01	0.02	0.18	0.01	0.03	0.04	0.15	0.14	0.26	0.01	0.89
Cr_2O_3	0.002	0.031	0.026	0.033	0.010	0.008	0.008	0.009	0.005	0.008	0.002
LOI	-5.1	3.7	3.6	11.1	0.5	0.9	2.3	1.1	2.8	0.6	8.7
Sum		99.84	99.88	99.89	99.98	99.97	99.90	99.91	99.80	100.00	99.22
ppm											
Ba	1	1748	898	2434	99	398	718	275	767	461	8
Ni	20	170	79	41	38	58	<20	33	25	<20	<20
Sc	1	21	18	23	3	4	5	7	10	3	41
Be	1	2	1	<1	1	1	<1	2	3	<1	2
Co	0.2	32.1	29.3	2.4	3.8	10.6	7.9	9.0	10.5	3.1	61.4
Cs	0.1	6.7	9.1	4.3	0.6	0.7	7.0	2.2	6.7	1.3	<0.1
Ga	0.5	21.2	19.2	21.4	3.0	5.4	18.0	10.5	16.0	4.2	26.7
Hf	0.1	3.8	4.1	3.6	0.8	1.1	4.7	4.9	5.2	0.8	19.2
Nb	0.1	8.9	8.5	9.5	1.3	1.6	11.6	9.9	10.5	2.2	82.4
Rb	0.1	152.5	167.9	138.3	14.5	22.3	136.7	47.9	106.7	24.1	0.2
Sn	1	3	2	3	<1	<1	6	3	3	1	4
Sr	0.5	41.3	56.4	22.6	8.9	11.5	47.4	91.7	136.4	7.1	104.7
Ta	0.1	0.7	0.6	0.7	<0.1	0.1	1.1	0.9	0.7	0.2	4.6
Th	0.2	11.1	8.5	10.8	4.4	4.1	15.7	12.1	13.8	1.8	8.0
U	0.1	5.0	1.2	7.8	1.1	1.2	8.9	3.6	2.9	0.9	5.3
V	8	167	113	234	75	69	22	25	30	13	356
W	0.5	3.5	2.4	3.9	0.7	0.8	1.3	1.1	1.4	1.5	1.5
Zr	0.1	126.4	148.4	128.2	36.2	35.0	150.1	171.2	192.7	30.4	868.1
Y	0.1	29.5	12.6	28.9	8.9	8.2	38.3	26.3	27.0	8.5	83.2
La	0.1	47.8	25.7	37.5	6.5	6.5	37.7	36.4	43.5	4.6	93.0
Ce	0.1	95.8	53.3	69.2	14.9	12.4	78.9	69.5	85.7	11.0	206.1
Pr	0.02	10.90	6.01	8.06	1.67	1.54	8.94	7.71	9.67	1.26	26.52
Nd	0.3	42.1	22.8	30.9	7.8	6.3	32.9	28.4	34.9	5.5	109.6
Sm	0.05	7.79	4.24	5.60	1.85	1.59	6.85	5.18	6.24	1.63	22.37
Eu	0.02	1.87	0.99	1.14	0.43	0.39	0.53	0.83	1.18	0.33	5.83
Gd	0.05	6.99	3.34	4.77	1.86	1.85	6.60	4.62	5.42	1.70	20.24

Continue...

Tb	0.01	1.02	0.42	0.72	0.30	0.30	1.09	0.72	0.79	0.24	2.78
Dy	0.05	5.53	2.30	4.71	1.60	1.62	6.81	4.84	4.85	1.24	15.57
Ho	0.02	1.10	0.47	0.99	0.35	0.33	1.34	0.89	1.00	0.26	3.09
Er	0.03	3.09	1.53	2.74	1.01	0.97	3.90	2.95	3.26	0.77	9.05
Tm	0.01	0.43	0.21	0.40	0.13	0.13	0.55	0.44	0.45	0.10	1.23
Yb	0.05	2.87	1.60	2.56	0.81	0.75	3.45	2.79	3.01	0.62	7.92
Lu	0.01	0.44	0.24	0.43	0.11	0.11	0.50	0.44	0.48	0.09	1.20
Mo	0.1	0.8	1.3	3.1	3.8	3.3	1.4	2.3	2.7	3.4	0.2
Cu	0.1	8.1	1.1	8.5	4.1	3.4	36.0	15.1	798.9	27.9	1073.4
Pb	0.1	8.4	3.3	3.4	1.2	1.5	3.2	6.2	9.0	1.5	21.0
Zn	1	301	66	78	14	20	39	53	73	6	429
Ni	0.1	155.4	70.5	33.2	26.4	45.8	12.5	19.2	26.0	4.9	13.0
As	0.5	1.0	1.6	7.4	1.4	1.8	1.7	0.8	0.8	6.0	2.2
Cd	0.1	<0.1	<0.1	<0.1	<0.1	<0.1	<0.1	<0.1	<0.1	<0.1	<0.1
Sb	0.1	<0.1	<0.1	<0.1	<0.1	<0.1	<0.1	<0.1	<0.1	<0.1	<0.1
Bi	0.1	0.9	0.2	<0.1	<0.1	<0.1	0.2	0.1	1.5	<0.1	0.1
Ag	0.1	0.4	<0.1	<0.1	<0.1	<0.1	<0.1	<0.1	0.5	<0.1	5.3
Au	0.5	5.2	0.5	1.2	2.1	1.5	1.8	<0.5	4.4	<0.5	4.2
Hg	0.01	<0.01	<0.01	<0.01	<0.01	<0.01	<0.01	<0.01	<0.01	<0.01	0.01
Se	0.5	1.5	<0.5	<0.5	<0.5	<0.5	<0.5	<0.5	<0.5	<0.5	<0.5

Sample	Detection limit	MPN-84a	MPN-84b	MPN-84c	MPN-60a	MPN-60b	MPS-185a	MPS-231a	MOES-19	MOES-20
wt%										
SiO_2	0.01	40.50	47.53	42.57	53.51	74.22	44.40	45.46	56.71	46.25
Al_2O_3	0.01	11.44	29.46	13.02	22.10	12.40	20.38	14.26	12.22	15.30
Fe_2O_3	0.04	12.38	6.26	9.01	8.44	3.59	13.28	9.04	15.63	12.59
MgO	0.01	5.21	3.65	6.70	4.42	2.15	8.71	9.56	6.91	7.43
CaO	0.01	12.81	0.26	11.95	0.45	0.04	0.91	10.31	0.76	5.62
Na_2O	0.01	0.31	2.51	2.99	1.05	0.10	1.80	2.78	0.11	0.13
K_2O	0.01	0.46	3.31	<0.01	3.49	4.89	2.53	0.10	2.42	3.92
TiO_2	0.01	2.82	0.88	0.60	0.76	0.17	0.86	0.48	2.03	1.07
P_2O_5	0.01	0.40	0.08	0.05	0.07	<0.01	0.08	0.06	0.46	0.16
MnO	0.01	0.28	0.04	0.22	0.06	0.02	0.15	0.17	0.14	0.42
Cr_2O_3	0.002	0.007	0.050	0.017	0.037	0.004	0.128	0.056	0.005	0.005
LOI	-5.1	13.1	5.7	12.7	5.4	2.1	6.4	7.5	2.3	6.8
Sum		99.76	99.81	99.81	99.83	99.77	99.75	99.76	99.76	99.71
ppm										
Ba	1	77	558	6	488	323	512	29	347	388
Ni	20	50	205	102	129	<20	475	193	23	78
Sc	1	22	27	34	22	<1	33	34	25	23
Be	1	<1	6	<1	2	3	3	3	<1	4
Co	0.2	37.3	39.6	38.6	38.4	5.5	67.0	40.5	40.8	18.2
Cs	0.1	0.4	3.5	<0.1	2.0	6.4	1.9	0.1	5.0	4.8
Ga	0.5	18.0	34.5	9.3	26.1	39.6	22.7	9.7	24.1	23.4
Hf	0.1	5.5	5.0	1.1	4.0	26.7	3.3	0.8	8.8	11.0
Nb	0.1	29.6	13.4	1.4	10.9	167.9	7.2	2.3	20.2	20.8
Rb	0.1	18.3	130.2	0.4	127.4	214.1	65.9	2.4	55.5	102.3
Sn	1	2	4	<1	3	20	2	<1	3	3
Sr	0.5	93.5	202.3	103.8	75.3	6.5	89.6	208.2	8.7	84.9
Ta	0.1	1.8	1.1	<0.1	1.0	11.4	0.6	0.1	1.3	2.1
Th	0.2	3.2	15.9	0.5	12.5	69.9	7.0	1.2	7.2	27.0
U	0.1	2.0	4.7	0.2	4.5	17.0	1.9	0.2	4.1	20.0
V	8	330	209	210	169	13	248	213	186	274
W	0.5	2.0	3.1	<0.5	2.7	5.0	2.6	1.5	1.2	2.8
Zr	0.1	223.0	178.6	36.4	149.9	759.7	119.8	35.5	346.6	399.7
Y	0.1	30.5	31.9	12.1	23.6	112.2	20.0	12.8	63.1	64.5
La	0.1	32.7	36.3	4.6	29.2	32.3	21.2	3.2	38.3	71.2
Ce	0.1	68.1	67.5	7.8	54.4	193.6	40.3	8.1	84.0	139.1
Pr	0.02	8.73	7.46	1.02	6.00	7.89	4.69	0.86	10.79	15.68
Nd	0.3	36.7	27.6	4.8	21.8	28.4	17.6	3.8	46.4	59.8
Sm	0.05	7.24	5.01	1.35	4.15	8.33	3.67	1.13	10.57	12.13
Eu	0.02	1.85	1.28	0.71	1.11	0.22	1.06	0.40	3.08	2.65
Gd	0.05	6.81	5.23	1.92	4.17	10.28	3.92	1.58	11.69	12.35
Tb	0.01	0.98	0.85	0.30	0.65	2.41	0.62	0.29	1.90	1.94
Dy	0.05	5.47	5.18	2.13	4.05	17.31	3.80	2.30	11.25	11.37

Continue...

Ho	0.02	1.17	1.09	0.44	0.81	3.97	0.76	0.48	2.43	2.35
Er	0.03	3.41	3.41	1.27	2.38	13.56	2.17	1.55	6.91	7.05
Tm	0.01	0.48	0.47	0.20	0.36	2.23	0.33	0.21	1.01	0.98
Yb	0.05	3.10	3.06	1.29	2.18	15.74	2.23	1.35	6.46	6.43
Lu	0.01	0.44	0.44	0.23	0.35	2.30	0.32	0.23	0.97	0.95
Mo	0.1	2.4	3.2	0.5	3.3	3.3	1.7	0.8	3.2	8.1
Cu	0.1	116.8	56.8	1.7	46.9	5.4	69.6	3.9	4.1	2.8
Pb	0.1	5.9	1.8	8.1	2.9	5.7	1.9	3.3	2.8	11.0
Zn	1	124	87	121	87	39	125	52	13	24
Ni	0.1	45.5	209.9	89.9	123.6	7.2	459.9	127.4	21.8	59.0
As	0.5	0.7	37.9	0.7	29.3	2.1	32.1	24.8	0.5	9.9
Cd	0.1	0.1	<0.1	0.3	<0.1	<0.1	<0.1	<0.1	<0.1	<0.1
Sb	0.1	1.0	0.1	0.8	5.4	4.6	<0.1	0.1	<0.1	<0.1
Bi	0.1	<0.1	<0.1	<0.1	0.6	<0.1	0.2	<0.1	<0.1	<0.1
Ag	0.1	<0.1	<0.1	<0.1	0.2	<0.1	<0.1	<0.1	<0.1	<0.1
Au	0.5	<0.5	<0.5	<0.5	64.9	5.4	0.6	<0.5	0.8	<0.5
Hg	0.01	<0.01	0.02	<0.01	<0.01	<0.01	<0.01	<0.01	<0.01	<0.01
Se	0.5	<0.5	<0.5	<0.5	<0.5	<0.5	<0.5	<0.5	<0.5	<0.5

APPENDIX B – U-PB LA-ICPMS DATA

U-Pb-Th LA-ICPMS data of detrital zircon grains from sample 03-084

grain	^{207}Pb[a]	U[b]	Pb[b]	Th[b]	^{206}Pbc[c]	^{206}Pb[d]	±2σ	^{207}Pb[d]	±2σ	^{207}Pb[d]	±2σ	rho[e]	^{206}Pb	±2σ	^{207}Pb	±2σ	^{207}Pb	±2σ	conc.[f]
	(cps)	(ppm)	(ppm)	U	(%)	^{238}U	(%)	^{235}U	(%)	^{206}Pb	(%)		^{238}U	(Ma)	^{235}U	(Ma)	^{206}Pb	(Ma)	(%)
U113	39928	88	40	0.63	0.43	0.40000	1.7	7.462	1.9	0.1353	0.7987	0.91	2169	32	2168	17	2168	14	100
U114	290335	378	221	0.70	0.22	0.49110	1.6	12.42	1.8	0.1834	0.677	0.92	2576	35	2636	17	2684	11	96
U115	80120	263	104	1.43	0.10	0.30020	1.6	4.981	1.8	0.1203	0.6432	0.93	1692	25	1816	15	1961	11	86
U116	6013	13	6	0.69	b.d.	0.39730	1.5	7.302	2.2	0.1333	1.635	0.67	2157	27	2149	20	2142	29	101
U117	82198	1603	139	0.02	0.17	0.09190	1.5	0.8121	2.2	0.06409	1.574	0.70	567	8	604	10	744	33	76
U118	123335	293	122	0.33	0.11	0.39350	1.5	7.257	1.7	0.1338	0.8465	0.87	2139	27	2144	16	2148	15	100
U119	179767	222	132	0.56	0.20	0.51300	1.5	13.01	1.6	0.184	0.4818	0.95	2669	33	2680	15	2689	8	99
U120	39914	249	33	0.19	1.26	0.12550	3.2	1.665	4.8	0.09621	3.522	0.67	762	23	995	31	1552	66	49
U121	63756	137	55	0.79	0.22	0.33760	1.7	6.261	1.9	0.1345	0.8186	0.90	1875	27	2013	16	2158	14	87
U122	49647	121	51	0.57	0.25	0.37740	1.5	6.737	1.6	0.1295	0.764	0.88	2064	26	2077	15	2091	13	99
U123	35431	80	37	0.79	b.d.	0.39100	1.5	7.156	1.8	0.1327	0.9152	0.85	2128	27	2131	16	2134	16	100
U124	39311	87	35	0.31	0.12	0.37960	1.8	6.829	2.1	0.1305	0.9424	0.89	2075	33	2090	18	2104	17	99
U125	161068	193	121	0.70	b.d.	0.52590	1.6	13.46	1.7	0.1856	0.5519	0.94	2724	35	2712	16	2703	9	101
U126	28769	78	32	0.71	2.14	0.35430	1.6	6.313	1.9	0.1292	1.042	0.84	1955	27	2020	17	2087	18	94
U127c	55821	107	57	1.07	0.51	0.42750	1.6	8.59	1.7	0.1457	0.7909	0.89	2295	30	2296	16	2296	14	100
U128r	72103	1696	137	0.01	1.15	0.08536	1.6	0.6944	3.0	0.059	2.578	0.52	528	8	535	13	567	56	93
U129	35988	77	33	0.23	b.d.	0.40590	1.4	7.719	1.6	0.1379	0.8208	0.86	2196	26	2199	15	2201	14	100
U130	90400	2140	166	0.01	0.22	0.08409	1.5	0.6746	1.7	0.05818	0.7612	0.90	520	8	523	7	537	17	97
U131	131166	422	171	0.47	0.05	0.37880	1.4	6.696	1.7	0.1282	0.9998	0.81	2071	25	2072	15	2074	18	100
U132	16986	410	33	0.13	0.29	0.08464	1.7	0.6728	2.1	0.05765	1.205	0.82	524	9	522	9	516	26	101
U133	85774	187	82	0.52	0.28	0.39430	1.4	7.287	1.6	0.134	0.7053	0.90	2143	26	2147	14	2152	12	100
U134	38211	118	40	0.50	1.52	0.29530	3.0	5.752	3.6	0.1413	2.016	0.83	1668	44	1939	32	2243	35	74
U135	149702	483	153	0.23	0.07	0.30670	1.7	5.218	1.8	0.1234	0.676	0.93	1725	26	1855	16	2006	12	86
U136	54082	147	54	0.38	0.20	0.34190	1.5	6.105	1.7	0.1295	0.689	0.91	1896	25	1991	15	2091	12	91
U137	60629	138	58	0.48	b.d.	0.38340	1.5	6.872	1.7	0.13	0.7596	0.89	2092	27	2095	15	2098	13	100

U138	138994	409	129	0.43	0.13	0.27880	1.6	5.62	1.9	0.1462	0.9048	0.88	1585	23	1919	16	2302	16	69
U139	125624	301	143	1.08	b.d.	0.38400	1.8	6.878	1.9	0.1299	0.7028	0.93	2095	32	2096	17	2097	12	100
U140	48844	92	46	0.78	0.56	0.42650	1.7	8.584	1.9	0.146	0.7031	0.93	2290	33	2295	17	2299	12	100
U141	105145	246	98	0.24	0.21	0.38310	1.6	7.062	1.8	0.1337	0.6776	0.92	2091	29	2119	16	2147	12	97
U142c	39734	85	37	0.36	0.29	0.40350	1.5	7.61	1.8	0.1368	0.9787	0.85	2185	29	2186	17	2187	17	100
U143r	89457	969	104	0.05	0.05	0.11090	2.0	1.294	2.9	0.08464	2.169	0.67	678	13	843	17	1307	42	52
U144	46797	73	37	0.32	b.d.	0.47350	1.9	10.65	2.1	0.1631	0.8654	0.91	2499	39	2493	19	2488	15	100
U145	139820	379	146	0.67	0.23	0.33540	1.5	5.896	1.6	0.1275	0.6171	0.93	1864	25	1961	14	2064	11	90
U146	77688	349	82	0.36	0.48	0.21670	1.7	3.493	1.9	0.1169	0.7631	0.91	1264	20	1526	15	1910	14	66
U147	117540	2787	216	0.01	0.17	0.08409	1.7	0.6765	1.8	0.05834	0.6992	0.92	521	8	525	8	543	15	96
U148	154531	173	107	0.67	b.d.	0.51880	1.5	13.27	1.7	0.1855	0.6688	0.92	2694	34	2699	16	2703	11	100
U149	203521	286	158	0.58	b.d.	0.47630	1.4	11.97	1.5	0.1823	0.6283	0.91	2511	28	2602	14	2674	10	94
U150	49477	118	49	0.61	b.d.	0.36330	2.1	7.534	2.5	0.1504	1.445	0.82	1998	36	2177	23	2350	25	85
U157	18051	42	20	1.18	0.81	0.38680	1.4	6.986	1.9	0.131	1.306	0.72	2108	25	2110	17	2111	23	100
U158	65630	141	65	0.63	b.d.	0.41130	1.4	7.816	1.6	0.1378	0.7785	0.87	2221	26	2210	14	2200	14	101
U159	78021	218	60	0.54	0.10	0.23430	4.1	4.482	4.3	0.1387	1.353	0.95	1357	51	1728	37	2212	23	61
U160	38331	117	33	0.47	0.29	0.24640	3.8	4.271	4.1	0.1257	1.508	0.93	1420	49	1688	34	2039	27	70
U161	137682	423	122	0.20	0.15	0.28120	3.1	5.064	3.4	0.1306	1.322	0.92	1597	44	1830	29	2106	23	76
U162	45602	131	44	0.75	0.32	0.27200	1.9	5.079	2.1	0.1354	0.7268	0.94	1551	27	1833	18	2169	13	72
U163	120754	204	85	0.50	0.07	0.35980	1.9	8.599	2.1	0.1733	0.8668	0.91	1981	32	2296	19	2590	14	77
U164	60808	135	60	0.65	0.12	0.39660	1.5	7.329	1.7	0.134	0.87	0.87	2153	28	2152	16	2152	15	100
U165	105607	573	63	0.27	0.27	0.09037	7.2	1.358	8.1	0.109	3.783	0.88	558	38	871	49	1782	69	31
U166	78963	216	78	0.46	0.33	0.32940	1.5	5.809	1.7	0.1279	0.8354	0.87	1835	24	1948	15	2070	15	89
U167	52325	118	53	0.68	0.34	0.39560	1.8	7.279	2.1	0.1334	0.9753	0.88	2149	33	2146	19	2144	17	100
U169	286199	386	203	0.36	0.26	0.47170	1.8	12.22	1.9	0.1878	0.6729	0.94	2491	38	2621	18	2723	11	91
U170	95640	248	103	0.66	0.17	0.36790	1.7	6.361	1.8	0.1254	0.7181	0.92	2020	30	2027	16	2035	13	99
U171	33922	79	33	0.87	0.97	0.33720	2.0	6.093	2.3	0.1311	1.171	0.86	1873	32	1989	20	2112	21	89
U172	14606	36	16	0.60	2.84	0.38930	2.5	7.116	3.1	0.1326	1.809	0.81	2120	45	2126	28	2132	32	99
U173	24470	100	31	0.74	1.23	0.28520	1.8	4.584	2.4	0.1166	1.525	0.76	1617	26	1746	20	1904	27	85
U174	83280	185	87	0.66	0.71	0.41320	2.2	7.894	3.2	0.1386	2.366	0.67	2230	41	2219	29	2209	41	101

U175	60071	148	65	0.55	0.54	0.39520	1.8	7.306	2.0	0.1341	0.8977	0.90	2147	33	2149	18	2152	16	100
U176	57563	130	57	0.70	0.03	0.38430	1.8	7.128	2.0	0.1345	0.8848	0.90	2096	33	2127	18	2158	15	97
U177	121612	239	111	0.49	0.11	0.41790	1.6	8.458	1.7	0.1468	0.6196	0.93	2251	31	2281	16	2309	11	97
U178	130419	279	123	0.40	0.28	0.40670	1.5	7.849	1.6	0.14	0.5527	0.94	2200	28	2214	14	2227	10	99
U179	133530	173	104	0.54	0.15	0.52290	1.4	13.23	1.6	0.1835	0.6726	0.90	2712	31	2696	15	2685	11	101
U180	68529	188	74	0.42	0.31	0.36940	1.7	6.622	1.9	0.13	0.9262	0.87	2027	29	2062	17	2098	16	97
U181	237210	251	167	0.75	b.d.	0.54710	1.8	15.44	2.0	0.2047	0.946	0.88	2813	41	2843	20	2864	15	98
U182	92025	215	93	0.58	b.d.	0.38750	1.5	7.258	1.7	0.1359	0.7068	0.91	2111	27	2144	15	2175	12	97
U183	23911	54	28	1.48	b.d.	0.38910	1.5	7.017	1.8	0.1308	1.07	0.81	2119	27	2114	16	2109	19	100
U184	44766	102	44	0.49	0.95	0.39190	1.7	7.146	2.0	0.1323	0.9968	0.87	2132	31	2130	18	2128	17	100
U185	96571	2234	176	0.01	0.26	0.08510	1.4	0.6851	1.6	0.05839	0.8311	0.85	526	7	530	7	544	18	97
U186	94895	65	51	0.81	b.d.	0.60520	1.8	23.26	2.0	0.2788	0.8547	0.90	3051	44	3238	20	3356	13	91
U187	90386	706	81	0.39	0.70	0.10020	3.5	1.169	6.8	0.08459	5.804	0.52	616	21	786	38	1306	113	47
U188c	38602	109	35	0.42	1.02	0.28510	2.0	4.681	3.9	0.1191	3.38	0.52	1617	29	1764	34	1942	60	83
U189r	113172	458	122	0.32	0.06	0.25280	1.7	4.156	2.0	0.1192	1.009	0.86	1453	22	1665	16	1945	18	75
U190	71313	166	69	0.40	b.d.	0.38480	1.6	7.175	1.7	0.1352	0.6168	0.93	2099	29	2133	15	2167	11	97
U191	35476	87	37	0.82	0.29	0.38120	2.5	6.777	2.7	0.129	1.122	0.91	2082	45	2083	25	2084	20	100
U192	31831	741	58	0.05	b.d.	0.08395	2.5	0.6817	2.8	0.0589	1.305	0.88	520	12	528	12	563	28	92
U193	125857	154	93	0.66	0.34	0.51300	1.5	12.91	1.7	0.1826	0.767	0.89	2669	33	2673	16	2676	13	100
U194	43927	74	25	0.98	b.d.	0.24670	2.7	6.274	5.8	0.1845	5.093	0.47	1421	34	2015	52	2693	84	53
U195	82607	74	52	0.65	0.59	0.58410	1.8	18.51	1.9	0.2298	0.7366	0.92	2965	42	3016	19	3051	12	97
U196	114772	357	126	0.39	b.d.	0.32770	2.7	5.689	2.8	0.1259	0.732	0.97	1827	44	1930	25	2042	13	89
U197	103532	130	77	0.55	0.31	0.51210	1.6	12.92	1.8	0.183	0.6264	0.93	2666	36	2674	17	2680	10	99
U198	69051	229	82	0.45	0.17	0.33170	1.5	5.717	2.1	0.125	1.462	0.72	1847	24	1934	18	2029	26	91
U199	59108	401	69	0.15	b.d.	0.16850	2.0	2.47	2.2	0.1063	1.117	0.87	1004	18	1263	16	1737	20	58
U200	71939	211	75	0.61	0.30	0.31020	1.8	5.518	2.0	0.129	0.9238	0.89	1741	28	1903	18	2085	16	84
U206	35970	70	36	0.96	b.d.	0.42400	2.1	8.397	2.3	0.1436	1.088	0.88	2279	40	2275	21	2271	19	100
U207	55686	95	49	0.36	b.d.	0.46980	2.4	10.53	2.5	0.1626	0.6965	0.96	2483	49	2483	23	2483	12	100
U208	50884	98	52	1.13	0.09	0.42120	1.8	8.333	2.0	0.1435	0.8746	0.90	2266	35	2268	19	2270	15	100
U209	81807	280	89	0.43	0.10	0.29600	1.7	5.006	1.8	0.1227	0.6314	0.94	1671	25	1820	16	1996	11	84

Continue...

U210	165279	467	160	0.04	0.07	0.34660	1.6	6.28	1.7	0.1314	0.6023	0.94	1918	27	2016	15	2117	11	91
U211	103721	465	141	1.17	0.57	0.28310	1.6	4.014	1.7	0.1028	0.6605	0.92	1607	23	1637	14	1676	12	96
U212	120429	335	132	0.34	0.03	0.37510	2.0	6.562	2.2	0.1269	0.877	0.91	2053	35	2054	19	2055	15	100
U213	92781	205	81	0.48	0.00	0.35840	1.6	6.78	1.7	0.1372	0.6221	0.93	1975	27	2083	15	2192	11	90
U214	23828	61	36	2.57	b.d.	0.35870	1.7	6.215	1.9	0.1257	0.9989	0.86	1976	29	2007	17	2038	18	97
U215	97791	291	112	0.17	0.11	0.37860	1.9	6.708	2.1	0.1285	0.8204	0.92	2070	34	2074	18	2077	14	100
U216	59208	136	57	0.39	0.08	0.38900	2.1	7.056	2.3	0.1315	0.9543	0.91	2118	37	2119	20	2119	17	100
U217	34100	88	34	0.35	0.55	0.36540	1.8	6.568	1.9	0.1303	0.8315	0.90	2008	30	2055	17	2103	15	95
U218	105822	2463	192	0.01	0.17	0.08457	1.5	0.6739	1.9	0.05779	1.073	0.82	523	8	523	8	522	24	100
U219	90537	258	74	0.52	0.17	0.24950	2.3	4.56	2.7	0.1326	1.422	0.85	1436	29	1742	23	2132	25	67
U220	95459	2250	177	0.01	0.08	0.08510	1.7	0.6789	2.1	0.05786	1.265	0.81	527	9	526	9	524	28	100
U221	127611	734	139	0.24	b.d.	0.18000	2.8	2.677	3.3	0.1079	1.787	0.84	1067	28	1322	25	1764	33	60
U222	26578	64	36	2.19	0.61	0.37280	2.1	6.498	2.4	0.1264	1.212	0.86	2042	36	2046	21	2049	21	100
U223	114170	377	88	0.57	0.01	0.17770	2.3	3.98	2.5	0.1624	1.094	0.90	1055	22	1630	21	2481	18	43
U224	99102	1059	125	0.06	0.82	0.11550	2.2	1.558	2.7	0.09783	1.666	0.79	705	15	954	17	1583	31	45
U225	63889	1494	117	0.02	0.26	0.08421	1.4	0.6708	3.0	0.05777	2.606	0.48	521	7	521	12	521	57	100
U226	139183	481	110	0.38	b.d.	0.20130	2.9	3.518	3.1	0.1267	1.108	0.93	1183	31	1531	25	2053	20	58
U227	75523	177	81	0.67	0.18	0.39860	1.7	7.442	1.9	0.1354	0.8196	0.90	2163	31	2166	17	2169	14	100
U228	42443	268	40	0.25	0.12	0.13490	2.9	2.211	3.6	0.1188	2.085	0.81	816	22	1184	25	1939	37	42
U229	82747	331	100	0.84	0.19	0.24420	2.5	4.168	2.8	0.1238	1.286	0.89	1409	32	1668	23	2011	23	70
U230	34862	72	33	0.51	b.d.	0.40550	1.7	7.678	1.9	0.1373	0.756	0.91	2194	32	2194	17	2194	13	100
U231	31390	93	30	0.26	b.d.	0.30210	1.8	5.255	2.1	0.1262	1.177	0.84	1702	27	1862	18	2045	21	83
U232	32272	72	33	0.27	b.d.	0.43410	1.8	8.979	2.1	0.15	0.9039	0.90	2324	36	2336	19	2346	15	99
U233	35879	847	66	0.01	b.d.	0.08414	1.5	0.678	1.8	0.05844	0.9888	0.83	521	7	526	7	546	22	95
U234	224556	397	181	0.74	0.32	0.37410	1.9	9.031	2.0	0.1751	0.577	0.96	2048	34	2341	19	2607	10	79
U235	30273	69	28	0.40	b.d.	0.38020	1.8	6.764	2.1	0.129	1.011	0.87	2077	32	2081	18	2085	18	100
U236	24205	53	24	0.66	0.73	0.39370	1.7	7.198	1.9	0.1326	0.9458	0.87	2140	31	2136	18	2133	17	100
U237	156603	379	139	0.46	0.15	0.33190	1.6	6.062	1.7	0.1325	0.68	0.92	1847	25	1985	15	2131	12	87
U238	54416	700	56	0.11	0.34	0.07617	3.5	0.8915	5.4	0.08488	4.181	0.64	473	16	647	26	1313	81	36
U239	195976	141	113	1.04	0.00	0.59200	1.6	22	1.8	0.2696	0.8918	0.87	2998	39	3184	18	3303	14	91

Continue...

U240	307975	382	143	0.16	0.51	0.32730	2.1	11.22	2.2	0.2486	0.6486	0.95	1825	33	2542	20	3176	10	57
U241	85334	373	43	0.16	0.14	0.10490	5.9	1.743	6.6	0.1205	2.953	0.89	643	36	1024	43	1963	53	33
U242	87728	2041	158	0.01	0.25	0.08369	1.6	0.6608	2.3	0.05727	1.676	0.69	518	8	515	9	502	37	103
U243	43438	175	48	0.35	0.52	0.25080	1.9	4.111	2.2	0.1189	0.9545	0.90	1443	25	1657	18	1939	17	74
U244	96152	121	88	1.48	0.46	0.52890	1.9	14.39	2.1	0.1973	0.9647	0.89	2737	42	2776	20	2804	16	98
U245	52274	122	54	0.69	0.30	0.39080	1.5	7.129	1.7	0.1323	0.8535	0.87	2126	27	2128	15	2129	15	100
U246	45574	139	42	0.52	0.58	0.27480	2.3	4.479	2.5	0.1182	0.9724	0.92	1565	32	1727	21	1929	17	81
U247	48238	102	48	0.71	1.15	0.41180	1.3	7.825	1.5	0.1378	0.7245	0.88	2223	25	2211	14	2200	13	101
U248	103243	375	97	0.10	0.23	0.25740	1.9	4.285	2.2	0.1207	0.9404	0.90	1477	26	1690	18	1967	17	75
U249	116946	1072	119	0.10	0.71	0.10720	2.6	1.597	3.5	0.1081	2.312	0.75	656	16	969	22	1767	42	37

Notes

Spot size = 25µm; depth of crater ~15µm. $^{206}Pb/^{238}U$ error is the quadratic additions of the within run precision (2 SE) and the external reproducibility (2 SD) of the reference zircon. $^{207}Pb/^{206}Pb$ error propagation (^{207}Pb signal dependent) following Gerdes & Zeh (2009). $^{207}Pb/^{235}U$ error is the quadratic addition of the $^{207}Pb/^{206}Pb$ and $^{206}Pb/^{238}U$ uncertainty.

[a]Within run background-corrected mean ^{207}Pb signal in cps (counts per second).

[b] U and Pb content and Th/U ratio were calculated relative to BB1 reference zircon.

[c] percentage of the common Pb on the ^{206}Pb. b.d. = below dectection limit.

[d] corrected for background, within-run Pb/U fractionation (in case of $^{206}Pb/^{238}U$) and common Pb using Stacy and Kramers (1975) model Pb composition and subsequently normalised to BB1 (ID-TIMS value/measured value); $^{207}Pb/^{235}U$ calculated using $^{207}Pb/^{206}Pb/(^{238}U/^{206}Pb*1/137.88)$

[e] rho is the $^{206}Pb/^{238}U/^{207}Pb/^{235}U$ error correlation coefficient.

[f] degree of concordance = $^{206}Pb/^{238}U$ age / $^{207}Pb/^{206}Pb$ age x 100

U-Pb-Th LA-ICPMS data of detrital zircon grains from sample 07-001

grain	^{207}Pb[a] (cps)	U[b] (ppm)	Pb[b] (ppm)	$\frac{Th}{U}$[b]	^{206}Pbc[c] (%)	$\frac{^{206}Pb}{^{238}U}$[d]	±2σ (%)	$\frac{^{207}Pb}{^{235}U}$[d]	±2σ (%)	$\frac{^{207}Pb}{^{206}Pb}$[d]	±2σ (%)	rho[e]	$\frac{^{206}Pb}{^{238}U}$	±2σ (Ma)	$\frac{^{207}Pb}{^{235}U}$	±2σ (Ma)	$\frac{^{207}Pb}{^{206}Pb}$	±2σ (Ma)	conc.[f] (%)
U289	35312	116	43	0.87	b.d.	0.31310	1.8	4.622	2.0	0.1071	0.8165	0.91	1756	28	1753	17	1750	15	100
U290	104705	880	140	1.72	2.85	0.09972	4.0	1.083	5.8	0.07874	4.187	0.69	613	23	745	31	1166	83	53
U291	17655	57	21	0.70	1.81	0.31660	1.9	4.714	2.1	0.108	1.055	0.87	1773	29	1770	18	1766	19	100
U292	43406	145	54	0.82	0.23	0.31400	2.1	4.652	4.6	0.1074	4.078	0.46	1760	32	1759	39	1756	75	100
U293	74800	264	97	0.86	0.12	0.31330	2.0	4.645	2.1	0.1075	0.7664	0.93	1757	31	1757	18	1758	14	100

Continue...

U294	95169	586	128	1.12	1.73	0.17010	1.7	2.114	3.1	0.09014	2.594	0.56	1012	16	1153	22	1428	50	71
U295	88830	471	113	1.16	0.90	0.18650	1.9	2.499	2.6	0.09715	1.796	0.73	1103	20	1272	19	1570	34	70
U296	21899	78	28	0.71	b.d.	0.31350	1.9	4.643	2.2	0.1074	1.126	0.86	1758	29	1757	18	1756	21	100
U297	76434	372	101	1.18	1.18	0.21670	3.7	2.838	4.5	0.09499	2.516	0.83	1264	42	1366	34	1528	47	83
U298	90203	339	105	0.82	0.14	0.26280	1.7	3.818	1.9	0.1053	0.7397	0.92	1504	23	1596	15	1720	14	87
U299	73259	409	94	1.05	0.48	0.18200	1.6	2.466	1.8	0.09828	0.7352	0.91	1078	16	1262	13	1592	14	68
U306	69268	245	92	1.06	b.d.	0.30610	2.0	4.48	2.2	0.1061	0.8046	0.93	1722	31	1727	18	1734	15	99
U307	20747	65	23	0.77	2.93	0.30990	2.4	4.535	7.2	0.1061	6.755	0.34	1740	37	1737	61	1734	124	100
U308	27094	83	31	0.80	0.50	0.31580	1.8	4.723	2.1	0.1085	1.097	0.85	1769	27	1771	18	1774	20	100
U309	75571	383	83	1.06	1.01	0.16400	2.2	2.237	3.6	0.09892	2.832	0.62	979	20	1193	26	1604	53	61
U310	56315	188	68	0.90	0.71	0.29970	1.8	4.501	2.8	0.1089	2.194	0.63	1690	27	1731	24	1781	40	95
U311	78605	343	122	1.11	0.93	0.29510	1.7	4.277	2.0	0.1051	1.007	0.87	1667	26	1689	17	1716	19	97
U312	22339	75	27	0.70	b.d.	0.31590	1.6	4.727	2.1	0.1085	1.309	0.78	1770	25	1772	18	1775	24	100
U313	37822	130	49	0.90	0.78	0.31540	1.8	4.714	2.0	0.1084	0.8281	0.91	1767	28	1770	17	1773	15	100
U314	23541	80	30	1.01	b.d.	0.31340	1.8	4.649	2.2	0.1076	1.27	0.82	1757	28	1758	19	1759	23	100
U315	67881	228	89	1.18	0.29	0.31260	1.7	4.636	1.9	0.1076	0.8266	0.90	1753	26	1756	16	1758	15	100
U316	100828	482	119	1.24	0.89	0.18280	2.2	2.466	2.9	0.09782	1.804	0.78	1082	22	1262	21	1583	34	68
U317	34725	137	44	0.81	0.40	0.27850	1.7	3.949	4.2	0.1028	3.862	0.39	1584	23	1624	35	1676	71	95
U318	28538	95	35	0.80	1.64	0.32080	1.9	4.85	2.2	0.1097	0.9363	0.90	1793	31	1794	18	1794	17	100
U319	25648	86	32	0.82	b.d.	0.32220	1.9	4.895	2.2	0.1102	1.139	0.86	1800	30	1801	19	1802	21	100
U320	54284	236	80	0.87	0.76	0.29060	2.0	4.152	2.2	0.1036	0.8998	0.91	1645	29	1665	18	1690	17	97
U321	50321	160	63	1.39	0.35	0.30940	1.9	4.611	2.2	0.1081	1.038	0.88	1738	29	1751	18	1767	19	98
U322	64210	210	78	0.98	0.28	0.30920	1.8	4.497	2.0	0.1055	0.7329	0.93	1737	28	1730	17	1723	13	101
U323	84354	350	75	1.04	0.85	0.15490	6.6	2.165	6.9	0.1014	2.021	0.96	928	57	1170	49	1649	37	56
U324	25974	83	31	0.85	0.56	0.31470	1.8	4.671	2.0	0.1077	0.9223	0.89	1764	27	1762	17	1760	17	100
U325	150679	667	174	1.26	1.27	0.20110	2.2	3.35	2.9	0.1208	1.887	0.76	1181	24	1493	23	1968	34	60
U326	19937	67	24	0.80	1.26	0.30310	1.7	4.596	2.0	0.11	1.027	0.86	1706	26	1749	17	1799	19	95
U327	63343	218	66	0.70	0.42	0.25400	2.4	3.863	2.8	0.1103	1.386	0.86	1459	31	1606	22	1804	25	81
U328	43736	142	52	0.71	0.27	0.31820	1.6	4.777	2.0	0.1089	1.174	0.81	1781	25	1781	17	1781	21	100
U329	20387	67	24	0.76	1.18	0.31820	1.9	4.777	2.2	0.1089	1.116	0.87	1781	30	1781	19	1781	20	100

Continue...

U330	105933	660	141	1.11	2.16	0.16520	1.7	2.022	3.3	0.08877	2.833	0.51	986	15	1123	23	1399	54	70
U331	79065	537	115	1.11	0.94	0.17050	1.6	2.157	3.1	0.09175	2.604	0.53	1015	15	1167	21	1462	49	69
U332	50865	169	65	1.17	0.92	0.31240	2.0	4.614	2.2	0.1071	0.9809	0.90	1753	31	1752	19	1751	18	100
U333	19099	64	23	0.67	0.60	0.31570	2.1	4.676	2.5	0.1074	1.287	0.86	1769	33	1763	21	1756	24	101
U334	98413	603	149	2.66	1.54	0.16400	2.4	1.867	3.8	0.08257	2.9	0.64	979	22	1070	25	1259	57	78
U335	93878	517	134	1.21	1.78	0.20770	1.8	2.633	3.6	0.09194	3.177	0.48	1217	19	1310	27	1466	60	83
U336	30956	107	38	0.82	0.45	0.30880	1.6	4.488	2.0	0.1054	1.163	0.80	1735	24	1729	16	1722	21	101
U337	91429	646	139	1.16	0.81	0.17140	2.2	2.142	3.0	0.09065	2.106	0.72	1020	20	1163	21	1439	40	71
U338	88917	436	111	1.12	0.68	0.19890	1.8	2.678	2.7	0.09765	2.023	0.66	1170	19	1323	20	1580	38	74
U339	93518	524	130	0.82	1.01	0.21410	1.8	2.747	2.9	0.09308	2.324	0.61	1250	21	1341	22	1490	44	84
U340	83937	651	147	1.17	0.88	0.18500	2.1	2.158	3.5	0.08461	2.757	0.61	1094	22	1168	25	1307	54	84
U341	101316	713	145	1.16	1.41	0.15710	2.1	1.918	3.0	0.08852	2.075	0.72	941	19	1087	20	1394	40	68
U342	92377	579	134	1.12	2.36	0.18410	2.3	2.168	4.4	0.0854	3.741	0.53	1089	23	1171	31	1325	72	82
U343	94573	450	162	1.11	1.10	0.30620	1.7	4.459	2.1	0.1056	1.182	0.82	1722	25	1723	17	1725	22	100
U345	100602	711	146	1.26	2.05	0.15560	1.6	1.845	3.4	0.086	2.975	0.47	932	14	1062	22	1338	58	70
U346	23993	73	28	0.75	1.13	0.32270	2.4	4.922	3.6	0.1106	2.652	0.68	1803	39	1806	31	1809	48	100
U347	97905	696	148	1.21	2.84	0.16590	2.1	1.853	4.6	0.08102	4.056	0.45	989	19	1064	30	1222	80	81
U348	105642	800	149	1.12	4.32	0.14110	1.8	1.465	5.1	0.0753	4.765	0.35	851	14	916	31	1076	96	79
U349	69094	254	98	1.12	0.60	0.31340	2.2	4.666	2.3	0.108	0.7464	0.95	1757	34	1761	20	1766	14	100
U350	88092	351	129	1.15	0.39	0.30170	2.7	4.383	3.0	0.1054	1.208	0.91	1700	41	1709	25	1721	22	99
U356	73367	250	91	0.94	0.69	0.30400	1.6	4.467	1.9	0.1066	0.9797	0.85	1711	24	1725	16	1742	18	98
U357	27902	91	34	0.88	0.23	0.31710	1.9	4.765	2.1	0.109	0.897	0.90	1776	30	1779	18	1782	16	100
U358	29355	102	37	0.83	0.85	0.31200	1.7	4.598	2.0	0.1069	1.055	0.85	1751	26	1749	17	1747	19	100
U359	80575	354	102	0.88	0.46	0.24260	1.7	3.466	1.9	0.1036	0.7625	0.92	1400	22	1519	15	1689	14	83
U360	84001	565	124	0.97	0.48	0.18260	1.9	2.43	2.1	0.09655	0.9522	0.89	1081	19	1252	15	1558	18	69
U361	65695	185	73	1.34	0.48	0.31050	2.4	4.559	2.6	0.1065	0.9218	0.93	1743	37	1742	22	1740	17	100
U362	61466	200	75	0.85	0.36	0.31790	1.7	4.785	2.0	0.1092	1.051	0.85	1779	27	1782	17	1785	19	100
U363	32556	108	40	0.89	0.30	0.31230	1.9	4.602	2.2	0.1069	1.055	0.87	1752	29	1750	18	1747	19	100
U364	20391	65	24	0.77	1.14	0.31410	1.8	4.662	2.2	0.1076	1.285	0.81	1761	27	1760	18	1760	23	100
U365	17888	65	23	0.63	1.56	0.31720	2.4	4.757	2.9	0.1088	1.647	0.83	1776	38	1777	25	1779	30	100

Continue...

U366	50419	174	64	0.84	b.d.	0.31460	2.2	4.668	2.5	0.1076	1.18	0.88	1763	34	1762	21	1760	22	100
U367	94548	508	109	0.68	0.99	0.18290	1.8	2.427	3.1	0.09624	2.477	0.60	1083	18	1251	22	1553	47	70
U368	27758	93	34	0.79	b.d.	0.31500	1.9	4.689	2.2	0.1079	1.189	0.85	1765	29	1765	19	1765	22	100
U369	91474	418	107	1.05	3.22	0.19460	4.0	2.614	5.9	0.09743	4.302	0.68	1146	42	1305	44	1576	81	73
U370	36962	123	47	1.04	0.15	0.31440	1.9	4.684	2.1	0.1081	0.7647	0.93	1762	30	1764	17	1767	14	100
U371	87227	330	99	1.05	0.45	0.23300	4.5	3.363	4.8	0.1047	1.794	0.93	1350	55	1496	38	1709	33	79
U372	83790	370	92	1.20	0.77	0.18390	2.4	2.49	3.1	0.09819	1.993	0.76	1088	24	1269	23	1590	37	68
U373	50093	167	62	0.84	0.08	0.31270	1.6	4.617	1.9	0.1071	1.058	0.84	1754	25	1752	16	1750	19	100
U374	28566	99	36	0.87	0.44	0.31270	1.7	4.629	2.2	0.1074	1.289	0.80	1754	27	1755	18	1755	24	100
U375	40946	147	56	0.96	1.05	0.31460	1.8	4.681	2.3	0.1079	1.393	0.80	1763	28	1764	19	1765	25	100
U376	84023	595	127	0.72	0.70	0.18410	2.2	2.286	2.9	0.09006	1.912	0.76	1089	22	1208	21	1427	37	76
U377	91838	332	122	1.09	0.20	0.29660	2.0	4.363	2.1	0.1067	0.7987	0.93	1674	29	1705	18	1744	15	96
U378	27984	95	36	0.91	b.d.	0.31290	1.7	4.619	2.0	0.107	1.017	0.86	1755	27	1753	17	1750	19	100
U379	87012	344	126	1.16	0.18	0.29860	1.8	4.356	1.9	0.1058	0.7892	0.91	1684	26	1704	16	1728	14	97
U380	64506	315	92	1.18	0.98	0.23120	1.8	3.289	2.1	0.1032	0.9176	0.90	1341	22	1478	16	1682	17	80
U381	84331	568	112	0.91	1.42	0.16060	2.1	1.992	3.6	0.08994	2.852	0.60	960	19	1113	24	1424	54	67
U382	99922	624	121	1.20	2.07	0.13900	3.0	1.721	4.5	0.08977	3.35	0.66	839	23	1016	29	1421	64	59
U383	69250	236	86	0.92	0.21	0.30470	1.6	4.55	1.8	0.1083	0.8294	0.89	1715	25	1740	15	1771	15	97
U384	95645	358	136	1.05	0.27	0.31260	1.8	4.604	2.0	0.1068	0.9776	0.88	1754	27	1750	17	1746	18	100
U385	58204	163	67	1.18	2.42	0.31530	1.9	4.693	4.0	0.108	3.559	0.47	1767	29	1766	34	1765	65	100
U386	87323	308	114	1.04	0.07	0.29750	2.0	4.446	2.2	0.1084	0.766	0.93	1679	30	1721	18	1773	14	95
U387	55323	190	69	0.76	0.56	0.31630	2.5	4.709	2.7	0.108	1.116	0.91	1772	38	1769	23	1766	20	100
U388	29296	95	35	0.88	0.62	0.31280	1.8	4.681	2.2	0.1085	1.212	0.83	1754	28	1764	18	1775	22	99
U389	91040	378	125	1.02	0.20	0.26700	1.7	3.826	2.1	0.1039	1.197	0.81	1525	23	1598	17	1696	22	90
U390	43516	142	52	0.69	0.63	0.31970	1.9	4.809	2.1	0.1091	1.044	0.87	1788	29	1787	18	1785	19	100
U391	81610	459	118	0.95	0.39	0.21500	1.7	2.961	1.9	0.09988	0.8514	0.89	1255	19	1398	14	1622	16	77
U392	38407	139	45	1.17	0.40	0.25680	2.3	3.776	2.5	0.1066	0.979	0.92	1474	30	1588	20	1743	18	85
U393	24271	86	31	0.79	0.45	0.31450	2.1	4.681	2.5	0.108	1.432	0.82	1763	32	1764	21	1765	26	100
U394	17777	60	22	0.70	3.35	0.32210	2.2	4.896	2.5	0.1103	1.298	0.86	1800	34	1802	22	1804	24	100
U396	82113	297	101	1.03	0.08	0.27230	1.7	4.011	1.9	0.1068	0.7419	0.92	1552	24	1636	15	1746	14	89

Continue...

U397	24582	83	30	0.80	b.d.	0.31310	1.6	4.643	2.0	0.1076	1.085	0.83	1756	25	1757	16	1758	20	100
U398	81885	463	109	1.09	1.97	0.18310	1.6	2.368	3.5	0.09379	3.114	0.46	1084	16	1233	25	1504	59	72
U399	35606	116	43	0.81	1.13	0.31540	2.2	4.716	2.7	0.1084	1.462	0.84	1767	34	1770	23	1773	27	100
U400	27625	95	35	0.84	0.61	0.31470	1.7	4.69	2.1	0.1081	1.251	0.80	1764	26	1765	18	1768	23	100
U406	55102	186	72	1.02	0.76	0.31620	1.6	4.711	1.8	0.1081	0.8857	0.87	1771	24	1769	15	1767	16	100

Notes

Spot size = 25µm; depth of crater ~15µm. $^{206}Pb/^{238}U$ error is the quadratic additions of the within run precision (2 SE) and the external reproducibility (2 SD) of the reference zircon. $^{207}Pb/^{206}Pb$ error propagation (^{207}Pb signal dependent) following Gerdes & Zeh (2009). $^{207}Pb/^{235}U$ error is the quadratic addition of the $^{207}Pb/^{206}Pb$ and $^{206}Pb/^{238}U$ uncertainty.

[a]Within run background-corrected mean ^{207}Pb signal in cps (counts per second).

[b] U and Pb content and Th/U ratio were calculated relative to BB1 reference zircon.

[c] percentage of the common Pb on the ^{206}Pb. b.d. = below dectection limit.

[d] corrected for background, within-run Pb/U fractionation (in case of $^{206}Pb/^{238}U$) and common Pb using Stacy and Kramers (1975) model Pb composition and subsequently normalised to BB1 (ID-TIMS value/measured value); $^{207}Pb/^{235}U$ calculated using $^{207}Pb/^{206}Pb/(^{238}U/^{206}Pb*1/137.88)$

[e] rho is the $^{206}Pb/^{238}U/^{207}Pb/^{235}U$ error correlation coefficient.

[f] degree of concordance = $^{206}Pb/^{238}U$ age / $^{207}Pb/^{206}Pb$ age x 100

U-Pb-Th LA-ICPMS data of detrital zircon grains from sample 08-001

grain	^{207}Pb[a] (cps)	U[b] (ppm)	Pb[b] (ppm)	Th[b] / U	^{206}Pbc[c] (%)	^{206}Pb[d] / ^{238}U	±2σ (%)	^{207}Pb[d] / ^{235}U	±2σ (%)	^{207}Pb[d] / ^{206}Pb	±2σ (%)	rho[e]	^{206}Pb / ^{238}U	±2σ (Ma)	^{207}Pb / ^{235}U	±2σ (Ma)	^{207}Pb / ^{206}Pb	±2σ (Ma)	conc.[f] (%)
U07	179944	1437	198	0.41	2.22	0.12530	2.0	1.578	3.2	0.09132	2.473	0.62	761	14	961	20	1453	47	52
U08	247679	453	204	0.75	0.75	0.38480	1.8	9.267	2.0	0.1747	0.8128	0.91	2099	32	2365	18	2603	14	81
U09	214775	1344	210	0.73	2.33	0.12280	10.4	1.822	11.5	0.1077	4.816	0.91	746	74	1053	78	1760	88	42
U10	174512	1317	190	0.38	1.47	0.12870	1.6	1.766	3.9	0.0995	3.55	0.41	781	12	1033	26	1615	66	48
U11	196855	1206	204	0.50	1.06	0.14500	2.5	2.217	2.9	0.1109	1.476	0.86	873	21	1187	21	1815	27	48
U12	240550	1177	258	0.42	2.04	0.19310	2.0	3.283	2.7	0.1233	1.803	0.74	1138	21	1477	21	2005	32	57
U13	158345	1160	206	0.42	1.23	0.16170	1.8	2.191	2.6	0.09829	1.846	0.70	966	16	1178	18	1592	34	61
U14	183310	1594	192	0.32	7.93	0.10140	2.0	1.185	6.7	0.08476	6.449	0.29	623	12	794	38	1310	125	48
U15	214299	990	174	0.38	1.19	0.15580	2.4	2.766	3.1	0.1288	1.977	0.77	933	21	1346	23	2081	35	45
U16	215439	1135	216	0.72	1.01	0.14940	2.7	2.48	3.1	0.1204	1.522	0.87	898	22	1266	22	1962	27	46

Continue...

U17	220346	1207	214	0.31	2.10	0.15550	2.3	2.532	3.1	0.1181	2.071	0.75	932	20	1281	23	1928	37	48
U18	180281	1319	211	0.28	0.91	0.14970	2.9	2.123	3.3	0.1029	1.632	0.87	899	24	1156	23	1676	30	54
U19	249677	983	279	0.31	1.71	0.25980	2.7	5.045	4.5	0.1408	3.636	0.59	1489	35	1827	39	2237	63	67
U20	198124	251	151	0.51	b.d.	0.52180	1.9	13.49	2.1	0.1875	0.6961	0.94	2707	43	2715	20	2721	11	99
U21	181334	1050	211	0.36	0.55	0.18580	1.9	2.822	2.4	0.1101	1.414	0.81	1099	20	1361	18	1802	26	61
U22	272356	421	268	1.62	0.54	0.44920	2.0	11.4	2.1	0.184	0.5577	0.96	2392	41	2556	20	2689	9	89
U23	197618	1086	236	0.52	0.75	0.19300	1.5	3.167	2.7	0.119	2.22	0.57	1137	16	1449	21	1942	40	59
U24	193866	1158	206	0.37	0.93	0.16010	5.4	2.525	6.6	0.1144	3.879	0.81	957	48	1279	49	1871	70	51
U25	187052	412	174	1.48	0.50	0.30690	1.7	7.077	1.9	0.1673	0.8202	0.90	1725	26	2121	17	2530	14	68
U26	146798	1470	187	0.47	1.71	0.11400	4.2	1.304	5.6	0.08293	3.753	0.75	696	28	847	33	1267	73	55
U27	243290	402	237	0.69	0.33	0.50320	1.8	12.36	2.1	0.1781	1.179	0.83	2627	38	2632	20	2635	20	100
U28	177497	431	153	0.74	0.99	0.27560	2.0	6.13	2.6	0.1613	1.586	0.79	1569	28	1995	23	2469	27	64
U29	185687	1254	219	0.51	1.50	0.15340	1.8	2.191	2.6	0.1036	1.856	0.70	920	16	1178	18	1689	34	54
U30	190476	560	195	0.54	1.80	0.28340	3.3	6.158	4.1	0.1576	2.422	0.80	1609	46	1999	36	2430	41	66
U37	228319	1765	281	0.23	2.12	0.14770	1.7	2.143	3.3	0.1053	2.852	0.51	888	14	1163	23	1719	52	52
U38	176388	1328	212	0.34	0.57	0.14880	2.3	2.067	2.8	0.1007	1.54	0.83	894	19	1138	19	1638	29	55
U39	206667	1367	234	0.77	2.33	0.15300	2.7	2.131	4.3	0.101	3.322	0.63	918	23	1159	30	1643	62	56
U40	171350	781	143	0.42	2.60	0.15750	1.8	2.676	2.9	0.1232	2.368	0.59	943	15	1322	22	2003	42	47
U41	204055	972	221	0.42	2.01	0.20030	4.3	3.51	5.8	0.1271	3.841	0.75	1177	47	1530	47	2058	68	57
U42	291438	1022	213	0.33	16.43	0.13610	2.9	2.301	8.0	0.1226	7.458	0.36	823	23	1213	58	1995	133	41
U43	204550	897	192	0.61	0.82	0.18200	3.2	3.3	3.6	0.1315	1.659	0.89	1078	32	1481	29	2118	29	51
U44	155506	639	161	0.49	1.62	0.22060	1.9	4.124	2.6	0.1356	1.689	0.75	1285	22	1659	21	2172	29	59
U45	253614	1485	282	0.69	1.15	0.16120	1.6	2.55	2.1	0.1148	1.388	0.76	963	14	1286	16	1876	25	51
U46	277433	1043	227	0.55	6.63	0.16450	2.7	2.999	4.8	0.1322	3.94	0.57	982	25	1407	37	2128	69	46
U47	153609	1645	253	1.17	2.12	0.12360	2.4	1.335	3.7	0.07831	2.717	0.67	751	17	861	21	1155	54	65
U48	146942	1191	164	0.22	1.58	0.13560	1.7	1.668	3.1	0.08918	2.558	0.56	820	13	996	20	1408	49	58
U49	153236	1233	213	0.44	1.04	0.15880	2.0	2.113	3.2	0.09653	2.506	0.62	950	17	1153	22	1558	47	61
U50	182293	989	211	0.32	1.71	0.19420	2.5	3.106	3.5	0.116	2.44	0.71	1144	26	1434	27	1895	44	60
U51	201410	1140	230	0.52	1.18	0.18110	2.0	2.862	2.7	0.1146	1.726	0.76	1073	20	1372	20	1874	31	57
U52	82642	627	138	1.17	0.47	0.17380	1.9	2.16	2.7	0.09015	1.859	0.72	1033	19	1168	19	1429	35	72

Continue...

U53	21501	80	29	0.70	0.39	0.31380	1.7	4.664	1.9	0.1078	0.8267	0.90	1759	26	1761	16	1763	15	100
U54	109704	254	70	0.49	2.68	0.21300	2.7	4.797	3.3	0.1633	2.023	0.80	1245	30	1784	29	2490	34	50
U55	204680	672	154	0.46	0.28	0.19360	1.9	4.074	2.5	0.1526	1.568	0.77	1141	20	1649	20	2376	27	48
U56	127705	438	103	2.41	5.27	0.17770	4.1	3.185	5.4	0.13	3.598	0.75	1054	40	1454	43	2098	63	50
U57	171826	1260	173	0.37	0.54	0.12280	3.2	1.701	4.1	0.1005	2.582	0.77	747	22	1009	26	1632	48	46
U58	263661	1009	208	0.55	1.31	0.17050	2.8	3.226	3.2	0.1373	1.614	0.86	1015	26	1463	25	2193	28	46
U59	186648	697	159	0.50	2.08	0.18960	4.8	3.606	5.3	0.138	2.183	0.91	1119	50	1551	43	2202	38	51
U60	163047	1610	208	0.38	1.03	0.12000	2.3	1.459	3.1	0.08819	2.036	0.75	730	16	914	19	1387	39	53
U67	139436	859	143	0.57	0.72	0.15280	2.3	2.334	2.9	0.1108	1.7	0.81	916	20	1223	21	1813	31	51
U68	197919	821	178	0.64	0.75	0.19850	2.0	3.663	2.5	0.1339	1.504	0.79	1167	21	1563	20	2149	26	54
U69	170344	1602	204	0.27	7.26	0.11260	2.6	1.232	7.3	0.0793	6.824	0.35	688	17	815	42	1180	135	58
U70	177115	1044	182	0.53	0.51	0.15360	2.3	2.497	2.8	0.1179	1.609	0.81	921	19	1271	20	1924	29	48
U71	262994	672	228	0.47	0.29	0.30520	1.7	6.678	1.9	0.1587	0.8812	0.88	1717	25	2070	17	2442	15	70
U72	249985	1576	275	0.50	0.66	0.16130	3.3	2.578	3.8	0.1159	1.75	0.88	964	30	1294	28	1894	31	51
U73	226138	1341	303	0.37	1.10	0.20800	1.6	3.375	3.5	0.1177	3.126	0.46	1218	18	1499	28	1921	56	63
U74	125460	421	130	0.99	0.69	0.27920	2.9	4.672	3.4	0.1214	1.877	0.84	1587	40	1762	29	1976	33	80

Notes

Spot size = 25µm; depth of crater ~15µm. $^{206}Pb/^{238}U$ error is the quadratic additions of the within run precision (2 SE) and the external reproducibility (2 SD) of the reference zircon. $^{207}Pb/^{206}Pb$ error propagation (^{207}Pb signal dependent) following Gerdes & Zeh (2009). $^{207}Pb/^{235}U$ error is the quadratic addition of the $^{207}Pb/^{206}Pb$ and $^{206}Pb/^{238}U$ uncertainty.

[a]Within run background-corrected mean ^{207}Pb signal in cps (counts per second).

[b] U and Pb content and Th/U ratio were calculated relative to BB1 reference zircon.

[c] percentage of the common Pb on the ^{206}Pb. b.d. = below dectection limit.

[d] corrected for background, within-run Pb/U fractionation (in case of $^{206}Pb/^{238}U$) and common Pb using Stacy and Kramers (1975) model Pb composition and subsequently normalised to BB1 (ID-TIMS value/measured value); $^{207}Pb/^{235}U$ calculated using $^{207}Pb/^{206}Pb/(^{238}U/^{206}Pb*1/137.88)$

[e] rho is the $^{206}Pb/^{238}U/^{207}Pb/^{235}U$ error correlation coefficient.

[f] degree of concordance = $^{206}Pb/^{238}U$ age / $^{207}Pb/^{206}Pb$ age x 100

U-Pb-Th LA-ICPMS data of detrital zircon grains from sample 08-002

grain	^{207}Pb[a]	U[b]	Pb[b]	Th[b]	^{206}Pbc[c]	^{206}Pb[d]	±2σ	^{207}Pb[d]	±2σ	^{207}Pb[d]	±2σ	rho[e]	^{206}Pb	±2σ	^{207}Pb	±2σ	^{207}Pb	±2σ	conc.[f]
	(cps)	(ppm)	(ppm)	U	(%)	^{238}U	(%)	^{235}U	(%)	^{206}Pb	(%)		^{238}U	(Ma)	^{235}U	(Ma)	^{206}Pb	(Ma)	(%)
U75	384952	479	206	0.03	0.11	0.40530	2.0	11.89	2.2	0.2127	0.7423	0.94	2193	38	2596	20	2926	12	75
U76	114470	2701	207	0.08	1.26	0.08110	1.5	0.6416	2.7	0.05738	2.183	0.57	503	7	503	11	506	48	99
U77	141973	346	83	0.19	1.04	0.21670	2.0	5.036	2.6	0.1686	1.674	0.77	1264	23	1825	23	2543	28	50
U78	95207	203	77	0.47	1.02	0.32670	1.8	7.768	2.8	0.1724	2.064	0.67	1822	29	2204	25	2581	34	71
U79	222925	610	124	0.30	1.24	0.17180	2.2	3.936	2.7	0.1662	1.516	0.83	1022	21	1621	22	2520	25	41
U80	82720	365	104	0.79	0.43	0.23500	2.1	3.385	2.2	0.1045	0.633	0.96	1360	26	1501	17	1706	12	80
U81	139810	575	177	0.93	0.44	0.25520	1.8	3.694	1.9	0.105	0.7423	0.92	1465	24	1570	16	1714	14	85
U82	271393	1764	227	0.04	6.40	0.11090	2.0	1.397	5.1	0.09132	4.62	0.40	678	13	888	30	1453	88	47
U83	250401	421	185	0.45	0.16	0.37590	1.8	9.877	1.9	0.1906	0.7148	0.93	2057	32	2423	18	2747	12	75
U84	87044	174	65	0.42	1.25	0.32490	2.2	7.484	2.8	0.1671	1.767	0.78	1814	35	2171	25	2528	30	72
U85	220191	621	187	0.31	1.75	0.26930	2.0	5.984	2.6	0.1612	1.653	0.77	1537	27	1973	23	2468	28	62
U86	8349	192	15	0.00	1.14	0.08207	2.5	0.6477	3.0	0.05724	1.593	0.84	508	12	507	12	501	35	102
U87	240151	418	93	0.45	0.25	0.17180	6.0	4.607	6.1	0.1945	1.133	0.98	1022	57	1750	52	2781	19	37
U88	70861	163	60	0.11	1.17	0.35340	2.7	8.102	3.1	0.1663	1.603	0.86	1951	45	2242	29	2521	27	77
U89	139311	272	52	0.42	0.78	0.13570	5.5	3.376	6.2	0.1805	2.828	0.89	820	43	1499	50	2658	47	31
U90	163484	480	182	0.32	1.05	0.33990	3.1	7.773	4.4	0.1659	3.153	0.70	1886	51	2205	41	2516	53	75
U91	402946	454	290	0.59	0.04	0.53760	1.7	15.18	1.8	0.2048	0.6319	0.93	2773	38	2827	17	2865	10	97
U92	88594	307	111	1.18	0.40	0.30090	1.4	4.459	2.0	0.1075	1.342	0.73	1696	21	1723	16	1757	25	97
U93	223585	827	198	0.29	1.31	0.21430	1.7	4.424	2.2	0.1497	1.379	0.78	1252	19	1717	18	2343	24	53
U94	127388	1853	145	0.02	2.50	0.07785	2.3	0.7422	4.2	0.06914	3.498	0.54	483	11	564	18	903	72	54

Notes

Spot size = 25µm; depth of crater ~15µm. $^{206}Pb/^{238}U$ error is the quadratic additions of the within run precision (2 SE) and the external reproducibility (2 SD) of the reference zircon. $^{207}Pb/^{206}Pb$ error propagation (^{207}Pb signal dependent) following Gerdes & Zeh (2009). $^{207}Pb/^{235}U$ error is the quadratic addition of the $^{207}Pb/^{206}Pb$ and $^{206}Pb/^{238}U$ uncertainty.

[a]Within run background-corrected mean ^{207}Pb signal in cps (counts per second).

[b] U and Pb content and Th/U ratio were calculated relative to BB1 reference zircon.

[c] percentage of the common Pb on the ^{206}Pb. b.d. = below dectection limit.

[d] corrected for background, within-run Pb/U fractionation (in case of $^{206}Pb/^{238}U$) and common Pb using Stacy and Kramers (1975) model Pb composition and subsequently normalised to BB1 (ID-TIMS value/measured value); $^{207}Pb/^{235}U$ calculated using $^{207}Pb/^{206}Pb/(^{238}U/^{206}Pb*1/137.88)$

[e] rho is the $^{206}Pb/^{238}U/^{207}Pb/^{235}U$ error correlation coefficient.

[f] degree of concordance = $^{206}Pb/^{238}U$ age / $^{207}Pb/^{206}Pb$ age x 100

U-Pb-Th LA-ICPMS data of detrital zircon grains from sample 10-001

grain	^{207}Pb[a]	U[b]	Pb[b]	Th[b]	^{206}Pbc[c]	^{206}Pb[d]	±2σ	^{207}Pb[d]	±2σ	^{207}Pb[d]	±2σ	rho[e]	^{206}Pb	±2σ	^{207}Pb	±2σ	^{207}Pb	±2σ	conc.[f]
	(cps)	(ppm)	(ppm)	U	(%)	^{238}U	(%)	^{235}U	(%)	^{206}Pb	(%)		^{238}U	(Ma)	^{235}U	(Ma)	^{206}Pb	(Ma)	(%)
U07	175806	217	121	0.29	0.13	0.51110	1.5	13.44	1.6	0.1907	0.6307	0.92	2661	32	2711	15	2749	10	97
U08	59830	542	90	1.15	2.83	0.12640	1.6	1.371	4.8	0.07867	4.504	0.34	767	12	877	28	1164	89	66
U09	136277	242	108	1.16	0.38	0.35250	1.7	8.225	2.3	0.1692	1.531	0.73	1947	28	2256	21	2550	26	76
U10	79041	409	96	1.80	1.62	0.19060	2.1	2.719	3.3	0.1035	2.593	0.62	1125	21	1334	25	1687	48	67
U100	82387	262	105	0.77	0.27	0.36880	2.4	6.299	2.5	0.1239	0.7091	0.96	2024	41	2018	22	2013	13	101
U107	14635	21	10	0.63	0.50	0.36630	3.7	9.504	4.0	0.1882	1.476	0.93	2012	64	2388	37	2726	24	74
U108	114138	131	87	1.22	0.74	0.53410	1.7	14.16	2.2	0.1923	1.381	0.78	2759	38	2761	21	2762	23	100
U109	150265	160	105	0.97	0.10	0.54560	1.7	14.81	1.8	0.1969	0.6277	0.94	2807	38	2803	17	2801	10	100
U11	116043	502	137	0.94	1.40	0.22170	2.1	3.874	2.7	0.1267	1.641	0.79	1291	25	1608	22	2053	29	63
U110	196117	271	157	1.42	0.50	0.42220	1.7	10.6	1.7	0.1822	0.4472	0.97	2270	32	2489	16	2673	7	85
U111	174106	216	122	0.34	0.32	0.51480	1.5	13.02	1.8	0.1835	0.9541	0.85	2677	34	2681	17	2684	16	100
U112	78963	301	91	1.56	0.95	0.19610	3.6	3.242	3.7	0.1199	0.8985	0.97	1154	38	1467	29	1955	16	59
U12	12986	41	16	0.88	0.46	0.32580	2.5	4.964	2.8	0.1105	1.353	0.88	1818	39	1813	24	1808	25	101
U13	64586	404	79	1.17	2.37	0.14320	1.6	1.875	4.2	0.09492	3.845	0.38	863	13	1072	28	1527	72	57
U14	76307	243	76	1.00	0.67	0.26150	1.7	4.482	2.5	0.1243	1.867	0.67	1497	23	1728	21	2019	33	74
U15	165173	287	129	1.13	0.30	0.35380	1.8	8.216	2.2	0.1685	1.185	0.84	1952	31	2255	20	2542	20	77
U16	68443	676	80	0.52	4.14	0.09532	2.9	0.9669	6.2	0.07357	5.543	0.46	587	16	687	32	1030	112	57
U17	77745	540	128	0.52	1.39	0.21950	1.9	2.87	4.2	0.09485	3.799	0.45	1279	22	1374	32	1525	72	84
U18	80163	473	81	0.51	3.84	0.14490	1.7	2.132	4.5	0.1067	4.18	0.37	873	14	1159	32	1743	77	50
U19	87260	205	100	1.26	0.08	0.38540	2.0	6.985	2.3	0.1315	1.089	0.88	2101	36	2110	20	2117	19	99
U20	150053	307	122	1.64	0.59	0.28530	2.7	6.631	3.1	0.1686	1.533	0.87	1618	39	2064	28	2544	26	64
U21	58696	138	81	2.99	0.13	0.37180	1.7	6.457	2.1	0.126	1.139	0.84	2038	30	2040	18	2042	20	100

Continue...

U22	7520	26	11	1.42	0.54	0.31040	1.5	4.557	2.1	0.1065	1.495	0.70	1743	23	1741	18	1740	27	100
U23	193658	297	143	0.20	0.16	0.45320	1.4	10.31	1.5	0.165	0.5588	0.93	2410	28	2463	14	2507	9	96
U24	67902	137	63	1.02	b.d.	0.40790	1.4	8.109	1.6	0.1442	0.7859	0.88	2205	27	2243	15	2278	14	97
U25	118320	474	102	0.94	1.43	0.16770	1.8	3.321	2.1	0.1436	1.106	0.85	999	17	1486	17	2271	19	44
U26	190541	114	91	1.82	0.29	0.63270	1.9	23.63	2.0	0.2709	0.6715	0.94	3160	47	3253	19	3311	11	95
U27	28899	98	36	0.81	0.57	0.31590	1.6	4.711	1.8	0.1081	0.915	0.87	1770	25	1769	15	1768	17	100
U28	121558	122	87	1.01	0.28	0.56010	1.6	15.89	1.7	0.2058	0.605	0.93	2867	37	2870	16	2872	10	100
U29	52006	118	53	0.66	0.03	0.39070	1.9	7.104	2.1	0.1319	0.7134	0.94	2126	35	2124	18	2123	12	100
U30	175589	173	126	0.95	0.77	0.59580	2.3	19.14	2.5	0.233	1.039	0.91	3013	55	3049	24	3073	17	98
U37	107111	109	88	1.90	0.25	0.54740	1.6	14.98	1.8	0.1985	0.8353	0.89	2814	38	2814	18	2814	14	100
U38	177598	327	130	1.19	0.82	0.31510	1.7	8.553	2.0	0.1968	0.9766	0.87	1766	27	2292	18	2800	16	63
U39	142362	457	111	0.60	0.16	0.20780	2.3	4.325	2.9	0.151	1.752	0.80	1217	26	1698	24	2357	30	52
U40	62621	67	48	1.17	0.10	0.54540	1.4	14.76	1.6	0.1963	0.7262	0.89	2806	33	2800	15	2796	12	100
U41	85383	276	78	1.04	0.59	0.21150	2.2	4.023	2.4	0.138	1.003	0.91	1237	25	1639	20	2202	17	56
U42	222310	303	189	0.78	b.d.	0.53620	1.8	14.35	2.1	0.1941	1.126	0.85	2768	41	2773	20	2778	18	100
U43	65835	134	56	0.57	0.66	0.38630	2.7	7.072	2.8	0.1328	0.7622	0.96	2106	49	2121	25	2135	13	99
U44	278826	219	133	0.56	0.18	0.51790	1.6	18.91	1.8	0.2649	0.6376	0.93	2690	36	3037	17	3276	10	82
U45	159882	113	94	0.86	b.d.	0.64540	1.7	22.54	1.9	0.2533	0.8421	0.90	3210	43	3207	19	3206	13	100
U46	44569	84	41	0.56	0.84	0.42220	1.8	8.45	2.0	0.1452	0.8506	0.91	2270	35	2281	19	2290	15	99
U47	137542	174	107	0.74	0.10	0.51390	1.3	12.91	1.4	0.1822	0.4915	0.94	2673	29	2673	14	2673	8	100
U48	37538	80	38	0.71	0.36	0.41190	1.5	7.759	1.8	0.1366	1.003	0.83	2224	28	2204	16	2185	17	102
U49	97048	194	96	0.89	0.86	0.41730	1.7	8.151	2.2	0.1417	1.359	0.78	2248	32	2248	20	2248	23	100
U50	175852	365	163	1.06	0.34	0.37970	1.6	9.796	2.4	0.1871	1.836	0.65	2075	28	2416	22	2717	30	76
U51	157661	196	119	0.63	0.10	0.52060	1.7	13.37	1.9	0.1863	0.8612	0.89	2702	37	2706	18	2710	14	100
U52	140050	183	103	0.84	0.10	0.45380	1.6	11.42	1.9	0.1825	1.001	0.84	2412	32	2558	17	2676	17	90
U53	76681	421	82	0.92	1.64	0.15340	3.2	2.144	4.4	0.1014	3.119	0.71	920	27	1163	31	1649	58	56
U54	110661	361	74	0.71	1.49	0.15860	2.7	3.154	3.6	0.1443	2.375	0.75	949	24	1446	28	2279	41	42
U55	164095	304	161	1.08	1.06	0.46320	2.8	12.71	4.4	0.199	3.402	0.64	2454	58	2658	43	2818	56	87
U56	64905	59	37	0.68	1.59	0.53610	1.8	15.03	3.0	0.2033	2.388	0.59	2767	40	2817	29	2853	39	97
U57	248374	227	193	1.57	0.47	0.62390	1.6	20.82	1.8	0.242	0.8551	0.89	3125	41	3130	18	3133	14	100

Continue...

U58	47007	160	65	1.45	0.22	0.31220	2.3	4.595	2.5	0.1067	0.9045	0.93	1752	36	1748	21	1744	17	100
U59	178476	253	105	0.70	0.18	0.35170	1.6	8.723	2.0	0.1799	1.158	0.81	1943	27	2309	18	2652	19	73
U60	136937	141	102	1.41	0.51	0.55710	1.8	15.9	2.0	0.207	0.7461	0.92	2855	42	2871	19	2882	12	99
U67	89825	299	117	0.86	0.23	0.33740	1.5	5.653	1.7	0.1215	0.5804	0.94	1874	25	1924	14	1979	10	95
U68	117925	148	88	0.57	0.54	0.51360	2.2	12.91	2.3	0.1824	0.891	0.92	2672	47	2673	22	2675	15	100
U69	210106	283	160	0.91	b.d.	0.45930	1.8	12.05	2.1	0.1903	0.9768	0.88	2436	37	2608	19	2745	16	89
U70	185653	190	128	0.81	0.30	0.55400	1.6	15.39	1.8	0.2015	0.7909	0.90	2842	37	2840	17	2839	13	100
U71	70738	364	86	1.46	2.03	0.16740	1.7	2.283	3.9	0.0989	3.496	0.43	998	15	1207	28	1604	65	62
U72	45145	56	39	1.24	0.93	0.52530	2.2	13.55	2.4	0.187	0.9118	0.93	2722	50	2719	23	2716	15	100
U73	62553	115	55	0.70	0.80	0.40620	1.9	7.761	5.9	0.1386	5.623	0.32	2198	35	2204	55	2209	98	99
U74	156556	218	127	2.31	0.39	0.35310	1.8	9.271	2.0	0.1904	1.012	0.87	1949	30	2365	19	2746	17	71
U75	15414	49	18	0.75	2.91	0.32130	1.5	5.038	2.1	0.1137	1.498	0.70	1796	23	1826	18	1860	27	97
U76	87981	320	82	0.76	0.53	0.21300	1.8	3.548	2.0	0.1208	0.7993	0.91	1245	20	1538	16	1969	14	63
U77	65086	364	109	2.13	1.33	0.23110	2.2	3.603	2.6	0.1131	1.442	0.83	1340	26	1550	21	1849	26	72
U78	23674	43	21	0.53	0.26	0.43030	1.6	8.69	1.8	0.1465	0.884	0.87	2307	31	2306	17	2305	15	100
U79	65262	82	56	1.49	0.50	0.50250	1.7	12.3	1.8	0.1775	0.6886	0.93	2625	37	2627	17	2629	11	100
U80	186987	508	167	0.62	0.76	0.28930	2.2	6.73	2.6	0.1687	1.415	0.84	1638	31	2077	23	2545	24	64
U81	102346	349	95	0.62	0.54	0.25640	1.7	4.523	1.9	0.128	0.6406	0.94	1471	23	1735	16	2070	11	71
U82	134416	349	130	1.21	0.50	0.29090	1.6	6.394	1.8	0.1594	0.7309	0.91	1646	24	2031	16	2449	12	67
U83	103900	240	121	1.26	0.13	0.41300	2.3	9.062	2.6	0.1592	1.095	0.91	2228	44	2344	24	2447	19	91
U84	37995	103	39	1.01	1.47	0.31290	1.8	5.058	4.6	0.1172	4.257	0.39	1755	28	1829	40	1915	76	92
U85	215880	225	162	0.97	0.18	0.56780	2.0	19.02	2.6	0.2429	1.71	0.76	2899	46	3043	26	3139	27	92
U86	67943	174	75	1.14	0.05	0.36860	1.5	6.435	1.7	0.1266	0.8365	0.88	2023	27	2037	15	2052	15	99
U87	200314	294	182	0.57	1.73	0.52290	1.6	13.43	2.0	0.1862	1.323	0.76	2712	35	2710	20	2709	22	100
U88	26685	87	32	0.87	1.05	0.31220	1.6	4.625	1.9	0.1075	1.058	0.84	1751	25	1754	16	1757	19	100
U89	88465	263	107	1.53	0.32	0.31260	1.5	5.345	1.6	0.124	0.667	0.91	1753	23	1876	14	2015	12	87
U90	120257	223	114	0.47	0.25	0.45760	1.9	10	2.6	0.1586	1.875	0.71	2429	38	2435	25	2440	32	100
U91	218564	276	148	0.68	b.d.	0.47530	1.5	12.83	1.6	0.1957	0.5939	0.93	2507	32	2667	16	2791	10	90
U92	91897	416	98	0.62	2.57	0.19250	1.7	2.815	3.1	0.1061	2.566	0.55	1135	18	1360	23	1733	47	65
U93	4716	16	7	1.82	b.d.	0.31190	3.8	4.624	4.4	0.1075	2.191	0.87	1750	58	1754	37	1758	40	100

Continue...

U94	140157	387	115	0.75	0.57	0.25080	3.0	5.669	3.7	0.164	2.142	0.82	1443	39	1927	33	2497	36	58
U95	95712	368	90	0.23	0.70	0.23450	1.7	3.861	1.9	0.1194	0.7594	0.92	1358	21	1606	15	1948	14	70
U96	55668	119	56	0.69	b.d.	0.40670	1.8	7.756	2.1	0.1383	1.1	0.85	2200	33	2203	19	2206	19	100
U97	154147	153	113	1.27	b.d.	0.56450	2.6	16.33	2.9	0.2098	1.239	0.90	2885	61	2896	28	2904	20	99
U98	64058	174	69	0.72	0.23	0.33690	1.6	5.813	1.9	0.1251	0.9337	0.87	1872	26	1948	16	2031	17	92
U99	92232	237	120	1.61	0.09	0.37440	1.5	6.537	1.7	0.1266	0.8176	0.88	2050	26	2051	15	2052	14	100

Notes

Spot size = 25µm; depth of crater ~15µm. $^{206}Pb/^{238}U$ error is the quadratic additions of the within run precision (2 SE) and the external reproducibility (2 SD) of the reference zircon. $^{207}Pb/^{206}Pb$ error propagation (^{207}Pb signal dependent) following Gerdes & Zeh (2009). $^{207}Pb/^{235}U$ error is the quadratic addition of the $^{207}Pb/^{206}Pb$ and $^{206}Pb/^{238}U$ uncertainty.

[a]Within run background-corrected mean ^{207}Pb signal in cps (counts per second).

[b] U and Pb content and Th/U ratio were calculated relative to BB1 reference zircon.

[c] percentage of the common Pb on the ^{206}Pb. b.d. = below dectection limit.

[d] corrected for background, within-run Pb/U fractionation (in case of $^{206}Pb/^{238}U$) and common Pb using Stacy and Kramers (1975) model Pb composition and subsequently normalised to BB1 (ID-TIMS value/measured value); $^{207}Pb/^{235}U$ calculated using $^{207}Pb/^{206}Pb/(^{238}U/^{206}Pb*1/137.88)$

[e] rho is the $^{206}Pb/^{238}U/^{207}Pb/^{235}U$ error correlation coefficient.

[f] degree of concordance = $^{206}Pb/^{238}U$ age / $^{207}Pb/^{206}Pb$ age x 100

APPENDIX C – LU-HF ISOTOPE DATA

Lu-Hf isotope data of detrital zircon grains from sample 03-084

grain	$^{176}Yb/^{177}Hf$ [a]	±2σ	$^{176}Lu/^{177}Hf$ [a]	±2σ	$^{178}Hf/^{177}Hf$	Sig_{Hf} [b] (V)	$^{176}Hf/^{177}Hf$	±2σ [c]	$^{176}Hf/^{177}Hf_{(t)}$ [d]	$\varepsilon Hf_{(t)}$ [d]	±2σ [c]	T_{NC} [e] (Ga)	age [f] (Ma)	±2σ	conc.
U113	0.0424	37	0.00125	9	1.46721	12	0.281428	18	0.281377	**-0.7**	**1.0**	2.63	2168	14	100
U114	0.0268	22	0.00066	4	1.46725	12	0.280889	24	0.280855	**-7.3**	**1.2**	3.39	2684	11	96
U116	0.0097	9	0.00027	2	1.46724	13	0.281406	22	0.281395	**-0.7**	**1.1**	2.61	2142	29	101
U118	0.0353	34	0.00086	6	1.46726	15	0.281348	20	0.281313	**-3.5**	**1.1**	2.76	2148	15	100
U119	0.0343	28	0.00083	5	1.46724	13	0.280906	18	0.280863	**-6.8**	**1.0**	3.37	2689	8	99
U122	0.0210	39	0.00053	9	1.46724	17	0.281398	13	0.281377	**-2.5**	**0.9**	2.67	2091	13	99
U123	0.0132	19	0.00036	5	1.46724	13	0.281252	17	0.281237	**-6.5**	**1.0**	2.92	2134	16	100
U124	0.0526	55	0.00131	12	1.46727	17	0.281376	19	0.281324	**-4.1**	**1.1**	2.76	2104	17	99
U125	0.0412	40	0.00097	7	1.46720	13	0.280966	19	0.280915	**-4.6**	**1.0**	3.26	2703	9	101
U126	0.0375	38	0.00094	8	1.46727	10	0.281434	24	0.281397	**-1.9**	**1.2**	2.63	2087	18	94
U127c	0.0263	24	0.00072	5	1.46726	13	0.281356	18	0.281324	**0.4**	**1.0**	2.67	2296	14	100
U128r	0.0172	20	0.00044	5	1.46724	16	0.281423	22	0.281419	**-36.6**	**1.1**	3.28	528	8	93
U129	0.0315	25	0.00088	5	1.46722	14	0.281336	18	0.281299	**-2.7**	**1.0**	2.76	2201	14	100
U130	0.0245	20	0.00060	4	1.46725	18	0.281495	19	0.281490	**-34.2**	**1.1**	3.15	520	8	97
U131	0.0341	28	0.00095	6	1.46721	14	0.281372	16	0.281335	**-4.4**	**1.0**	2.76	2074	18	100
U132	0.0313	31	0.00080	7	1.46725	15	0.281514	17	0.281506	**-33.6**	**1.0**	3.12	524	9	101
U133	0.0070	10	0.00019	2	1.46728	15	0.281253	21	0.281246	**-5.8**	**1.1**	2.89	2152	12	100
U136	0.0421	46	0.00108	11	1.46727	14	0.281423	18	0.281380	**-2.4**	**1.0**	2.66	2091	12	91
U137	0.0239	19	0.00058	4	1.46724	13	0.281441	21	0.281418	**-0.9**	**1.1**	2.58	2098	13	100
U139	0.0343	33	0.00075	6	1.46722	11	0.281212	23	0.281182	**-9.3**	**1.2**	3.04	2097	12	100
U140	0.0259	24	0.00075	6	1.46723	12	0.281370	19	0.281337	**0.9**	**1.1**	2.64	2299	12	100
U141	0.0261	22	0.00069	4	1.46726	16	0.281313	19	0.281285	**-4.5**	**1.0**	2.82	2147	12	97
U142c	0.0171	15	0.00043	3	1.46721	15	0.281305	17	0.281287	**-3.5**	**1.0**	2.79	2187	17	100
U144	0.0298	37	0.00083	9	1.46723	13	0.281252	23	0.281212	**0.9**	**1.1**	2.79	2488	15	100
U147	0.0224	18	0.00051	3	1.46725	21	0.281542	15	0.281537	**-32.6**	**1.0**	3.06	521	8	96
U148	0.0330	30	0.00081	6	1.46724	14	0.280920	22	0.280878	**-6.0**	**1.1**	3.33	2703	11	100

U149	0.0342	31	0.00083	6	1.46726	14	0.280900	22	0.280858	**-7.4**	**1.1**	3.39	2674	10	94
U157	0.0421	35	0.00100	6	1.46728	12	0.281455	16	0.281415	**-0.7**	**1.0**	2.58	2111	23	100
U158	0.0269	23	0.00065	4	1.46722	12	0.281327	16	0.281300	**-2.7**	**1.0**	2.76	2200	14	101
U164	0.0325	32	0.00085	7	1.46723	15	0.281197	23	0.281162	**-8.7**	**1.1**	3.05	2152	15	100
U167	0.0227	20	0.00057	4	1.46723	16	0.281421	19	0.281398	**-0.5**	**1.0**	2.60	2144	17	100
U169	0.0107	9	0.00029	2	1.46727	14	0.280839	20	0.280824	**-7.4**	**1.1**	3.43	2723	11	91
U170	0.0296	24	0.00070	4	1.46728	14	0.281196	16	0.281169	**-11.2**	**1.0**	3.10	2035	13	99
U172	0.0103	9	0.00030	2	1.46722	11	0.281352	17	0.281340	**-2.8**	**1.0**	2.72	2132	32	99
U174	0.0330	29	0.00095	7	1.46726	13	0.281344	16	0.281304	**-2.4**	**1.0**	2.75	2209	41	101
U175	0.0679	60	0.00186	13	1.46727	11	0.281491	18	0.281414	**0.2**	**1.0**	2.56	2152	16	100
U176	0.0403	34	0.00099	6	1.46724	14	0.281453	17	0.281413	**0.3**	**1.0**	2.56	2158	15	97
U177	0.0459	37	0.00115	7	1.46723	12	0.281390	21	0.281340	**1.2**	**1.1**	2.63	2309	11	97
U178	0.0178	16	0.00044	3	1.46726	15	0.281321	17	0.281302	**-2.0**	**1.0**	2.74	2227	10	99
U179	0.0353	29	0.00086	5	1.46720	14	0.280925	17	0.280881	**-6.3**	**1.0**	3.34	2685	11	101
U180	0.0329	32	0.00083	7	1.46727	14	0.281437	16	0.281404	**-1.4**	**1.0**	2.61	2098	16	97
U181	0.0477	39	0.00124	8	1.46724	15	0.280799	27	0.280731	**-7.4**	**1.2**	3.54	2864	15	98
U182	0.0204	18	0.00054	4	1.46724	15	0.281463	19	0.281441	**1.7**	**1.0**	2.50	2175	12	97
U183	0.0393	32	0.00101	6	1.46722	13	0.281235	19	0.281195	**-8.6**	**1.0**	3.01	2109	19	100
U184	0.0230	22	0.00064	5	1.46724	15	0.281539	22	0.281513	**3.2**	**1.1**	2.38	2128	17	100
U185	0.0195	16	0.00045	3	1.46721	28	0.281552	23	0.281548	**-32.1**	**1.1**	3.04	526	7	97
U186	0.0281	24	0.00071	5	1.46723	12	0.280650	20	0.280604	**-0.3**	**1.1**	3.52	3356	13	91
U190	0.0199	19	0.00050	4	1.46726	15	0.281310	18	0.281289	**-3.8**	**1.0**	2.80	2167	11	97
U191	0.0332	28	0.00085	6	1.46728	13	0.281316	20	0.281283	**-6.0**	**1.1**	2.85	2084	20	100
U192	0.0462	47	0.00122	11	1.46726	14	0.281405	17	0.281393	**-37.7**	**1.0**	3.33	520	12	92
U193	0.0367	30	0.00090	5	1.46727	14	0.280976	18	0.280930	**-4.7**	**1.0**	3.24	2676	13	100
U195	0.0260	53	0.00068	13	1.46732	19	0.280717	23	0.280678	**-4.9**	**1.1**	3.54	3051	12	97
U197	0.0323	26	0.00079	5	1.46731	13	0.280926	18	0.280886	**-6.2**	**1.0**	3.33	2680	10	99
U198	0.0299	27	0.00077	5	1.46728	15	0.281467	20	0.281437	**-1.8**	**1.1**	2.58	2029	26	91
U206	0.0292	29	0.00073	6	1.46721	18	0.281420	19	0.281389	**2.1**	**1.0**	2.55	2271	19	100
U207	0.0299	25	0.00078	5	1.46725	12	0.281326	19	0.281289	**3.5**	**1.0**	2.64	2483	12	100
U208	0.0273	22	0.00078	5	1.46724	13	0.281327	17	0.281293	**-1.3**	**1.0**	2.74	2270	15	100

U210	0.0070	13	0.00021	3	1.46726	18	0.281449	24	0.281441	**0.4**	**1.2**	2.53	2117	11	91
U211	0.0701	56	0.00157	10	1.46726	14	0.281353	20	0.281303	**-14.7**	**1.1**	3.01	1676	12	96
U212	0.0314	28	0.00084	5	1.46721	15	0.281483	19	0.281450	**-0.7**	**1.1**	2.54	2055	15	100
U213	0.0240	21	0.00063	5	1.46722	14	0.281362	19	0.281335	**-1.6**	**1.0**	2.70	2192	11	90
U214	0.0169	19	0.00049	4	1.46722	15	0.281188	19	0.281169	**-11.1**	**1.0**	3.10	2038	18	97
U215	0.0199	19	0.00060	5	1.46731	15	0.281385	17	0.281361	**-3.4**	**1.0**	2.70	2077	14	100
U216	0.0438	39	0.00104	7	1.46721	14	0.281555	21	0.281513	**3.0**	**1.1**	2.38	2119	17	100
U217	0.0411	39	0.00113	9	1.46722	14	0.281504	17	0.281458	**0.7**	**1.0**	2.50	2103	15	95
U218	0.0181	15	0.00041	2	1.46723	22	0.281571	13	0.281567	**-31.5**	**0.9**	3.01	523	8	100
U220	0.0306	25	0.00082	5	1.46727	22	0.281548	18	0.281540	**-32.3**	**1.0**	3.05	527	9	100
U222	0.0139	13	0.00035	3	1.46722	12	0.280984	20	0.280971	**-17.9**	**1.1**	3.47	2049	21	100
U225	0.0371	36	0.00092	7	1.46726	13	0.281224	22	0.281215	**-43.9**	**1.1**	3.67	521	7	100
U227	0.0287	24	0.00078	5	1.46731	14	0.281480	18	0.281448	**1.8**	**1.0**	2.49	2169	14	100
U230	0.0152	13	0.00043	3	1.46725	12	0.281340	17	0.281322	**-2.1**	**1.0**	2.72	2194	13	100
U232	0.0243	30	0.00063	7	1.46724	13	0.281399	16	0.281371	**3.2**	**1.0**	2.55	2346	15	99
U233	0.0219	24	0.00053	5	1.46726	9	0.281109	36	0.281104	**-47.9**	**1.5**	3.87	521	7	95
U235	0.0223	20	0.00055	4	1.46724	15	0.281460	17	0.281438	**-0.5**	**1.0**	2.55	2085	18	100
U236	0.0520	42	0.00126	8	1.46727	11	0.281567	22	0.281516	**3.4**	**1.1**	2.37	2133	17	100
U239	0.0434	45	0.00115	11	1.46724	13	0.280676	18	0.280603	**-1.6**	**1.0**	3.55	3303	14	91
U242	0.0252	21	0.00063	4	1.46724	16	0.281433	20	0.281427	**-36.5**	**1.1**	3.27	518	8	103
U244	0.0242	21	0.00064	4	1.46718	12	0.280694	18	0.280660	**-11.4**	**1.0**	3.71	2804	16	98
U245	0.0603	57	0.00146	12	1.46727	14	0.281514	27	0.281454	**1.1**	**1.3**	2.50	2129	15	100
U247	0.0105	10	0.00030	2	1.46727	12	0.281307	18	0.281295	**-2.9**	**1.0**	2.77	2200	13	101

Notes

Quoted uncertainties (absolute) relate to the last quoted figure. The effect of the inter-element fractionation on the Lu/Hf was estimated to be about 6 % or less based on analyses of the GJ-1 and Temora zircon. Accuracy and reproducibilty was checked by repeated analyses of reference zircon GJ-1 and Temora (data given as mean with 2 standard deviation uncertainties)

(a) $^{176}Yb/^{177}Hf = (^{176}Yb/^{173}Yb)true \times (^{173}Yb/^{177}Hf)meas \times (M^{173}(Yb)/M^{177}(Hf))\beta(Hf)$, $\beta(Hf) = \ln(^{179}Hf/^{177}Hf\ true\ /\ ^{179}Hf/^{177}Hf measured)/\ln(M^{179}(Hf)/M^{177}(Hf))$, M=mass of respective isotope. The $^{176}Lu/^{177}Hf$ were calculated in a similar way by using the $^{175}Lu/^{177}Hf$ and β(Yb).

(b) Mean Hf signal in volt.

(c) Uncertainties are quadratic additions of the within-run precision and the daily reproducibility of GJ1 zircon at 2SD (2 standard deviation).

(d) Initial $^{176}Hf/^{177}Hf$ and eHf calculated using the apparent Pb-Pb age determined by LA-ICP-MS dating (see column f), and the CHUR parameters: $^{176}Lu/^{177}Hf = 0.0336$, and $^{176}Hf/^{177}Hf = 0.282785$ (Bouvier et al., 2008).

(e) two stage model age in 10^9 years using the measured $^{176}Lu/^{177}Lu$ of each spot (first stage = age of zircon), a value of 0.0113 for the average continental crust (second stage), and a juvenile crust (NC) $^{176}Lu/^{177}Lu$ and $^{176}Hf/^{177}Hf$ of 0.0384 and 0.28318, respectively.

(f) Pb-Pb age determined by LA-ICP-MS

Lu-Hf isotope data of detrital zircon grains from sample 07-001

grain	$^{176}Yb/^{177}Hf$ [a]	±2σ	$^{176}Lu/^{177}Hf$ [a]	±2σ	$^{178}Hf/^{177}Hf$	Sig_{Hf} [b] (V)	$^{176}Hf/^{177}Hf$	±2σ [c]	$^{176}Hf/^{177}Hf_{(t)}$ [d]	$\varepsilon Hf_{(t)}$ [d]	±2σ [c]	T_{NC} [e] (Ga)	age [f] (Ma)	±2σ	conc.
U289	0.0238	20	0.00057	3	1.46724	11	0.281238	20	0.281219	**-16.0**	**1.1**	3.14	1750	15	100
U290	0.0670	60	0.00158	11	1.46726	8	0.281165	35	0.281130	**-32.5**	**1.5**	3.57	1166	83	53
U291	0.0170	14	0.00040	3	1.46730	12	0.281270	16	0.281256	**-14.3**	**1.0**	3.06	1766	19	100
U292	0.0292	32	0.00067	6	1.46723	14	0.281281	19	0.281259	**-14.4**	**1.0**	3.06	1756	75	100
U293	0.0619	54	0.00134	9	1.46727	16	0.281293	29	0.281248	**-14.8**	**1.3**	3.08	1758	14	100
U294	0.0907	75	0.00205	13	1.46725	14	0.281243	19	0.281188	**-24.4**	**1.1**	3.34	1428	50	71
U295	0.0652	63	0.00151	12	1.46718	10	0.281186	28	0.281141	**-22.9**	**1.3**	3.37	1570	34	70
U296	0.0240	20	0.00058	4	1.46729	13	0.281236	20	0.281217	**-15.9**	**1.1**	3.14	1756	21	100
U297	0.0741	66	0.00169	13	1.46723	13	0.281228	27	0.281179	**-22.5**	**1.3**	3.32	1528	47	83
U298	0.0375	31	0.00087	5	1.46725	14	0.281229	16	0.281200	**-17.3**	**1.0**	3.19	1720	14	87
U299	0.0693	56	0.00159	10	1.46726	13	0.281251	22	0.281203	**-20.2**	**1.1**	3.24	1592	14	68
U328	0.0199	17	0.00048	3	1.46725	13	0.281252	21	0.281236	**-14.7**	**1.1**	3.09	1781	21	100
U306	0.0742	65	0.00169	12	1.46729	13	0.281287	29	0.281231	**-15.9**	**1.3**	3.12	1734	15	99
U307	0.0249	21	0.00059	4	1.46723	13	0.281266	20	0.281246	**-15.4**	**1.1**	3.09	1734	124	100
U308	0.0236	19	0.00057	3	1.46725	12	0.281278	21	0.281259	**-14.0**	**1.1**	3.05	1774	20	100
U309	0.1015	87	0.00231	16	1.46730	14	0.281249	23	0.281178	**-20.8**	**1.1**	3.28	1604	53	61
U310	0.0387	38	0.00088	8	1.46721	16	0.281218	24	0.281188	**-16.4**	**1.2**	3.18	1781	40	95
U311	0.0576	48	0.00134	9	1.46722	13	0.281252	19	0.281208	**-17.1**	**1.1**	3.17	1716	19	97
U312	0.0168	14	0.00041	2	1.46724	13	0.281253	15	0.281239	**-14.7**	**1.0**	3.09	1775	24	100
U313	0.0216	19	0.00052	3	1.46721	11	0.281229	20	0.281212	**-15.7**	**1.1**	3.14	1773	15	100
U314	0.0276	34	0.00063	6	1.46725	14	0.281225	33	0.281204	**-16.3**	**1.4**	3.16	1759	23	100
U315	0.0456	41	0.00101	7	1.46718	16	0.281234	24	0.281200	**-16.5**	**1.2**	3.17	1758	15	100

U316	0.0781	67	0.00176	12	1.46720	14	0.281248	34	0.281195	**-20.7**	**1.5**	3.26	1583	34	68
U317	0.0359	30	0.00081	5	1.46721	14	0.281234	17	0.281209	**-18.0**	**1.0**	3.19	1676	71	95
U318	0.0210	17	0.00050	3	1.46722	12	0.281249	19	0.281232	**-14.5**	**1.0**	3.09	1794	17	100
U319	0.0335	29	0.00080	5	1.46730	11	0.281234	26	0.281207	**-15.2**	**1.2**	3.14	1802	21	100
U320	0.0254	25	0.00059	5	1.46726	13	0.281254	25	0.281235	**-16.8**	**1.2**	3.13	1690	17	97
U321	0.0278	28	0.00065	5	1.46723	11	0.281321	25	0.281300	**-12.7**	**1.2**	2.97	1767	19	98
U322	0.0305	26	0.00071	4	1.46722	14	0.281231	19	0.281208	**-17.0**	**1.0**	3.17	1723	13	101
U323	0.0327	42	0.00075	8	1.46727	13	0.281247	26	0.281223	**-18.1**	**1.2**	3.18	1649	37	56
U324	0.0204	16	0.00049	3	1.46724	13	0.281281	16	0.281264	**-14.1**	**1.0**	3.04	1760	17	100

Notes

Quoted uncertainties (absolute) relate to the last quoted figure. The effect of the inter-element fractionation on the Lu/Hf was estimated to be about 6 % or less based on analyses of the GJ-1 and Temora zircon. Accuracy and reproducibilty was checked by repeated analyses of reference zircon GJ-1 and Temora (data given as mean with 2 standard deviation uncertainties)

(a) $^{176}Yb/^{177}Hf = (^{176}Yb/^{173}Yb)true \times (^{173}Yb/^{177}Hf)meas \times (M^{173}(Yb)/M^{177}(Hf))\beta(Hf)$, $\beta(Hf) = \ln(^{179}Hf/^{177}Hf\ true\ /\ ^{179}Hf/^{177}Hf measured)/\ln(M^{179}(Hf)/M^{177}(Hf))$, M=mass of respective isotope. The $^{176}Lu/^{177}Hf$ were calculated in a similar way by using the $^{175}Lu/^{177}Hf$ and β(Yb).

(b) Mean Hf signal in volt.

(c) Uncertainties are quadratic additions of the within-run precision and the daily reproducibility of GJ1 zircon at 2SD (2 standard deviation).

(d) Initial $^{176}Hf/^{177}Hf$ and eHf calculated using the apparent Pb-Pb age determined by LA-ICP-MS dating (see column f), and the CHUR parameters: $^{176}Lu/^{177}Hf = 0.0336$, and $^{176}Hf/^{177}Hf = 0.282785$ (Bouvier et al., 2008).

(e) two stage model age in 10^9 years using the measured $^{176}Lu/^{177}Lu$ of each spot (first stage = age of zircon), a value of 0.0113 for the average continental crust (second stage), and a juvenile crust (NC) $^{176}Lu/^{177}Lu$ and $^{176}Hf/^{177}Hf$ of 0.0384 and 0.28318, respectively.

(f) Pb-Pb age determined by LA-ICP-MS

Lu-Hf isotope data of detrital zircon grains from sample 08-001

grain	$^{176}Yb/^{177}Hf$ [a]	±2σ	$^{176}Lu/^{177}Hf$ [a]	±2σ	$^{178}Hf/^{177}Hf$	Sig_{Hf} [b] (V)	$^{176}Hf/^{177}Hf$	±2σ [c]	$^{176}Hf/^{177}Hf_{(t)}$ [d]	$\varepsilon Hf_{(t)}$ [d]	±2σ [c]	T_{NC} [e] (Ga)	age [f] (Ma)	±2σ	conc.
U08	0.0560	56	0.00145	14	1.46733	15	0.280941	21	0.280869	**-8.7**	**1.1**	3.40	2603	14	81
U11	0.0695	61	0.00197	13	1.46720	11	0.280869	24	0.280802	**-29.3**	**1.2**	3.91	1815	27	48
U12	0.0829	67	0.00232	15	1.46728	15	0.281096	34	0.281008	**-17.6**	**1.4**	3.42	2005	32	57
U13	0.0614	50	0.00161	10	1.46728	15	0.281028	25	0.280980	**-28.1**	**1.2**	3.67	1592	34	61
U14	0.0945	76	0.00264	16	1.46724	9	0.281497	31	0.281431	**-18.5**	**1.7**	2.93	1310	125	48
U15	0.0588	48	0.00163	10	1.46726	16	0.281157	18	0.281093	**-12.8**	**1.5**	3.22	2081	35	45
U16	0.0661	56	0.00173	11	1.46721	10	0.281045	24	0.280980	**-19.6**	**1.6**	3.50	1962	27	46

U17	0.0873	71	0.00234	15	1.46726	14	0.281139	23	0.281053	**-17.8**	**1.5**	3.37	1928	37	48
U18	0.0622	53	0.00164	11	1.46726	17	0.281059	17	0.281007	**-25.2**	**1.4**	3.58	1676	30	54
U19	0.0653	59	0.00185	13	1.46723	10	0.280982	35	0.280903	**-16.0**	**1.8**	3.52	2237	63	67
U20	0.0407	34	0.00090	6	1.46724	13	0.280867	25	0.280820	**-7.6**	**1.6**	3.44	2721	11	99
U21	0.0727	59	0.00195	12	1.46723	13	0.281072	26	0.281005	**-22.4**	**1.6**	3.52	1802	26	61
U22	0.0552	48	0.00151	11	1.46724	15	0.281005	23	0.280928	**-4.5**	**1.5**	3.24	2689	9	89
U23	0.0829	69	0.00214	13	1.46723	16	0.280994	20	0.280915	**-22.4**	**1.5**	3.63	1942	40	59
U24	0.0744	61	0.00200	12	1.46723	19	0.281179	26	0.281108	**-17.1**	**1.6**	3.29	1871	70	51
U25	0.0452	39	0.00110	7	1.46723	13	0.281008	20	0.280955	**-7.3**	**1.5**	3.27	2530	14	68
U26	0.0668	55	0.00173	11	1.46725	14	0.281067	24	0.281026	**-33.9**	**1.6**	3.72	1267	73	55
U27	0.0631	51	0.00169	10	1.46726	13	0.281074	17	0.280989	**-3.6**	**1.4**	3.15	2635	20	100
U53	0.0200	16	0.00048	3	1.46722	13	0.281275	15	0.281259	**-14.3**	**1.4**	3.05	1763	15	100
U74	0.0444	73	0.00108	18	1.46728	16	0.281239	33	0.281199	**-11.5**	**1.7**	3.07	1976	33	80

Notes

Quoted uncertainties (absolute) relate to the last quoted figure. The effect of the inter-element fractionation on the Lu/Hf was estimated to be about 6 % or less based on analyses of the GJ-1 and Temora zircon. Accuracy and reproducibilty was checked by repeated analyses of reference zircon GJ-1 and Temora (data given as mean with 2 standard deviation uncertainties)

(a) $^{176}Yb/^{177}Hf = (^{176}Yb/^{173}Yb)true \times (^{173}Yb/^{177}Hf)meas \times (M^{173}(Yb)/M^{177}(Hf))\beta(Hf)$, $\beta(Hf) = \ln(^{179}Hf/^{177}Hf\ true\ /\ ^{179}Hf/^{177}Hf measured)/\ln(M^{179}(Hf)/M^{177}(Hf))$, M=mass of respective isotope. The $^{176}Lu/^{177}Hf$ were calculated in a similar way by using the $^{175}Lu/^{177}Hf$ and β(Yb).

(b) Mean Hf signal in volt.

(c) Uncertainties are quadratic additions of the within-run precision and the daily reproducibility of GJ1 zircon at 2SD (2 standard deviation).

(d) Initial $^{176}Hf/^{177}Hf$ and eHf calculated using the apparent Pb-Pb age determined by LA-ICP-MS dating (see column f), and the CHUR parameters: $^{176}Lu/^{177}Hf = 0.0336$, and $^{176}Hf/^{177}Hf = 0.282785$ (Bouvier et al., 2008).

(e) two stage model age in 10^9 years using the measured $^{176}Lu/^{177}Lu$ of each spot (first stage = age of zircon), a value of 0.0113 for the average continental crust (second stage), and a juvenile crust (NC) $^{176}Lu/^{177}Lu$ and $^{176}Hf/^{177}Hf$ of 0.0384 and 0.28318, respectively.

(f) Pb-Pb age determined by LA-ICP-MS

Lu-Hf isotope data of detrital zircon grains from sample 08-002

grain	$^{176}Yb/^{177}Hf$ [a]	±2σ	$^{176}Lu/^{177}Hf$ [a]	±2σ	$^{178}Hf/^{177}Hf$	Sig_{Hf} [b] (V)	$^{176}Hf/^{177}Hf$	±2σ [c]	$^{176}Hf/^{177}Hf_{(t)}$ [d]	$\varepsilon Hf_{(t)}$ [d]	±2σ [c]	T_{NC} [e] (Ga)	age [f] (Ma)	±2σ	conc.
U75	0.0102	9	0.00038	2	1.46727	19	0.280877	15	0.280856	**-1.5**	**1.4**	3.26	2926	12	75
U76	0.0534	44	0.00140	9	1.46725	24	0.281128	23	0.281115	**-47.9**	**1.5**	3.86	503	7	99

U77	0.0679	56	0.00163	10	1.46723	16	0.280658	22	0.280579	**-20.3**	**1.5**	3.99	2543	28	50
U78	0.0161	27	0.00040	7	1.46720	16	0.280960	24	0.280940	**-6.6**	**1.6**	3.27	2581	34	71
U79	0.0751	61	0.00190	12	1.46727	16	0.280717	22	0.280626	**-19.2**	**1.5**	3.91	2520	25	41
U80	0.0774	64	0.00176	11	1.46726	15	0.281034	22	0.280978	**-25.6**	**1.5**	3.62	1706	12	80
U81	0.0462	43	0.00114	8	1.46727	14	0.281327	27	0.281289	**-14.3**	**1.6**	3.02	1714	14	85
U82	0.0401	33	0.00110	7	1.46726	20	0.280986	18	0.280956	**-32.1**	**1.5**	3.77	1453	88	47
U83	0.0473	38	0.00127	8	1.46726	18	0.281146	25	0.281079	**2.2**	**1.6**	2.91	2747	12	75
U84	0.0131	13	0.00038	3	1.46729	12	0.281140	20	0.281122	**-1.4**	**1.5**	2.94	2528	30	72
U85	0.0595	53	0.00155	11	1.46726	20	0.280856	17	0.280783	**-14.9**	**1.4**	3.63	2468	28	62
U87	0.0652	53	0.00177	11	1.46727	16	0.280839	20	0.280745	**-8.9**	**1.5**	3.55	2781	19	37
U88	0.0094	11	0.00028	3	1.46726	13	0.281112	27	0.281099	**-2.4**	**1.6**	2.99	2521	27	77
U89	0.0494	40	0.00123	7	1.46727	15	0.280878	22	0.280815	**-9.3**	**1.5**	3.48	2658	47	31
U90	0.0786	63	0.00208	13	1.46724	16	0.280803	18	0.280703	**-16.6**	**1.4**	3.76	2516	53	75
U91	0.0670	54	0.00161	10	1.46724	17	0.280730	18	0.280641	**-10.6**	**1.5**	3.71	2865	10	97
U92	0.0670	58	0.00159	11	1.46726	11	0.281150	21	0.281097	**-20.2**	**1.5**	3.37	1757	25	97
U93	0.0806	66	0.00221	15	1.46728	17	0.280711	23	0.280612	**-23.9**	**1.5**	4.02	2343	24	53
U94	0.0315	27	0.00086	6	1.46725	24	0.281155	23	0.281147	**-47.2**	**1.5**	3.81	483	11	54

Notes

Quoted uncertainties (absolute) relate to the last quoted figure. The effect of the inter-element fractionation on the Lu/Hf was estimated to be about 6 % or less based on analyses of the GJ-1 and Temora zircon. Accuracy and reproducibilty was checked by repeated analyses of reference zircon GJ-1 and Temora (data given as mean with 2 standard deviation uncertainties)

(a) $^{176}Yb/^{177}Hf = (^{176}Yb/^{173}Yb)true \times (^{173}Yb/^{177}Hf)meas \times (M^{173}(Yb)/M^{177}(Hf))\beta(Hf)$, $\beta(Hf) = \ln(^{179}Hf/^{177}Hf\ true\ /\ ^{179}Hf/^{177}Hf measured)/\ln(M^{179}(Hf)/M^{177}(Hf))$, M=mass of respective isotope. The $^{176}Lu/^{177}Hf$ were calculated in a similar way by using the $^{175}Lu/^{177}Hf$ and β(Yb).

(b) Mean Hf signal in volt.

(c) Uncertainties are quadratic additions of the within-run precision and the daily reproducibility of GJ1 zircon at 2SD (2 standard deviation).

(d) Initial $^{176}Hf/^{177}Hf$ and eHf calculated using the apparent Pb-Pb age determined by LA-ICP-MS dating (see column f), and the CHUR parameters: $^{176}Lu/^{177}Hf = 0.0336$, and $^{176}Hf/^{177}Hf = 0.282785$ (Bouvier et al., 2008).

(e) two stage model age in 10^9 years using the measured $^{176}Lu/^{177}Lu$ of each spot (first stage = age of zircon), a value of 0.0113 for the average continental crust (second stage), and a juvenile crust (NC) $^{176}Lu/^{177}Lu$ and $^{176}Hf/^{177}Hf$ of 0.0384 and 0.28318, respectively.

(f) Pb-Pb age determined by LA-ICP-MS

Lu-Hf isotope data of detrital zircon grains from sample 10-001

grain	$^{176}Yb/^{177}Hf$ [a]	±2σ	$^{176}Lu/^{177}Hf$ [a]	±2σ	$^{178}Hf/^{177}Hf$	Sig_{Hf} [b] (V)	$^{176}Hf/^{177}Hf$	±2σ [c]	$^{176}Hf/^{177}Hf_{(t)}$ [d]	$\varepsilon Hf_{(t)}$ [d]	±2σ [c]	T_{NC} [e] (Ga)	age [f] (Ma)	±2σ	conc.
U07	0.0431	43	0.00103	8	1.46728	15	0.280944	21	0.280890	**-4.5**	**1.1**	3.29	2749	10	97
U100	0.0166	22	0.00040	4	1.46719	18	0.281151	25	0.281136	**-12.9**	**1.2**	3.17	2013	13	101
U108	0.0338	31	0.00083	6	1.46727	11	0.280899	29	0.280856	**-5.4**	**1.3**	3.35	2762	23	100
U109	0.0207	17	0.00050	3	1.46726	12	0.280932	25	0.280905	**-2.7**	**1.2**	3.23	2801	10	100
U110	0.0229	20	0.00056	4	1.46721	13	0.280889	23	0.280860	**-7.3**	**1.1**	3.38	2673	7	85
U111	0.0791	85	0.00185	16	1.46723	16	0.280960	27	0.280865	**-6.9**	**1.3**	3.37	2684	16	100
U19	0.0735	98	0.00177	22	1.46715	10	0.281279	30	0.281208	**-7.9**	**1.3**	2.98	2117	19	99
U21	0.0206	19	0.00048	3	1.46726	12	0.281079	20	0.281060	**-14.9**	**1.1**	3.30	2042	20	100
U22	0.0287	24	0.00069	4	1.46730	11	0.281318	19	0.281295	**-13.5**	**1.0**	2.99	1740	27	100
U23	0.0078	6	0.00018	1	1.46722	17	0.281165	16	0.281156	**-0.7**	**1.0**	2.89	2507	9	96
U24	0.0123	11	0.00031	2	1.46723	9	0.281374	21	0.281361	**1.3**	**1.1**	2.60	2278	14	97
U26	0.0163	14	0.00040	3	1.46723	14	0.280575	18	0.280550	**-3.3**	**1.0**	3.66	3311	11	95
U27	0.0220	18	0.00052	3	1.46726	14	0.281261	15	0.281244	**-14.7**	**1.0**	3.08	1768	17	100
U28	0.0207	18	0.00052	4	1.46731	13	0.280877	26	0.280848	**-3.0**	**1.2**	3.30	2872	10	100
U29	0.0247	20	0.00060	4	1.46723	13	0.281296	17	0.281272	**-5.5**	**1.0**	2.85	2123	12	100
U30	0.0483	41	0.00127	8	1.46724	11	0.280752	19	0.280677	**-4.4**	**1.0**	3.53	3073	17	98
U37	0.0118	10	0.00030	2	1.46726	15	0.280882	18	0.280866	**-3.8**	**1.0**	3.30	2814	14	100
U40	0.0314	26	0.00077	5	1.46726	16	0.280857	21	0.280815	**-6.0**	**1.1**	3.41	2796	12	100
U42	0.0628	50	0.00150	9	1.46726	15	0.280784	21	0.280704	**-10.4**	**1.1**	3.63	2778	18	100
U43	0.0327	28	0.00080	5	1.46718	17	0.281489	16	0.281457	**1.4**	**1.0**	2.49	2135	13	99
U45	0.0361	31	0.00092	6	1.46724	13	0.280681	22	0.280624	**-3.2**	**1.1**	3.57	3206	13	100
U46	0.0896	79	0.00220	16	1.46722	13	0.281415	22	0.281319	**0.1**	**1.1**	2.68	2290	15	99
U47	0.0234	19	0.00061	4	1.46722	12	0.280867	18	0.280836	**-8.2**	**1.0**	3.43	2673	8	100
U48	0.0401	37	0.00109	8	1.46724	13	0.281388	17	0.281342	**-1.6**	**1.0**	2.69	2185	17	102
U49	0.0801	71	0.00193	13	1.46725	14	0.281326	21	0.281243	**-3.6**	**1.1**	2.85	2248	23	100
U51	0.0283	23	0.00069	4	1.46723	15	0.280916	15	0.280881	**-5.7**	**1.0**	3.32	2710	14	100
U52	0.0334	28	0.00092	6	1.46721	13	0.280927	18	0.280880	**-6.5**	**1.0**	3.34	2676	17	90

U55	0.0564	49	0.00148	10	1.46723	17	0.280709	19	0.280629	**-12.1**	**1.0**	3.76	2818	56	87
U56	0.0240	20	0.00063	4	1.46725	12	0.280918	18	0.280883	**-2.3**	**1.0**	3.24	2853	39	97
U57	0.1668	137	0.00397	25	1.46723	10	0.280648	17	0.280409	**-12.5**	**1.0**	4.02	3133	14	100
U58	0.0750	64	0.00170	11	1.46725	12	0.281186	32	0.281129	**-19.3**	**1.4**	3.31	1744	17	100
U60	0.0398	32	0.00098	6	1.46720	11	0.280792	21	0.280738	**-6.7**	**1.1**	3.51	2882	12	99
U67	0.0414	53	0.00092	10	1.46727	15	0.281039	22	0.281005	**-18.3**	**1.1**	3.44	1979	10	95
U68	0.0319	27	0.00081	5	1.46720	11	0.280922	21	0.280881	**-6.5**	**1.1**	3.34	2675	15	100
U69	0.0635	53	0.00146	9	1.46726	14	0.280910	19	0.280834	**-6.6**	**1.0**	3.40	2745	16	89
U70	0.0423	34	0.00106	7	1.46724	14	0.280847	18	0.280789	**-6.0**	**1.0**	3.44	2839	13	100
U72	0.0266	22	0.00063	4	1.46724	14	0.280650	17	0.280617	**-14.9**	**1.0**	3.83	2716	15	100
U73	0.0232	22	0.00060	5	1.46728	13	0.281494	19	0.281469	**3.5**	**1.0**	2.43	2209	98	99
U75	0.0187	15	0.00045	3	1.46721	13	0.281247	18	0.281231	**-13.0**	**1.0**	3.06	1860	27	97
U78	0.0509	57	0.00139	13	1.46725	12	0.281281	19	0.281220	**-3.1**	**1.0**	2.87	2305	15	100
U79	0.0429	46	0.00098	9	1.46722	13	0.280974	20	0.280925	**-6.0**	**1.1**	3.28	2629	11	100
U83	0.0615	54	0.00155	10	1.46724	7	0.280990	29	0.280917	**-10.6**	**1.3**	3.38	2447	19	91
U84	0.0254	23	0.00064	4	1.46724	12	0.281490	22	0.281467	**-3.4**	**1.1**	2.58	1915	76	92
U85	0.0272	28	0.00075	6	1.46719	12	0.280729	29	0.280684	**-2.6**	**1.3**	3.48	3139	27	92
U86	0.0402	41	0.00098	9	1.46730	12	0.281093	21	0.281055	**-14.9**	**1.1**	3.31	2052	15	99
U87	0.0381	41	0.00089	8	1.46723	15	0.280905	20	0.280859	**-6.5**	**1.1**	3.37	2709	22	100
U88	0.0314	40	0.00071	9	1.46724	18	0.281332	20	0.281308	**-12.7**	**1.1**	2.96	1757	19	100
U90	0.0140	13	0.00036	2	1.46728	15	0.281013	16	0.280996	**-7.9**	**1.0**	3.23	2440	32	100
U91	0.0245	22	0.00058	4	1.46721	15	0.280795	18	0.280764	**-8.0**	**1.0**	3.51	2791	10	90
U93	0.0299	25	0.00076	5	1.46728	9	0.281500	25	0.281475	**-6.7**	**1.2**	2.64	1758	40	100
U96	0.0206	17	0.00049	3	1.46726	12	0.281355	20	0.281335	**-1.3**	**1.1**	2.69	2206	19	100
U97	0.0324	32	0.00082	6	1.46721	15	0.280869	20	0.280823	**-3.2**	**1.1**	3.33	2904	20	99
U98	0.0155	13	0.00037	2	1.46724	16	0.281310	16	0.281296	**-6.8**	**1.0**	2.85	2031	17	92
U99	0.0396	34	0.00096	7	1.46732	14	0.281045	18	0.281007	**-16.5**	**1.0**	3.40	2052	14	100

Notes

Quoted uncertainties (absolute) relate to the last quoted figure. The effect of the inter-element fractionation on the Lu/Hf was estimated to be about 6 % or less based on analyses of the GJ-1 and Temora zircon. Accuracy and reproducibilty was checked by repeated analyses of reference zircon GJ-1 and Temora (data given as mean with 2 standard deviation uncertainties)

(a) $^{176}Yb/^{177}Hf = (^{176}Yb/^{173}Yb)true \times (^{173}Yb/^{177}Hf)meas \times (M^{173}(Yb)/M^{177}(Hf))\beta(Hf)$, $\beta(Hf) = \ln(^{179}Hf/^{177}Hf\ true\ /\ ^{179}Hf/^{177}Hf measured)/\ln(M^{179}(Hf)/M^{177}(Hf))$, M=mass of respective isotope. The $^{176}Lu/^{177}Hf$ were calculated in a similar way by using the $^{175}Lu/^{177}Hf$ and $\beta(Yb)$.

(b) Mean Hf signal in volt.

(c) Uncertainties are quadratic additions of the within-run precision and the daily reproducibility of GJ1 zircon at 2SD (2 standard deviation).

(d) Initial $^{176}Hf/^{177}Hf$ and eHf calculated using the apparent Pb-Pb age determined by LA-ICP-MS dating (see column f), and the CHUR parameters: $^{176}Lu/^{177}Hf = 0.0336$, and $^{176}Hf/^{177}Hf = 0.282785$ (Bouvier et al., 2008).

(e) two stage model age in 10^9 years using the measured $^{176}Lu/^{177}Lu$ of each spot (first stage = age of zircon), a value of 0.0113 for the average continental crust (second stage), and a juvenile crust (NC) $^{176}Lu/^{177}Lu$ and $^{176}Hf/^{177}Hf$ of 0.0384 and 0.28318, respectively.

(f) Pb-Pb age determined by LA-ICP-MS

APPENDIX D – U-PB LA-ICPMS DATA – SAMPLE 351

U-Pb-Th LA-ICPMS data of detrital zircon grains from sample 351

grain	^{207}Pb[a] (cps)	U[b] (ppm)	Pb[b] (ppm)	Th[b]/U	^{206}Pbc[c] (%)	$^{206}Pb/^{238}U$[d]	±2σ (%)	$^{207}Pb/^{235}U$[d]	±2σ (%)	$^{207}Pb/^{206}Pb$[d]	±2σ (%)	rho[e]	$^{206}Pb/^{238}U$	±2σ (Ma)	$^{207}Pb/^{235}U$	±2σ (Ma)	$^{207}Pb/^{206}Pb$	±2σ (Ma)	conc.[f] (%)
U07	146836	170	112	0.52	0.05	0.50150	1.9	12.8	2.0	0.1851	0.6705	0.94	2620	41	2665	19	2699	11	97
U08	109810	68	66	0.70	b.d.	0.66600	2.0	24.49	2.2	0.2667	0.9639	0.90	3290	52	3288	22	3287	15	100
U09	52874	69	38	0.68	0.73	0.39510	3.2	10.7	3.4	0.1963	0.9449	0.96	2146	59	2497	32	2796	15	77
U10	167079	130	93	0.04	0.05	0.58160	1.8	18.83	2.2	0.2349	1.234	0.82	2955	43	3033	21	3086	20	96
U11	78518	74	57	0.55	b.d.	0.56350	1.9	16.07	2.1	0.2068	0.9323	0.90	2881	45	2881	21	2881	15	100
U12c	132841	116	91	0.49	0.35	0.58290	2.2	17.52	2.4	0.218	0.9941	0.91	2961	52	2964	23	2966	16	100
U13r	123242	104	76	0.23	0.90	0.58080	2.1	17.36	2.3	0.2168	0.8655	0.93	2952	51	2955	22	2957	14	100
U14	116385	80	49	0.26	b.d.	0.46350	2.2	14.66	2.6	0.2294	1.533	0.81	2455	44	2793	25	3048	25	81
U15	123813	107	93	0.29	0.62	0.65150	2.8	22.94	3.1	0.2554	1.26	0.91	3234	72	3224	30	3218	20	100
U16	52435	45	34	0.35	1.39	0.57480	2.2	17.11	2.3	0.2159	0.6973	0.95	2928	52	2941	22	2950	11	99
U17	101067	125	85	0.52	0.97	0.51900	2.3	13.3	2.4	0.1858	0.6406	0.96	2695	52	2701	23	2706	11	100
U18	177597	197	110	0.21	0.33	0.44280	3.9	12.93	4.0	0.2119	0.9468	0.97	2363	78	2675	39	2920	15	81
U19	70863	74	59	0.61	b.d.	0.56990	2.7	16.18	2.8	0.2059	0.7466	0.96	2907	64	2887	27	2874	12	101
U20	110275	96	76	0.52	b.d.	0.58040	2.2	17.29	2.4	0.2161	0.9253	0.92	2950	53	2951	23	2952	15	100
U21	60672	67	49	0.64	b.d.	0.52370	2.0	13.41	2.3	0.1857	1.136	0.87	2715	45	2709	22	2705	19	100
U22c	114815	125	102	1.00	0.86	0.54330	2.0	14.83	2.2	0.198	0.9816	0.90	2797	45	2805	21	2810	16	100
U23r	114170	113	88	0.72	0.55	0.55330	2.0	15.3	2.2	0.2005	0.8362	0.93	2839	47	2834	21	2831	14	100
U24	72160	44	43	0.68	1.13	0.66010	2.1	24.24	2.3	0.2664	0.9314	0.91	3268	53	3278	22	3285	15	99
U25c	200150	179	147	0.71	0.06	0.57990	1.9	17.21	2.0	0.2152	0.7335	0.93	2948	45	2947	20	2945	12	100
U26r	89279	75	58	0.44	0.16	0.58290	1.8	17.39	2.0	0.2163	0.9591	0.88	2961	42	2956	19	2954	15	100
U27	147240	149	126	1.27	0.60	0.53210	1.8	13.68	1.9	0.1865	0.5949	0.95	2750	40	2728	18	2711	10	101
U28	188029	156	131	0.73	0.69	0.59010	1.8	18	2.0	0.2212	0.7952	0.92	2990	44	2990	19	2990	13	100
U29c	65946	85	63	0.70	0.29	0.53000	1.6	13.57	1.9	0.1857	1.049	0.84	2742	36	2720	18	2704	17	101

U30r	47393	52	37	0.63	b.d.	0.52410	1.9	13.38	2.1	0.1852	0.9016	0.90	2717	43	2707	20	2700	15	101
U37	191427	119	112	0.49	b.d.	0.67300	1.8	25.01	2.1	0.2695	1.103	0.86	3317	48	3309	21	3303	17	100
U38c	264565	179	177	0.69	b.d.	0.67630	2.3	25.11	2.5	0.2693	0.9024	0.93	3330	60	3312	24	3302	14	101
U39r	173016	146	95	0.14	b.d.	0.52710	2.1	17.11	2.2	0.2354	0.8352	0.93	2729	46	2941	22	3089	13	88
U40	88057	52	50	0.56	b.d.	0.68250	2.1	25.93	2.4	0.2756	1.254	0.86	3354	55	3344	24	3338	20	100
U41	137109	127	90	0.25	0.16	0.56180	2.8	15.71	2.9	0.2028	0.8717	0.95	2874	65	2859	28	2849	14	101
U42	60821	60	46	0.53	b.d.	0.56520	2.1	15.98	2.3	0.2051	0.8403	0.93	2888	49	2876	22	2867	14	101
U43	149530	191	121	0.67	b.d.	0.46870	2.2	11.62	2.4	0.1798	0.8503	0.93	2478	45	2574	22	2651	14	93
U44c	37737	34	23	0.70	b.d.	0.45430	2.9	16.98	3.1	0.2711	1.137	0.93	2415	58	2934	30	3312	18	73
U45r	137411	99	73	0.29	0.58	0.56420	2.3	17.94	2.4	0.2307	0.7689	0.95	2884	53	2987	23	3057	12	94
U46	126914	107	91	0.75	0.35	0.59080	2.0	18.15	2.2	0.2228	0.9079	0.91	2993	48	2998	21	3001	15	100
U47	89484	86	63	0.42	0.73	0.55660	2.0	15.55	2.1	0.2026	0.7175	0.94	2853	45	2849	20	2847	12	100
U48	280771	248	192	0.42	b.d.	0.58260	1.7	17.33	1.9	0.2157	0.7895	0.91	2959	41	2953	18	2949	13	100
U49	87520	49	48	0.71	1.02	0.68010	1.9	25.25	2.1	0.2692	0.896	0.90	3345	49	3318	21	3301	14	101
U50	270211	200	166	0.31	0.23	0.62890	1.8	20.69	2.1	0.2386	0.9601	0.89	3145	46	3124	20	3111	15	101
U51	118156	157	110	0.53	0.55	0.52300	1.9	13.26	2.1	0.1839	0.7139	0.94	2712	43	2698	20	2689	12	101
U52	73992	71	59	0.76	0.84	0.58470	1.9	16.58	2.1	0.2056	0.8315	0.92	2968	46	2911	20	2871	14	103
U53	320434	323	206	0.05	0.35	0.52400	1.8	15.94	2.7	0.2207	2.094	0.64	2716	39	2873	26	2986	34	91
U54	122088	232	127	0.60	0.23	0.40080	3.0	9.725	3.1	0.176	0.6095	0.98	2173	55	2409	29	2615	10	83
U55	43327	41	33	0.71	b.d.	0.56310	2.1	15.93	2.4	0.2052	1.312	0.84	2879	48	2873	24	2868	21	100
U56	128797	186	105	0.31	0.06	0.44740	1.9	11.22	2.1	0.1818	0.8926	0.91	2384	39	2541	20	2669	15	89
U57	140724	126	106	0.67	b.d.	0.59470	2.1	17.92	2.3	0.2185	1.016	0.90	3008	50	2985	22	2970	16	101
U58	140441	261	131	0.89	0.88	0.32430	2.6	8.138	2.7	0.182	0.816	0.95	1811	42	2246	25	2671	14	68
U59	72635	87	53	0.69	0.15	0.44920	2.5	12.16	2.6	0.1964	0.8143	0.95	2392	50	2617	25	2796	13	86
U60	108736	94	80	0.77	b.d.	0.59030	1.9	17.66	2.1	0.2169	0.7846	0.92	2991	46	2971	20	2958	13	101
U67	161668	140	112	0.49	0.03	0.59320	1.9	18.06	2.0	0.2208	0.6971	0.94	3003	45	2993	19	2987	11	101
U68	218957	207	157	0.52	0.17	0.55590	2.2	15.38	2.3	0.2007	0.9017	0.92	2850	50	2839	23	2832	15	101
U69	25833	30	22	0.81	0.16	0.52600	2.0	13.6	2.3	0.1875	1.184	0.86	2725	44	2722	22	2720	20	100

U70	34073	29	23	0.46	b.d.	0.59000	2.1	17.73	2.2	0.218	0.8102	0.93	2989	50	2975	22	2966	13	101
U71	106109	115	107	1.32	b.d.	0.58300	1.9	16.49	2.1	0.2052	0.7052	0.94	2961	46	2906	20	2868	11	103
U72	75060	63	47	0.13	0.06	0.60090	2.1	18.39	2.5	0.222	1.302	0.85	3033	51	3011	24	2995	21	101
U73	101179	112	84	0.81	b.d.	0.52610	2.2	13.6	2.3	0.1876	0.6362	0.96	2725	50	2723	22	2721	10	100
U74	178146	158	116	0.28	0.07	0.57430	2.1	16.79	2.3	0.212	0.9417	0.91	2926	49	2923	22	2921	15	100
U75	66388	68	45	0.28	b.d.	0.52270	2.2	13.38	2.4	0.1857	1.078	0.90	2711	49	2707	23	2704	18	100
U76	72849	63	47	0.63	0.63	0.53340	2.2	16.16	2.4	0.2197	0.9836	0.91	2756	49	2886	23	2979	16	93
U77	75606	77	62	0.91	0.11	0.55750	1.9	15.35	2.2	0.1997	1.006	0.89	2856	45	2837	21	2823	16	101
U78	308717	210	198	0.57	b.d.	0.66030	2.6	24.23	2.7	0.2661	0.8328	0.95	3268	67	3278	27	3283	13	100
U79	152771	181	109	0.26	0.00	0.47480	4.3	12.22	4.5	0.1867	1.041	0.97	2505	91	2622	43	2713	17	92
U80	145441	174	117	0.36	0.43	0.52010	2.4	14.51	2.5	0.2024	0.7669	0.95	2699	52	2784	24	2846	12	95
U81	113480	124	106	1.45	0.35	0.51980	2.1	13.2	2.3	0.1842	0.9649	0.90	2698	45	2694	22	2691	16	100
U82	160359	127	101	0.60	0.45	0.57810	2.4	17.27	2.6	0.2167	0.9725	0.93	2941	58	2950	26	2956	16	99
U83	226919	232	172	0.58	b.d.	0.54180	2.0	15.05	2.3	0.2015	1.127	0.87	2791	46	2819	22	2839	18	98
U84	84200	96	71	0.69	b.d.	0.52960	2.4	13.57	2.6	0.1859	0.9377	0.93	2740	54	2720	25	2706	15	101
U85	109404	110	81	0.38	0.47	0.56460	1.9	15.88	2.0	0.204	0.79	0.92	2886	44	2870	20	2859	13	101
U86	134780	254	143	0.42	1.85	0.43660	3.9	10.11	4.1	0.1679	1.149	0.96	2335	77	2445	38	2537	19	92
U87	189857	183	132	0.45	0.09	0.53370	1.9	15	2.0	0.2038	0.7977	0.92	2757	42	2815	19	2857	13	96
U88	69222	57	46	0.59	2.43	0.57380	2.2	16.79	2.4	0.2122	0.9103	0.93	2924	53	2923	24	2923	15	100
U89	190923	209	133	0.45	0.14	0.47470	3.4	13.27	3.6	0.2027	1.107	0.95	2504	71	2699	34	2848	18	88
U90	127170	140	102	0.34	b.d.	0.56460	2.7	15.31	2.9	0.1966	1.085	0.93	2886	63	2835	28	2798	18	103
U91	64541	65	53	0.81	0.70	0.56240	2.1	15.93	2.3	0.2055	0.7451	0.94	2876	50	2873	22	2870	12	100
U92	82252	81	59	0.37	0.52	0.55530	1.9	15.43	2.2	0.2016	1.103	0.87	2847	44	2842	21	2839	18	100
U93	143600	162	116	0.60	0.05	0.52540	1.9	13.54	2.1	0.1868	0.7625	0.93	2722	43	2718	20	2714	13	100
U94	148690	178	107	0.51	0.47	0.43050	2.2	12.02	2.5	0.2026	1.228	0.87	2308	42	2606	24	2847	20	81
U95	69919	66	53	0.67	1.15	0.57580	1.7	16.25	1.9	0.2046	0.772	0.91	2932	40	2891	18	2864	13	102
U96	113352	99	74	0.25	0.29	0.58710	1.9	17.59	2.0	0.2173	0.6652	0.95	2978	46	2968	20	2961	11	101
U97	106517	65	69	1.10	b.d.	0.67280	1.9	24.82	2.2	0.2676	1.012	0.89	3317	51	3301	22	3292	16	101

U98	112819	98	84	0.84	b.d.	0.58480	2.0	17.6	2.4	0.2183	1.34	0.83	2968	48	2968	23	2968	22	100
U99	68613	58	47	0.60	0.23	0.58400	1.9	17.41	2.3	0.2162	1.392	0.80	2965	45	2958	23	2953	22	100
U100	123227	132	84	0.36	0.28	0.49810	1.9	12.92	2.2	0.1881	1.024	0.88	2606	41	2674	21	2726	17	96
U107	117538	110	91	0.47	0.78	0.61980	1.8	18.59	1.9	0.2175	0.7539	0.92	3109	44	3021	19	2962	12	105
U108	178425	153	143	1.07	0.04	0.60780	1.8	18.46	2.0	0.2203	0.9793	0.87	3061	43	3014	20	2983	16	103
U109	341607	230	146	0.06	0.16	0.51410	2.6	16.7	2.8	0.2356	1.163	0.91	2674	57	2918	27	3091	19	87
U110	101610	93	77	0.85	0.08	0.56110	2.1	15.82	2.3	0.2045	0.9013	0.92	2871	50	2866	22	2863	15	100
U111	167010	145	116	0.48	0.93	0.59060	1.9	17.58	2.0	0.2159	0.6571	0.95	2992	46	2967	20	2950	11	101
U112	226242	175	134	0.12	0.23	0.61940	1.8	20.05	2.1	0.2347	1.041	0.87	3108	45	3094	21	3084	17	101
U113	196932	173	152	0.89	0.00	0.59040	1.9	17.63	2.2	0.2166	0.9965	0.89	2991	47	2970	21	2956	16	101
U114	129865	180	106	0.72	0.65	0.42260	4.4	10.84	4.5	0.186	0.8464	0.98	2272	85	2509	42	2707	14	84
U115	222232	223	175	1.09	b.d.	0.54090	1.9	14.83	2.0	0.1988	0.6432	0.95	2787	42	2804	19	2816	11	99
U116	99035	86	71	0.49	1.22	0.60930	2.0	17.87	2.2	0.2127	0.9603	0.90	3067	48	2983	21	2926	16	105
U117r	168494	178	112	0.01	0.56	0.51800	2.2	15.97	2.6	0.2236	1.388	0.84	2691	48	2875	25	3007	22	89
U118c	115689	96	73	0.03	0.17	0.62370	2.3	20.5	2.5	0.2384	1.004	0.91	3125	56	3115	24	3109	16	100
U119	173891	148	113	0.08	0.35	0.62000	1.9	19.09	2.2	0.2233	1.042	0.88	3110	48	3046	21	3004	17	104
U120	167410	204	161	0.70	0.20	0.55690	2.5	15.47	2.6	0.2015	0.7146	0.96	2854	58	2845	25	2838	12	101
U121	81107	91	70	0.99	0.50	0.52170	1.9	13.32	2.0	0.1851	0.7401	0.93	2706	42	2702	19	2700	12	100
U122	73691	71	52	0.44	0.60	0.55940	1.8	15.62	1.9	0.2025	0.6406	0.94	2864	42	2854	19	2846	10	101
U123	40662	32	24	0.45	1.77	0.55580	3.2	18.4	3.8	0.2401	1.995	0.85	2849	74	3011	37	3120	32	91
U124	197774	234	155	0.35	0.37	0.52770	2.0	13.62	2.2	0.1872	0.8784	0.92	2732	45	2724	21	2718	14	101
U125	95545	69	58	0.50	0.66	0.59780	2.0	21.46	2.4	0.2604	1.419	0.81	3021	48	3160	24	3249	22	93
U126	133175	135	104	0.54	0.35	0.55350	2.1	15.33	2.2	0.2009	0.824	0.93	2840	48	2836	21	2834	13	100
U127	140509	80	79	0.54	0.63	0.68110	1.9	26	2.0	0.2768	0.6842	0.94	3349	50	3346	20	3345	11	100
U128	139743	158	116	0.61	b.d.	0.54020	2.3	14.62	2.7	0.1962	1.36	0.86	2784	52	2791	26	2795	22	100
U129	35951	38	29	0.45	0.26	0.56370	2.1	15.16	2.4	0.1951	1.122	0.88	2882	49	2825	23	2785	18	103
U130	68330	87	61	0.41	1.23	0.53470	2.4	13.88	2.6	0.1882	1.034	0.92	2761	53	2741	25	2726	17	101
U131	146339	170	121	0.89	0.05	0.47730	2.7	12.44	2.8	0.189	0.6313	0.97	2515	57	2638	26	2733	10	92

U132	92256	82	64	0.43	b.d.	0.58290	2.1	17.49	2.3	0.2176	1.058	0.89	2961	49	2962	23	2963	17	100
U133	262259	202	152	0.04	0.05	0.61400	2.1	19.9	2.4	0.2351	0.9691	0.91	3086	53	3087	23	3087	15	100
U134	211159	191	135	0.05	b.d.	0.58110	2.1	17.47	2.2	0.218	0.8056	0.93	2953	50	2961	22	2966	13	100
U135	171906	295	166	0.22	b.d.	0.45010	2.3	11.8	2.7	0.1902	1.263	0.88	2396	47	2589	25	2744	21	87
U136	196330	217	148	0.45	0.33	0.46300	5.0	17.18	5.2	0.2692	1.223	0.97	2453	103	2945	51	3301	19	74
U137	23451	21	16	0.29	0.37	0.58230	4.6	18.57	4.8	0.2314	1.075	0.97	2958	111	3020	47	3061	17	97
U138	140151	161	117	0.67	b.d.	0.52270	2.1	13.54	2.4	0.1878	1.066	0.90	2711	48	2718	23	2723	18	100
U139	102284	129	94	0.46	0.83	0.53420	4.0	14.32	4.2	0.1943	1.267	0.95	2759	90	2771	41	2779	21	99
U140	117200	117	88	0.49	b.d.	0.55500	1.9	15.47	2.1	0.2022	0.8712	0.91	2846	44	2845	20	2844	14	100
U141	233043	174	142	0.03	0.26	0.66510	2.2	22.04	2.3	0.2404	0.9095	0.92	3287	56	3186	23	3122	14	105
U142	179729	150	128	0.42	0.52	0.63790	2.0	19.41	2.2	0.2207	0.9823	0.90	3181	50	3062	22	2986	16	107
U143	151753	143	121	0.68	b.d.	0.59990	1.7	17.09	2.1	0.2065	1.284	0.80	3030	41	2940	21	2879	21	105
U144	256446	128	130	0.53	b.d.	0.70740	1.9	28.49	2.2	0.2921	1.173	0.85	3449	51	3436	22	3429	18	101
U145	144113	167	115	0.25	0.36	0.54830	3.3	15.01	3.4	0.1985	0.9396	0.96	2818	76	2816	33	2814	15	100
U146	233602	222	166	0.38	0.77	0.55650	3.9	18.76	4.4	0.2445	1.996	0.89	2852	90	3030	43	3150	32	91
U147c	145999	147	108	0.69	0.57	0.52370	2.7	14.77	2.9	0.2046	1.162	0.92	2715	60	2801	28	2863	19	95
U148r	207419	202	150	0.36	0.47	0.56920	2.5	16.19	2.6	0.2063	0.8535	0.94	2905	58	2888	25	2877	14	101
U149	174492	176	136	0.65	0.15	0.55450	1.9	15.53	2.1	0.2032	0.8167	0.92	2844	44	2848	20	2852	13	100
U150	220153	196	151	0.44	0.02	0.58060	1.8	17.1	2.1	0.2136	0.9656	0.88	2951	43	2940	20	2933	16	101
U157c	156135	136	110	0.52	0.19	0.59230	2.0	18.09	2.3	0.2216	1.012	0.90	2999	49	2995	22	2992	16	100
U158r	111231	101	80	0.26	b.d.	0.61710	2.0	18.57	2.2	0.2183	0.8368	0.92	3098	50	3020	21	2968	13	104
U159	185007	176	138	0.45	0.56	0.58890	2.0	16.72	2.3	0.206	1.02	0.89	2985	49	2919	22	2874	17	104
U160	141642	149	112	0.50	0.52	0.55670	2.1	15.35	2.3	0.2	0.9172	0.92	2853	49	2837	22	2826	15	101
U161	142484	161	122	0.44	b.d.	0.57080	2.1	16.21	2.6	0.206	1.502	0.82	2911	50	2889	25	2874	24	101
U162	44398	45	38	2.07	2.67	0.59080	4.6	18.49	4.8	0.227	1.39	0.96	2992	110	3016	47	3031	22	99
U163	227236	237	180	0.45	0.31	0.56830	2.2	16.26	2.4	0.2075	1.076	0.90	2901	51	2892	23	2886	17	101
U164	32805	21	20	0.54	0.50	0.65640	2.3	23.86	2.5	0.2636	1.049	0.91	3253	59	3263	25	3268	17	100
U165	253450	255	181	0.09	0.15	0.57520	3.3	17.27	3.4	0.2177	1.026	0.95	2929	77	2950	33	2964	17	99

U166	106080	131	68	0.69	b.d.	0.37040	3.6	9.589	3.9	0.1878	1.378	0.93	2031	64	2396	36	2723	23	75
U167	110123	96	70	0.39	b.d.	0.54120	3.7	14.99	4.0	0.2008	1.462	0.93	2789	85	2814	39	2833	24	98
U168	199365	172	155	1.05	0.18	0.58550	1.9	17.66	2.0	0.2188	0.5838	0.95	2971	45	2971	19	2972	9	100
U169	178098	186	133	0.50	0.06	0.52130	2.1	14.3	2.3	0.199	1.059	0.89	2705	46	2770	22	2818	17	96
U170	172570	186	131	0.38	0.16	0.53870	3.2	15.59	3.3	0.2099	0.7789	0.97	2778	73	2852	32	2905	13	96
U171	153806	341	234	0.52	1.18	0.53220	4.6	14.48	5.0	0.1974	1.974	0.92	2751	105	2782	49	2805	32	98
U172	184998	176	132	0.52	0.02	0.55390	2.5	15.77	2.6	0.2064	0.8606	0.94	2842	57	2863	25	2878	14	99
U173	118605	158	98	0.46	0.66	0.47120	2.6	11.73	2.8	0.1805	0.9928	0.94	2489	55	2583	27	2657	16	94
U174	123662	140	96	0.56	0.67	0.49880	2.1	13.93	2.3	0.2025	0.9403	0.91	2609	46	2745	22	2847	15	92
U175	168023	165	134	0.43	0.16	0.60420	2.1	17.93	2.2	0.2153	0.7442	0.94	3047	51	2986	21	2946	12	103
U176	59702	36	34	0.53	b.d.	0.66860	2.2	25.06	2.4	0.2719	1.011	0.91	3300	56	3311	24	3317	16	99
U177	150964	262	119	0.37	0.58	0.33910	4.1	9.04	4.3	0.1934	1.203	0.96	1882	68	2342	40	2771	20	68
U178	129151	158	121	0.58	b.d.	0.55050	2.2	15.74	2.3	0.2074	0.8817	0.93	2827	50	2861	23	2885	14	98
U179	129502	122	95	0.52	0.08	0.57660	1.8	16.04	1.9	0.2017	0.6348	0.94	2935	43	2879	18	2840	10	103
U180	140799	131	105	0.43	0.49	0.60000	2.5	17.16	2.8	0.2074	1.287	0.89	3030	61	2944	27	2886	21	105

Notes

Spot size = 25µm; depth of crater ~15µm. $^{206}Pb/^{238}U$ error is the quadratic additions of the within run precision (2 SE) and the external reproducibility (2 SD) of the reference zircon. $^{207}Pb/^{206}Pb$ error propagation (^{207}Pb signal dependent) following Gerdes & Zeh (2009). $^{207}Pb/^{235}U$ error is the quadratic addition of the $^{207}Pb/^{206}Pb$ and $^{206}Pb/^{238}U$ uncertainty.

[a]Within run background-corrected mean ^{207}Pb signal in cps (counts per second).

[b] U and Pb content and Th/U ratio were calculated relative to BB1 reference zircon.

[c] percentage of the common Pb on the ^{206}Pb. b.d. = below dectection limit.

[d] corrected for background, within-run Pb/U fractionation (in case of $^{206}Pb/^{238}U$) and common Pb using Stacy and Kramers (1975) model Pb composition and subsequently normalised to BB1 (ID-TIMS value/measured value); $^{207}Pb/^{235}U$ calculated using $^{207}Pb/^{206}Pb/(^{238}U/^{206}Pb*1/137.88)$

[e] rho is the $^{206}Pb/^{238}U/^{207}Pb/^{235}U$ error correlation coefficient.

[f] degree of concordance = $^{206}Pb/^{238}U$ age / $^{207}Pb/^{206}Pb$ age x 100